

Development of suspended thermorefectance technique and its application in  
thermal property measurement of semiconductor materials

by

Dipta Sarkar

B.S., Chittagong University of Engineering and Technology, 2014

AN ABSTRACT OF A DISSERTATION

submitted in partial fulfillment of the requirements for the degree

DOCTOR OF PHILOSOPHY

Alan Levin Department of Mechanical and Nuclear Engineering  
Carl R. Ice College of Engineering

KANSAS STATE UNIVERSITY  
Manhattan, Kansas

2020

## **Abstract**

This dissertation details the development of a new scientific tool for the thermal characterization of freestanding micro/nano-scale materials, with specific application to thin films. The tool consists of a custom-designed and calibrated opto-electric system with superior spatial and temporal resolutions in thermal measurement. The tool, termed as Suspended ThermoReflectance (STR), can successfully perform thermal mappings at the submicron level and is able to produce unconstrained thermal conductivity unlike other optical measurement techniques where independent conductivity measurement is not possible due to their reliance on heat capacity. STR works by changing the temperature of a material and collecting the associated change in light reflection from multiple points on the sample surface. The reflection is a function of the material being tested, the wavelength of the probe light and the composition of the specimen for transparent and quasi-transparent materials. Coupling the change in reflection, along the sample's length, with the knowledge of heat conduction allows for the determination of the thermal properties of interest. A thermal analytical model is developed and incorporated with optical equations to characterize the conductivity of thin films. The analytical model is compared with a finite element model to check its applicability in the STR experiment and data analysis. Ultimately, thermal conductivity of 2  $\mu\text{m}$  and 3  $\mu\text{m}$  thick Si samples were determined using STR at a temperature range of 20K – 350K and compared to literature as a validation of the technique.

The system was automated using a novel LabView-based program. This program allowed the user to control the equipment including electronics, optics and optical cryostat. Moreover, data acquisition and real-time monitoring of the system are also accomplished through this computer application.

A description of the development, fabrication and characterization of the freestanding thin films is detailed in this dissertation. For the most part, the thin films were fabricated using standard microfabrication techniques. However, different dry and wet etching techniques were compared for minimum surface roughness to reduce light scattering. The best etching technique was used to trim the Si films for the desired thicknesses. Besides, vapor HF was used to avoid stiction-failure during the release of suspended films.

Development of suspended thermorefectance technique and its application in  
thermal property measurement of semiconductor materials

by

Dipta Sarkar

B.S., Chittagong University of Engineering and Technology, 2014

A DISSERTATION

submitted in partial fulfillment of the requirements for the degree

DOCTOR OF PHILOSOPHY

Alan Levin Department of Mechanical and Nuclear Engineering  
Carl R. Ice College of Engineering

KANSAS STATE UNIVERSITY  
Manhattan, Kansas

2020

Approved by:

Major Professor  
Gurpreet Singh



# **Copyright**

© Dipta Sarkar 2020.

## **Abstract**

This dissertation details the development of a new scientific tool for the thermal characterization of freestanding micro/nano-scale materials, with specific application to thin films. The tool consists of a custom-designed and calibrated opto-electric system with superior spatial and temporal resolutions in thermal measurement. The tool, termed as Suspended ThermoReflectance (STR), can successfully perform thermal mappings at the submicron level and is able to produce unconstrained thermal conductivity unlike other optical measurement techniques where independent conductivity measurement is not possible due to their reliance on heat capacity. STR works by changing the temperature of a material and collecting the associated change in light reflection from multiple points on the sample surface. The reflection is a function of the material being tested, the wavelength of the probe light and the composition of the specimen for transparent and quasi-transparent materials. Coupling the change in reflection, along the sample's length, with the knowledge of heat conduction allows for the determination of the thermal properties of interest. A thermal analytical model is developed and incorporated with optical equations to characterize the conductivity of thin films. The analytical model is compared with a finite element model to check its applicability in the STR experiment and data analysis. Ultimately, thermal conductivity of 2  $\mu\text{m}$  and 3  $\mu\text{m}$  thick Si samples were determined using STR at a temperature range of 20K – 350K and compared to literature as a validation of the technique.

The system was automated using a novel LabView-based program. This program allowed the user to control the equipment including electronics, optics and optical cryostat. Moreover, data acquisition and real-time monitoring of the system are also accomplished through this computer application.

A description of the development, fabrication and characterization of the freestanding thin films is detailed in this dissertation. For the most part, the thin films were fabricated using standard microfabrication techniques. However, different dry and wet etching techniques were compared for minimum surface roughness to reduce light scattering. The best etching technique was used to trim the Si films for the desired thicknesses. Besides, vapor HF was used to avoid stiction-failure during the release of suspended films.

## **Acknowledgement**

I would like to extend my deepest gratitude to Dr. Gurpreet Singh for unparalleled support he has provided me in last six months. He started guiding me when I needed it most and helped me a lot to determine my career. I also want to thank Dr. Zayd Leseman who introduced me to the amazing world of micro/nano-fabrication and characterization. His knowledge and guidance, at the beginning of my PhD research, made me passionate about this field.

I appreciate the continuous support from Mechanical and Nuclear Engineering Department in last 4 years through teaching assistantship. I am grateful to Dr. Steven Eckels who made this happen. My special thanks to Dr. Terry Beck for his suggestions and encouragement in heat transfer related problems.

I had great pleasure of working with, and taking help at different stages of my research, from my friends and colleagues: Priyarshini Ghosh and Mohammadhosein Baboly. A big part of my research involves micro-fabrication which would not have been possible without using the cleanroom of SMART laboratory at Kansas State University.

## **Dedication**

This dissertation is dedicated to my mother, **Mrs. Rina Sarkar**, and my father, **Mr. Dipak Kanti Sarkar**, who never fail to amaze me with their insightful suggestions at every aspect of my life. They are my inspiration to reach great heights, and comfort when I am in distress.

# Table of Contents

List of Figures .....	xiii
List of Tables .....	xix
List of Abbreviations and Acronyms .....	xx
Nomenclature .....	xxii
<b>Chapter 1 - Introduction .....</b>	<b>1</b>
1.1 Contact Temperature Measurement Techniques.....	2
1.1.1 Steady-state Measurement Techniques .....	2
1.1.2 Transient Measurement Techniques.....	3
1.2 Non-Contact or Thermorefectance Techniques .....	4
1.2.1 Transient Thermorefectance.....	5
1.2.2 Time Domain Thermorefectance .....	7
1.2.3 Frequency Domain Thermorefectance .....	9
1.3 Previous Measurement of Thermal Conductivity .....	10
1.4 Suspended Thermorefectance (STR) .....	12
1.4.1 Significance of STR Over Other Techniques.....	14
<b>Chapter 2 - Theory: Thermorefectance and Heat Transfer .....</b>	<b>16</b>
2.1 Correlation Between Temperature and Reflection.....	16
2.2 One-Dimensional Heat Transfer Model.....	19
2.2.1 Steady-State Regime .....	34
2.2.2 Transient Regime .....	35
2.2.3 Harmonic Regime .....	36
2.3 Comparison of 1D Model with FEM .....	36
2.4 Phase Shift Along the Cantilever .....	39
<b>Chapter 3 - Experimental Consideration .....</b>	<b>41</b>
3.1 Comparison Between 1D Analytical Model and 3D FEM with Application of Heat Perpendicular to Tip .....	41
3.2 Backside Probing Validation .....	47
3.3 Cantilever's Base Temperature Validation .....	49
3.4 Probe Heating and Its Application .....	55

<b>Chapter 4 - Experimental Setup.....</b>	<b>61</b>
4.1 Optics .....	61
4.2 Electronics.....	65
4.3 Laser Selection .....	69
4.4 Sample Holder.....	74
4.5 High Vacuum System .....	77
4.6 Cryogenic Setup .....	80
4.6.1 The Gifford-McMahon refrigeration cycle .....	81
<b>Chapter 5 - Sample Fabrication .....</b>	<b>83</b>
5.1 Thinning Processes for Silicon Film.....	85
5.1.1 Tetramethylammonium Hydroxide (TMAH) Etch .....	85
5.1.2 Potassium Hydroxide (KOH) Etch.....	86
5.1.3 Xenon Difluoride (XeF <sub>2</sub> ) Etch .....	87
5.1.4 Plasma Etch .....	88
5.1.5 Oxide Growth and Removal.....	89
5.2 Relation Between Light Scattering and Surface Roughness.....	91
5.3 Photomask Design.....	94
5.4 The Suspended Cantilevers .....	96
5.4.1 Cleaning Procedure .....	96
5.4.2 Cantilever Fabrication .....	98
5.4.3 Cantilever Beam Geometry Characterization.....	100
<b>Chapter 6 - Experimental Results .....</b>	<b>102</b>
6.1 Laser Beam profile.....	102
6.2 Suspended ThermoReflectance Data .....	104
6.2.1 Probe Frequency Selection.....	105
6.2.2 Temperature and Thermal Conductivity Measurement.....	106
<b>Chapter 7 - Conclusion and Future Work.....</b>	<b>111</b>
7.1 Suggestions for Future work .....	112
List of Publications .....	115
<b>References .....</b>	<b>116</b>
<b>Appendices.....</b>	<b>133</b>

Appendix A - 1D Heat Diffusion Model .....	134
Appendix B – Wavelength Dependence of Optical Properties.....	141
Appendix C – Thickness Dependence of Optical Properties.....	154
Appendix D – STR Control and Data Collection Program .....	158



## List of Figures

Figure 1.1 Steady-state methods for measuring a) cross-plane and b) in-plane thermal conductivity of thin films. In cross-plane measurement, the metal strip serves as both heater and temperature sensor, but in-plane measurement requires a separate temperature sensor.[45].....	3
Figure 1.2 Schematic diagram of a typical $3\omega$ method for thermal characterization of thin films, measuring thermal conductivity of the device layer of a silicon-on-insulator (SOI) wafer.[12].....	4
Figure 1.3 Basic thermoreflectance measurement principle. a) Pump & probe are on the same side and Si layer is attached to a substrate[53], [56], b) Pump & probe are on the opposite side and Si layer is suspended from the substrate. ....	5
Figure 1.4 a) Relation between pump-probe delay and TTR signal for 20 nm Au film evaporated on a glass substrate.[58] b) Laser path and electrical signals in TTR experiment.[53] .....	6
Figure 1.5 TDTR measurement technique: (a) modulated pump beam input; (b) surface temperature of the sample in response to the pump input; (c) probe pulses at the sample delayed by a time $\tau$ ; and (d) measured probe and reference signal.[76] .....	8
Figure 1.6 Transfer function, $Z(\omega)$ , with the thermal response of the system (analytical model) and the properties of the pump and probe beams.[73] .....	9
Figure 1.7 Two experimental arrangements for FDTR: (a) system based on CW lasers; (b) system based on pulsed laser.[13] .....	10
Figure 1.8 STR setup to measure temperature along the sample. Samples are inside a cryostat to ensure ultra-high vacuum and low-temperature environment.[95] .....	13
Figure 2.1 Thermal conductivity of Si: Variation with temperature change for bulk silicon and thin films of silicon of different doping and crystallinity. (Adapted from Ref. [29] - [32]). 20	
Figure 2.2 1D solid bar with heat flux at the tip and constant temperature at the opposite end. Steady-State and transient heat flux have a constant flux component, but harmonic heat flux has frequency. ....	21
Figure 2.3 Direction of applied heat in FEM .....	37
Figure 2.4 Comparison of 1D model and FEM for steady-state heat conduction, including three L/w ratios (5, 50, and 100). ....	38

Figure 2.5 Comparison of 1D model and FEM for transient heat conduction, including three L/w ratios (5, 50, and 100). .....	38
Figure 2.6 Comparison of 1D model and FEM for harmonic heat conduction, including three L/w ratios (5, 50, and 100). .....	39
Figure 2.7 Phase shift from Eqn. (149) for the temperature profile along the cantilever of various L/w. ....	40
Figure 3.1 a) Cantilever beam with fixed end attached to the substrate with L/w of 10; b) STR experimental setup, laser heating of the sample, and backside probing along the length; c) surface temperature and heat flow direction only for the cantilever beam; d) isotherm contour plot for the cantilever (Kelvin).[125].....	42
Figure 3.2 Temperature along the beam via 1D steady state heat equation (line) and FEM (points) .....	43
Figure 3.3 Temperature-time relationship for transient heat transfer in the cantilever beam at a dimensionless position of 0.995 obtained via heat equation (line) and FEM (points).....	44
Figure 3.4 Periodic change of temperature in the cantilever beam at a dimensionless position of 0.995 obtained via heat equation (line) and FEM (points). Diffusivity of the silicon changed the phase of harmonic temperature distribution along the beam. ....	45
Figure 3.5 Difference in temperature between developed 1D model and 3D FEM model with respect to L/w ratio of cantilever beam.....	46
Figure 3.6 Temperature distribution in 13 points along the length of the cantilever for a) L/w ratio of 10, b) L/w ratio of 100. Length equal to one width is shown in the x-axis. Insets show points considered in y-z plane and the color of each points represent the same color line in the graph. ....	47
Figure 3.7 Temperature distribution in 13 points along the length of the cantilever for a) width to thickness ratio of 2, b) width to thickness ratio of 0.5. Length equal to two width is shown in the x-axis. Inset shows the points considered in y-z plane and color of each points represent the same color line in the graph. ....	48
Figure 3.8 Distance from the tip, shown as the percentage of width, when temperature difference of all points in the y-z plane become 1% and 0.5%. Inset shows the points considered in the y-z plane to compare temperatures. ....	49

Figure 3.9 Geometric considerations for FEM analysis of the sample; the Si bar is attached to the SOI substrate like a cantilever. ....	51
Figure 3.10 Isothermal contours on the surface of the cantilever and substrate.....	52
Figure 3.11 1 mW and 15 mW laser power applied to several Si cantilevers with L/w ratios of 5, 50 and 100. Inset shows the base temperature of the cantilevers. ....	53
Figure 3.12 Base temperature rise of Si cantilevers at different thermal conductivity.....	54
Figure 3.13 Base and tip temperature ratio of Si cantilever for L/w = 5 (left y-axis) and L/w = 100 (right y-axis) with respect to the change in thermal conductivity.....	54
Figure 3.14 Temperature rise along the cantilever beam with only probe heating. The probe heat source is moved to various positions along the length of the cantilever of 100 L/w ratio. ..	56
Figure 3.15 Temperature rise along the cantilever of 100 L/w ratio. Both pump and probe lasers are heating the cantilever while pump is fixed at the tip, but probe moves along the points shown in the legend where x represents the dimensionless length of the cantilever. ....	57
Figure 3.16 Temperature rise by pump, probe and pump & probe heating along the cantilever. Temperature of probing points are shown where probe heating is applicable and temperatures at every 0.1 dimensionless length are shown for only pump heating. ....	58
Figure 3.17 Effect of probe power on the temperature measurement along the cantilever. ....	60
Figure 4.1 Schematic of the Suspended ThermoReflectance (STR) setup. BS: beam splitter, OL: objective lens, PD: photodetector, HV System: high vacuum system. Solid green line: pump laser train, Dotted green line: reflected pump laser train, Solid red line: probe laser train, Dotted red line: reflected probe laser train, Solid yellow line: control signal to the device either from computer or from another device, Dotted yellow line: high frequency signal from the signal generator, Solid blue line: data collection from the sensors to the devices and the computer. ....	62
Figure 4.2 Optical components of the experimental setup. The cryostat sits on a plate which can be adjusted on x, y, z and $\theta$ direction independently from rest of the setup. The full pump and probe side sit on separate x, y and z plate. ....	65
Figure 4.3 a) Simplified circuit of the photodetector and its connection. The dashed line contains circuit within the detector. b) A clean output signal from photodetector. The signal is measured with oscilloscope for visual representation.....	68

Figure 4.4 Anti-static polyester black fabric covers the full experimental setup. It restricts ambient light entering measurement area and keeps the setup dust free. ....	69
Figure 4.5 Light interaction with the layers of materials. Secondary reflection and transmission within the layers are omitted for simplicity.[134].....	70
Figure 4.6 Reflectivity, absorptivity and transmittivity of a 2 $\mu\text{m}$ silicon film at different laser wavelength. ....	72
Figure 4.7 (a) Reflectivity and Absorptivity of pump and probe lasers at different thicknesses of the silicon films, (b) The shadowed area from ‘figure a’ is zoomed to show the proper sample thickness for the experiment. ....	74
Figure 4.8 Schematic diagram of the optical cryostat head (model: ARS DMX-20)[142]. The sample holder position is depicted in highlighted area. ....	75
Figure 4.9 Solidworks drawing of a) Plain sample holder with base plate and top plate together, b) Pogo-pin sample holder with base and top plate, c) Only base plate of the sample holder, d) sample installer, Actual e) Plain and pogo-pin sample holder before chrome plating, e) pogo-pin sample holder sitting on the sample installer after chrome plating. ....	77
Figure 4.10 a) Schematic of the high vacuum system used to reduce the cryostat pressure, b) Actual vacuum system. ....	78
Figure 4.11 a) Scroll pump is on but turbo pump is off. The system is under medium vacuum. b) Both scroll and turbo pumps are on. The system is under high vacuum. ....	79
Figure 4.12 Basic schematic of the closed cycle optical cryostat. The cooling water pipes are connected to the cooler and vacuum valve is attached to the high vacuum system.[146]....	81
Figure 4.13 Schematic of the expander demonstrating the Gifford-McMahon refrigeration cycle.[146] a)High pressure helium enters the expander from the compressor, b) Low pressure helium goes out of the expander. ....	82
Figure 5.1 Schematic of silicon on insulator (SOI) wafer with $\{100\}$ crystal orientation. a) The 500 $\mu\text{m}$ thick silicon layer is termed as handle layer, b) 1 $\mu\text{m}$ buried silicon dioxide or BOX layer sits on top of the handle layer, c) 2 $\mu\text{m}$ device layer rests on top of the BOX layer, d) Final SOI wafer contains all the three layers. ....	84
Figure 5.2 Schematic diagram representing the chemical structure of: surface and respective binding of hydroxide ions during a wet etch process for (a) $\{100\}$ and (b) $\{111\}$ silicon wafers. ....	85

Figure 5.3 Relation between etch depth and surface roughness of the sample for different etching techniques. Samples are etched with # 25% TMAH at 65°C [198], ## 25% and 20 % TMAH at 70°C -80°C [199], \$ 5.6% to 57% KOH at 25°C [200], * XeF <sub>2</sub> gas by Chu et al.[180], ** XeF <sub>2</sub> gas by Sugano et al.[181], & Cl <sub>2</sub> and SF <sub>6</sub> plasma[187], ξ removal of thermally grown SiO <sub>2</sub> at 1100°C and 920°C [201].....	90
Figure 5.4 Relation between scattered light and etch depth of different etching technique. The scattered light percentage is calculated as the ration of scattered and incident light.....	93
Figure 5.5 (a) Photomask containing cantilever's patterns, (b) Die D13, D11, D1 and D7 is enlarged.....	95
Figure 5.6 Fabrication steps for the free-standing Si cantilever: a) Beginning SOI wafer, b) Dry oxide is grown on the device layer, c) The pattern from the mask is transferred using photolithographic, d) BOE etches away the exposed oxide, e) TMAH etches the silicon, f) Cantilevers are released using a vapor HF.....	99
Figure 5.7 SEM image of 200 μm wide freestanding silicon cantilever beams, (a) larger area, (b) zoomed at the tip. Cantilevers with different lengths were fabricated but only 7.5 mm long cantilevers are used as their L/w ratio is above 30. ....	100
Figure 5.8 A profilometer scan of the step from silicon dioxide to ~3μm thick silicon cantilever. ....	101
Figure 6.1 Pump and probe laser spot size on the sample. X and Y profile represents the major and minor axis of the elliptical spot.....	103
Figure 6.2 Signal to noise ratio relation with the probe laser frequency. Experiments are conducted at 15 K, 100 K, 200 K and 300 K temperatures. ....	106
Figure 6.3 Experimentally measured temperature along 2.03±0.09 μm thick cantilever. Dots represent the measured value while dashed line are the fitted curve. Experiments are done at 7 different temperatures from 20 K to 300 K.....	107
Figure 6.4 The thermal conductivity of 2μm sample changes with the temperature. Reference data is adopted from literature for 1.6 μm silicon film[29] and 3 μm silicon film[30]. ....	108
Figure 6.5 Change of temperature along cantilever's length for 2.93±0.06 μm thick silicon sample. Measurement are done in the temperature range of 20 K to 300 K.....	109
Figure 6.6 Thermal conductivity change of 3 μm sample with temperature. Reference data are for {100} single crystal and comes from literature for 3 μm doped Si [30] and bulk Si [14]..	110

Figure 7.1 Thermal boundary conductance measurement steps. Temperature measured a) only on Si, b) only on metal film, c) on Si + metal film .....	113
Figure 7.2 Scanning electron microscope image of Phononic crystals fabricated in silicon.....	114
Figure D.1 Full user interface for STR data collection and control. Five sections are (upper left to right) cryostat temperature control, cryostat temperature collection, lock-in amplifiers data collection, (lower left to right) function generator control, nanovolt meters data collection. ....	159
Figure D.2 This section controls the cryostat temperature by setting values for PID controller.	159
Figure D.3 This section measures the cryostat and sample temperature. It also sets the temperature ramp rate for cryostat. ....	160
Figure D.4 Lock-in amplifiers data is collected using this section of the program. Parameters like signal and reference type, sensitivity, filter type, time interval etc. are set here. ....	160
Figure D.5 Function generator parameters are controlled through this section.....	161
Figure D.6 This section sets the parameters for nanovoltmeter data collection. ....	161

## **List of Tables**

Table 1.1 Previous studies on thermal conductivity measurement of single-crystal silicon films	11
Table 1.2 Previous thermal conductivity measurements of poly/amorphous-silicon films.....	11
Table 3.1 Constants of fitted curves in Figure 3.17 and their determination coefficient value....	60

## **List of Abbreviations and Acronyms**

STR	Suspended ThermoReflectance
IC	Integrated Circuits
TTR	Transient ThermoReflectance
TDTR	Time Domain ThermoReflectance
FDTR	Frequency Domain ThermoReflectance
RMS	Root Mean Square
EOM	Electro-optic Modulator
$C_{TR}$	Thermoreflectance Coefficient
FEM	Finite Element Method
TBC	Thermal Boundary Conductance
TC	Thermal Conductivity
L/w	Length to Width ratio
SOI	Silicon on Insulator
BOX	Buried Oxide
CW	Continuous Wave
PD	Photodetector
HV	High Vacuum
BS	Beam Splitter
OL	Objective Lens
PIN	Positive Intrinsic Negative
GM	Gifford-McMahon
PECVD	Plasma Enhanced Chemical Vapor Deposition



QAH	Quaternary Ammonium Hydroxide
TMAH	Tetramethylammonium Hydroxide
BOE	Buffered Oxide Etch
CMP	Chemical Mechanical Planarization
PSD	Power Spectral Density
DI	Deionized Water
IPA	Isopropyl Alcohol
ML	Monolayer
ADC	Analog to Digital Conversion
MFP	Mean Free Path
FWHM	Full width at half maximum
SEM	Scanning Electron Microscope

## Nomenclature

$u$	Temperature, K
$T_{\text{sub}}$	Environment temperature, K
$x$	Distance in horizontal direction
$\rho$	Material density, kg/m <sup>3</sup>
$C$	Specific heat capacity, J/(kg.k)
$\kappa$	Thermal conductivity, W/(m.k)
$\alpha$	Thermal diffusivity, m <sup>2</sup> /s
$L$	Length of the sample, $\mu\text{m}$
$x$	Distance along horizontal direction, m
$\hat{x}$	Dimensionless distance along horizontal direction
$t$	Time, s
$\hat{t}$	Dimensionless time
$I$	Intensity of laser, W/m <sup>2</sup>
$A$	Intensity of modulated frequency, W/m <sup>2</sup>
$\omega$	Angular frequency, rad/s
$\theta$	Dimensionless temperature distribution
$C_{\text{TR}}$	Thermoreflectance coefficient, K <sup>-1</sup>
$\phi$	Phase of the heat wave
$\varepsilon$	Dielectric function
$R$	Reflectivity
$\alpha_s, \beta_s$	Seraphine coefficients
$\tilde{n}$	Complex refractive index

$E_g$	Energy gap
$\hat{I}$	Dimensionless laser intensity
$\hat{A}$	Dimensionless modulation intensity
$\hat{\omega}$	Dimensionless angular frequency
$S(\hat{x}, \hat{t})$	Dimensionless flux boundary temperature distribution
$\lambda_n$	Eigenvalue constant
$\Theta(\hat{x}, \hat{t})$	Dimensionless transient temperature distribution
$k_n$	Eigenvalue constant
$\theta_{ss}(\hat{x})$	Dimensionless steady-state temperature
$\theta_{transient}$	Dimensionless transient temperature
$\theta_{harmonic}$	Dimensionless harmonic temperature
$n$	Integers
$\tau$	Time constant, s
$L_p$	Thermal penetration depth
$\Delta T$	Change in temperature, K
$f$	Frequency, Hz

## Chapter 1 - Introduction

Integrated circuits (ICs) and electronic and optoelectronic devices generate heat and increase temperature under various operating conditions. Poor thermal management, however, can result in decreased reliability or catastrophic failure of these devices.[1], [2] Additionally, thermal characterization of these devices has become difficult due to their size reduction and monolithic integration of sub-micrometer devices on a chip.[3] Therefore, more efficient thermal management and temperature distribution is essential for improved performance such as less heat generation and faster functionality.[4] Thin films, or membranes, with thicknesses ranging from one atomic layer to hundreds of micrometers have been extensively used to improve the electrical, optical, and thermal functionalities in engineering systems such as the gate electrode of MOS devices,[5] solar cells,[6] polysilicon resistive temperature sensors,[7] and thermoelectrics.[8], [9] Thermal conductivity of the film differs significantly from its bulk counterpart, with millimeter or above dimensions, due to the geometric constraints and scattering of phonons (dominant energy carriers in silicon) of the film.[10] Studies of silicon films have found that room-temperature thermal conductivity decreases by more than 10% for approximately 1  $\mu\text{m}$  of thin film[11] and up to 50% for films of 100 nm[12], [13] compared to bulk silicon. The size effect becomes more pronounced at lower temperatures as the mean free path of the bulk counterpart increases.[14], [15]

Since the 1950s, extensive efforts have been made to characterize thermal conductivity and thermal contact resistance in bulk materials.[16]–[24] However, most conventional thermal conductivity measurement techniques lack the spatial resolution to measure the temperature gradient/difference or heat flux across a length scale below tens of micrometers.[25], [26] Thus, research interest has increased to identify techniques to determine submicron temperature distributions. This study explored experimental techniques to measure in-plane thermal

conductivity of thin films. To obtain meaningful results, this research sought to understand the suitability and limitations of various techniques that depend on film thickness, expected thermal conductivity relative to the substrate or supporting measurement structure, and sample preparation restrictions related to microstructural defects or device simulation requirements.[10]

## **1.1 Contact Temperature Measurement Techniques**

In contact methods, current is passed through a metal bridge machined on a sample film to generate Joule heat and facilitate precise local heating and temperature measurement simultaneously. This section briefly describes two common types of contact temperature measurement techniques. More details about these techniques can be found in the literature.[10], [26]–[28]

### **1.1.1 Steady-state Measurement Techniques**

Several studies have used steady-state electrical techniques to measure in-plane thermal conductivity of single-crystal silicon films,[29]–[32] polycrystalline silicon microcantilevers, [33]–[37] microbridges,[38], [39] suspended membranes,[10], [40], [41] and cross-plane thermal conductivity of amorphous-silicon.[42]–[44]

The thin film, whose temperature will be measured, is sandwiched between two metal plates, which act as heater and sensor for measuring cross-plane thermal conductivity. The entire device is fabricated on a large substrate or metal plate to increase its usability and allow it to operate as a heat sink (Figure 1.1a). Two heaters/sensors are placed on the thin film for the in-plane thermal conductivity measurement, as shown in Figure 1.1(b).

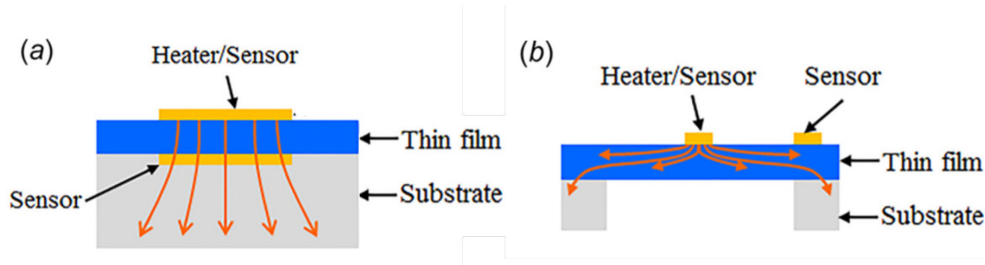


*Figure 1.1 Steady-state methods for measuring a) cross-plane and b) in-plane thermal conductivity of thin films. In cross-plane measurement, the metal strip serves as both heater and temperature sensor, but in-plane measurement requires a separate temperature sensor.[45]*

### 1.1.2 Transient Measurement Techniques

Cahill et al. first introduced the  $3\omega$  method, a transient electrical technique, to measure out-of-plane thermal conductivity for disordered film, such as amorphous silicon dioxide, which has low thermal conductivity.[46] Due to high thermal conductivity of the Si film, heat spread in all directions, proving that the  $3\omega$  method can be used to measure in-plane and out-of-plane thermal conductivity.[10], [47]

The studies grew or deposited a passivation oxide layer on the thin film and measured the thermal conductivity (Figure 1.2). Low thermal conductivity of the passivation layer ensured lateral heat conduction in the thin film (Si layer). An Al heater line was deposited on the oxide layer. Out-of-plane thermal conductivity can be measured when the heater line is wider than the Si layer, but heat dissipated in lateral and perpendicular directions when the heater line was thin, allowing both in-plane and out-plane thermal conductivity measurement.[48], [49] A current of  $1\omega$  frequency was sent to the heater wire, causing temperature and resistance to fluctuate at  $2\omega$  due to Joule heating. When multiplied by the sinusoidal current, this temperature fluctuation resulted in a  $3\omega$  voltage component, which was measured by a lock-in amplifier.[50], [51]

Although this method requires a complex and rigorous data analysis procedure, sample fabrication is relatively easier than the steady-state contact method due to the use of simple aluminum heater line.

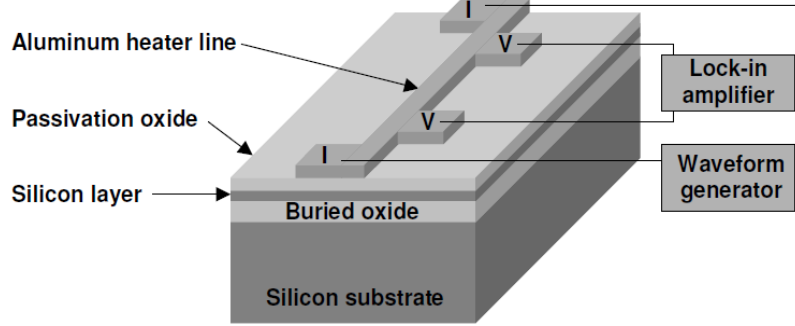


*Figure 1.2* Schematic diagram of a typical  $3\omega$  method for thermal characterization of thin films, measuring thermal conductivity of the device layer of a silicon-on-insulator (SOI) wafer.[12]

## 1.2 Non-Contact or Thermoreflectance Techniques

The thermoreflectance (TR) technique is a cost-effective, non-contact, non-destructive, ultra-fast optical approach for probing steady-state, transient, and periodic surface temperatures. Moreover, this technique provides accurate results for submicron features with excellent spatial, temporal, and thermal resolutions.[52]

In the TR technique, a pump laser heats the sample and, as the temperature of the sample rises, a probe laser registers the change in reflectivity. Based on the position of the lasers, this technique can work in two ways, as shown in Figure 1.3. A common technique[13], [53], [54] uses both pump and probe lasers on the same side of the sample (Figure 1.3a), while a novel technique, described in this dissertation, applies pump and probe lasers on the opposite side of a suspended thin film (Figure 1.3b).[55] As described in the following sections, existing TR techniques can be divided into three main categories.

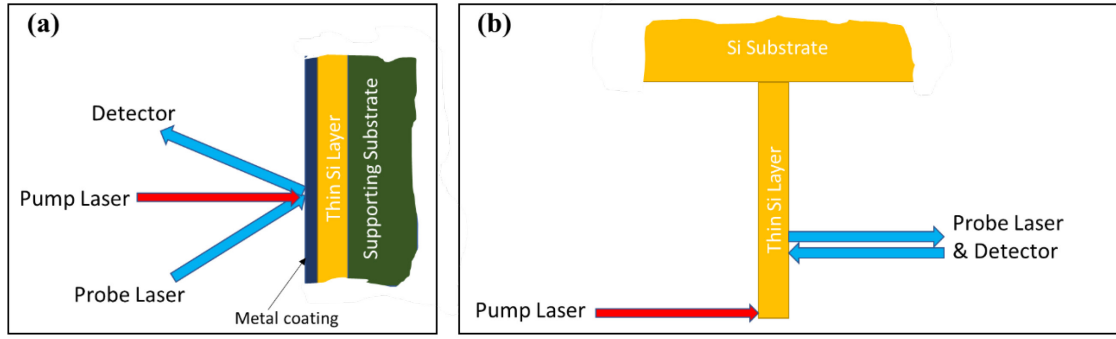


*Figure 1.3 Basic thermoreflectance measurement principle. a) Pump & probe are on the same side and Si layer is attached to a substrate[53], [56], b) Pump & probe are on the opposite side and Si layer is suspended from the substrate.*

### 1.2.1 Transient Thermoreflectance

Transient thermoreflectance (TTR) is a pump-probe measurement to produce a sample's transient heating or cooling time, which is then correlated to the thermal properties of the material using heat transfer models. In this technique, the pump and probe lasers are focused at the same point on the sample from the same side. The pump laser power is pulsed with a duration of picosecond to femtosecond and a repetition period of millisecond. The temperature difference induced by the pump laser changes the reflectivity, which is measured with a second weaker laser that can be variably delayed with respect to the heating pulse. Due to the very short heating period, thermal penetration depth into the substrate is very small (  $\sim 20$  nm for visible light), and heat diffusion out of this region is monitored by the TR signal as a function of time delay.[57]

Hopkins et al. showed the relationship between pump-probe time delay and TTR signal for gold film on glass substrate (Figure 1.4a).[58] As shown in the figure, the heating cycle is the negative delay time, whereas the cooling cycle is the positive delay time. Each point at the cooling curve was collected by moving the delay stage on the probe side by  $30\text{ }\mu\text{m}$  from the previous position. Figure 1.4b presents a typical TTR setup used by Goodson et al.[53] As shown in the



figure, the continuous wave (CW) probe beam coupled with a high-power optical microscope could be focused on the smallest spot limited by diffraction, while the pulsed pump beam had a diameter of approximately 1 mm at the sample surface to ensure one-dimensional (1D) heat conduction at measurement timescales. Another variation of this technique replaces CW laser with pulsed laser, but signal is analyzed in a similar way from the time constant.

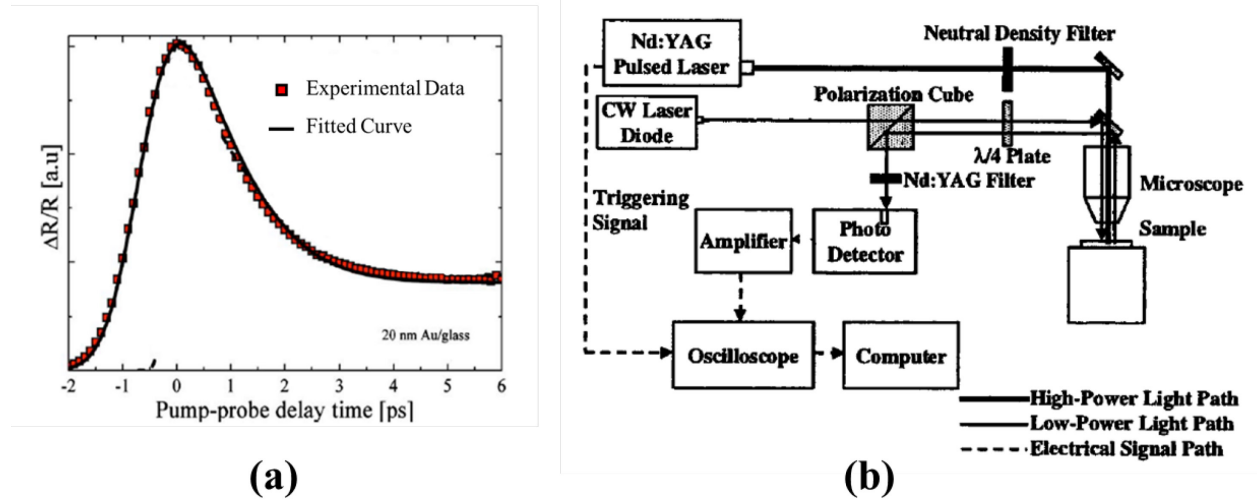


Figure 1.4 a) Relation between pump-probe delay and TTR signal for 20 nm Au film evaporated on a glass substrate.[58] b) Laser path and electrical signals in TTR experiment.[53]

By attributing 1D nature to heat conduction, the TTR signal is analyzed by the conduction equation using the finite difference method and curve fitting. The heat conduction equation correlates thermal diffusivity with the time constant measured in the experiment. Thermal diffusivity is a function of heat capacity and thermal conductivity. A value of heat capacity is assumed, using the bulk material, considering it does not change with length-scale reduction. The curve is then fitted with the experimental data by varying thermal conductivity until the best fit is obtained.[57], [59]

### 1.2.2 Time Domain Thermoreflectance

Time domain thermoreflectance (TDTR), a sophisticated variation of the TTR method, splits a pulsed laser into two distinct routes: the pump path is modulated at a frequency, and the probe course is pulsed signal similar to TTR method. The most common implementation of TDTR uses an Al-coated sample ( $C_{TR} = 10^{-4} \text{ K}^{-1}$ )[60], [61] and a mode-locked Ti:sapphire laser as the light source.[62], [63] The laser produces a train of sub-picosecond optical pulses at a high repetition rate of approximately 80 MHz.[64] Although typical laser wavelengths for TDTR are approximately 800 nm,[65] researchers also have used wavelengths of 632 nm[66] and 1030 nm.[61] Pump and probe paths are focused on the sample via a single microscope objective after the pump laser passes through an electro-optic modulator (EOM) and the probe laser travels through a mechanical delay stage.[67], [68] Smaller probe to pump beam profile on the sample is needed to assess lateral thermal conduction. The beam profile is generated by expanding the laser beam before the delay stage and later focusing by objective lens. This expansion also decreases beam divergence in the long propagation range. Because the pump and probe laser have identical wavelengths, the photodetector detects both types of reflected laser, thereby affecting the experimental outcome. This effect is prevented by a polarizing beam splitter (PBS), which is effective for the cross polarization of the reflected laser beams, or by a spatial separation of the reflected pump and probe beam for an optically smooth ( $< 15 \text{ nm RMS}$  surface roughness[64]) sample. Detailed discussions of various TDTR setups are presented in the literature.[69]–[75]

The TDTR measurement process is presented graphically in Figure 1.5. Figure 1.5a depicts heat input to the sample using a pump laser (modulation frequency  $< 10 \text{ MHz}$ ).[64] Each impulse of heat generates a temperature response in the sample (Figure 1.5b), which generally does not abate before the next pulse arrives. Figure 1.5c shows that the probe pulses arrive at the sample

delayed from the pump pulses by time  $\tau$ , determined by the position of the delay stage, and Figure 1.5d depicts the probe pulses as they sample the surface temperature.[73] Probe excitation does not affect the measurement because it has no frequency component at the modulation frequency and is not captured by the lock-in amplifier.

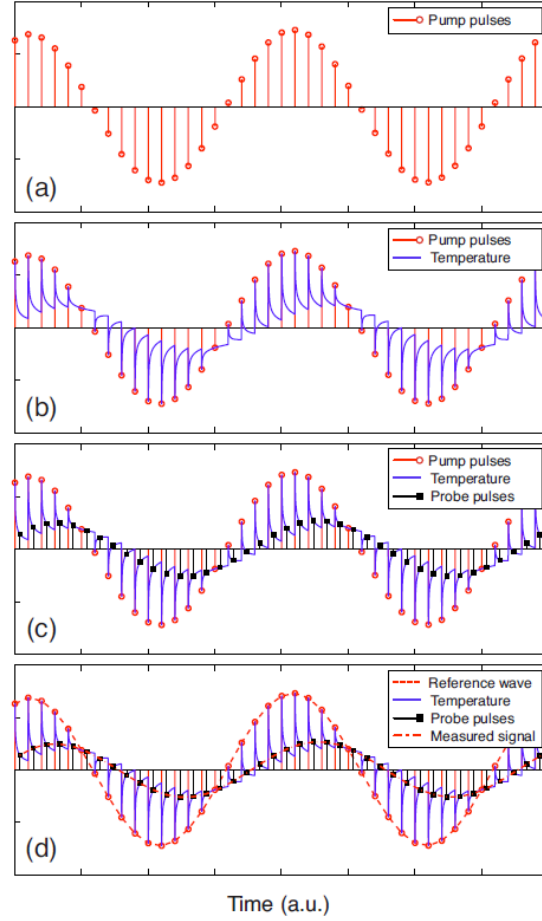


*Figure 1.5* TDTR measurement technique: (a) modulated pump beam input; (b) surface temperature of the sample in response to the pump input; (c) probe pulses at the sample delayed by a time  $\tau$ ; and (d) measured probe and reference signal.[76]

TDTR signal is analyzed by transfer function  $Z(\omega)$ , where  $\omega$  is the thermal input frequency. The transfer function is shown in Figure 1.6. Amplitude  $A$  and phase  $\phi$  of the lock-in output,  $Ae^{i(\omega_0 t + \phi)}$ , are functions of the delay between the pump and probe pulses and the physical

properties of the sample. Reference frequency  $\omega_0$  is set by the EOM modulation of the pump beam.[73], [77]

$$e^{i\omega_0 t} \Rightarrow \boxed{Z(\omega)} \Rightarrow Z(\omega_0)e^{i\omega_0 t} = Ae^{i(\omega_0 t + \phi)}$$

*Figure 1.6 Transfer function,  $Z(\omega)$ , with the thermal response of the system (analytical model) and the properties of the pump and probe beams.[73]*

### 1.2.3 Frequency Domain Thermorefectance

The frequency domain thermorefectance (FDTR) method utilizes the advantageous spot geometry and analysis approach of TDTR while incorporating experimental simplicity by making frequency, not time delay, the independent parameter.[13] FDTR can therefore be easily accomplished using the same TDTR method by setting the delay stage at a certain location and by adjusting the frequency of modulation. Moreover, the FDTR method can eliminate the difficulty of the beam walk-off and the divergence involved with the mechanical delay stage owing to the fixation of the probe period. The FDTR system can also be implemented using cost-effective CW lasers (shown in Figure 1.7b), which achieve similar accuracy to TDTR measurement for thermal conductivity of many thin film materials.[45], [69], [78], [79]

Two experimental FDTR setups are shown in Figure 1.7, with Figure 1.7a showing the use of two CW lasers and Figure 1.7b demonstrating the use of one pulsed laser, as in the TDTR method.[13], [80] The probe beam is pointed directly on the sample without going through a mechanical stage of delay. To ensure surface heat deposition and adequate thermorefectance, the samples are coated with a gold transducer layer with high pump wavelength absorptivity and high probe wavelength thermorefectance coefficient.[81], [82] Using a photodetector and a lock-in

amplifier, the thermoreflectance change incorporated in the reflected probe beam is also extracted.  
[45]

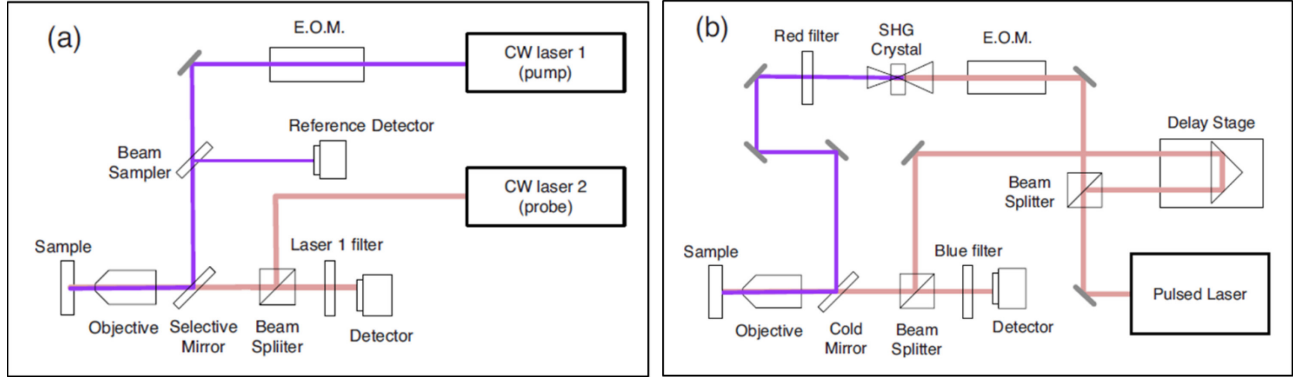


Figure 1.7 Two experimental arrangements for FDTR: (a) system based on CW lasers; (b) system based on pulsed laser.[13]

As mentioned, FDTR data is analyzed in a similar way to TDTR with the exclusion of delta function (defines pulses) for CW lasers. Schmidt et al. and Malen et al. describe the complete data analysis process.[13][83]

### 1.3 Previous Measurement of Thermal Conductivity

Table 1.1 and Table 1.2 summarize experimental data from contact and non-contact methods. Since crystalline silicon and poly-silicon demonstrate different trends in thermal conductivity, they are presented separately in Table 1.2 and Table 1.2, respectively. TR measurements are plotted in Figure 1.8, with contact method measurements for comparison. It can be readily noticed that most of the silicon thermal conductivity measurements are done using steady-state joule heating method since it is a very old and established technique. On the other hand, though optical methods have gained much popularity in recent times, few measurements on silicon are conducted using these methods.

*Table 1.1 Previous studies on thermal conductivity measurement of single-crystal silicon films*

Article	Year	Film Thickness	Doping	Measurement Method	Temperature Range (K)	$\kappa$ (W/mK) @ 300 K
Yu et al.[84]	1996	4 $\mu\text{m}$	Intrinsic	Thermal wave technique	300	128
Zheng et al.[32]	1996	155 nm	Intrinsic	Steady-state Joule heating and electrical resistance thermometry	300	2.2
Asheghi et al.[29]	1998	0.42 - 1.6 $\mu\text{m}$	Intrinsic	Steady-state Joule heating and electrical resistance thermometry	20 - 300	88 - 138
Ju et al.[12]	1999	74 – 240 nm	Intrinsic	Periodic Joule heating	300	74.7 - 101
Völklein et al.[34]	2000	174 nm	As/B Doped	Steady-state Joule heating and electrical resistance thermometry	100 – 350	82 – 67.1/ 61.9 – 56.2
Sverdrup et al.[85]	2001	5 $\mu\text{m}$	N-type	Steady-state Joule heating	100 – 200	-
Asheghi et al.[30]	2002	3 $\mu\text{m}$	P/B Doped	Steady-state Joule heating and electrical resistance thermometry	20 – 300	133 – 113/ 128 - 107
Aubain et al.[86]	2010	68 – 258 nm	B Doped	Scanning thermoreflectance with electrical heating	300	70 - 125
Aubain et al.[87]	2011	68 – 258 nm	B Doped	Scanning thermoreflectance with electrical heating	300	50 – 110
Anufriev et al.[88]	2016	80 nm	Intrinsic	TDTR	300	180
Wang et al.[89]	2016	Bulk	Intrinsic	FDTR	300	120
Li et al.[90]	2018	Bulk	Intrinsic	TDTR	300	118

*Table 1.2 Previous thermal conductivity measurements of poly/amorphous-silicon films*

Article	Year	Film Thickness	Doping	Measurement Method	Temperature Range (K)	$\kappa$ (W/mK) @ 300 K
Mastrangelo et al.[91]	1988	1.3 $\mu\text{m}$	P-type	AC heating microbridge	300	27.9
Tai et al.[39]	1988	1.5 $\mu\text{m}$	P-type	Steady-state current-voltage characteristics	300 – 425	32

Völklein et al.[34]	1992	370 nm	P-type	Steady-state Joule heating	80 – 400	29
Henager et al.[92]	1993	2.2 – 9.9 $\mu\text{m}$	Intrinsic	Thermal comparator technique	300	0.97
Paul et al.[36]	1994	340 nm	P-type	Steady-state Joule heating	100 – 420	15 - 18
Wei et al.[56]	1995	0.7 – 1.6 $\mu\text{m}$	Intrinsic	Thermal wave technique	300	15 - 23
Irace et al.[41]	1999	300 nm	B doped	Steady-state Joule heating	300	34.5
McConnel et al.[40]	2001	1 $\mu\text{m}$	P doped	Steady-state Joule heating	20 – 320	57.5 – 49.1
Graham et al.[93]	2003	2 – 4 $\mu\text{m}$	Intrinsic	Steady-state Joule heating	200 – 320	59.2 – 51.4
Shiga et al.[94]	2018	20, 58, 109 nm	Intrinsic	TDTR	50 – 300	1 – 9, 2 – 11, 10 - 48

## 1.4 Suspended Thermoreflectance (STR)

The new Suspended Thermoreflectance (STR) technique combines the advantages of steady-state measurement and TTR technique. In fact, it not only has the ability to conduct measurement on completely suspended films, but it can also independently measure thermal conductivity without assuming any heat capability value from the bulk material.

In STR, a pump laser heats the sample from one side, and a probe laser scans through the other side to detect the change in the reflectivity. The sample is so thin that there is negligible temperature gradient along the thickness. Therefore, backside probing represents the actual temperature of the structure. Figure 1.8 is a simplified representation of the measurement technique. The pump laser beam goes through a beam expander, which expands the beam into a 1:8 ratio. The laser train then passes through beam splitter and is split into two equal parts. One of which falls onto the sample after being focused by the lens, and the other goes to a Photodiode 2 where incident laser power on the beam is determined. Photodiode 1 captures any light which is

reflected from the sample and this reflection is subtracted from the measured power of photodiode 2 to calculate the actual incident laser power. The same sequence is repeated on the probe side, except that photodiode 4 reports the reflection from the structure associated with the temperature change. In addition, the probe laser beam has a high divergence which is reduced by the use of two collimating lenses.

Probe laser is excited with a sinusoidal signal from signal generator. This is so that the reflected signal from photodiode 4 can be measured against the reference signal in lock-in amplifier, which allows the detection of very small changes in reflection even if buried in external noise. Photodiode 3 helps normalizing the probe side reflected signal to exclude the noise of probe laser itself. A detailed description and function of each component is provided in Chapter 4.

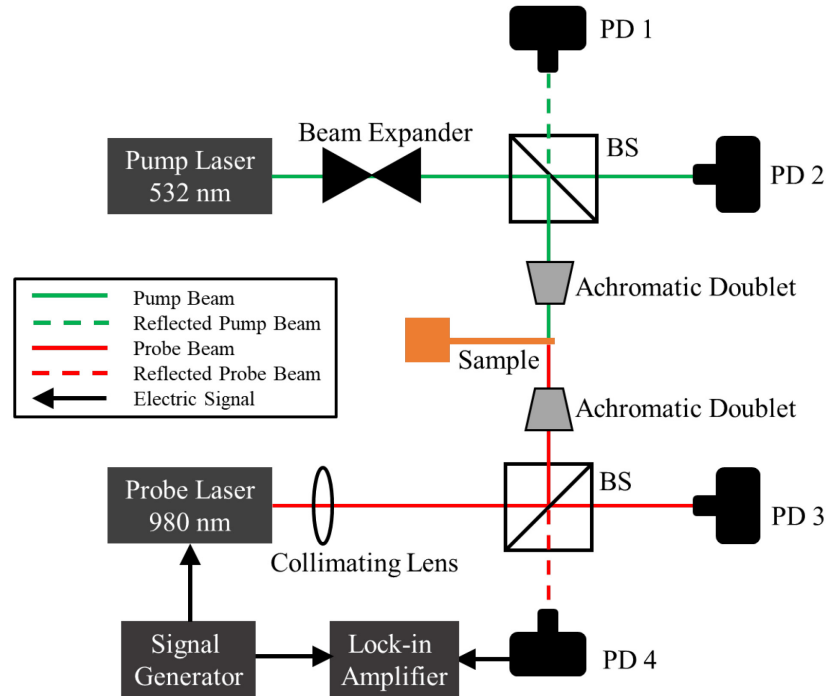


*Figure 1.8 STR setup to measure temperature along the sample. Samples are inside a cryostat to ensure ultra-high vacuum and low-temperature environment.[95]*



### 1.4.1 Significance of STR Over Other Techniques

Compared to contact methods, the advantages of TR methods include no observer effect in the measurement and significantly higher spatial and temporal resolution. Likewise, compared to other optical methods, STR can advantageously obtain measurements on a completely suspended film. Because the TTR, TDTR, and FDTR methods have the assumption of a semi-infinite substrate and no influence from subsequent layers in the multilayered structure, these systems do not have the spatial constraints of many semiconductor devices.[13] Therefore, this new Suspended Thermoreflectance (STR) method is developed.[95], [96] A freely suspended  $\mu$ -cantilever beam is thermally characterized using the method.

A time constant is determined in the transient techniques by measuring the heating or cooling time of the sample. Heat transfer models yield thermal diffusivity from the time constant. But thermal diffusivity is a function of thermal conductivity (TC) and heat capacity. Therefore, thermal conductivity of thin films is determined by assuming that heat capacity of the bulk material does not change with a change in dimension. However, recent studies suggest that heat capacity is also a function of sample thickness and temperature.[97]–[99] This characteristic of heat capacity makes reliable thermal conductivity measurement difficult in transient techniques. On the other hand, direct thermal conductivity is determined in STR by measuring the temperature gradient along the length of the cantilever. Thus, TC does not depend on heat capacity.

Most of the TDTR and FDTR techniques require a metal film (Aluminum/Platinum etc.) on top of the sample for higher light absorbance and to increase thermoreflective coefficient. In some cases, such as GaN deposited on top of Si or SiC [100], metal to sample thermal boundary conductance (TBC) is low, but the sample has a very high thermal conductivity (TC). As a result, very little amount of heat is transferred to the sample and the heat will dissipate to the substrate as

soon as it reaches the sample due to its high TC. This makes the measurement very difficult. Application of only the thin film (with no metal absorber) helps STR avoid such issues.

Moreover, TDTR and FDTR use femtosecond to picosecond laser pulses for the measurement. Short pulses help to achieve good temporal resolution and higher precision for high thermally conductive materials. But they cannot penetrate deep into the substrate (normally  $<20$  nm) due to their short duration. [101] As a result, measurements are not carried out uniformly over the entire depth of the sample, but only on the top few nanometers. Because of the use of continuous wave (CW) lasers, STR does not have this problem.

Unlike previously used least-square techniques, where analytical solutions are fitted to the experimental data by varying an independent variable like thermal conductivity to find its best value[53], [59], [63], [102], thermal conductivity can be obtained independently in STR if the temperature of two or more points along the length of the cantilever is known.

To summarize, STR measures thermal conductivity independently without using any metal absorber. This technique characterizes TC uniformly over the entire depth of the sample with the help of CW lasers and a simple analytical model.

## Chapter 2 - Theory: Thermorefectance and Heat Transfer

This chapter presents the theory for STR measurement. The first section describes the relationship between surface temperature change and associated changes in reflection, and the second section derives a 1D heat transfer model to analyze thermal properties, such as thermal conductivity, of a suspended cantilever when temperatures of two or more points along the length of cantilever are known. The third section of the chapter verifies the 1D model using FEM simulation, and last section describes phase change along the cantilever when sample absorbs the probe beam.

### 2.1 Correlation Between Temperature and Reflection

A rise in temperature triggers a change in the energy gap and extends the associated critical point. The energy gap occurs due to thermal expansion and the electron and phonon interaction. For most critical points, the change in thermal expansion has the same sign (i.e. direction) with magnitude similar to the phonon shift; broadening, which is only due to the electron–phonon interaction, is small compared to the total shift.[4], [103]

For non-magnetic, isotropic, homogeneous media, in which optical constants can be treated as scalars, the phenomenological basis of TR spectroscopy[104] can be understood by studying the change in the complex dielectric function.[4] The TR technique primarily measures the change of the complex dielectric function.

$$\hat{\varepsilon} = \varepsilon_1 + i\varepsilon_2 \quad (1)$$

where  $\varepsilon_1$  and  $\varepsilon_2$  are the real and imaginary parts of the dielectric function, respectively. The complex refractive index is related to the dielectric function  $\varepsilon$  by:[105]

$$\varepsilon = (\tilde{n})^2 \quad (2)$$

$$\varepsilon_1 = n^2 - k^2 \quad (3)$$

$$\varepsilon_2 = 2nk \quad (4)$$

where  $n$  is the index of refraction and  $k$  is the extinction coefficient. In general, change induced by external or internal perturbation can be observed in transmission or reflection measurements. When changes in the reflection spectrum caused by thermal excitation are observed, the method is classified as TR thermometry.

The relationship between reflectance change and corresponding change of dielectric function can be presented with the Seraphine coefficients  $\alpha_s$  and  $\beta_s$ . [105]

$$\frac{\Delta R}{R} = \alpha_s \Delta \varepsilon_1 + \beta_s \Delta \varepsilon_2 \quad (5)$$

where

$$\alpha_s = \frac{2A}{A^2 + B^2} \quad (6)$$

$$\beta_s = \frac{2B}{A^2 + B^2} \quad (7)$$

and

$$A = n(n^2 - 3k^2 - 1) \quad (8)$$

$$B = k(3n^2 - k^2 - 1) \quad (9)$$

In general,  $n$  and  $k$  are the real and imaginary parts, respectively, of the complex refractive index  $\tilde{n} = n + ik$  and can be expressed through the real and imaginary parts of the dielectric function. [106]

$$n = \left( \frac{(\varepsilon_1^2 + \varepsilon_2^2)^{\frac{1}{2}} + \varepsilon_1}{2} \right)^{\frac{1}{2}} \quad (10)$$

$$k = \left( \frac{(\varepsilon_1^2 + \varepsilon_1^2)^{\frac{1}{2}} - \varepsilon_1}{2} \right)^{\frac{1}{2}} \quad (11)$$

Finally, the change in reflection can be calculated as

$$\frac{\Delta R}{R} = \frac{4(n^2 - 3k^2 - 1)\Delta n + 8nk\Delta k}{[(n + 1)^2 + k^2][(n + 1)^2 - k^2]} \quad (12)$$

where  $\Delta n$  and  $\Delta k$  are the change in  $n$  and  $k$  resulting from the temperature change. The temperature increase causes a shift in the energy gap ( $E_g$ ) and broadens the critical parameter ( $\Gamma$ ) involved.

Combining these two effects, one can write

$$\Delta \varepsilon = \frac{\partial \varepsilon}{\partial E_g} \frac{dE_g}{dT} \Delta T + \frac{\partial \varepsilon}{\partial \Gamma} \frac{d\Gamma}{dT} \Delta T \quad (13)$$

When the broadening parameter is assumed to be constant, the relationship between dielectric function and temperature is obtained.[4]

$$\Delta \varepsilon = \frac{\partial \varepsilon}{\partial T} \Delta T \quad (14)$$

Likewise, the equation for the TR coefficient can be obtained by taking a first-order approximation of the relationship between surface temperature change and reflectivity change. [60], [105]

$$\frac{\Delta R}{R} = \frac{1}{R} \frac{\partial R}{\partial T} \Delta T = C_{TR} \Delta T \quad (15)$$

Relative change in the optical reflectance per unit temperature change is termed the thermorefectance coefficient ( $C_{TR}$ ). This coefficient depends on probed material[107] and on the wavelength of probe light[108] due to the association of these properties with the dielectric function.

## 2.2 One-Dimensional Heat Transfer Model

Due to the simplicity of calculation, 1D heat transfer models are commonly utilized for thin films in non-contact methods such as TTR, TDTR, and FDTR. Moreover, in order to attribute a 1D model to TTR and TDTR, heat conduction in the lateral direction is typically assumed to be several orders of magnitude larger than the penetration depth into the substrate.[53], [59], [76], [77] In FDTR, application of a 1D model includes the assumption that heat flows in the planar direction of thin films.[83], [102] All these models assume a semi-infinite substrate and require a complex heat transfer model to analyze thermal property in a multilayered structure.[13] Thus, by definition, these systems do not contain the spatial constraints that many semiconductor devices utilize.[7]–[9] Therefore, a new method was recently developed termed Suspended Thermoreflectance (STR).[55], [96]

Heat carriers for conduction (electrons and phonons) have characteristic lengths and time constants, and when a system's geometry or conditions are comparable to these characteristic values, the material's thermal conductivity,  $\kappa$ , change.[109]–[116] Figure 2.1 shows the thermal conductivity of bulk silicon with geometry significantly longer than its characteristic length[117] and silicon thin films with geometries on the order of characteristic length.[29], [40], [118] As shown in the figure, thermal conductivity decreased by a factor of 10 when bulk transitioned to thin film. However, these bulk and thin films are two extreme cases in which dimensional ratios are not comparable. Therefore, the equations in this paper use a continuum-based model that does not consider quantum, atomic, or ballistic effects. This equation will provide a fair comparison between bulk material and microns size films [119]. Because the heat equation is a diffusive model, deviation from this model indicated the potential presence of the aforementioned effects.

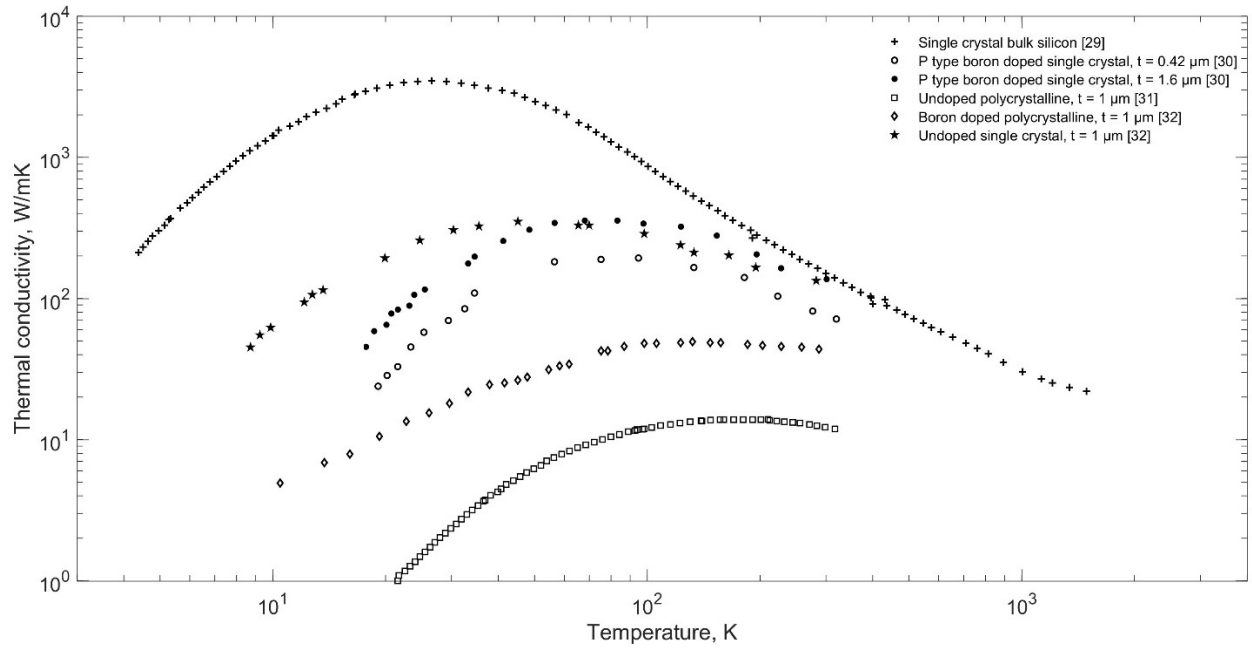


*Figure 2.1 Thermal conductivity of Si: Variation with temperature change for bulk silicon and thin films of silicon of different doping and crystallinity. (Adapted from Ref. [29] - [32])*

The steady-state part of the 1D heat transfer model presented in this dissertation is directly applicable to measure thermal conductivity using the Suspended Thermoreflectance (STR) technique.[55], [96] Transient and harmonic parts are for better understanding of heat flow in the cantilever. The model in this research was developed based on assumptions from experimental conditions. The first assumption was that the beam is under vacuum to the extent that convection becomes negligible. The second assumption presumed that the sample experiences a small increase in temperature,  $\Delta T \leq 10\text{K}$ , making radiative effects negligible.[83] Thirdly, when temperature changes are small, temperature-dependent physical properties of the material were assumed to remain constant. The fourth assumption supposed heat carriers to be in local thermal equilibrium, and are explained adequately by a diffusive transport model .[120], [121]

The heat transfer behavior of micro/nano-cantilevers examined in this work is theoretically divided into three regimes. In the first regime, the beam has been heated by a constant heat flux at the free end and is operating at steady-state conditions. Analysis of this regime reveals the thermal conductivity of the material. In the second regime, the cantilever is initially at the same temperature as the fixed end and is then instantaneously heated at its tip. As its temperature increases, it exists in a transient state until enough time has passed, after which it is identical to the steady-state regime. In the third regime, the heat flux has a sinusoidal oscillation superimposed at its tip and the system reacts harmonically. Analysis of transient and harmonic regimes provides more in-depth comparison with finite element simulation when checking the heat diffusion equation's applicability to analyze thermal conductivity in the experiment. A schematic of a cantilever beam with heat flux at the tip is shown in Figure 2.2.

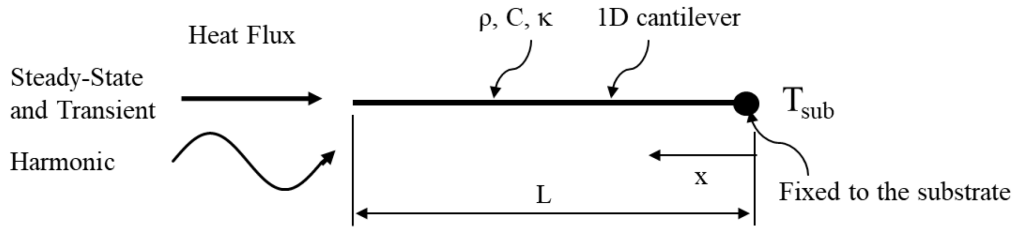


*Figure 2.2 1D solid bar with heat flux at the tip and constant temperature at the opposite end. Steady-State and transient heat flux have a constant flux component, but harmonic heat flux has frequency.*

As shown in the figure, the physically fixed end of the beam is set as the origin, and the beam extends in the positive  $x$ -direction to its full length ( $L$ ). The governing equation for 1D heat diffusion in this beam is

$$\rho C \frac{\partial u}{\partial t}(x, t) = K \frac{\partial^2 u}{\partial x^2}(x, t) \quad (16)$$



where the temperature ( $u$ ) is a function of both time ( $t$ ) and position ( $x$ ), and it represents the absolute temperature at any position on the cantilever, at any given time. The other variables are taken from the material properties of the cantilever/sample: density ( $\rho$ ), heat capacity ( $C$ ), and the coefficient of thermal conductivity ( $\kappa$ ). The three material constants are combined to form the thermal diffusivity ( $\alpha$ ), and the heat transfer equation is rewritten.

$$\alpha = \frac{\kappa}{\rho C} \quad (17)$$

$$\frac{\partial u}{\partial t} = \alpha \frac{\partial^2 u}{\partial x^2}, \quad 0 \leq x \leq L, \quad 0 \leq t \leq \infty \quad (18)$$

Initial and boundary conditions mimics conditions in STR experiment.[96] Therefore, the fixed end is permanently set to the temperature of the substrate ( $T_{sub}$ ).

$$u(0, t) = T_{sub}, \quad 0 \leq t \leq \infty \quad (19)$$

The other end of the cantilever is excited with constant intensity or heat flux ( $I$ ) and harmonic flux. The harmonic flux contains amplitude ( $A$ ) and frequency ( $\omega$ ). For the modeled system, the oscillation amplitude cannot exceed the constant intensity.

$$\frac{\partial u}{\partial x}(L, t) = \frac{I}{\kappa} + \frac{A}{\kappa} \sin(\omega t), \quad 0 \leq t \leq \infty \quad (20)$$

$$A \leq I \quad (21)$$

The initial condition specifies that the entire cantilever is initially all at the substrate temperature.

$$u(x, 0) = T_{sub}, \quad 0 \leq x \leq L \quad (22)$$

Taken together, the partial differential equation, boundary conditions, and initial condition are written as

$$\begin{cases} \frac{\partial u}{\partial t} = \alpha \frac{\partial^2 u}{\partial x^2}, & 0 \leq x \leq L, & 0 \leq t \leq \infty \\ u(0, t) = T_{sub}, & 0 \leq t \leq \infty \\ \frac{\partial u}{\partial x}(L, t) = \frac{I}{\kappa} + \frac{A}{\kappa} \sin(\omega t), & 0 \leq t \leq \infty \\ u(x, 0) = T_{sub}, & 0 \leq x \leq L \end{cases} \quad (23)$$

Through the process of nondimensionalization, the system becomes generalized and easier to solve. The  $x$  interval is divided by length to generate dimensionless distance ( $\hat{x}$ ):

$$\frac{0 \leq x \leq L}{L} = 0 \leq \frac{x}{L} \leq 1 \quad (24)$$

$$\hat{x} = \frac{x}{L} \quad (25)$$

Utilizing the chain rule, the spatial partial derivatives with respect to the dimensionless distance become:

$$\frac{\partial u}{\partial x} = \frac{\partial u}{\partial \hat{x}} \frac{d\hat{x}}{dx} = \frac{1}{L} \frac{\partial u}{\partial \hat{x}} \quad (26)$$

$$\frac{\partial^2 u}{\partial x^2} = \frac{\partial}{\partial x} \left( \frac{\partial u}{\partial x} \right) = \frac{\partial}{\partial x} \left( \frac{1}{L} \frac{\partial u}{\partial \hat{x}} \right) = \frac{1}{L^2} \frac{\partial^2 u}{\partial \hat{x}^2} \quad (27)$$

To nondimensionalize time, dimensionless time ( $\hat{t}$ ) becomes a function of time, and the chain rule is used again to take the partial derivative with respect to time. Then the partial time and spatial derivatives are equated using Eqn. (18).

$$\hat{t} = \hat{t}(t) \quad (28)$$

$$\frac{\partial u}{\partial t} = \frac{\partial u}{\partial \hat{t}} \frac{d\hat{t}}{dt} \quad (29)$$

$$\frac{\partial u}{\partial \hat{t}} \frac{d\hat{t}}{dt} = \frac{\alpha}{L^2} \frac{\partial^2 u}{\partial \hat{x}^2} \quad (30)$$

$$\frac{d\hat{t}}{dt} = \frac{\alpha}{L^2} \quad (31)$$

$$\hat{t} = \frac{\alpha t}{L^2} \quad (32)$$

Because dimensionless temperature ( $\theta$ ) is a function of temperature, after taking derivatives again, the final dimensionless form of the heat transfer equation is

$$\theta(u) = \frac{u - T_{sub}}{T_{sub}} \quad (33)$$

$$\frac{\partial \theta}{\partial \hat{t}} = \frac{d\theta}{du} \frac{\partial u}{\partial \hat{t}} = \frac{1}{T_{sub}} \frac{\partial u}{\partial \hat{t}} \quad (34)$$

$$\frac{\partial \theta}{\partial \hat{x}} = \frac{d\theta}{du} \frac{\partial u}{\partial \hat{x}} = \frac{1}{T_{sub}} \frac{\partial u}{\partial \hat{x}} \quad (35)$$

$$\frac{\partial^2 \theta}{\partial \hat{x}^2} = \frac{\partial}{\partial \hat{x}} \left( \frac{\partial \theta}{\partial \hat{x}} \right) = \frac{1}{T_{sub}} \frac{\partial^2 u}{\partial \hat{x}^2} \quad (36)$$

$$\therefore \frac{\partial \theta}{\partial \hat{t}} = \frac{\partial^2 \theta}{\partial \hat{x}^2}, \quad 0 \leq \hat{x} \leq 1, \quad 0 \leq \hat{t} \leq \infty \quad (37)$$

Boundary and initial conditions are written in terms of the dimensionless parameters as

$$u(0, \hat{t}) = T_{sub}, \quad 0 \leq \hat{t} \leq \infty \quad (38)$$

$$\frac{\partial u}{\partial x}(L, t) = \frac{\partial u}{\partial \hat{x}}(1, \hat{t}) * \frac{d\hat{x}}{dx}(L) \quad (39)$$

$$\frac{\partial u}{\partial \hat{x}}(1, \hat{t}) = \frac{L}{\kappa} \left[ I + A \sin\left(\frac{\omega L^2}{\alpha} \hat{t}\right) \right], \quad 0 \leq \hat{t} \leq \infty \quad (40)$$

$$u(\hat{x}, 0) = T_{sub}, \quad 0 \leq x \leq L \quad (41)$$

Dimensionless boundary and initial conditions are then generated by applying Eqn. (33) to them.

$$\therefore \theta(0, \hat{t}) = \frac{u(0, \hat{t}) - T_{sub}}{T_{sub}} = 0, \quad 0 \leq \hat{t} \leq \infty \quad (42)$$

$$\frac{\partial \theta}{\partial \hat{x}}(1, \hat{t}) = \frac{\partial}{\partial \hat{x}} \left( \frac{u(1, \hat{t}) - T_{sub}}{T_{sub}} \right) = \frac{L}{\kappa T_{sub}} \left[ I + A \sin\left(\frac{\omega L^2}{\alpha} \hat{t}\right) \right] \quad (43)$$

$$\therefore \theta(\hat{x}, 0) = \frac{u(\hat{x}, 0) - T_{sub}}{T_{sub}} = 0, \quad 0 \leq \hat{x} \leq 1 \quad (44)$$

Dimensionless intensity ( $\hat{I}$ ), amplitude ( $\hat{A}$ ), and frequency ( $\hat{\omega}$ ) are defined from the coefficients in Eqn. (43), and the boundary condition is rewritten as

$$\hat{I} = \frac{LI}{\kappa T_{sub}} \quad (45)$$

$$\hat{A} = \frac{LA}{\kappa T_{sub}} \quad (46)$$

$$\hat{\omega} = \frac{\omega L^2}{\alpha} \quad (47)$$

$$\therefore \frac{\partial \theta}{\partial \hat{x}}(1, \hat{t}) = \hat{I} + \hat{A} \sin(\hat{\omega} \hat{t}), \quad 0 \leq \hat{t} \leq \infty \quad (48)$$

Dimensionless partial differential equation and dimensionless boundary and initial conditions form the dimensionless initial boundary value problem shown in Eqn. (49).

$$\begin{cases} \frac{\partial \theta}{\partial \hat{t}} = \frac{\partial^2 \theta}{\partial \hat{x}^2}, & 0 \leq \hat{x} \leq 1, & 0 \leq \hat{t} \leq \infty \\ \theta(0, \hat{t}) = 0, & 0 \leq \hat{t} \leq \infty \\ \frac{\partial \theta}{\partial \hat{x}}(1, \hat{t}) = \hat{I} + \hat{A} \sin(\hat{\omega} \hat{t}), & 0 \leq \hat{t} \leq \infty \\ \theta(\hat{x}, 0) = 0, & 0 \leq \hat{x} \leq 1 \end{cases} \quad (49)$$

In order to solve the dimensionless initial boundary value problem, the boundary conditions has to be homogenized. Therefore, the dimensionless temperature function is rewritten as the sum of two functions ( $\Theta$  and  $S$ ). The first function will be used to solve the system, while the second function must satisfy the boundary conditions.

$$\theta(\hat{x}, \hat{t}) = \Theta(\hat{x}, \hat{t}) + S(\hat{x}, \hat{t}) \quad (50)$$

$$\frac{\partial \theta}{\partial \hat{t}} = \frac{\partial \Theta}{\partial \hat{t}} + \frac{\partial S}{\partial \hat{t}} \quad (51)$$

$$\frac{\partial^2 \theta}{\partial \hat{x}^2} = \frac{\partial^2 \Theta}{\partial \hat{x}^2} + \frac{\partial^2 S}{\partial \hat{x}^2} \quad (52)$$

Integration of the flux boundary condition and application of the first boundary condition to the constant of integration results in the homogenizing function.

$$\frac{\partial S}{\partial \hat{x}} = \frac{\partial \theta}{\partial \hat{x}}(1, \hat{t}) = \hat{I} + \hat{A} \sin(\hat{\omega} \hat{t}) \quad (53)$$

$$S(\hat{x}, \hat{t}) = \hat{x}[\hat{I} + \hat{A} \sin(\hat{\omega} \hat{t})] + s_0 \quad (54)$$

$$S(0, \hat{t}) = \theta(0, \hat{t}) = 0 \quad (55)$$

$$\therefore S(\hat{x}, \hat{t}) = \hat{x}[\hat{I} + \hat{A} \sin(\hat{\omega} \hat{t})] \quad (56)$$

$$\frac{\partial S}{\partial \hat{t}} = \hat{x} \hat{\omega} \hat{A} \cos(\hat{\omega} \hat{t}) \quad (57)$$

$$\frac{\partial^2 S}{\partial \hat{x}^2} = 0 \quad (58)$$

$$S(\hat{x}, 0) = \hat{x} \hat{I} \quad (59)$$

The forcing term in the partial differential equation and the initial condition value are defined with new functions, which are useful in subsequent steps.

$$\frac{\partial \Theta}{\partial \hat{t}} = \frac{\partial^2 \Theta}{\partial \hat{x}^2} - \frac{\partial S}{\partial \hat{t}} \quad (60)$$

$$F(\hat{x}, \hat{t}) = -\frac{\partial S}{\partial \hat{t}} = -\hat{x} \hat{\omega} \hat{A} \cos(\hat{\omega} \hat{t}) \quad (61)$$

$$\Theta(0, \hat{t}) = \theta(0, \hat{t}) - S(0, \hat{t}) = 0 \quad (62)$$

$$\frac{\partial \Theta}{\partial \hat{x}}(1, \hat{t}) = \frac{\partial \theta}{\partial \hat{x}}(1, \hat{t}) - \frac{\partial S}{\partial \hat{x}}(1, \hat{t}) = 0 \quad (63)$$

$$\Theta(\hat{x}, 0) = \theta(\hat{x}, 0) - S(\hat{x}, 0) = -S(\hat{x}, 0) \quad (64)$$

$$G(\hat{x}) = -S(\hat{x}, 0) = -\hat{x} \hat{I} \quad (65)$$

Taking the partial derivatives of  $S$  and rewriting the partial differential equation and the boundary and initial conditions in terms of  $\Theta$  results in the homogenized initial boundary value problem in Eqn. (66).

$$\begin{cases} \frac{\partial \Theta}{\partial \hat{t}} = \frac{\partial^2 \Theta}{\partial \hat{x}^2} + F(\hat{x}, \hat{t}), & 0 \leq \hat{x} \leq 1, & 0 \leq \hat{t} \leq \infty \\ \Theta(0, \hat{t}) = 0, & 0 \leq \hat{t} \leq \infty \\ \frac{\partial \Theta}{\partial \hat{x}}(1, \hat{t}) = 0, & 0 \leq \hat{t} \leq \infty \\ \Theta(\hat{x}, 0) = G(\hat{x}), & 0 \leq \hat{x} \leq 1 \end{cases} \quad (66)$$

When the boundary conditions were homogenized, a forcing term was added to the partial differential equation to make it inhomogeneous.

This type of partial differential equation is solved via eigenfunction expansion. The first step in eigenfunction expansion is to solve for the eigenvalues and eigenfunctions of the related homogenous partial differential equation, shown in Eqn. (67).

$$\frac{\partial \Theta}{\partial \hat{t}} = \frac{\partial^2 \Theta}{\partial \hat{x}^2} \quad (67)$$

Using the method of separation of variables,  $\Theta(\hat{x}, \hat{t})$  is a product of two functions ( $X$  and  $T$ ), which are each functions of a single variable.

$$\Theta(\hat{x}, \hat{t}) = X(\hat{x})T(\hat{t}) \quad (68)$$

$$\frac{\partial \Theta}{\partial \hat{t}} = \frac{\partial}{\partial \hat{t}}(X(\hat{x})T(\hat{t})) = X \frac{dT}{d\hat{t}} \quad (69)$$

$$\frac{\partial^2 \Theta}{\partial \hat{x}^2} = \frac{\partial^2}{\partial \hat{x}^2}(X(\hat{x})T(\hat{t})) = T \frac{d^2 X}{d\hat{x}^2} \quad (70)$$

The substitution of Eqn. (69) and (70) into Eqn. (67) and rearranging, reveals that both sides are functions of a single variable. Each side must be equal to a constant ( $\lambda$ ) with values of  $\hat{t}$  and  $\hat{x}$ .

$$\frac{1}{T} \frac{dT}{d\hat{t}} = \frac{1}{X} \frac{d^2 X}{d\hat{x}^2} = \lambda \quad (71)$$

$$\therefore \frac{d^2 X}{d\hat{x}^2} = \lambda X, \quad 0 \leq \hat{x} \leq 1 \quad (72)$$

Application of the product of functions to the boundary conditions results in

$$\Theta(0, \hat{t}) = X(0)T(\hat{t}) = 0 \quad (73)$$

$$\therefore X(0) = 0 \quad (74)$$

$$\frac{\partial \Theta}{\partial \hat{x}}(1, \hat{t}) = \frac{dX}{d\hat{x}}(1)T(\hat{t}) = 0 \quad (75)$$

$$\therefore \frac{dX}{d\hat{x}}(1) = 0 \quad (76)$$

Eqn. (72), (75), and (76) together form the eigenvalue problem shown in Eqn. (77):

$$\begin{cases} \frac{d^2 X}{d\hat{x}^2} = \lambda X, & 0 \leq \hat{x} \leq 1 \\ X(0) = 0 \\ \frac{dX}{d\hat{x}}(1) = 0 \end{cases} \quad (77)$$

This eigenvalue problem has potential solutions for three cases. In the first case,  $\lambda$  is greater than zero:

$$\lambda = k^2, \quad k > 0 \quad (78)$$

$$\begin{cases} \frac{d^2 X}{d\hat{x}^2} = k^2 X, & 0 \leq \hat{x} \leq 1 \\ X(0) = 0 \\ \frac{dX}{d\hat{x}}(1) = 0 \end{cases} \quad (79)$$

$$X(\hat{x}) = a_0 \cosh(k\hat{x}) + b_0 \sinh(k\hat{x}) \quad (80)$$

$$X(0) = [a_0 \cosh(k\hat{x}) + b_0 \sinh(k\hat{x})]_{\hat{x}=0} = a_0 = 0 \quad (81)$$

$$\frac{dX}{d\hat{x}}(1) = [a_0 k \sinh(k\hat{x}) + b_0 k \cosh(k\hat{x})]_{\hat{x}=1} = b_0 k \cosh(k) = 0 \quad (82)$$

Since the hyperbolic cosine function is never zero, and  $k$  is greater than zero, the only solution to the first case is the trivial solution.

$$\therefore X(\hat{x}) \equiv 0 \quad (83)$$

In the second case,  $\lambda$  is equal to zero:

$$\lambda = 0 \quad (84)$$

$$\begin{cases} \frac{d^2 X}{d\hat{x}^2} = 0, & 0 \leq \hat{x} \leq 1 \\ X(0) = 0 \\ \frac{dX}{d\hat{x}}(1) = 0 \end{cases} \quad (85)$$

$$X(\hat{x}) = a_0 \hat{x} + b_0 \quad (86)$$

$$X(0) = b_0 = 0 \quad (87)$$

$$\frac{dX}{d\hat{x}}(1) = a_0 = 0 \quad (88)$$

The only solution to the second case is also the trivial solution.

$$\therefore X(\hat{x}) \equiv 0 \quad (89)$$

In the third case,  $\lambda$  is less than zero:

$$\lambda = -k^2, \quad k > 0 \quad (90)$$

$$\begin{cases} \frac{d^2 X}{d\hat{x}^2} = -k^2 X, & 0 \leq \hat{x} \leq 1 \\ X(0) = 0 \\ \frac{dX}{d\hat{x}}(1) = 0 \end{cases} \quad (91)$$

$$X(\hat{x}) = a_0 \cos(k\hat{x}) + b_0 \sin(k\hat{x}) \quad (92)$$

$$X(0) = [a_0 \cos(k\hat{x}) + b_0 \sin(k\hat{x})]_{\hat{x}=0} = a_0 = 0 \quad (93)$$

$$\frac{dX}{d\hat{x}}(1) = [-a_0 k \sin(k\hat{x}) + b_0 k \cos(k\hat{x})]_{\hat{x}=1} = b_0 k \cos(k) = 0 \quad (94)$$

Since  $k$  is greater than zero, the only non-trivial solution to the third case is required cosine function to be zero:



$$\cos(k) = 0 \quad (95)$$

$$k_n = \cos^{-1}(0) = \left(n - \frac{1}{2}\right)\pi, \quad n = 1, 2, 3 \dots \quad (96)$$

Therefore, when the constant  $b_0$  is unity, the eigenfunction and eigenvalues are:

$$\therefore X_n(\hat{x}) = \sin(k_n \hat{x}) = \sin\left(\left(n - \frac{1}{2}\right)\pi \hat{x}\right), \quad n = 1, 2, 3 \dots \quad (97)$$

$$\therefore \lambda_n = -k_n^2 = -\left[\left(n - \frac{1}{2}\right)\pi\right]^2, \quad n = 1, 2, 3 \dots \quad (98)$$

The next step of eigenfunction expansion is to expand the partial differential equation and the initial condition using Fourier series.

$$\frac{\partial \Theta}{\partial \hat{t}} = \sum_{n=1}^{\infty} \frac{dT_n}{d\hat{t}} X_n(\hat{x}) \quad (99)$$

$$\frac{\partial^2 \Theta}{\partial \hat{x}^2} = \sum_{n=1}^{\infty} T_n(\hat{t}) \frac{d^2 X_n(\hat{x})}{d\hat{x}^2} = \sum_{n=1}^{\infty} -k_n^2 T_n(\hat{t}) X_n(\hat{x}) \quad (100)$$

$$\theta(\hat{x}, 0) = \sum_{n=1}^{\infty} T_n(0) X_n(\hat{x}) \quad (101)$$

The redefined forcing function  $F(\hat{x}, \hat{t})$  and initial condition value  $G(\hat{x})$  are also expanded as Fourier series.

$$F(\hat{x}, \hat{t}) = \sum_{n=1}^{\infty} f_n(\hat{t}) X_n(\hat{x}) \quad (102)$$

$$G(\hat{x}) = \sum_{n=1}^{\infty} g_n X_n(\hat{x}) \quad (103)$$

The coefficients of the forcing function's Fourier series are found using integration by parts.

$$f_n(\hat{t}) = \frac{2}{1} \int_0^1 F(\hat{x}, \hat{t}) X_n(\hat{x}) d\hat{x} = 2 \int_0^1 -\hat{x} \hat{\omega} \hat{A} \cos(\hat{\omega} \hat{t}) \sin(k_n \hat{x}) d\hat{x} \quad (104)$$

$$f_n(\hat{t}) = -2\hat{\omega}\hat{A} \cos(\hat{\omega}\hat{t}) \int_0^1 \hat{x} \sin(k_n \hat{x}) d\hat{x} \quad (105)$$

$$\int_0^1 \hat{x} \sin(k_n \hat{x}) d\hat{x} = \left[ (\hat{x}) \left( \frac{-\cos(k_n \hat{x})}{k_n} \right) - (1) \left( \frac{-\sin(k_n \hat{x})}{k_n^2} \right) \right]_{\hat{x}=0}^{\hat{x}=1} \quad (106)$$

$$\cos(k_n \hat{x}) = \cos\left(\left(n - \frac{1}{2}\right)\pi\right) = 0 \quad (107)$$

$$\sin(k_n \hat{x}) = \sin\left(\left(n - \frac{1}{2}\right)\pi\right) = (-1)^{n-1} \quad (108)$$

$$\therefore f_n(\hat{t}) = \frac{2\hat{\omega}\hat{A} \cos(\hat{\omega}\hat{t}) (-1)^n}{\left[\left(n - \frac{1}{2}\right)\pi\right]^2}, \quad n = 1, 2, 3 \dots \quad (109)$$

Coefficients of the value of the initial condition Fourier series are found the same way:

$$g_n = \frac{2}{1} \int_0^1 G(\hat{x}) X_n(\hat{x}) d\hat{x} = 2 \int_0^1 -\hat{x} \hat{I} \sin(k_n \hat{x}) d\hat{x} \quad (110)$$

$$g_n = -2\hat{I} \int_0^1 \hat{x} \sin(k_n \hat{x}) d\hat{x} \quad (111)$$

$$\therefore g_n = \frac{2\hat{I}(-1)^n}{\left[\left(n - \frac{1}{2}\right)\pi\right]^2}, \quad n = 1, 2, 3 \dots \quad (112)$$

Combining the expanded forms of the terms in the homogenized initial boundary value problem converts the problem from a single partial differential equation to infinite number of ordinary differential equations, each with an initial condition.

$$\frac{\partial \Theta}{\partial \hat{t}} - \frac{\partial^2 \Theta}{\partial \hat{x}^2} - F(\hat{x}, \hat{t}) = 0 \quad (113)$$

$$\sum_{n=1}^{\infty} \left\{ \frac{dT_n}{d\hat{t}} + k_n^2 T_n(\hat{t}) - f_n(\hat{t}) \right\} X_n(\hat{x}) = 0 \quad (114)$$

$$\therefore \frac{dT_n}{d\hat{t}} = -k_n^2 T(\hat{t}) + f_n(\hat{t}), \quad n = 1, 2, 3 \dots \quad (115)$$

$$\theta(\hat{x}, 0) - G(\hat{x}) = 0 \quad (116)$$

$$\sum_{n=1}^{\infty} \{T_n(0) - g_n\} X_n(\hat{x}) = 0 \quad (117)$$

$$\therefore T_n(0) = g_n, \quad n = 1, 2, 3 \dots \quad (118)$$

The infinite ordinary differential equations and their initial conditions combine to create infinite number of initial value problems, as shown in Eqn. (119).

$$\begin{cases} \frac{dT_n}{d\hat{t}} = -k_n^2 T(\hat{t}) + f_n(\hat{t}), & 0 \leq \hat{t} \leq \infty \\ T_n(0) = g_n \end{cases}, \quad n = 1, 2, 3 \dots \quad (119)$$

To simultaneously solve the infinite initial value problems requires the solution had to be derived to the related initial value problem in Eqn. (120).

$$\begin{cases} \frac{dy}{d\hat{t}} = a_1 y(\hat{t}) + a_2 \cos(\hat{\omega}\hat{t}) + a_3 \sin(\hat{\omega}\hat{t}), & 0 \leq \hat{t} \leq \infty \\ y(0) = a_0 \end{cases} \quad (120)$$

The general solution to the related homogenous ordinary differential equation is shown in Eqn. (123).

$$\frac{dy_h}{d\hat{t}} = a_1 y_h \quad (121)$$

$$y_h(\hat{t}) = c_1 e^{a_1 \hat{t}} \quad (122)$$

The particular solution to the initial value problem is derived as follows:

$$y_p(\hat{t}) = c_2 \cos(\hat{\omega}\hat{t}) + c_3 \sin(\hat{\omega}\hat{t}) \quad (123)$$

$$\frac{dy_p}{d\hat{t}} = -c_2 \hat{\omega} \sin(\hat{\omega}\hat{t}) + c_3 \hat{\omega} \cos(\hat{\omega}\hat{t}) = a_1 y_p + a_2 \cos(\hat{\omega}\hat{t}) + a_3 \sin(\hat{\omega}\hat{t}) \quad (124)$$

$$\begin{aligned}
& -c_2 \hat{\omega} \sin(\hat{\omega} \hat{t}) + c_3 \hat{\omega} \cos(\hat{\omega} \hat{t}) \\
& = a_1 [c_2 \cos(\hat{\omega} \hat{t}) + c_3 \sin(\hat{\omega} \hat{t})] + a_2 \cos(\hat{\omega} \hat{t}) + a_3 \sin(\hat{\omega} \hat{t})
\end{aligned} \tag{125}$$

$$\begin{cases} -c_2 \hat{\omega} = a_1 c_3 + a_3 \\ c_3 \hat{\omega} = a_1 c_2 + a_2 \end{cases} \tag{126}$$

$$c_2 = -\frac{a_1 a_2 + a_3 \hat{\omega}}{a_1^2 + \hat{\omega}^2} \tag{127}$$

$$c_3 = -\frac{a_1 a_3 - a_2 \hat{\omega}}{a_1^2 + \hat{\omega}^2} \tag{128}$$

When the homogenous and particular solution are combined and applied, the initial condition generates the solution to the initial value problem.

$$y(\hat{t}) = y_h(\hat{t}) + y_p(\hat{t}) = c_1 e^{a_1 \hat{t}} + c_2 \cos(\hat{\omega} \hat{t}) + c_3 \sin(\hat{\omega} \hat{t}) \tag{129}$$

$$y(0) = c_1 + c_2 = a_0 \tag{130}$$

$$c_1 = a_0 - c_2 = a_0 + \frac{a_1 a_2 + a_3 \hat{\omega}}{a_1^2 + \hat{\omega}^2} \tag{131}$$

$$\begin{aligned}
\therefore y(\hat{t}) = & \left[ a_0 + \frac{a_1 a_2 + a_3 \hat{\omega}}{a_1^2 + \hat{\omega}^2} \right] e^{a_1 \hat{t}} - \frac{a_1 a_2 + a_3 \hat{\omega}}{a_1^2 + \hat{\omega}^2} \cos(\hat{\omega} \hat{t}) \\
& - \frac{a_1 a_3 - a_2 \hat{\omega}}{a_1^2 + \hat{\omega}^2} \sin(\hat{\omega} \hat{t})
\end{aligned} \tag{132}$$

When the coefficient of Eqn. (119) and (120) are combined and applied to the solution derived in Eqn. (132), the solutions to the infinitely many initial value problems are

$$a_1 = -k_n^2 \tag{133}$$

$$a_2 = \frac{2\hat{\omega}\hat{A}(-1)^n}{k_n^2} \tag{134}$$

$$a_3 = 0 \tag{135}$$

$$a_0 = \frac{2\hat{I}(-1)^n}{k_n^2} \quad (136)$$

$$\begin{aligned} \therefore T_n(\hat{t}) = & \frac{2(-1)^n}{k_n^2(k_n^4 + \hat{\omega}^2)} \{ [\hat{I}(k_n^4 + \hat{\omega}^2) - k_n^2 \hat{\omega} \hat{A}] e^{-k_n^2 \hat{t}} + k_n^2 \hat{\omega} \hat{A} \cos(\hat{\omega} \hat{t}) \\ & + \hat{\omega}^2 \hat{A} \sin(\hat{\omega} \hat{t}) \}, \quad n = 1, 2, 3 \dots \end{aligned} \quad (137)$$

The solution to the initial boundary value problem is built from the solutions derived in the Eqn. (68). First, the solution to  $\Theta(\hat{x}, \hat{t})$  is built from Eqn. (97) and (138).

$$\Theta(\hat{x}, \hat{t}) = \sum_{n=1}^{\infty} T_n(\hat{t}) X_n(\hat{x}) \quad (138)$$

$$\begin{aligned} \Theta(\hat{x}, \hat{t}) = & \sum_{n=1}^{\infty} \left[ \frac{2(-1)^n}{k_n^2(k_n^4 + \hat{\omega}^2)} \{ [\hat{I}(k_n^4 + \hat{\omega}^2) - k_n^2 \hat{\omega} \hat{A}] e^{-k_n^2 \hat{t}} + k_n^2 \hat{\omega} \hat{A} \cos(\hat{\omega} \hat{t}) \right. \\ & \left. + \hat{\omega}^2 \hat{A} \sin(\hat{\omega} \hat{t}) \} \sin(k_n \hat{x}) \right] \end{aligned} \quad (139)$$

The solution to  $\theta(\hat{x}, \hat{t})$ , which was taken from Eqn. (56) and (140), was the solution to the dimensionless initial boundary value problem, including steady-state, transient, and harmonic terms, as expected

$$\begin{aligned} \theta(\hat{x}, \hat{t}) = & \hat{x} [\hat{I} + \hat{A} \sin(\hat{\omega} \hat{t})] \\ & + \sum_{n=1}^{\infty} \left[ \frac{2(-1)^n}{k_n^2(k_n^4 + \hat{\omega}^2)} \{ [\hat{I}(k_n^4 + \hat{\omega}^2) - k_n^2 \hat{\omega} \hat{A}] e^{-k_n^2 \hat{t}} \right. \\ & \left. + k_n^2 \hat{\omega} \hat{A} \cos(\hat{\omega} \hat{t}) + \hat{\omega}^2 \hat{A} \sin(\hat{\omega} \hat{t}) \} \sin(k_n \hat{x}) \right] \end{aligned} \quad (140)$$

### 2.2.1 Steady-State Regime

The steady-state solution is obtained by having the harmonic amplitude and frequency be zero and time be infinity.

$$\theta_{ss}(\hat{x}) = \lim_{\hat{t} \rightarrow \infty} \theta(\hat{x}, \hat{t}) = \hat{x}\hat{I} \quad (141)$$

Applying  $\hat{x}$  and  $\hat{I}$  from eqn.(25) and (45) into eqn. (141), the dimensionless steady-state temperature is obtained.

$$\theta_{ss}(\hat{x}) = \frac{xI}{\kappa T_{sub}} \quad (142)$$

Instead of using single point measurement, slope of 3 points is used to find  $\kappa$  for better accuracy.

### 2.2.2 Transient Regime

Although the operating conditions for the transient regime include constant intensity, but the amplitude of the harmonic intensity has to be zero, in Eqn. (140).

$$\therefore \theta_{transient} = \hat{x}\hat{I} + \sum_{n=1}^{\infty} \left[ \frac{2(-1)^n}{k_n^2} \{ \hat{I} e^{-k_n^2 \hat{t}} \} \sin(k_n \hat{x}) \right] \quad (143)$$

Time constant ( $\tau$ ) defines the two-third duration of the transient response. For this system, with an infinite number of decaying exponentials, the time constant was based on the slowest rate of decay:

$$\tau = \frac{1}{\min(\text{rate of decay})} \quad (144)$$

The dimensionless time constant ( $\hat{\tau}$ ) is based on the slowest rate of decay for the dimensionless time. In many engineering systems, the transient response is considered to be negligible after  $5\tau$ .

$$\hat{\tau} = \frac{1}{\min(k_n^2, n = 1, 2, 3 \dots)} = \frac{1}{\left[ \left( 1 - \frac{1}{2} \right) \pi \right]^2} = \frac{4}{\pi^2} \quad (145)$$

$$e^{-k_n^2 \hat{t}} \Big|_{\hat{t}=5\hat{\tau}} = e^{-\frac{\pi^2}{4} \left( \frac{5}{\pi^2} \right)} = e^{-5} \approx 0.674 \quad (146)$$

The relationship between dimensionless time constant and time constant is shown in Eqn. (147). The relationship between time constant, thermal diffusivity ( $\alpha$ ) and length ( $L$ ) is shown in Eqn. (148).

$$\frac{t}{\tau} = \frac{\hat{t}}{\hat{\tau}} \quad (147)$$

$$\therefore \tau = \hat{\tau} \frac{t}{\hat{t}} = \frac{4}{\pi^2} \frac{L^2}{\alpha} \quad (148)$$

### 2.2.3 Harmonic Regime

Dynamic operation in the harmonic regime means sufficient time has passed for the transient response to die out, meaning sinusoidal oscillations as the sole time-dependent effect.

$$\begin{aligned} \therefore \theta_{harmonic} = & \hat{x}[\hat{I} + \hat{A} \sin(\hat{\omega}\hat{t})] \\ & + \sum_{n=1}^{\infty} \left[ \frac{2(-1)^n}{k_n^2(k_n^4 + \hat{\omega}^2)} \{k_n^2 \hat{\omega} \hat{A} \cos(\hat{\omega}\hat{t}) \right. \\ & \left. + \hat{\omega}^2 \hat{A} \sin(\hat{\omega}\hat{t})\} \sin(k_n \hat{x}) \right] \end{aligned} \quad (149)$$

The first term of Eqn. (149) represents the steady oscillation of temperature along the cantilever while the summation term contributes to the gradual change of temperature. Coupling frequency with the time constant yields an equation for thermal penetration depth ( $L_p$ ), which researchers have used to interpret results.[73], [122]

$$L_p = 2\pi \sqrt{\frac{\alpha}{\omega}} \quad (150)$$

## 2.3 Comparison of 1D Model with FEM

Steady-state, transient and harmonic solutions from the previous section are compared to a three dimensional (3D) Finite Element Model (FEM) with identical geometry, boundary and initial conditions to verify their temperature measurement accuracy in 3D object. Silicon cantilevers with width of 50  $\mu\text{m}$ , thickness of 50  $\mu\text{m}$  and length to width ratios ( $L/w$ ) of 5-100 are considered in order to advantageously utilize symmetry and avoid unnecessary width/thickness and

length/thickness ratios. For steady-state and transient heat transfer analyses 0.705 mW heat is applied at  $\hat{x} = 1$ , and  $\hat{x} = 0$  is at a constant temperature of 300K. For harmonic analysis 0.58 mW of heat is modulated as a sine wave on top of 0.705 mW. The material properties for both the 1D and 3D models are: thermal conductivity[117] is 147 W/m-K, specific heat[123] is 679 J/kg-K and density[124] is 2.328 g/cm<sup>3</sup>.

Figure 2.3 shows how heat is applied at the tip of the cantilever of the FEM model to match the 1D model.

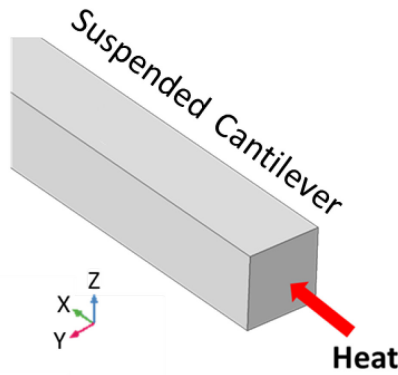


*Figure 2.3 Direction of applied heat in FEM*

Comparison results for the 1D and 3D models are shown in Figure 2.4 - 2.6. Dimensionless length, time, and temperature were calculated from Eqn. (25), (32), and (33), respectively. 300 K is used as the reference temperature to find dimensionless temperature. Although no differences were found between the two methods for the steady-state regime (Figure 2.4), differences between the analytical solution and the FEM varied from 0.003% to 0.2% when  $L/w$  varied from 5 to 100 in the transient regime (Figure 2.5). The harmonic mode (Figure 2.6) had a constant difference of approximately 0.6% for all  $L/w$  ratios. Comparison results revealed the accuracy of the analytical solution.[125]



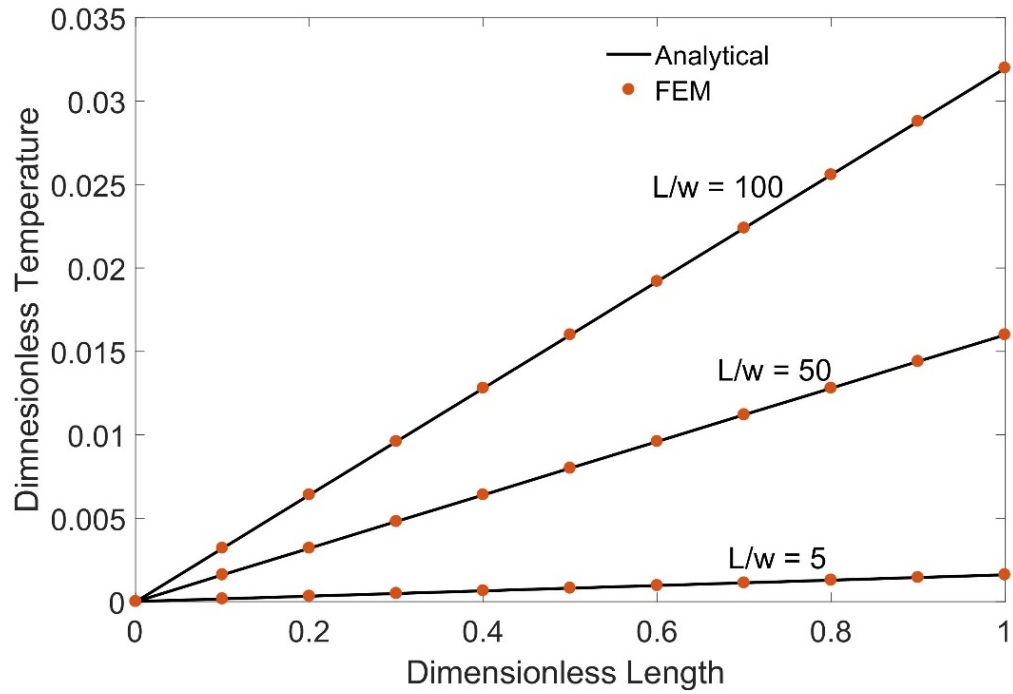


Figure 2.4 Comparison of 1D model and FEM for steady-state heat conduction, including three  $L/w$  ratios (5, 50, and 100).

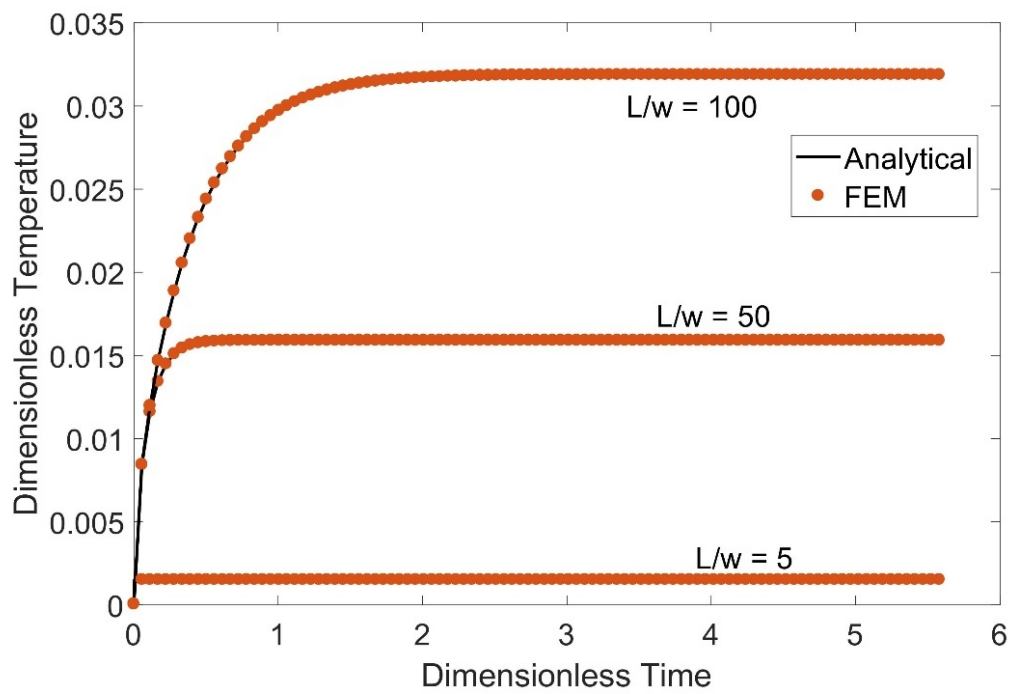


Figure 2.5 Comparison of 1D model and FEM for transient heat conduction, including three  $L/w$  ratios (5, 50, and 100).

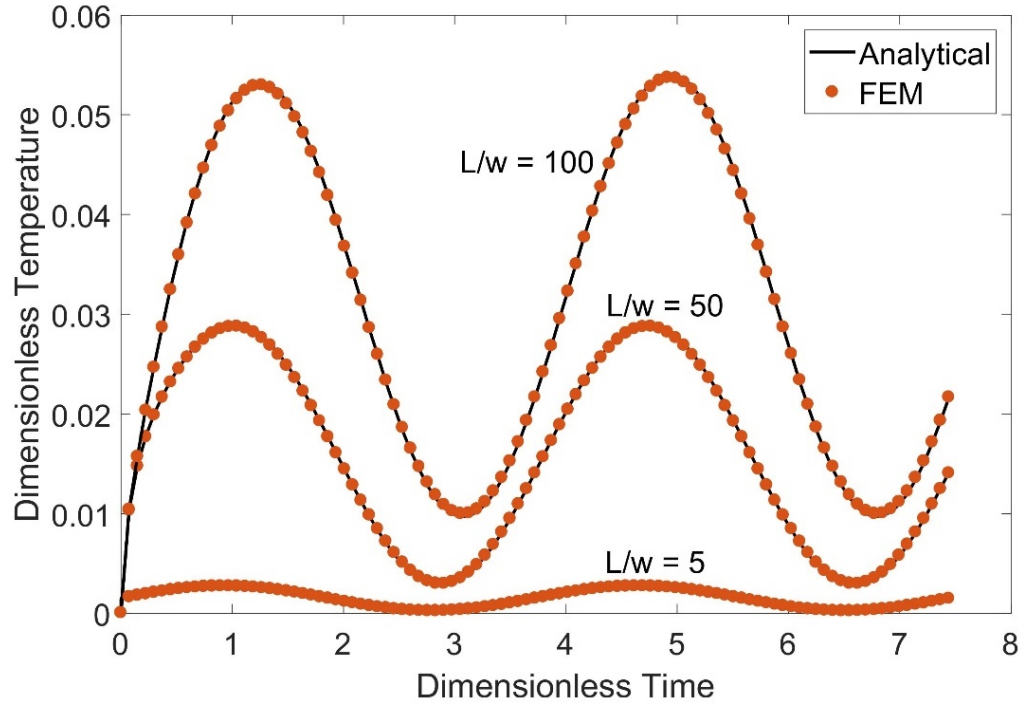


Figure 2.6 Comparison of 1D model and FEM for harmonic heat conduction, including three  $L/w$  ratios (5, 50, and 100).

## 2.4 Phase Shift Along the Cantilever

As the thermal wave propagates through the beam, a phase shift occurs due to time delay of thermal energy transport. The phase shift is calculated from the lag time between dimensionless position 1 and corresponding other positions along the beam by dividing the time delay with the period of a single wave and multiplying by the total phase of that wave. Figure 2.7 shows the expected occurs of a larger phase shifts for longer cantilever. For example, for the beam with  $L/w$  of 10, the phase shift was almost 0, indicating that heat propagated through the beam instantaneously.

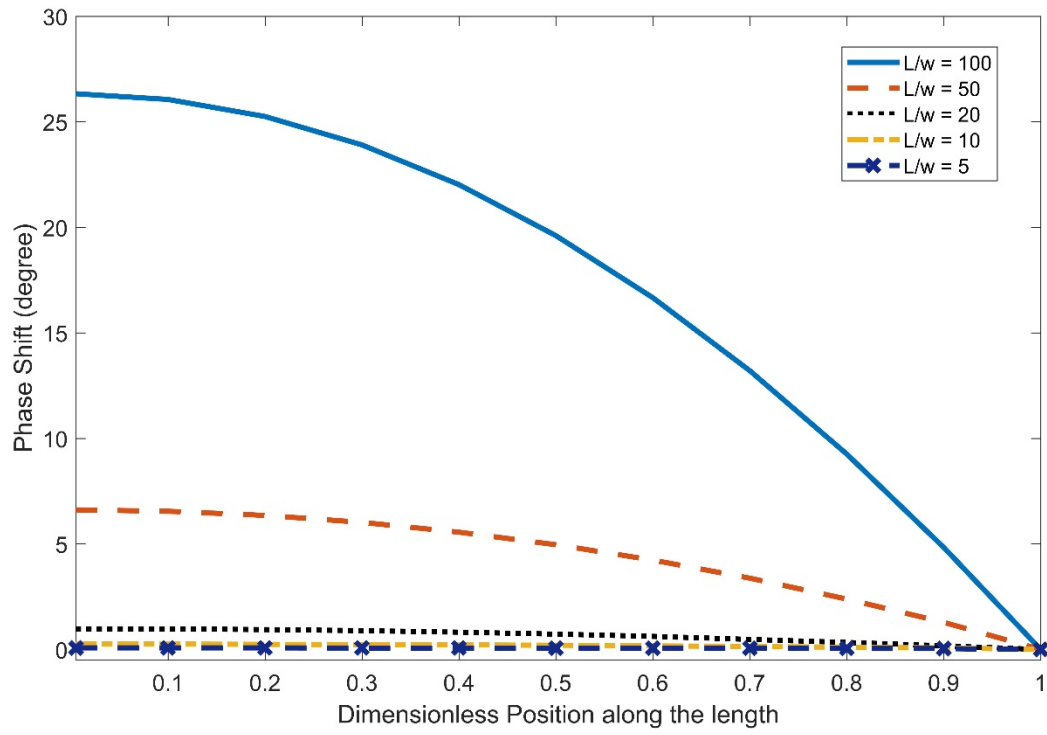


Figure 2.7 Phase shift from Eqn. (149) for the temperature profile along the cantilever of various  $L/w$ .

## **Chapter 3 - Experimental Consideration**

This chapter discusses 1D model applicability for real experiments in which laser heat is introduced perpendicularly to the tip of the cantilever. The chapter also describes the testing of temperature homogeneity in a plane (i.e., homogeneous isotherm) for backside probing and validates the cantilever's base temperature condition by accounting for aspects such as maximum applicable heat and minimum measurable thermal conductivity. The final section of this chapter quantifies the cantilever's temperature due to probe laser absorption, including a technique to eliminate probe absorption impact while evaluating thermal properties via STR.

### **3.1 Comparison Between 1D Analytical Model and 3D FEM with Application of Heat Perpendicular to Tip**

After verifying the 1D analytical model, this research seeks to determine its applicability in analyzing thermal properties in an STR experiment in which heat is applied perpendicularly to the tip of the cantilever. All material properties mentioned in the previous chapter, such as density, thermal conductivity, specific heat etc., are also used in the analysis. Figure 3.1 shows a 3D representation of the cantilever and respective isotherm diagrams. Figure 3.1a and 3.1b represent a system in which the fixed end of the cantilever is attached to a substrate. As shown in Figure 3.1a, the heat flux (laser heating) is applied laterally to the cantilever. However, since STR requires the use of two lasers to thermally characterize a suspended cantilever, Figure 3.1b shows the use of a pump laser to heat the cantilever perpendicularly at the tip from one side while a probe laser scans the temperature from the other side of the cantilever. The mobile probe laser can be focused at any point along the length of the cantilever, and a photodetector registers the change in probe reflectivity, which is correlated to the temperature of those points using a TR coefficient.[55], [96]

Challenges of this technique include laser selection since most of the pump and probe power has to be absorbed and reflected, respectively. In addition, similar to other TR techniques, the sample surface must be optically smooth to avoid unwanted scattering of light. The associated surface temperature and contour plots in Figure 3.1c and 3.1d, respectively, show how heat was transferred along the beam, demonstrating that, for Si with this geometry, the isotherms quickly, within one thickness of the cantilever, became perpendicular to the heat flow. Further analysis of the isotherm and homogeneity of temperature is presented in section 3.4.

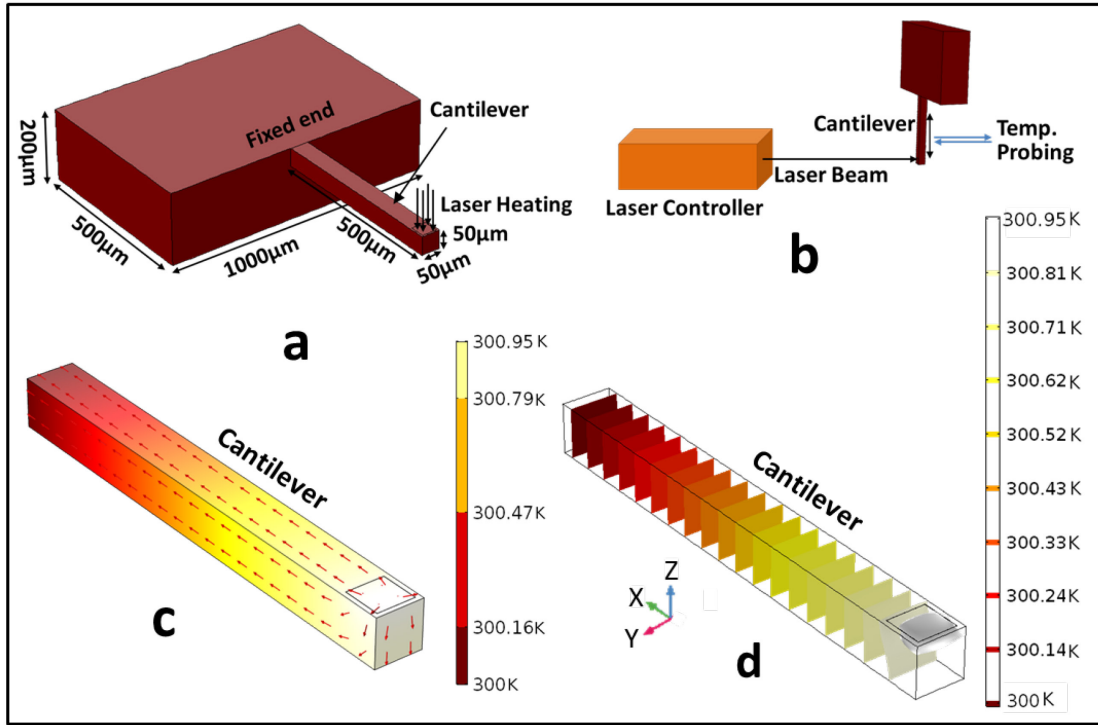


Figure 3.1 a) Cantilever beam with fixed end attached to the substrate with  $L/w$  of 10; b) STR experimental setup, laser heating of the sample, and backside probing along the length; c) surface temperature and heat flow direction only for the cantilever beam; d) isotherm contour plot for the cantilever (Kelvin).[125]

Figure 3.2 shows steady-state temperature distribution along the length of the cantilever with 5–100  $L/w$ . Dimensionless length and temperature were calculated using Eqn. (25) and (33),

respectively. Application of identical conditions to the FEM model revealed that the temperature difference, at a given point along the cantilever's length, between the two models decreased with increased  $L/w$  ratios: 4.8% for  $L/w$  of 5 to 0.05% for  $L/w$  of 100. The difference is illustrated in detail in Figure 3.5.

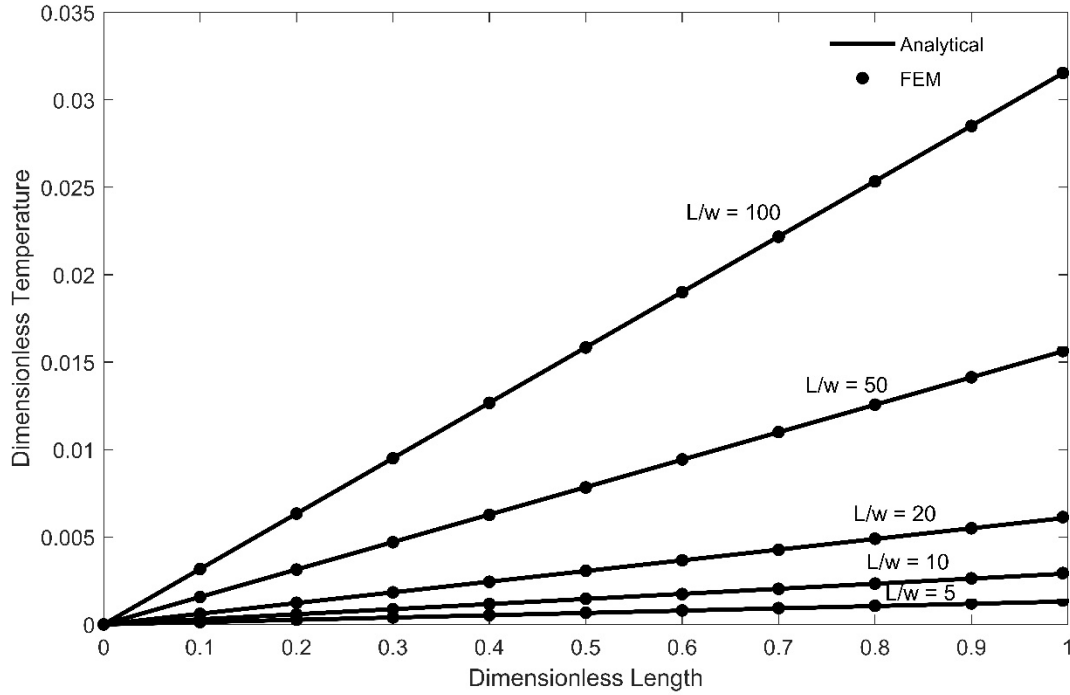
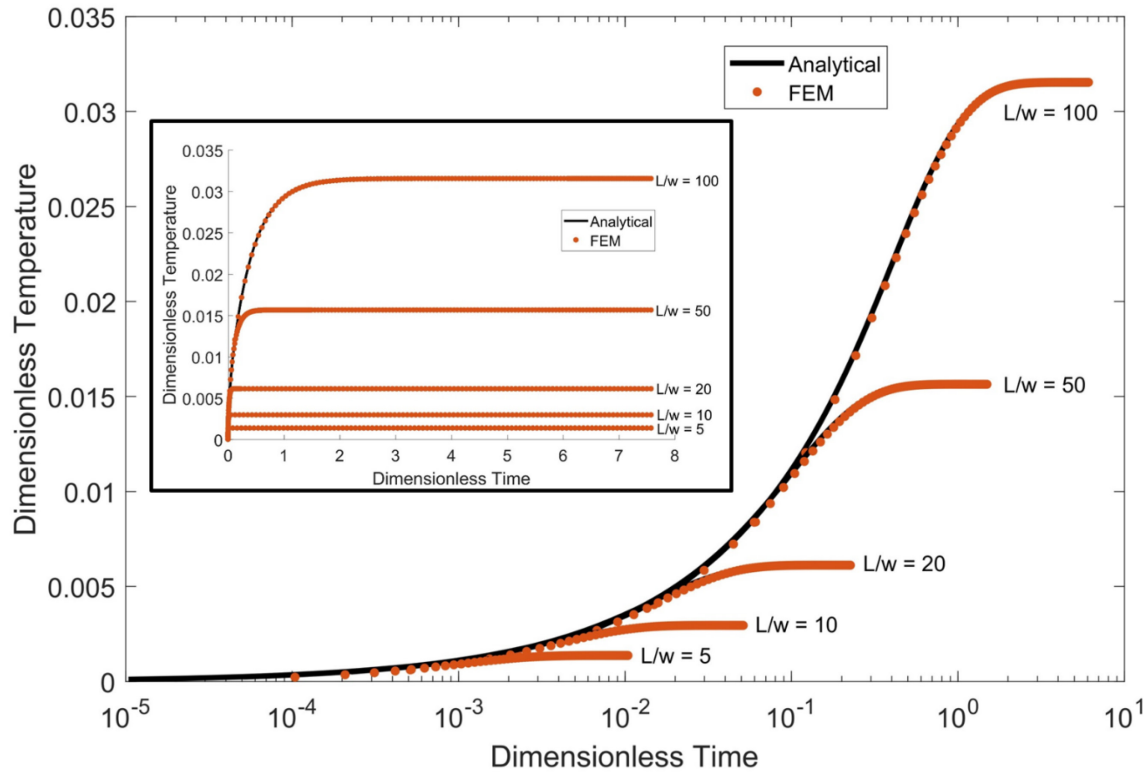


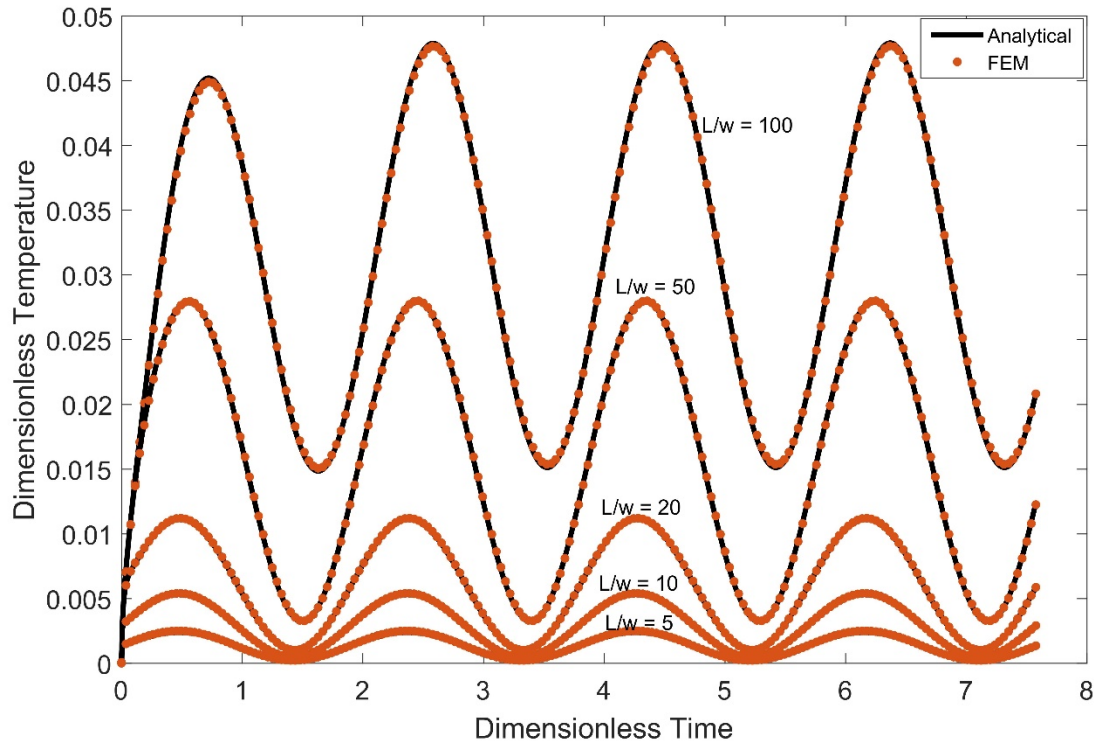
Figure 3.2 Temperature along the beam via 1D steady state heat equation (line) and FEM (points)

Figure 3.3 depicts the transient response of heat at a dimensionless position near the tip of the cantilever. The response of each  $L/w$  ratio was plotted to  $15\tau$ , while the figure inset shows the plot for 1.5 sec. Results in the figure show that deviation between the temperature of the analytical model and the FEM increased as the  $L/w$  ratio decreased. For example, the maximum deviation between the two models was 12.7% with  $L/w$  of 5, whereas the maximum deviation was only 0.85% for  $L/w$  of 100.



*Figure 3.3 Temperature-time relationship for transient heat transfer in the cantilever beam at a dimensionless position of 0.995 obtained via heat equation (line) and FEM (points).*

In harmonic analysis, heat is applied as a sinusoidal wave form with constant intensity and amplitude so that each point along the cantilever experiences periodic increase and decrease in temperature over time. Figure 3.4 shows good agreement between 1D and FEM models, with a difference of 4.8% at a L/w ratio of 5 but only 1% at L/w of 100. As shown in the figure, the cantilever temperature at one dimensionless point increases with increased cantilever length. A careful inspection of the position of the temperature peaks reveals that peaks are shifting to the right side on x-axis. This phenomenon indicates that, due to traveling longer distances, temperature is slowly reaching peaks with an increase in the L / w ratio.



*Figure 3.4 Periodic change of temperature in the cantilever beam at a dimensionless position of 0.995 obtained via heat equation (line) and FEM (points). Diffusivity of the silicon changed the phase of harmonic temperature distribution along the beam.*

Figure 3.5 illustrates the temperature differences between 1D and FEM models at one dimensionless point or time for all three heat conduction modes. The maximum temperature difference is calculated for the same dimensionless position at any given time using the 3D model as the base. For the steady-state mode, the difference between the models decreases from 4.8% to 0.05% as the  $L/w$  ratio increased from 5 to 100. The difference for transient heat transfer is 12.7% for  $L/w$  of 5; as the  $L/w$  ratio increases, the difference became 3.7%, 1.6%, and 0.85% at  $L/w$  of 20, 50, and 100, respectively. As in the steady-state mode, the largest difference for harmonic heat transfer is 4.8% at  $L/w$  ratio of 5, decreasing to 1% at  $L/w$  of 100.



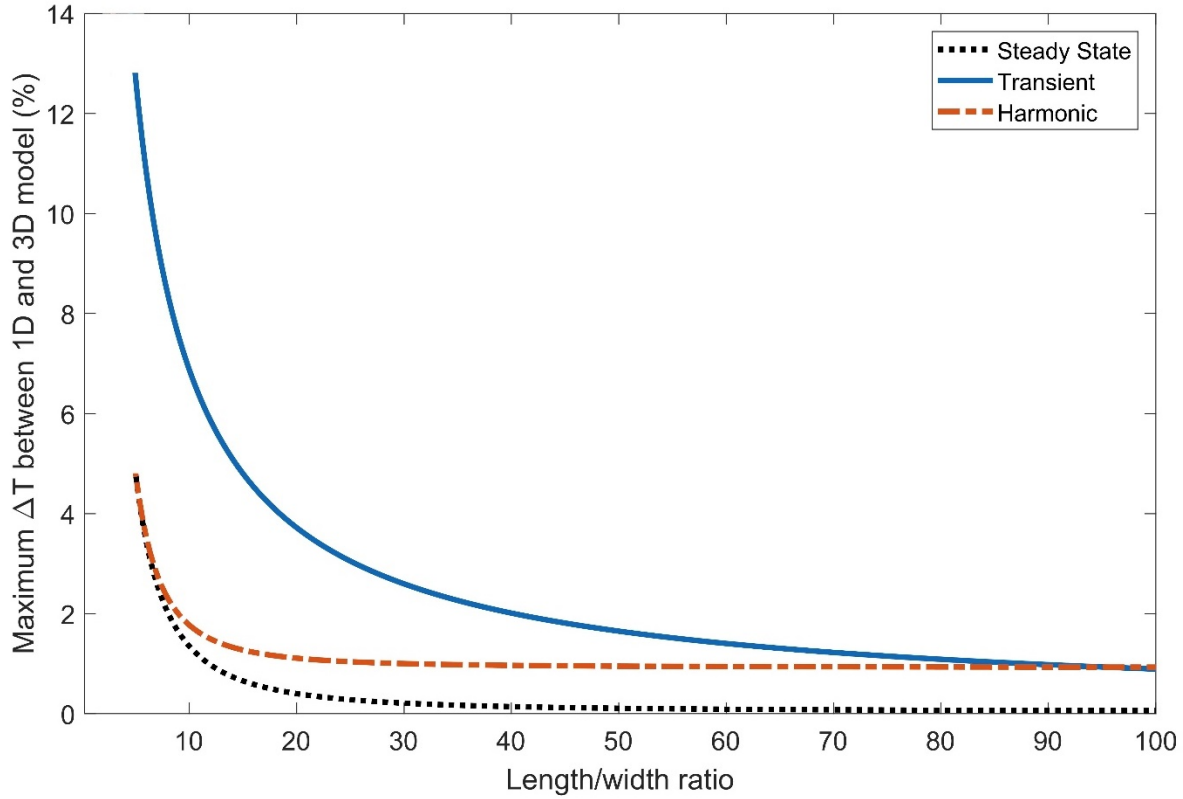


*Figure 3.5 Difference in temperature between developed 1D model and 3D FEM model with respect to  $L/w$  ratio of cantilever beam.*

Because silicon is the most important material in the semiconductor industry, the analytical solution is compared to a 3D FEM for silicon. The temperature difference between the models is high for smaller  $L/w$  ratios for all three regimes, indicating that a micro/nano-cantilever beam, with length comparable to width, acts like a 3D object, thereby preventing a 1D model from accurately predicting its properties. However, as the  $L/w$  ratio increases, specifically  $L/w > 20$ , the difference decreased to less than 4%, and at  $L/w$  of 100, the 3D beam demonstrates behavior similar to a 1D object (less than 1% difference). These results are significant for analyzing thermal properties of micro-nano electronics. Instead of using complex 3D models and finite element simulation, the closed-form temperature equations presented in this research can be used to analyze thermal conductivity of the micro-nano devices.

### 3.2 Backside Probing Validation

Since backside probing in STR measurement reports only one temperature at a point on the surface of the cantilever (Figure 3.1b), temperatures along a given  $y$ - $z$  plane must be equivalent, that is, the isotherms must be perpendicular to the heat flux (1D heat flow). This study modified the FEM to heat the tip of the cantilever, as shown in Figure 3.1a, and then 13 points in a  $y$ - $z$  plane were compared, as presented in the insets of Figure 3.6 and 3.7. Temperature differences of various  $L/w$  ratios reveals that isotherms became homogeneous at the same distance for both 10 and 100  $L/w$ , thereby proving that homogeneity does not depend on the  $L/w$  ratio (Figure 3.6).

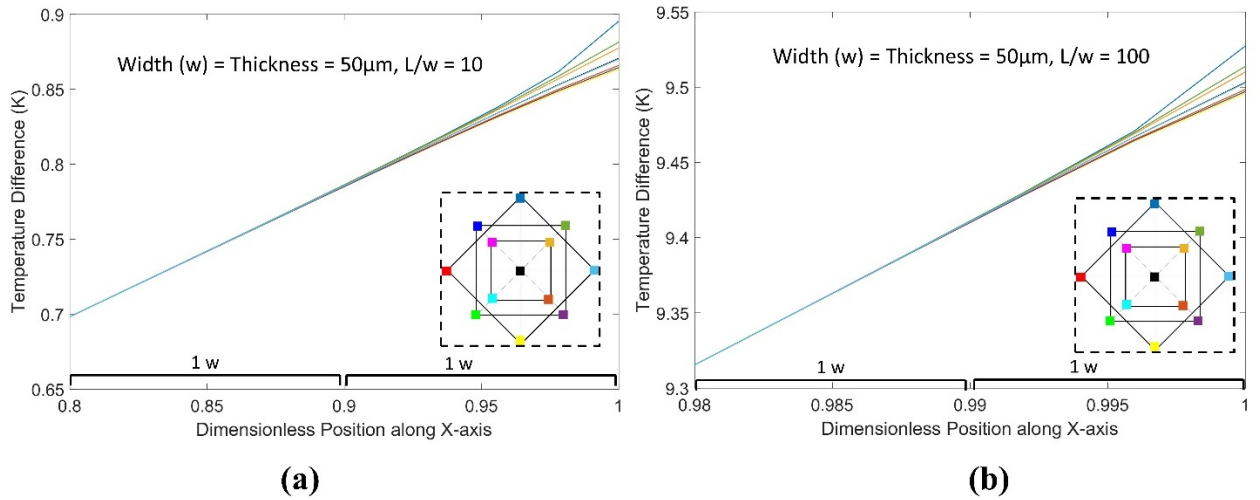
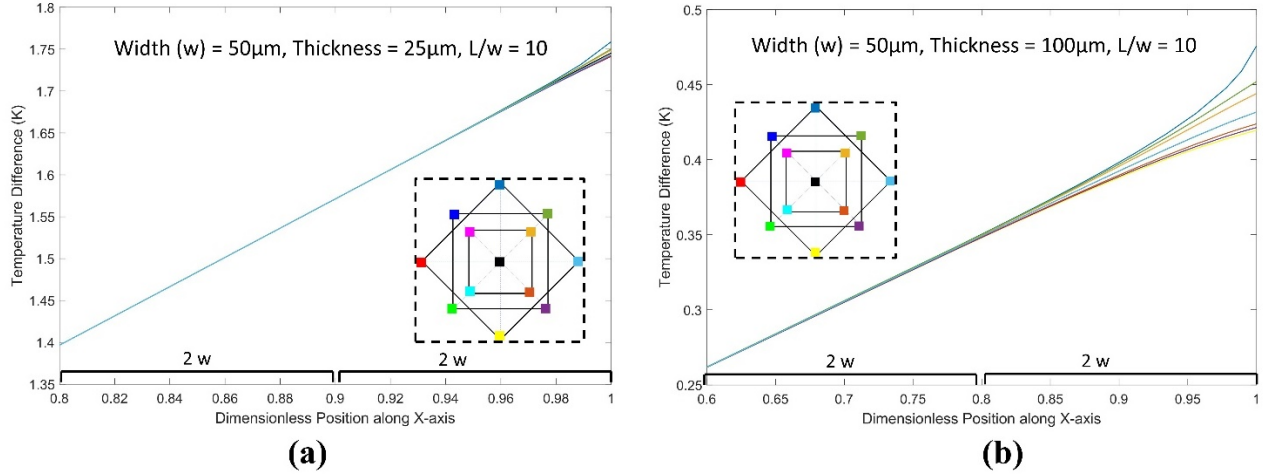


Figure 3.6 Temperature distribution in 13 points along the length of the cantilever for a)  $L/w$  ratio of 10, b)  $L/w$  ratio of 100. Length equal to one width is shown in the  $x$ -axis. Insets show points considered in  $y$ - $z$  plane and the color of each points represent the same color line in the graph.

This study then investigates the dependency of a homogeneous isotherm on the width-to-thickness ratio. As shown in Figure 3.7, the temperature of different points in a plane becomes identical at the very beginning of the tip when the width was double the thickness. However, temperatures of the 13 points do not become equivalent until the distance equaled twice the width

when width/thickness was 0.5, thereby proving that homogeneity certainly depends on the width-to-thickness ratio.



*Figure 3.7 Temperature distribution in 13 points along the length of the cantilever for a) width to thickness ratio of 2, b) width to thickness ratio of 0.5. Length equal to two width is shown in the x-axis. Inset shows the points considered in y-z plane and color of each points represent the same color line in the graph.*

Several simulations like those in Figure 3.7 are conducted for different width to thickness ratios and results are summarized in Figure 3.8 shows how far from the cantilever tip the difference among the points became negligible (i.e., the temperature profile became 1D). Temperature differences in the figure are shown as 1% and 0.5% standard deviation from the mean. As shown, when the thickness is greater than the width, the temperature profile does not become 1D until the distance from the tip equaled several widths. However, as the thickness becomes less than the width, both differences become zero within the distance from the cantilever tip equivalent to 50% of cantilever's width. The sample used in current study has width to thickness ratio of around 60. Thus, back side probing will yield homogenous temperature and thermal conductivity of the material.

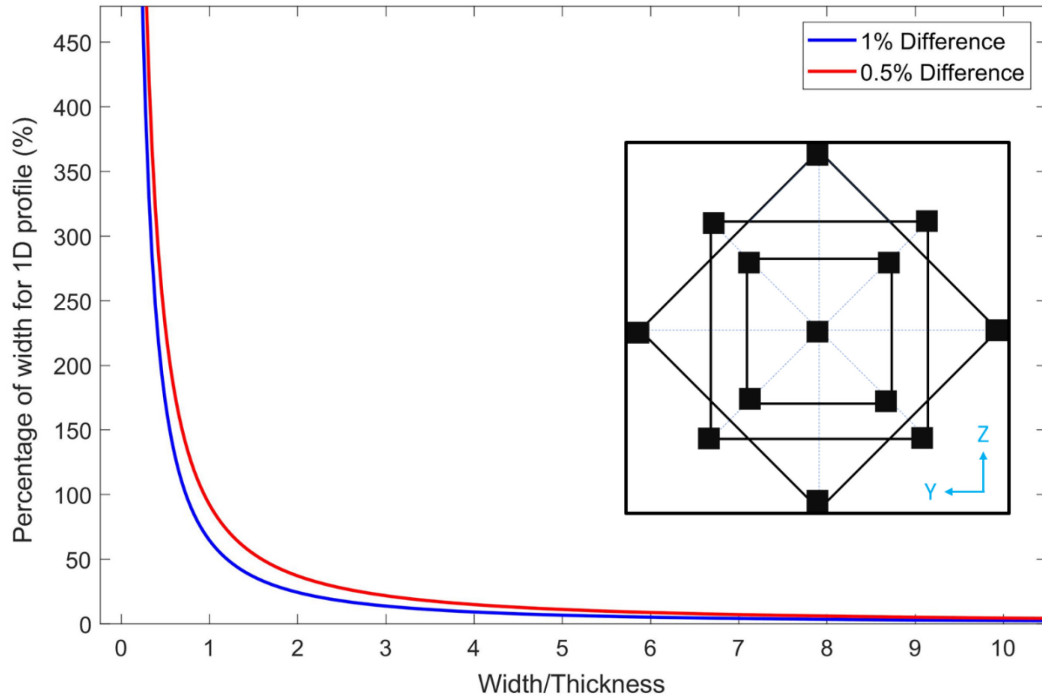


*Figure 3.8 Distance from the tip, shown as the percentage of width, when temperature difference of all points in the y-z plane become 1% and 0.5%. Inset shows the points considered in the y-z plane to compare temperatures.*

### 3.3 Cantilever's Base Temperature Validation

As a cantilever beam is heated at one end, heat propagates through to the fixed end. The 1D heat transfer model assumes that the fixed end (interface between cantilever beam and substrate) is always at room/environment temperature, meaning that this model provides optimal results for the thermal conductivity of the material when this boundary condition is satisfied. During the experiment, however, various factors may affect the base temperature and shift it from ideal condition. In order to verify the fixed-end boundary condition is correct, the following factors must be analyzed to determine how they affect the base temperature.

### **(i) Applied heat at the tip of the cantilever**

When heat was applied at the tip of the cantilever, the temperature of the beam increased. In a 1D model, however, the base temperature remains constant no matter how much heat is applied at the tip; applied heat only changes the steepness of the  $\Delta T$  versus  $x$  graph. In the experiment, the SOI substrate is clamped with a sample holder and attached to the cryostat head which keeps the base temperature at a constant value. Study results shows that if too much heat is applied at the tip, the base cannot dissipate all the heat to the substrate of the SOI wafer, resulting in increased temperature of the base.

### **(ii) Length/width (L/w) ratio of the Si cantilever**

For a fixed width, a small L/w ratio means a shorter cantilever, and a large L/w ratio means a long cantilever. Diffusion may have caused the short and long cantilevers to have the same increase in base temperature for the same heat flux applied at the tip. However, overall temperature rise along the length is relatively small for a shorter cantilever, the base temperature for a short cantilever demonstrates high impact on the stiffness of the  $\Delta T$  versus  $x$  graph by reducing the difference between tip and base temperature, but this rise has minimal impact on the long cantilever due to the small base-to-tip temperature ratio.

### **(iii) Thermal conductivity of the sample**

Low thermal conductivity means low heat diffusivity ( $\alpha \propto \kappa$ ), which can increase base temperature and temperature along the length of the cantilever, thereby limiting how low thermal conductivity can be analyzed by the 1D model. Moreover, very low thermal conductivity appears in two cases in this research: a very thin sample ( $< 100$  nm)[126] and a very low initial temperature

(< 10 K).[10] Ballistic transport dominated in both of cases, and 1D diffusive model cannot analyze thermal property of these cantilevers.[121], [127]

#### (iv) Substrate to cantilever volume ratio

If the substrate volume is comparable to the volume of the cantilever, the heat dissipated by the cantilever increases the temperature of the substrate, thereby increasing the cantilever's base temperature. But if substrate volume is few times greater than the cantilever's volume, the base temperature is not affected. In the FEM analysis for this research, the substrate was chosen such that the ratio between the two volumes was at least 2000.

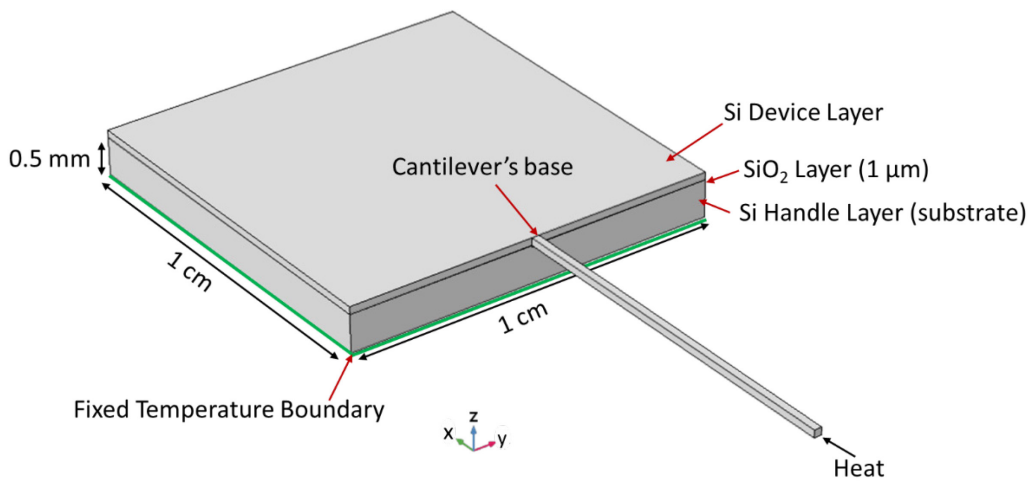


*Figure 3.9 Geometric considerations for FEM analysis of the sample; the Si bar is attached to the SOI substrate like a cantilever.*

The effects of the aforementioned factors on the base temperature are tested using FEM. Unlike sections 3.1 and 3.2, FEM model is modified to have all the SOI wafer properties. As shown in Figure 3.9, the SOI wafer consists of three layers: handle layer, buried oxide (BOX) layer, and device layer. Device and handle layers are made of silicon, while the BOX layer is made of silicon dioxide. The cantilever is fabricated from the device layer and suspended from the edge, as shown

in the figure. Fabrication is described in detail in chapter 5. The heat flux is applied at the tip of the cantilever, and the fixed-temperature boundary condition is applied either on the bottom surface of the BOX layer or the handle layer. Simulations are carried out for both cases, and minimal difference is observed in the cantilever's base temperature. Only the handle layer's fixed-boundary condition results are shown to minimize clutter in the figures.

Figure 3.10 shows the FEM simulation of heat flow in the Si cantilever beam ( $L/w$  of 5) with applied heat of 15 mW, to see best effect at base temperature, at its tip. The initial temperature of the beam and the substrate was 100 K. The color bar on the right side of the figure shows how much heat diffused into the surface.

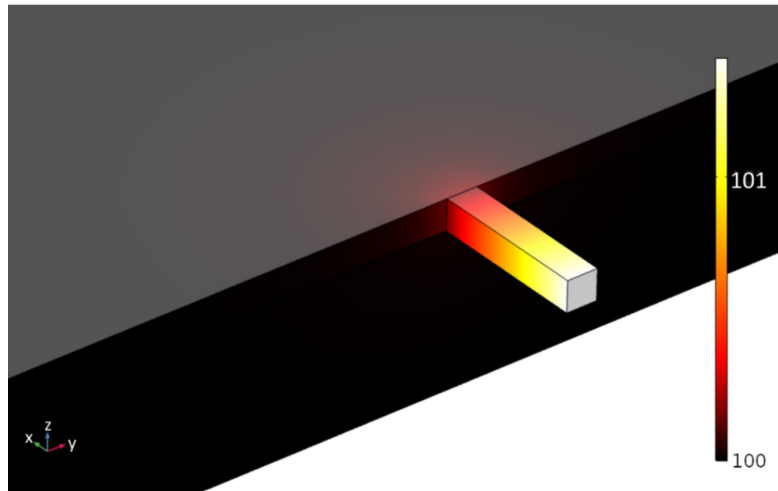


*Figure 3.10 Isothermal contours on the surface of the cantilever and substrate.*

Three  $L/w$  ratios (5, 50, and 100) are considered by maintaining widths and thickness at  $100\mu\text{m}$  to observe the effects of the  $L/w$  ratio on base temperature. Similarly, a pump laser applies a minimum power of 1 mW and a maximum power of 15 mW. Figure 3.11 shows that base temperature rose with increased applied power. Although the base temperature appears to be nearly

identical in all the  $L/w$  ratios, the short beam ( $L/w$  of 5) has a base-to-tip temperature ratio  $\left(\frac{\Delta T_{base}}{\Delta T_{base}} \%\right)$  as high as 13%, while the large beams ( $L/w$  of 50 and 100) has 1.5%–0.7% ratios. All analyses are done for 100 K initial temperature in order to obtain the maximum effect of thermal conductivity. The  $x$ -axis is made dimensionless by dividing  $x$ -coordinates by the cantilever lengths.

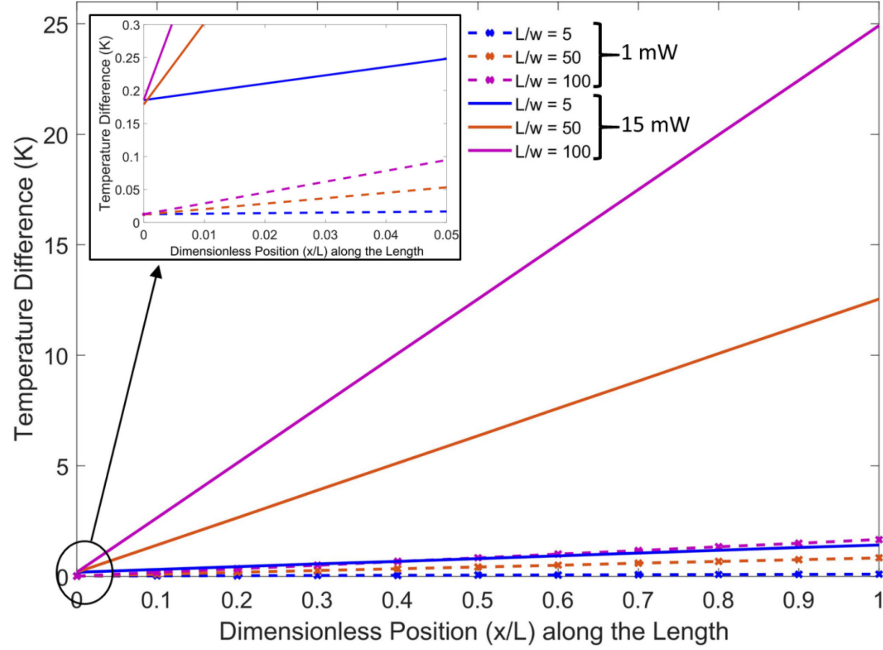


Figure 3.11 1 mW and 15 mW laser power applied to several Si cantilevers with  $L/w$  ratios of 5, 50 and 100. Inset shows the base temperature of the cantilevers.

Figure 3.12 depicts the effects of thermal conductivity on the base temperature. As shown in the figure, as thermal conductivity decreases, the base temperature increases exponentially, suggesting that the 1D model may not provide the best result in thermal conductivity characterization for the sample of low  $\kappa$ . Results also showed that  $L/w$  of 5 and 100 demonstrates the same trend in base temperature decrease with the increase of  $\kappa$ .

Although  $L/w$  ratios of 5 and 100 shows the same change in base temperature, Figure 3.13 shows that, in both cases, the base-to-tip temperature ratio increases when thermal conductivity



increased. However, at 10 W/mK, the ratio is approximately 10% for  $L/w$  of 5, while the ratio is only 0.5% for  $L/w$  of 100. Moreover, when thermal conductivity is maximized for Si (3000 W/mK[10], [40]), the ratio increases to 16% for  $L/w$  of 5 but remains under 1% for  $L/w$  of 100.

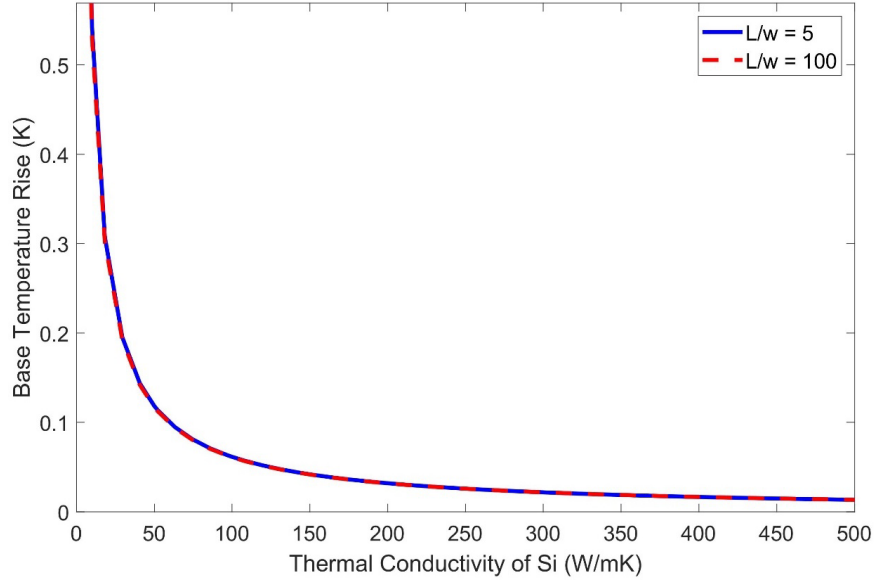


Figure 3.12 Base temperature rise of Si cantilevers at different thermal conductivity.

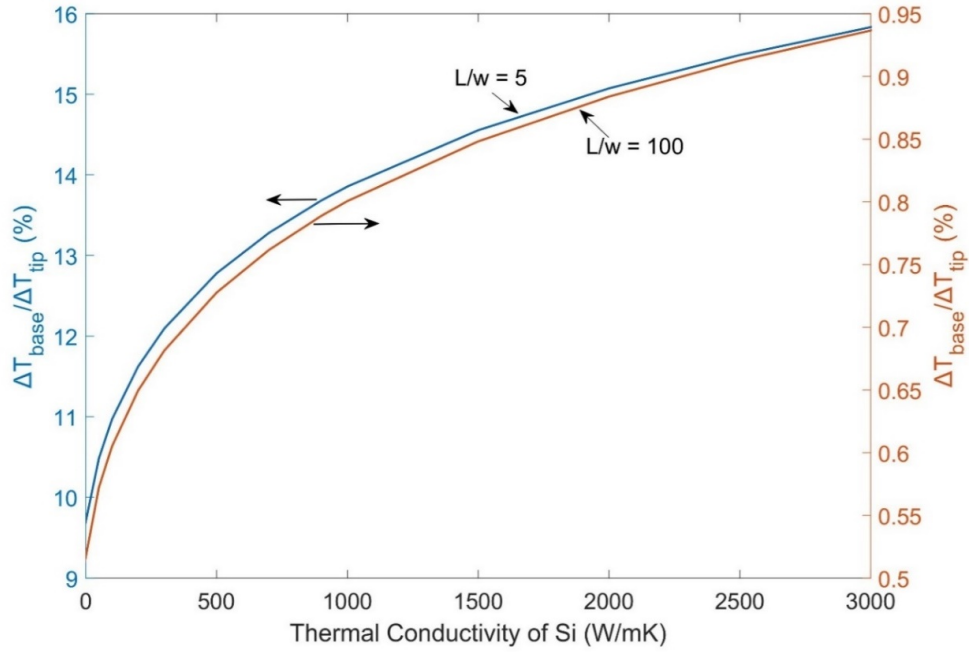


Figure 3.13 Base and tip temperature ratio of Si cantilever for  $L/w = 5$  (left y-axis) and  $L/w = 100$  (right y-axis) with respect to the change in thermal conductivity.

In summary, if the pump laser power stays within 1–5 mW, then for any L/w ratio of 20–100, the base temperature of the cantilever beam does not rise more than 0.9% compared to the rise in tip temperature. Because maximum temperature rise at any position of the cantilever beam does not exceed 10K, the base temperature rise is limited to 0–0.05 K, and the fixed-end boundary condition is justified for STR

### **3.4 Probe Heating and Its Application**

In the STR experiment, the probe laser is expected to reflect away from the sample without being absorbed. If the sample absorbs the probe laser power, the laser will supply additional heat to the sample, a process called probe heating. As shown in Chapter 4, the lasers are carefully selected to avoid this process to happen. Probe heating, which is not considered in the 1D thermal model, results in erroneous calculated thermal conductivity because the probe laser acts as a second heat source for the sample. In addition, temperature distribution along the sample length will not have an appropriate slope, which will create challenges for calculating thermal conductivity. However, STR is not limited to only evaluating a sample's thermal conductivity with specific thicknesses that have negligible laser wavelength absorbance. Although most TR techniques are wavelength dependent, in STR, CW laser diodes can be changed to the required wavelength via universal diode mounting.

This study introduces a technique to eliminate the impact of probe heating to increase versatility of the STR method and evaluate thermal properties of samples with considerable probe absorptivity, such as thermal characterization of thicknesses outside the probe wavelength spectrum described in section 4.3 or implementation of visible wavelength as a probe laser.

Probe heating was simulated using FEM to understand its effect on the cantilever beam. The same material properties, such as  $\kappa$ ,  $C$ ,  $\rho$  etc., are used from the last chapter. A heat source of

0.7 mW was applied at various positions along the length of the cantilever, where position 1 represented the tip and 0 represented the base, as shown in Figure 3.14. The probe laser beam radius was considered as  $22.5\text{ }\mu\text{m}$ .

As shown in the figure, the temperature of the cantilever from the probe heating point to the tip is constant, while the rest of the cantilever experiences a temperature gradient. The temperature at the probing point is the essential feature during the experiment because the temperature is measured at one point at a specific time. Therefore, the temperature of the probing point from each curve shown in Figure 3.14 are separated and plotted against the cantilever's length in Figure 3.16. As noted in the legend, this line is termed as probe heating.

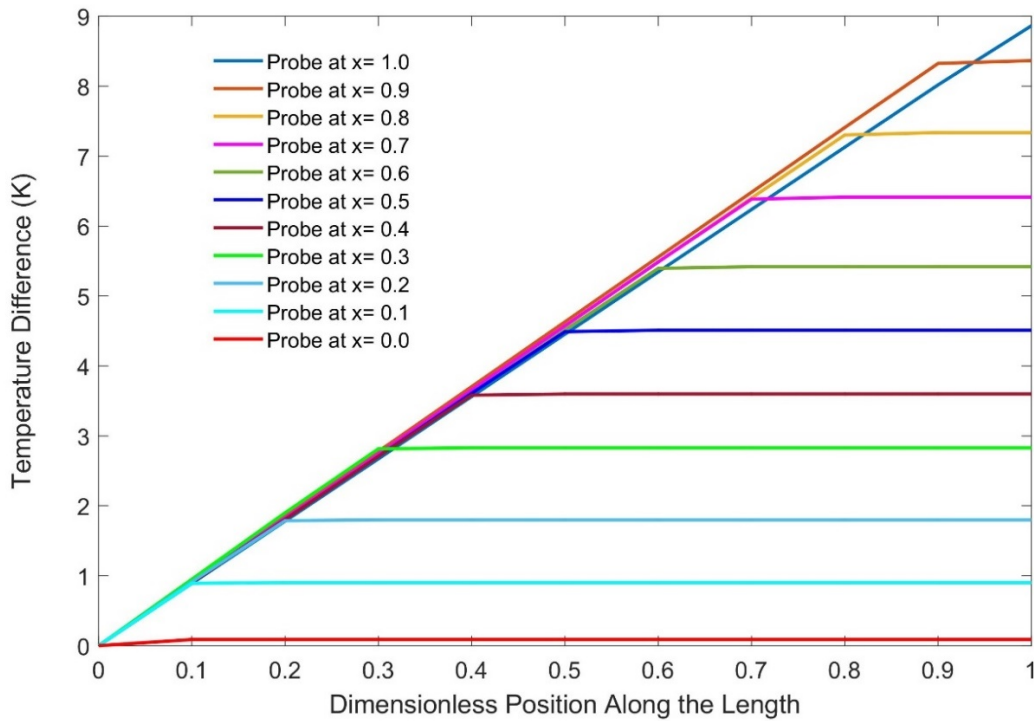


*Figure 3.14 Temperature rise along the cantilever beam with only probe heating. The probe heat source is moved to various positions along the length of the cantilever of 100 L/w ratio.*

FEM was also used to observe the effect of simultaneous pump and probe heating when a 0.7 mW heat source was added to the front side of the cantilever and another heat source of the same power was added to the back side of the cantilever. The backside (probe) heat source was moved along the cantilever's length, while the frontside (pump) heat source was fixed at the tip. The results are presented in Figure 3.15. Instead of one temperature gradient along the cantilever, as shown in Figure 3.2, several slopes are evident, indicating the effect of probe heating. As mentioned, however, only the points from which probe laser beam was reflected were of interest during the experiment, and those temperatures are plotted in Figure 3.16. The pump-probe heating line represents those points in the figure.

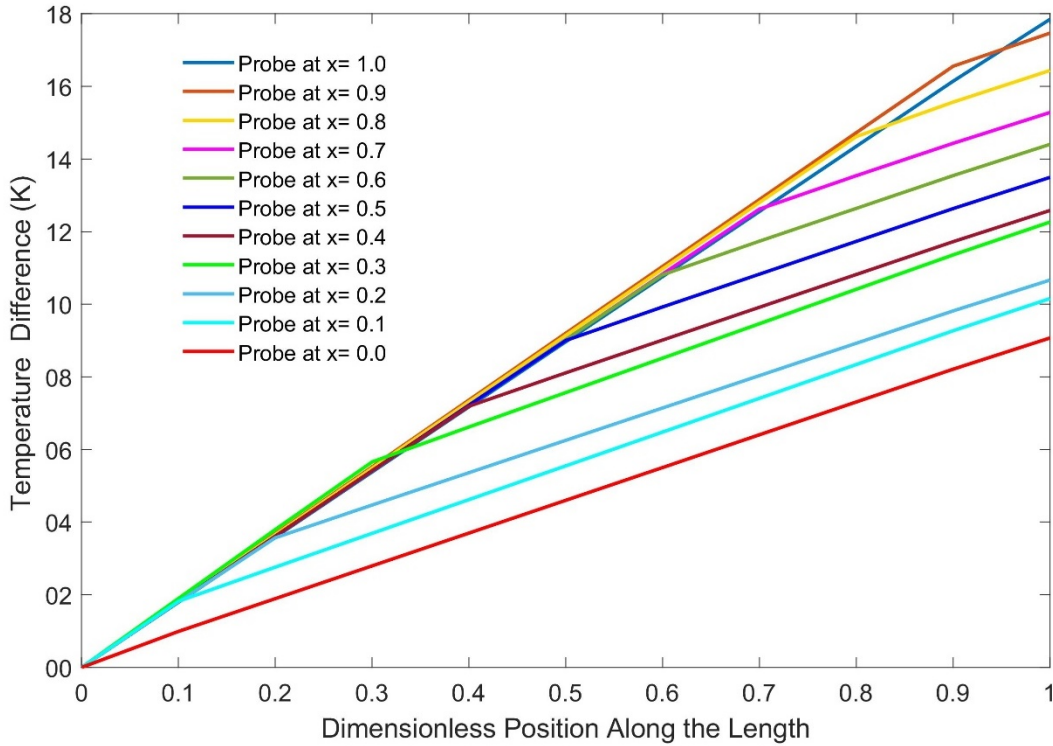


*Figure 3.15 Temperature rise along the cantilever of 100 L/w ratio. Both pump and probe lasers are heating the cantilever while pump is fixed at the tip, but probe moves along the points shown in the legend where  $x$  represents the dimensionless length of the cantilever.*

The temperature at the points of interest for probe heating and pump-probe heating from the above two figures are summarized in Figure 3.16. The effect of only pump heating along the cantilever, obtained using FEM, is also presented in the figure where the pump power is same as the probe power. The equations for fitted curve through those points are also presented. The equations show that subtracting the probe-heating equation from the combined-heating equation resulted in the pump-heating equation. Experimentally, these results mean that the temperature curve along the cantilever must be initially generated using only the probe laser (i.e., with pump laser off) in case of high absorbance of probe power. The same curve must be generated when both lasers are active. Then the equation of the former curve must be subtracted from the both laser equation to obtain the true temperature rise equation due to pump heating.

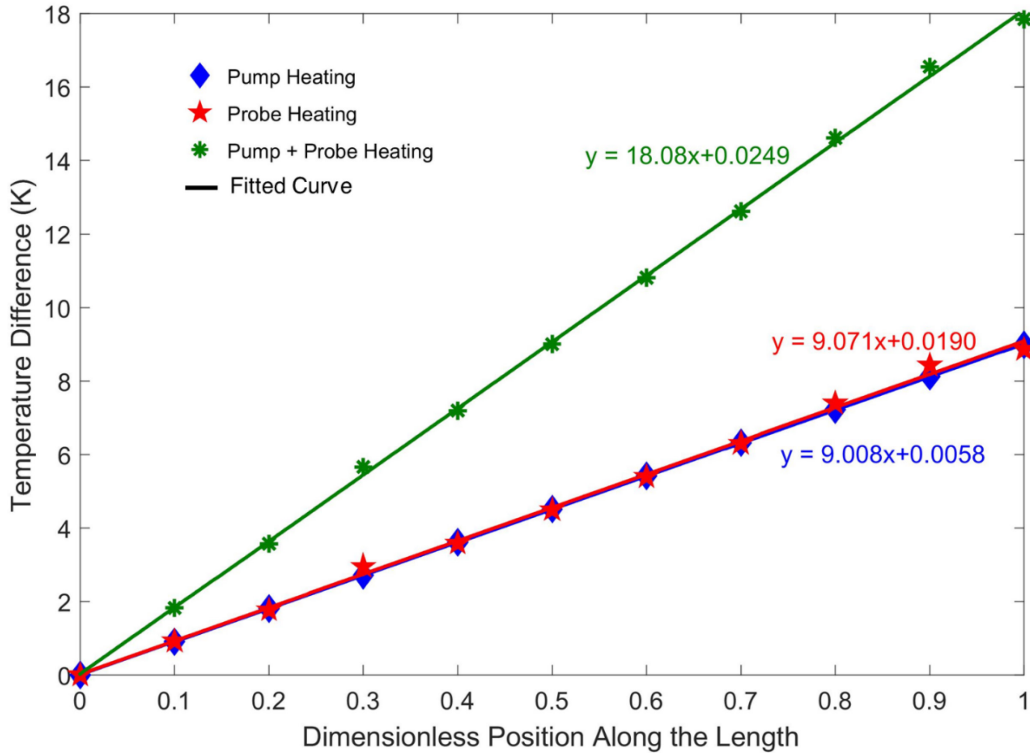


Figure 3.16 Temperature rise by pump, probe and pump & probe heating along the cantilever. Temperature of probing points are shown where probe heating is applicable and temperatures at every 0.1 dimensionless length are shown for only pump heating.

This research also seeks to determine how much probe laser power should be used in the case of high absorbance. Figure 3.17 shows the temperature rise along the cantilever for various probe laser powers. For ease of comparison, the probe powers are presented with respect to pump laser power, and dots represent probing point temperatures. The linearly fitted curves are made using the following equation:

$$T = ax + b \quad (151)$$

where  $a$  and  $b$  are constants,  $T$  is the temperature difference, and  $x$  is the dimensionless position along the length. The value of these constants and the coefficient of determination ( $R^2$ ) for all the lines are presented in Table 3.1. The  $R^2$  values in the table shows that the data deviates from the fitted regression line as the probe laser power decreases. Hence, the thermal conductivity calculated from the slope of the line will be erroneous and described method to eliminate the probe-heating effect cannot be followed. Therefore, probe power levels equal to or more than half the pump power are suggested for use in the measurement where samples tend to absorb probe laser power. Results also reveals that probe power should not exceed pump power since the elevated energy will trigger a large temperature increase and alter the sample's temperature-dependent material characteristics along the length of the cantilever.

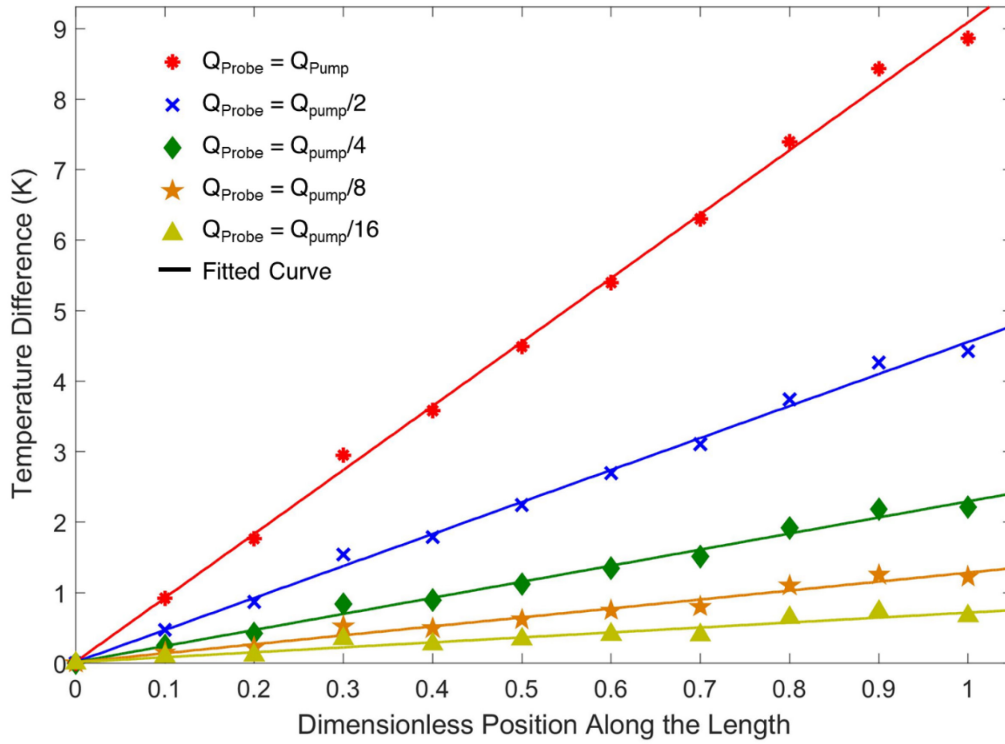


Figure 3.17 Effect of probe power on the temperature measurement along the cantilever.

Table 3.1 Constants of fitted curves in Figure 3.17 and their determination coefficient value.

Probe power	a	b	R <sup>2</sup>
$Q_{\text{Probe}} = Q_{\text{Pump}}$	9.071	0.0190	0.9979
$Q_{\text{Probe}} = Q_{\text{Pump}}/2$	4.539	0.0159	0.9958
$Q_{\text{Probe}} = Q_{\text{Pump}}/4$	2.280	0.0144	0.9893
$Q_{\text{Probe}} = Q_{\text{Pump}}/8$	1.240	0.0014	0.9727
$Q_{\text{Probe}} = Q_{\text{Pump}}/16$	0.703	0.0133	0.9243

## Chapter 4 - Experimental Setup

Some of the previous works on the pump-probe based thermal transport measurements in thin films and across interface were reviewed briefly in Chapter 1. Most of these methods are either transient or time or frequency dependent. This dissertation research takes a different approach of using continuous wave (CW) lasers to characterize thermal properties of suspended films. This technique provides a less complicated measurement process.

It was hard to achieve reliable and consistent results at the early stages of building and testing the Suspended Thermoreflectance technique. This, in retrospect, was not due to a single experimental or analysis mistake, but the product of many small factors each leading to the final result with uncertainty and error. These include effects due to improper laser diode selection, natural frequency of the suspended films, various sources of electronic and optical noise, variation in sample quality and preparation, and false assumptions in the data interpretation.

In this chapter, the design and implementation of our pump-probe system is described. All the details necessary to obtain an accurate measurement are included. The chapter begins with an overview of the optical system and its major components, moves on to some small but essential details of the instrumentation, and then finally discusses the various sources of noise that can affect the measurement.

### 4.1 Optics

A schematic containing the essential features of our pump-probe system is shown in Figure 4.1. As mentioned before, two different laser diodes are used as pump and probe lasers. Selection of these laser diodes is detailed in section 4.3 Laser Selection.





input for the photodiode are bipolar, thus any combination of the polarities can be set in the controller based on the diode requirements. The laser diode current, or its proportional output voltage, can be controlled using the controller. The laser mount is also connected to a Thorlabs TED200C thermoelectric temperature controller for precise temperature control of the diodes. Together with the laser diode controller, this provides a stable laser signal.

To simplify the laser alignment process, two mirrors, mounted on the kinetic mounts, are used in the 'Number-4' configuration, also known as perpendicular configuration. The mirrors are mounted at  $67.5^\circ$  angles which creates a '4' shape with the laser beam (Figure 4.1). This setup allows mirror 2 to be placed away from the source laser beam path. The laser beam is aligned at two reference points, with the first reference point being at mirror 2, and the second at the target. The first kinematic mount should be used to move the laser spot to the desired XY position on the surface of the second mirror. The second kinematic mount should then be used to compensate for the angular displacement and fine tune the alignment on the target.[129]

The pump laser is a well collimated laser with the beam diameter around 1mm. The bigger the beam diameter, the smaller will be the final spot size on the sample. Thus, a beam expander is used to increase the pump beam diameter. The beam expander consists of two plano-convex lenses of 12 mm and 100 mm focal length, respectively. The lenses provide an expansion of around 8 times of the original size. On the other hand, the probe laser beam has the divergence of  $13^\circ$  and  $30^\circ$  in lateral and longitudinal direction, respectively. This divergence makes it difficult to focus on the object and hence an aspheric lens of 8 mm focal length is used as the collimator. Though the collimating lens is placed in between the mirror and the beam splitter in Figure 4.1, it actually sits on the laser diode mount because of its smaller focal length. The adjustment is made on the figure for better visual representation.

The beam splitter divides the laser beams into 50/50 portion. Half of the beam goes toward the sample which is inside the cryostat, while the other half is transmitted through the splitter and captured by photodetector 2 and 3 in pump and probe side, respectively. The beams pass through a 10x objective lens and an achromatic doublet before arriving at PD2 and PD3, respectively. The objective lens helps focusing down the beam into a smaller photodetector area. The portion of the beams which go toward the sample, also pass through two achromatic doublets of 75 mm focal length. It is important to use achromatic doublets instead of objective lenses due to their high focal lengths, since the sample will be inside the cryostat expander and will be at least 66 mm away from the cryostat window on either side. The reflected beams from the sample passes through the beam splitter and get divided as before. The portion which is transmitted through the splitter reaches photodetector 1 and 4 in pump and probe side, respectively. Again, they pass through 10x objective lens and achromatic doublet in pump and probe side before arriving at the photodetector.

Two types of photodetectors are used in the experiment. Pump side photodetectors are Thorlabs DET10A and probe side detectors are Thorlabs DET100A. Both kinds have the same Si detector and working principle. The only difference is that DET10A photodetectors have smaller area ( $1 \text{ mm}^2$ ) than DET100A photodetectors ( $10 \text{ mm}^2$ ). PD2 works as a reference for pump laser power and helps determining how much power is sent to the sample, while PD1 registers the reflected power from the sample. On the other hand, PD3 captures the probe reference signal and helps normalize the probe reflected signal measured by PD4.

The actual experimental setup is presented in Figure 4.2. The pump and probe laser mount are labeled as pump and probe lasers, respectively, in the figure. Pump side optics, probe side optics and the sample can move in x, y and z directions independently.

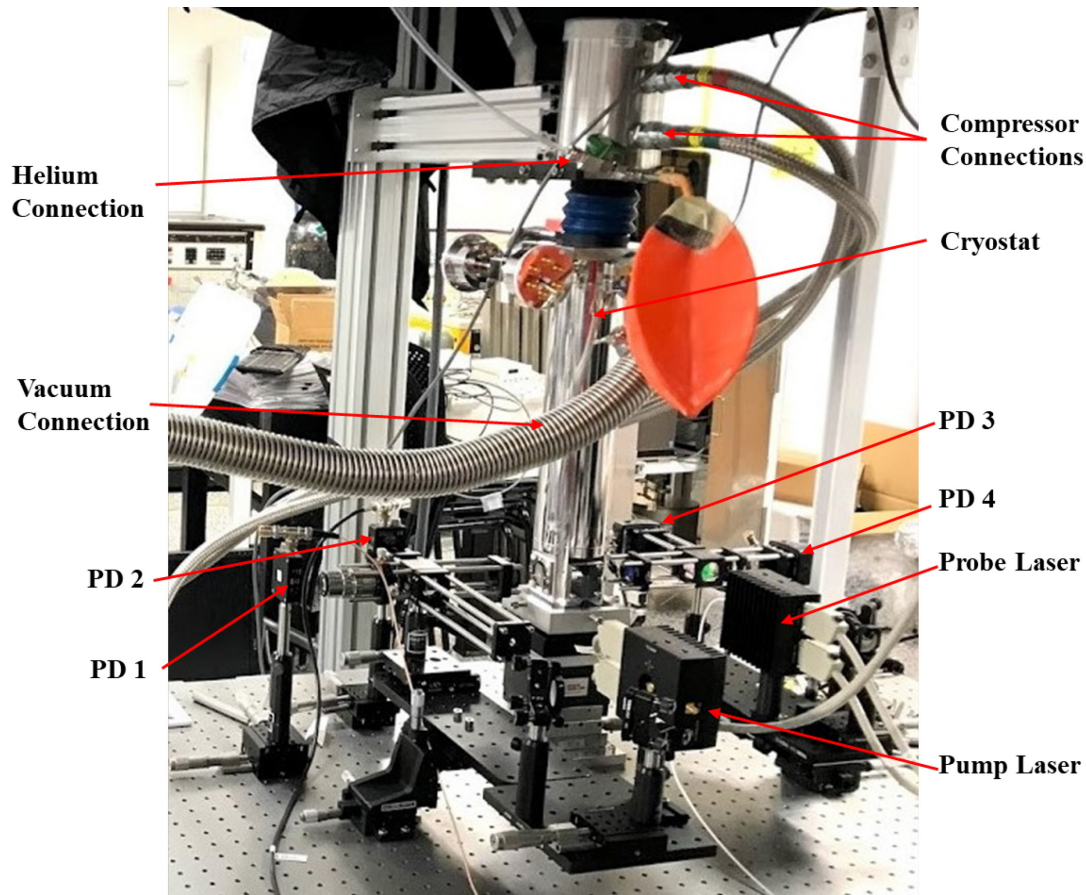


*Figure 4.2 Optical components of the experimental setup. The cryostat sits on a plate which can be adjusted on  $x$ ,  $y$ ,  $z$  and  $\theta$  direction independently from rest of the setup. The full pump and probe side sit on separate  $x$ ,  $y$  and  $z$  plate.*

## 4.2 Electronics

A good optical setup is necessary but not sufficient to obtain a good measurement; the right electronics and an understanding of their limits are also required. The core electronic components have already been mentioned: the PIN photodiode, the nano-voltmeter, and the lock-in amplifier. However, there are some additional components that play important nodes as well.

One of the key challenges in thermoreflectance measurement is that reflection change with temperature is small – on the order of  $10^{-4}$  and below. The large DC background component of reflection obscures the change in signal due to temperature. The standard technique to overcome

this issue is to use a lock-in amplifier, which employs phase-sensitive detection to extract the signal at a specified reference frequency from the background.[73] A good summary of the principle of lock-in detection is provided in the user manual of Stanford Research Systems model SR830 lock-in amplifier [130]. In this section lock-in detection is briefly discussed for understanding of the signal processing.

The SR830 multiplies the signal by a pure sine wave at the reference frequency. All components of the input signal are multiplied by the reference simultaneously. Mathematically speaking, sine waves of differing frequencies are orthogonal, i.e. the average of the product of two sine waves is zero unless the frequencies are exactly the same. In the SR830, the product of this multiplication yields a DC output signal proportional to the component of the signal whose frequency is exactly locked to the reference frequency. The low pass filter which follows the multiplier provides the average which removes the products of the reference with components at all other frequencies.[130]

The reference frequency needs to be very clean and hence this signal directly comes from the function generator to the lock-in amplifiers. The same signal goes to the RF input of the laser mount. The laser can be modulated up to 500 MHz using this RF input. This is a 50  $\Omega$  input that is AC-coupled directly to the laser through a bias-Tee network. The modulation amplitude does not matter for the lock-in amplifier since it works in the frequency domain, but too high of an amplitude may damage the laser. The desired RF power to modulate the laser is determined using the amount of modulating current from the laser manufacturer's data sheets and Eqn. (152).[131]

$$V_{RF} = (50 \Omega) I_{LD} \quad (152)$$

Where  $V_{RF}$  is the modulating voltage and  $I_{LD}$  is the laser diode modulating current.

The ability to modulate the laser diode directly has the advantage of excluding the electro-optic modulator (EOM) from the system. As a result, the signal does not contain any odd harmonics contributions of the reference frequency when mixed in the lock-in amplifier. This eliminates the use of inductor or resonant filters in between the photodetector and lock-in amplifier.

The full power in the incident wave is absorbed by the load when the impedances of the signal source, the transmission medium, and the load or termination system are equal. When there is impedance mismatch, i.e., the impedance of the load and/or the transmission medium isn't the same, some or all of the power in the incident wave is reflected back toward the photodetector. The magnitude of the reflection depends upon the severity of the impedance mismatch. The reflected signal will interfere with the incoming signal and give rise to noise like components. A 50  $\Omega$  BNC terminator is used near the photodetector to overcome this type of mismatch. [132] The terminator is connected to a BNC-'T' junction and other two sides of this junction are connected to the signal cable and the photodetector. The terminators absorb the electrical energy of the signal or current as it reaches the end of the cable, thus avoiding reflection of the signal and preventing noise. This ensures smooth flow of current from photodetector to the lock-in amplifier or nano-voltmeter. The photodetector and its connections are shown in Figure 4.3a and the signal from the photodetector is depicted in Figure 4.3b. The output signal from both the lock-in amplifier and the nano-voltmeter is in voltage. The lock-in signal doesn't need to be converted into power since lock-ins are only used on the probe side. Furthermore, only the change of reflectivity is of interest which is a normalized function. But, voltage measured by the nano-voltmeter needs to be converted to power to determine the absorbed power by the sample. The conversion can be done using Eqn. (153) and Eqn. (154). [133]

$$P = \frac{I_{PD}}{R(\lambda)} \quad (153)$$

$$I_{PD} = \frac{V_{PD}}{R_L} \quad (154)$$

Where P is the power,  $R(\lambda)$  is the responsivity of the diode, and  $I_{PD}$  and  $V_{PD}$  are the current and voltage of the detector, respectively. The responsivity depends on the wavelength of incident light and can be found from the detector manual[133].

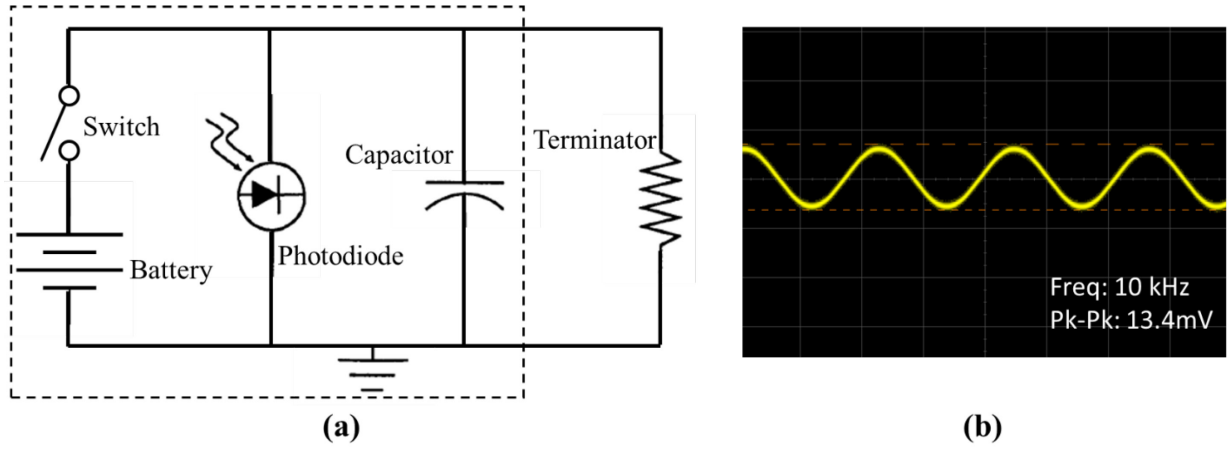
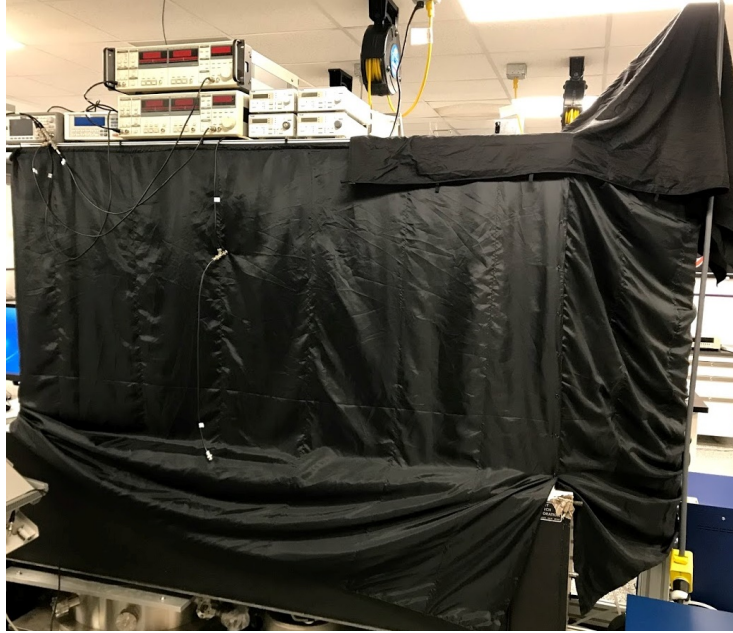


Figure 4.3 a) Simplified circuit of the photodetector and its connection. The dashed line contains circuit within the detector. b) A clean output signal from photodetector. The signal is measured with oscilloscope for visual representation.

The room temperature and dark current do not influence the photodetector on probe side because of the use of the lock-in amplifier and normalization of the signal. The room temperature does not affect the pump photodetectors as well, since it is constant during the whole experiment. But it is important to consider the effect of dark current and ambient light when the absorbed power is calculated using the pump side photodetectors. As shown in Figure 4.4, the full experimental setup is covered with anti-static polyester black fabric. Windows and doors are also covered with black curtain and lights are kept off during the experiment. However, it is still impossible to get rid of ambient light completely. Hence, the effect of ambient light and dark current will be termed

as dark voltage in this dissertation and is found by measuring the voltage from the photodetector in the dark room with no laser on. The average dark voltage is measured to be 150 nV, which is subtracted from the final measurement to determine absolute absorbed power by the sample.



*Figure 4.4 Anti-static polyester black fabric covers the full experimental setup. It restricts ambient light entering measurement area and keeps the setup dust free.*

### 4.3 Laser Selection

The primary thermorefectance criterion for laser selection is that the sample will absorb most of the pump laser power while reflecting the majority of the probe laser power. Reflected pump power is not utilized in the experiment and hence it is minimized. On the other hand, probe laser power will increase the local heat of the probing area if it is absorbed by the sample, that is it will introduce a second heat source to the sample. This probe effect will change the slope of the  $\Delta T$  vs  $x$  curve and will ultimately produce an error in thermal conductivity measurement.

Light has to pass through two Si-air/vacuum interfaces when interacting with a suspended silicon film on air/vacuum. The presence of two (or more) interfaces means that several light beams



will be produced by successive reflections and the properties of the film will be determined by the summation of these beams. A film is termed thin when full interference effects can be detected in the reflected or transmitted light. This case is described as coherent. When no interference effects can be detected, the film is described as thick and the case is described as incoherent. The coherent and incoherent cases depend on the presence or absence of a constant phase relationship between the various beams, and this will depend on the nature of the light and the receiver, and on the quality of the film. Due to the interference effects in thin films, absorption and reflection from any surface greatly depends on the thickness of the sample and wavelength of the lasers. The detailed explanation about this interference effect is provided in the literature[134]–[136]. Here only essential elements are repeated which are necessary to understand the results in this section.

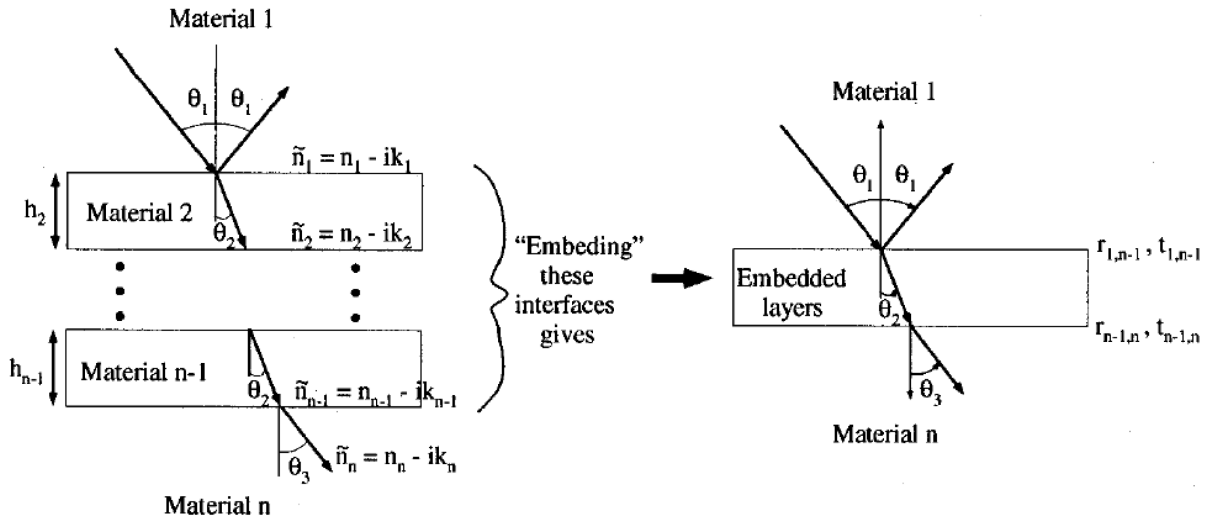


Figure 4.5 Light interaction with the layers of materials. Secondary reflection and transmission within the layers are omitted for simplicity.[134]

Figure 4.5 represents a simple thin layer system with incident, transmitted and reflected light. By assuming normal incidence of light onto the surface, equal permeabilities for all materials and smooth planar layers, equations for transmissivity, reflectivity and absorptivity of any thin film are obtained bellow.

$$\text{Transmissivity:} \quad T_r = \left| \frac{t_{1,n-1} t_{n-1,n} e^{i\beta}}{1 + r_{1,n-1} r_{n-1,n} e^{-i2\beta}} \right|^2 \left( \frac{n_n}{n_1} \right) \quad (155)$$

$$\text{Reflectivity:} \quad R = \left| \frac{r_{1,n-1} + r_{n-1,n} e^{i\beta}}{1 + r_{1,n-1} r_{n-1,n} e^{-i2\beta}} \right|^2 \quad (156)$$

$$\text{Absorptivity:} \quad A_p = 1 - T_r - R \quad (157)$$

$$\beta = \frac{2\pi \tilde{n} h}{\lambda} \quad (158)$$

$$\tilde{t}_{ij} = \frac{2\tilde{n}_i}{\tilde{n}_j + \tilde{n}_i}, \quad \tilde{r}_{ij} = \frac{\tilde{n}_j - \tilde{n}_i}{\tilde{n}_j + \tilde{n}_i} \quad (159)$$

$$\tilde{n} = n - ik \quad (160)$$

where  $h$  is the thickness of the sample,  $\lambda$  is the wavelength,  $\tilde{t}_{ij}$  and  $\tilde{r}_{ij}$  are the complex transmission coefficient and reflective coefficient, respectively, for an electromagnetic wave encountering the interface between material  $i$  and material  $j$ . To model the optical properties of Si cantilever it is assumed that there is air on either side of the film and that the thickness of the membrane is the free parameter. A MATLAB algorithm was then used to determine  $R$ ,  $T$ ,  $A$  of the Si film. The algorithm is in the appendix B, and the result is demonstrated in Figure 4.6. Refractive index values for this algorithm were obtained from literature.[137]–[139]

Figure 4.6 shows the reflectivity, absorptivity and transmittivity of a 2  $\mu\text{m}$  silicon film which is exposed to vacuum on both front and back sides. The laser incident is perpendicular to the surface of the film. This particular film thickness was considered since the primary intension of this experiment is to characterize the thermal properties of the films on the order of microns in thickness. Pump and probe lasers were selected at this step, and their applicability at different thicknesses were observed later. It can be observed from Figure 4.6 that the sample absorbs a major portion of light at the wavelength of 450 nm – 550 nm but cannot absorb more than 3% for

wavelength above 950 nm. Hence a good pump laser wavelength is in between 450 nm and 550 nm. Whereas, initially it seems like any wavelength larger than 950 nm will be good for probe laser due to low absorptivity, but reflectivity is seen to vary a lot in this range of wavelength. The proper wavelengths of probe laser are 970 nm – 1005 nm and 1035 nm – 1075 nm etc. These ranges of both pump and probe lasers were checked against the inventories of the common optics suppliers such as Thorlabs, Edmund Optics and Newport. The best pump laser wavelength was found to be 532 nm and best probe laser was found to be 980 nm taking divergence, laser stability and cost into consideration. The part number for pump laser diode is DJ532-10, and the probe laser diode part number is L980p010. Both diodes were purchased from Thorlabs.[140]

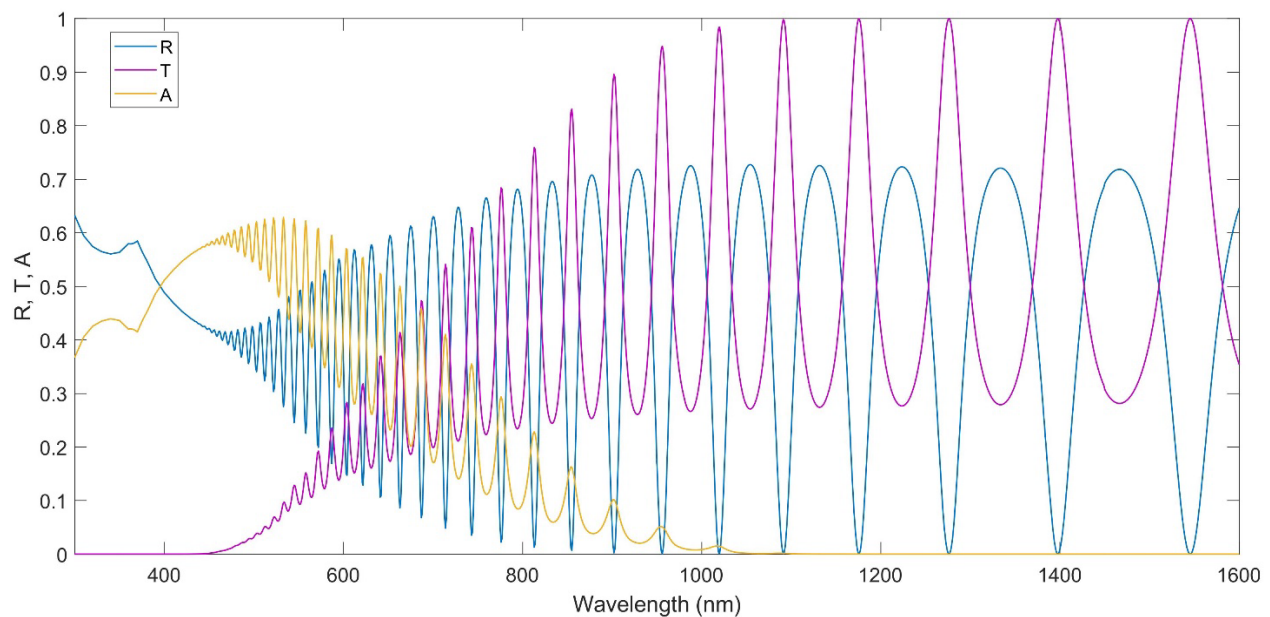


*Figure 4.6 Reflectivity, absorptivity and transmittivity of a 2  $\mu\text{m}$  silicon film at different laser wavelength.*

Both of the laser diodes are single mode. Being equipped with a single mode diode not only has the advantage of providing flexibility in transferring the light produced by the diode to the optics and aligning it properly, it also removes extra modes present in the light coming off the

diode. This eliminates interference from different modes of light.[141] Though a good amount of pump power is transmitted through the sample, it is captured by the probe side photodetectors due to the use of lock-in-amplifier which does not capture dc pump signal. Beside the desired outcome of this experiment is the net change in the reflectivity subjected to temperature change, which is not affected by the transmitted power. Similarly, reflected pump power will not affect the measurement, rather will help determining the absorbed pump power experimentally.

It is important to find out what other sample thicknesses can be tested using the lasers to characterize their thermal properties. This step proves the versatile applicability of the experiment. Another MATLAB algorithm was developed to vary the reflectivity, transmittivity and absorptivity with the sample thickness. The result is shown in the Figure 4.7 and the algorithm is provided in the appendix C. The sample should have higher absorptivity and lower reflectivity of the pump laser power, but lower absorptivity and higher reflectivity of the probe laser power. Thicknesses corresponding to all the peaks of R 980 nm line in Figure 4.7(a) have these properties and hence can be characterized using STR.

The shaded region from Figure 4.7(a) is illustrated in Figure 4.7(b) to demonstrate how to select a reasonable sample thickness. The ideal thicknesses are 2940 nm – 3010 nm as shown in the highlighted area of Figure 4.7(b). These thicknesses have less than 3% absorptivity and more than 70% reflectivity at probe laser wavelength, while pump laser absorption is also good (>60%). A thickness range is selected because a particular thickness is almost impossible to obtain in microfabrication. The device layer thickness always varies in a certain range owing to the curvature effect, thicker in the center but thinner near the edge, of the wafer surface.[134]

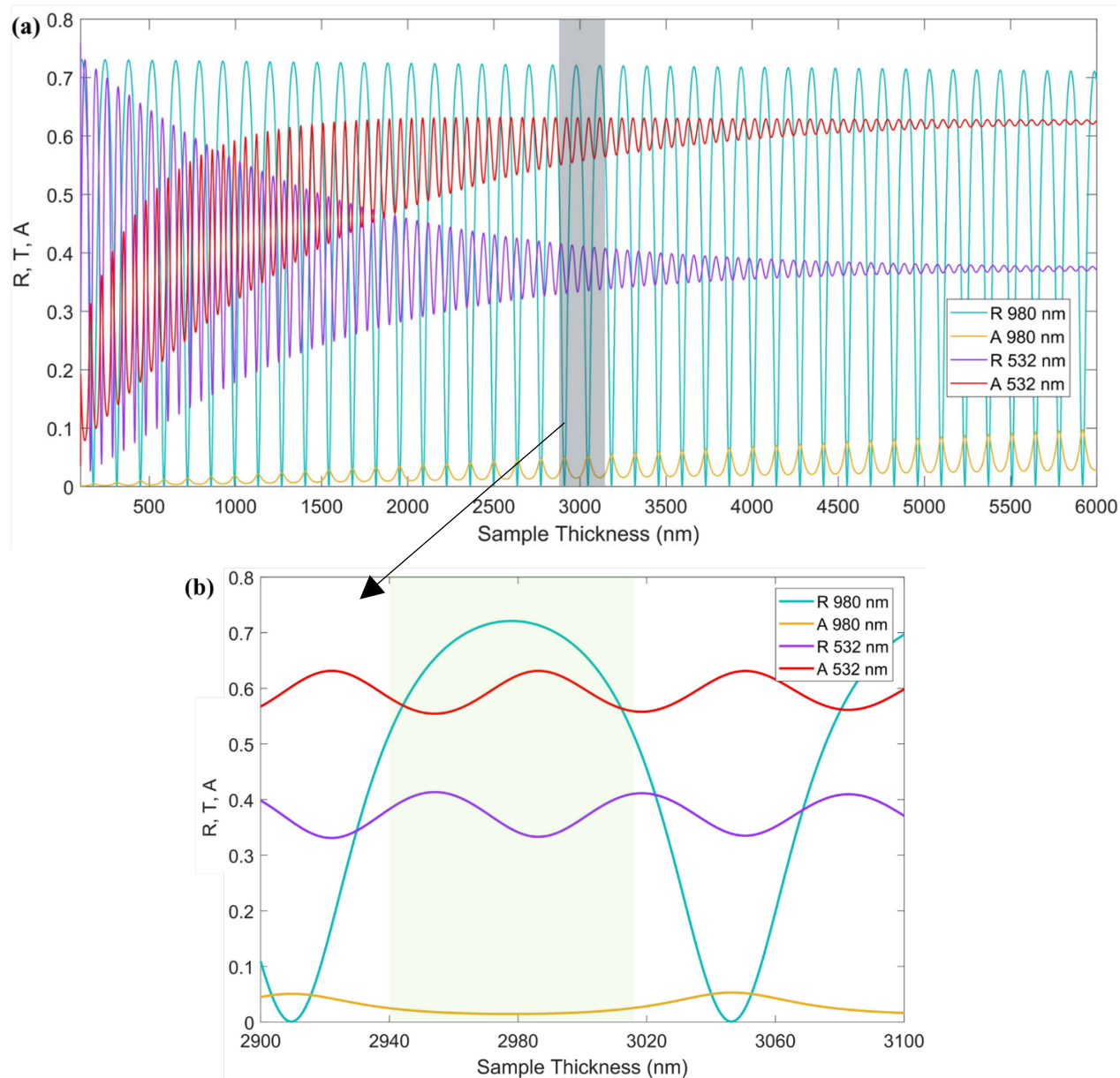


Figure 4.7 (a) Reflectivity and Absorptivity of pump and probe lasers at different thicknesses of the silicon films, (b) The shadowed area from 'figure a' is zoomed to show the proper sample thickness for the experiment.

#### 4.4 Sample Holder

A sample holder is a major part of the experimental setup. It plays the important role of conducting heat from the sample to the cryostat expander and helps the sample to cool down. The sample holder is mounted on the second stage heat station in the cryostat expander, as shown in

Figure 4.8. It is fitted in between the heat station and radiation shield, keeping a few centimeters distance from the latter to avoid radiation heat gain from the outside.

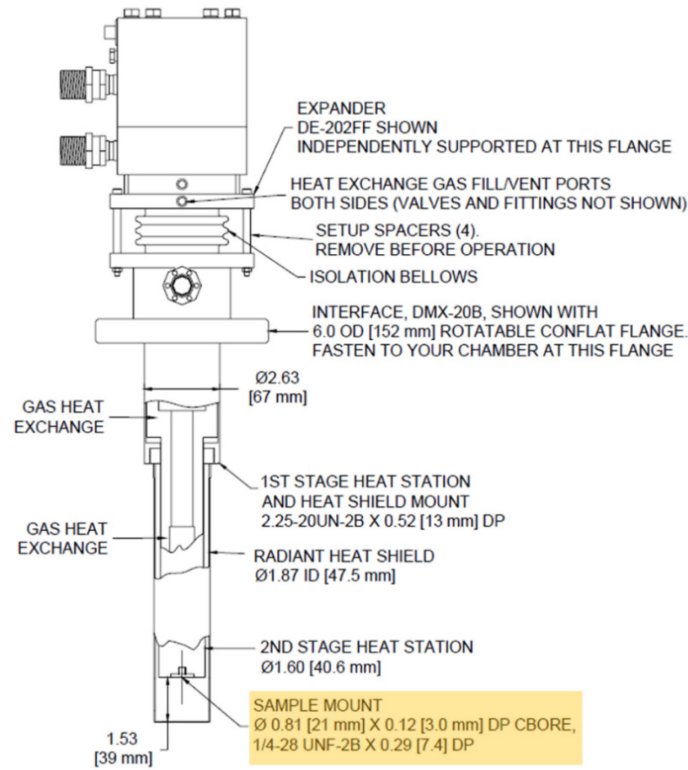


Figure 4.8 Schematic diagram of the optical cryostat head (model: ARS DMX-20)[142]. The sample holder position is depicted in highlighted area.

Design of a sample holder demands special consideration since it houses the ultra-thin fragile films during the experiment. The following aspects were considered during the design of the sample holder:

- (i) The sample holder must be made of high thermally conductive material to transfer the heat from the sample quickly to the expander.
- (ii) It must be made or coated with shiny metal to avoid absorption of radiated heat that comes through the window.

- (iii) The sample substrate should be in proper contact with the holder to aid the heat conduction.
- (iv) It should also be in good contact with the second stage heat station of the cryostat.
- (v) The sample holder should provide sufficient space to mount a temperature sensor on it which will provide real time substrate temperature.

Figure 4.9 presents the sample holders. Two types of holders were made. The first one has a plain top plate and this plate is pressed against the sample substrate which sits in the base plate grooves (Figure 4.9a). The second kind of holder has pogo-pin holes in the top plate and one side of the pogo-pins is pressed against the sample. The sample sits in the base plate grooves as before, but the top plate never comes in contact with the sample (Figure 4.9b). The first type of sample holder is mainly used for the experiments mentioned in this dissertation. The second kind will be useful where both optical and contact resistance measurements are necessary. Both sample holders are made of pure copper because of its high thermal conductivity ( $19600 \text{ W/mK} - 398 \text{ W/mK}$ )[143], [144] at cryogenic and room temperature. The holders are 3.5 cm long and 2.2 cm width. Thickness of the base plate is 0.38 cm and top plate is 0.25 cm. The base plate has 5-40 UNC thread to mount it on the cryostat. The sample holders are plated with nickel and chrome to reflect the radiation coming through the cryostat window. The holders before and after the chrome plating are shown in Figure 4.9e and Figure 4.9f, respectively. The sample is mounted to the holder following these steps.

- (i) The base plate is placed on the sample installer as shown in Figure 4.9d and Figure 4.9f.
- (ii) The substrate, from which the cantilevers are hanging, is put on the groove of the base plate. This substrate has the same dimensions as the groove to allow a better fit.
- (iii) The temperature sensor is placed at the predetermined spot in the base plate.

- (iv) The top plate is put on top of the sample and sensor.
- (v) Top and base plates are clamped together using screws.
- (vi) Finally, the sample holder is attached to the cryostat expander using the thread.

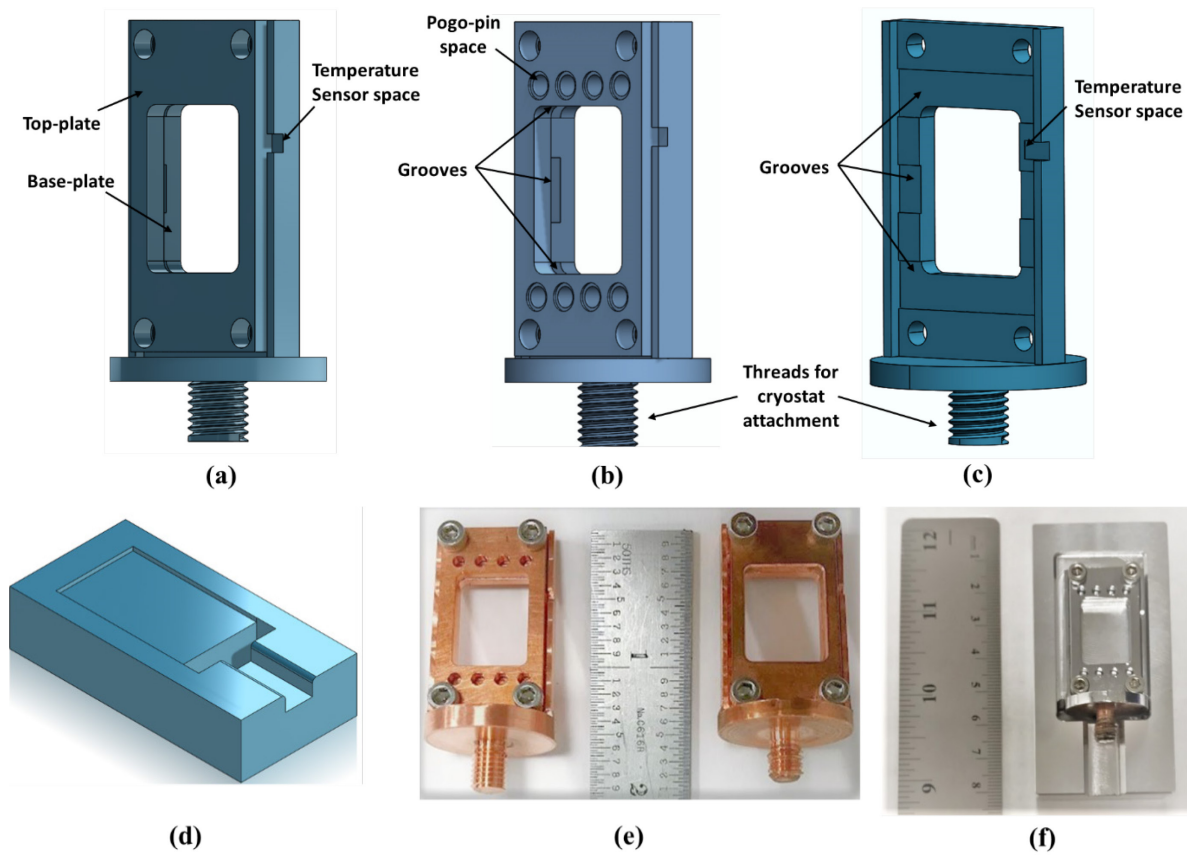


Figure 4.9 Solidworks drawing of a) Plain sample holder with base plate and top plate together, b) Pogo-pin sample holder with base and top plate, c) Only base plate of the sample holder, d) sample installer, Actual e) Plain and pogo-pin sample holder before chrome plating, e) pogo-pin sample holder sitting on the sample installer after chrome plating.

## 4.5 High Vacuum System

High vacuum is needed to run a cryostat properly. The presence of air molecule between the heat station and vacuum shroud works as a medium for convective transfer heat from outside to the sample. The amount of air is reduced by evacuating the system. In addition, the vacuum helps to keep the cryo-chamber dry and contamination free.



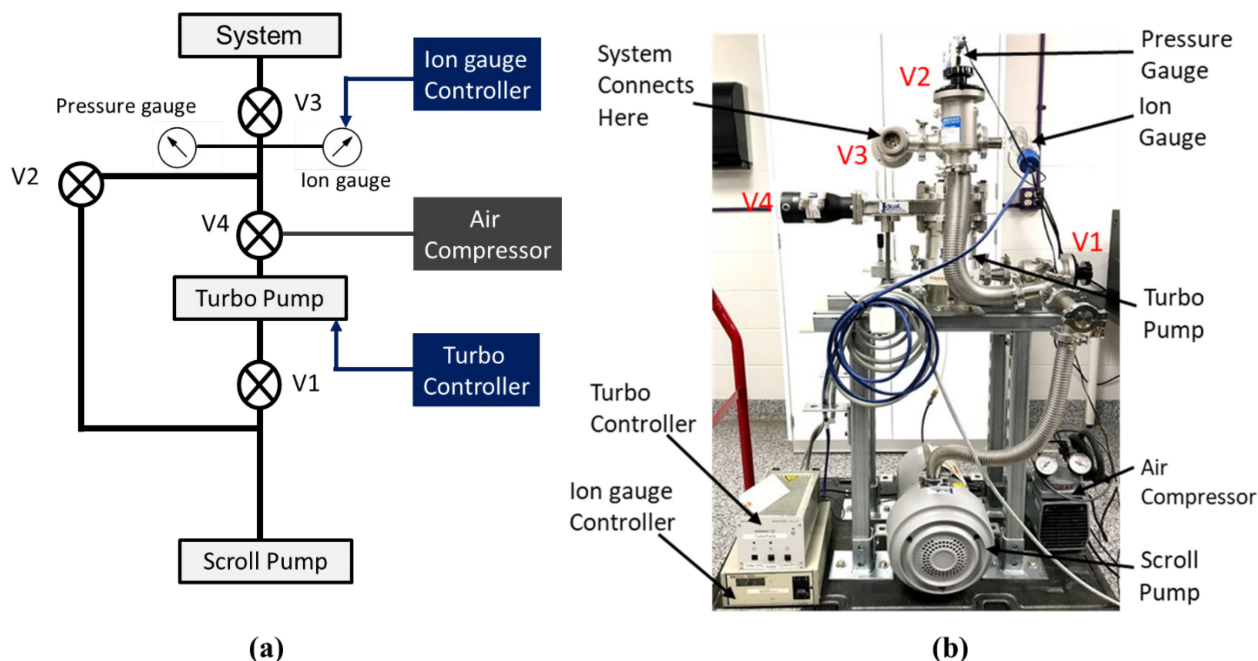
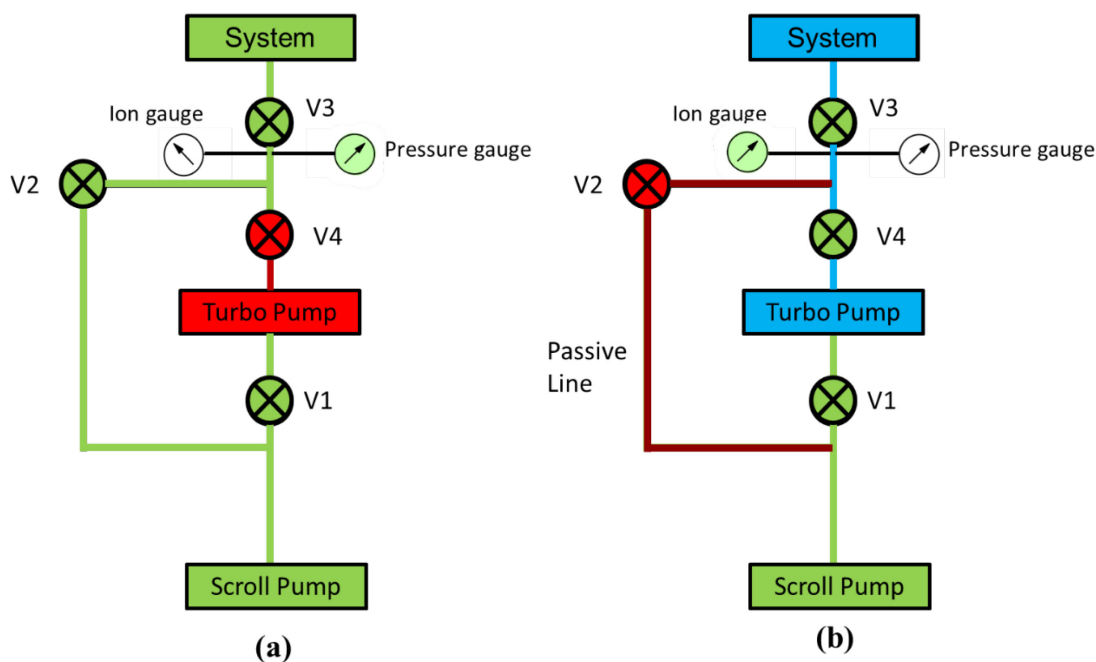


Figure 4.10 a) Schematic of the high vacuum system used to reduce the cryostat pressure, b) Actual vacuum system.

The high vacuum system consists of a scroll pump, a turbo pump, an ion gauge, a pressure gauge and 4 different valves, as shown in Figure 4.10. The cryostat expander is indicated as the system in the figure. The turbo pump can take the system to  $10^{-5}$  Torr. But it cannot start pumping from the atmospheric pressure because high pressure will damage its blades. The scroll pump first reduces the system pressure to  $10^{-3}$  Torr. Then the turbo pump takes it down further. Moreover, the scroll pump helps in removing the exhaust from the turbo and increases its functionality. The thermocouple-based pressure gauge indicates the initial pressure when the system is medium vacuum ( $10^{-1}$  Torr–  $10^{-3}$  Torr)[145]. The ion gauge displays the system's pressure at high vacuum ( $10^{-4}$  Torr –  $10^{-8}$  Torr)[145]. All the components of the vacuum system, including bellows, hoses and valves, are made of 300 series stainless steel. Plain iron or steel is undesirable because it rusts. Besides, 300 series stainless steel is not magnetic and is a poor conductor of heat and electricity.

Hence there is less chance of interference with electronic signals and cryostat temperature. This type of steel also does not have the outgassing problem with the temperature change as well.



*Figure 4.11 a) Scroll pump is on but turbo pump is off. The system is under medium vacuum. b) Both scroll and turbo pumps are on. The system is under high vacuum.*

The operating principle of the vacuum system is represented in Figure 4.11. Green indicates the medium vacuum, blue means high vacuum and red denotes closed valve or path. The operation can be divided into two stages; the first stage is roughing the system (the term used for the initial pump down from atmospheric pressure) by the scroll pump and the second stage is the reduction of the pressure to high vacuum using the turbo pump. In the first stage, as shown in Figure 4.11a, the scroll pump is turned on and the valves V1, V2 and V3 are open creating a path to pump down the system. The pressure is monitored using the pressure gauge mounted below the valve V3. This gauge can report pressure from atmospheric to mTorr. Normally it takes the scroll pump around an hour to bring the system under 20 mTorr. The second stage starts with turning on the turbo

pump (presented in Figure 4.11b). The valve V2 is turned off immediately while V4 is still off, otherwise the exhaust of the turbo will increase the system pressure. Besides, V2 has to be turned off before turning on V4. If this condition is not satisfied, the turbo will pump its own exhaust. Valve 4 is a pneumatic valve which opens at a pressure of 40 psi. A gas pump (not shown in the schematic) provides this pressure using air. This valve opens and closes within a second, which exposes the turbo to the system at once. If a hand-controlled valve like the three others is used in this case, some portions of the turbo pump will be exposed to the high system pressure while other portion will still be under low pressure during the opening process. This pressure difference will cause an imbalance in the turbo blades and could cause pump failure. Finally, after opening the valve V4, the system comes under high vacuum. The ion gauge counts the number of ions in the system by measuring ion current and provides gas density which is converted to the system pressure in the controller.

## **4.6 Cryogenic Setup**

The major components of the closed cycle cryostat are the expander, compressor, vacuum shroud, and radiation shield. The expander, commonly referred to as the cold head or cold finger, is where the Gifford-McMahon refrigeration cycle takes place. It is connected to a compressor by two gas lines and an electrical power cable (Figure 4.12). One of the gas lines supplies high pressure helium gas to the expander, while the other gas line returns low pressure helium gas from the expander. The compressor provides the necessary helium gas flow rate at the high and low pressure for the expander to convert into the desired refrigeration capacity. The vacuum shroud surrounds the cold end of the expander in vacuum limiting the heat load on the expander caused by conduction and convection. The radiation shield is actively cooled by the first stage of the

expander and insulates the second stage from the room temperature thermal radiation being emitted from the vacuum shroud.

In addition to these major components the closed cycle cryocooler is accompanied by several support systems such as an instrumentation skirt, which provides a vacuum port and electrical feedthroughs, as well as a temperature controller to measure and adjust the sample temperature. The system also requires electricity, cooling water for the compressor, and a vacuum pump for the sample space. [146] Appendix D provides the complete program for STR, which controls the cryostat, the lock-in amplifier, the function generator, the nanovoltmeter. The same program also collects the readings from all these devices.

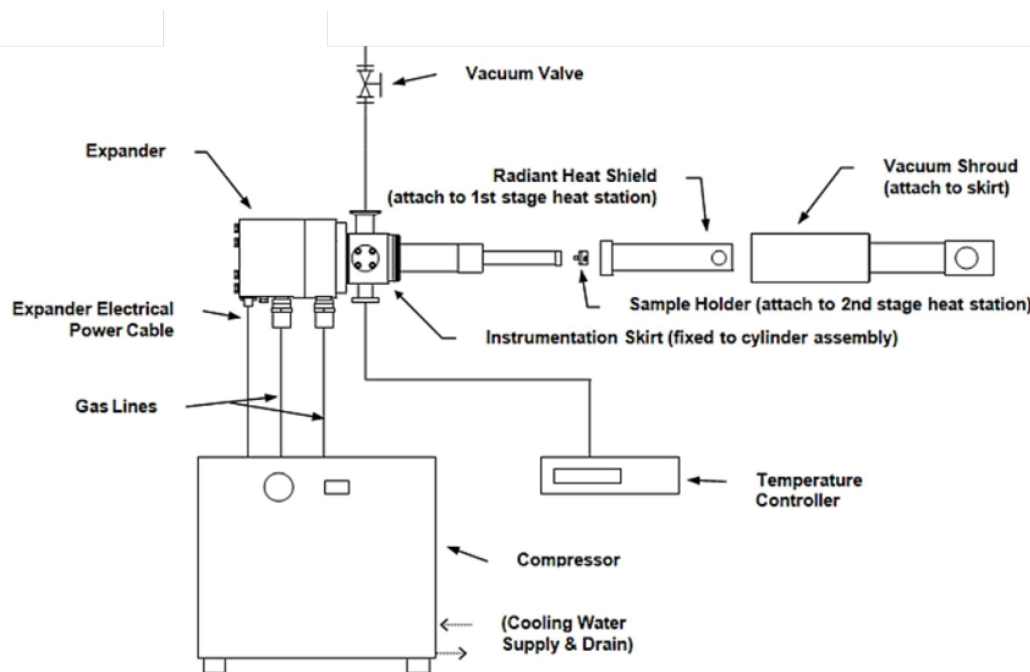


*Figure 4.12 Basic schematic of the closed cycle optical cryostat. The cooling water pipes are connected to the cooler and vacuum valve is attached to the high vacuum system.[146]*

#### 4.6.1 The Gifford-McMahon refrigeration cycle

The closed cycle cryocoolers operate on a pneumatically driven Gifford-McMahon refrigeration cycle, often shortened to GM Cycle or GM cooler as shown in Figure 4.13. The

pneumatically driven GM cooler is different from mechanically driven GM coolers in that it uses an internal pressure differential to move the displacer instead of a mechanical piston. This results in smaller vibrations.

The refrigeration cycle of the closed cycle cryostat starts with the rotation of the valve disk that opens the high-pressure path. This allows the high-pressure helium gas to pass through the regenerating material and into the expansion space. Second, the pressure differential drives the displacer "up", allowing the gas at the bottom to expand and cool. Third, the rotation of the valve disk next opens the low-pressure path, allowing the cold gas to flow through the regenerating material which removes heat from the system. Finally, the pressure differential returns the displacer to its original position, and the cycle is completed. [146]

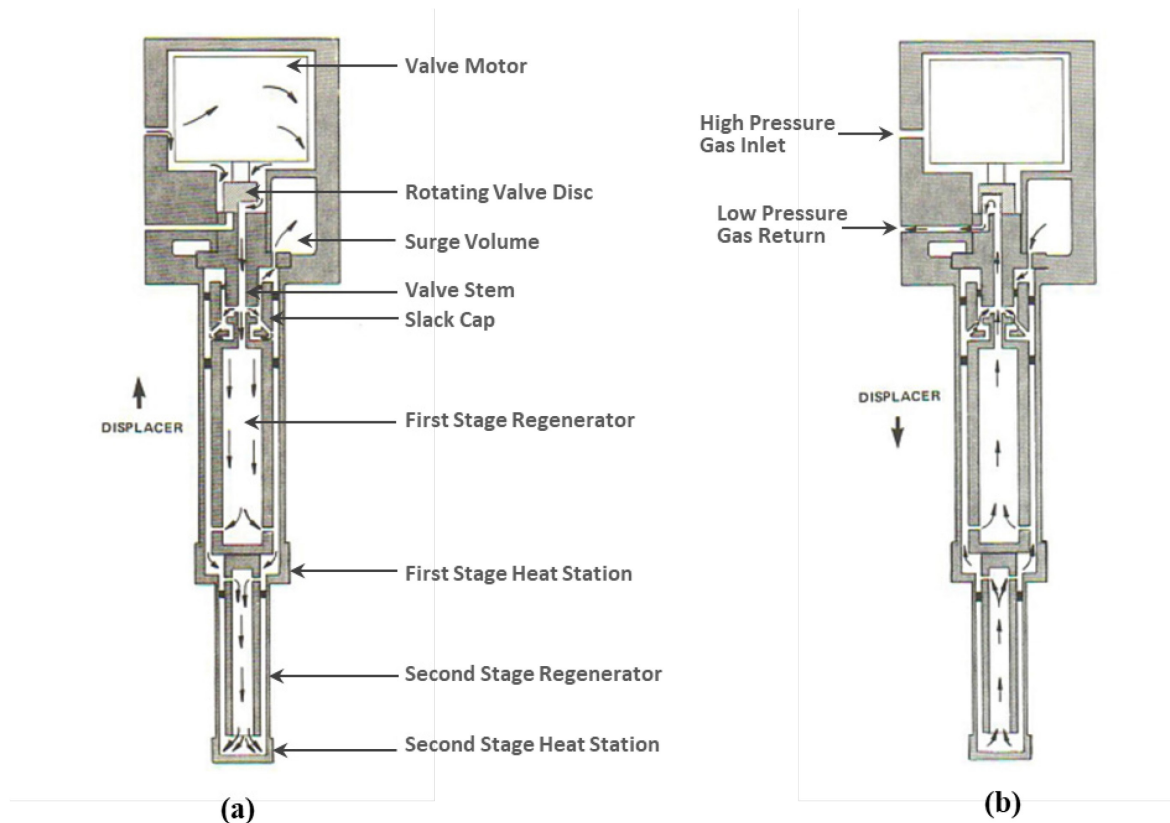


Figure 4.13 Schematic of the expander demonstrating the Gifford-McMahon refrigeration cycle.[146] a) High pressure helium enters the expander from the compressor, b) Low pressure helium goes out of the expander.

## Chapter 5 - Sample Fabrication

The STR method relies primarily on the change in light reflection from the surface correlated with the temperature change. The change of reflection is larger for the greater temperature difference between the base and the tip, and vice versa. Nevertheless, if the difference in temperature reaches 10 K, it affects the physical property of the specimen. Therefore, the highest temperature difference is restricted to 10 K in most thermoreflectance methods. The reflectivity from the surface changes in the range  $10^{-3}$  to  $10^{-4}$  per degree Kelvin of temperature, depending on the thermorefective coefficient. Consider 5 mW of laser energy is shining on a surface with 50% reflectivity. The surface reflects 2.5 mW of laser power. The change in reflected power is achieved by multiplying the reflected power by the coefficient of thermoreflectance. In this case, the reflected laser power varies between 2.5  $\mu$ W and 0.25  $\mu$ W. These powers correspond to 88  $\mu$ V and 8.8  $\mu$ V for the probe side photodetector signal, respectively. The photodetector signals are calculated using the eqn. 153 and 154 from last chapter. Due to such a small quantity, it is desirable to catch the full change in the reflectivity during the experiment. If the sample surface is rough, it will scatter light in various directions making it difficult for a photodetector to capture the total reflection. As a result, only a fraction of the above-mentioned signal will be detected by the photodetector. As can be seen, it is important that the probe laser beam falls and reflects perpendicularly from the surface without scattering. This makes surface roughness of the sample very significant for thermoreflectance measurement. The sample should therefore always be fabricated in a manner that produces a smoother surface.

The primary purpose of the STR experiment is to measure thermal properties of the thin films. There are several techniques including plasma-enhanced chemical vapor deposition (PECVD)[147], chemical bonding[148], and spin etching[149] to fabricate silicon thin films.

Fabrication from silicon on insulator (SOI) wafers is particularly popular because of process simplicity. The SOI wafers have two layers of silicon, the thinner layer known as the device layer and the thicker layer known as the handle layer. There is a buried layer of silicon dioxide between the two parts of silicon called the BOX layer. Samples are fabricated from the device layer. The schematic of different layers of a SOI wafer is depicted in Figure 5.1.

The sample thickness is very important since laser selection depends on it. It is very difficult to purchase an exact device thickness according to the experiment requirements. Besides, getting a customized order is time consuming. As a result, a SOI wafer is purchased mostly with a device thickness close to the desired sample thickness. Then the device layer is etched to obtain the required thickness. The finished sample's surface roughness is much dependent on the etching method used to produce the sample. It is therefore important to find surface roughness in these techniques at different etch depth. Popular etching techniques are Tetramethylammonium Hydroxide (TMAH), Potassium Hydroxide (KOH), Xenon Difluoride ( $\text{XeF}_2$ ) and deep reactive ion etching (DRIE). The surface roughness of thin films produced using these etching techniques and their associated light scattering at different sample thicknesses, are compared in the following section. Thicknesses between 100 nm and 50  $\mu\text{m}$  are considered for comparison.

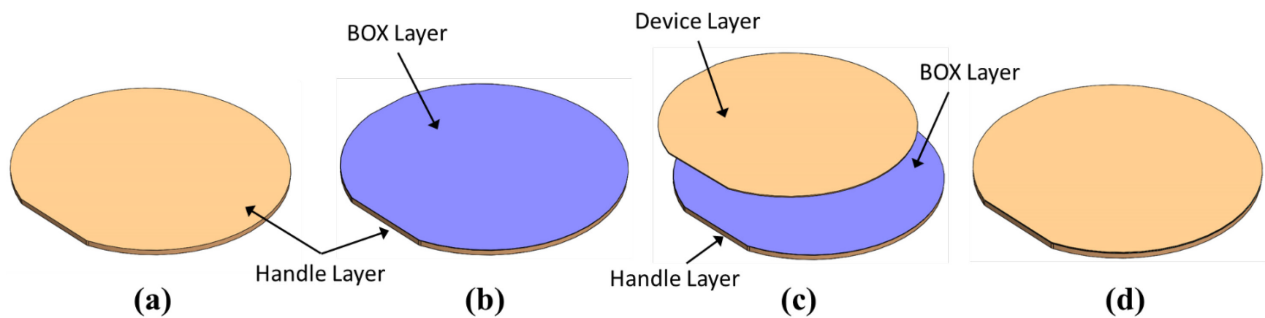


*Figure 5.1 Schematic of silicon on insulator (SOI) wafer with  $\{100\}$  crystal orientation. a) The 500  $\mu\text{m}$  thick silicon layer is termed as handle layer, b) 1  $\mu\text{m}$  buried silicon dioxide or BOX layer sits on top of the handle layer, c) 2  $\mu\text{m}$  device layer rests on top of the BOX layer, d) Final SOI wafer contains all the three layers.*

## 5.1 Thinning Processes for Silicon Film

The applicability of popular etching techniques for thinning of silicon film is discussed below.

### 5.1.1 Tetramethylammonium Hydroxide (TMAH) Etch

TMAH has become a popular etching technique in semiconductor industries because of its high compatibility with the CMOS process, easy handling and low toxicity. TMAH is a kind of quaternary ammonium hydroxide (QAH) solution that first was proposed by Asano[150] in 1979 as an etching and cleaning solution for silicon and silicon-dioxide surfaces.[151], [152] The process in which TMAH removes silicon atoms is well described in the literature. Etch rates vary with different crystallographic orientations due to the atomic bonds formed at the surface silicon atoms. Wafers with a {100} orientation present superficial atoms with two backbonds, connecting to two underlying silicon atoms, and two dangling bonds, capable of suffering a nucleophilic reaction with OH radicals, as shown in Figure 5.2a. Through the thermal excitation and injection of electrons from the backbond into the conduction band, energy is applied in breaking these bonds and releasing the silicon–hydroxide complex[153], [154].

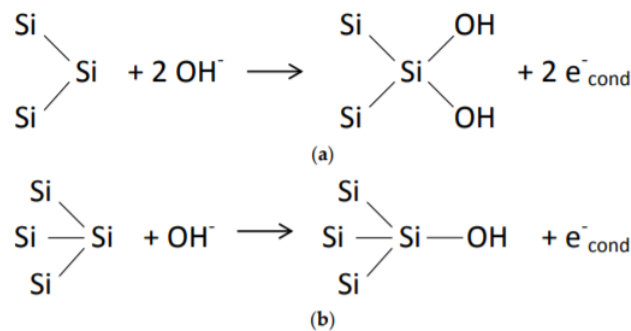


*Figure 5.2 Schematic diagram representing the chemical structure of: surface and respective binding of hydroxide ions during a wet etch process for (a) {100} and (b) {111} silicon wafers.*



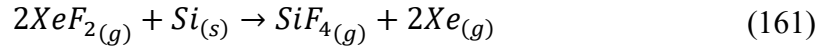
Anisotropy is achieved in different crystalline orientations since structural variations are present at the superficial atoms. For a  $\{111\}$  oriented plane, as depicted in Figure 1b, only one dangling bond exists for each superficial atom, thus making it harder to be etched compared to a  $\{100\}$  oriented plane, as in Figure 1a.[153], [154] As a consequence, the etch rate of silicon depends on the concentration of  $\text{OH}^-$ . That is to say, the PH value of the solution can be adjusted to change the etch rate.[155] A lower concentration of pure TMAH exhibits a higher etch rate, low corner undercutting, and low surface smoothness compared to a higher concentration of TMAH.[156]–[162] The effect of TMAH concentration on the sample surface roughness is shown in Figure 5.3. The effect of temperature on the roughness can also be observed from the figure. The surface is smoother at the lower temperature and vice versa.

### 5.1.2 Potassium Hydroxide (KOH) Etch

KOH is preferred where high etch rate and high etch selectivity between  $\{111\}$  and  $\{110\}/\{100\}$  planes are required. KOH reacts with silicon in a way similar to as TMAH, since the main reactant in KOH is also the OH radicals. When silicon is etched with KOH, it generally produces higher surface roughness due to the pseudomasking effect (on a macroscopic and/or microscopic scale). There are several reasons for this effect such as (1) stoichiometry and topography of the native oxide, (2) residues on the surface left from a cleaning process, (3) defects in the crystalline Si, (4) hydrogen bubbles growing on the surface, (5) diffusion of  $\text{H}_2\text{O}$  and  $\text{OH}^-$  to the surface and diffusion of silicates away from the surface, (6) Si-H and Si-F bonds left on the surface from the HF rinse and  $\text{H}_2\text{O}$  wash. But the pseudomasking by bubbles and perhaps silicates are the primary cause of roughness.[163]–[165] Shinmo et al. measured the surface ruggedness of silicone etched with KOH as shown in Figure 5.3.

### 5.1.3 Xenon Difluoride (XeF<sub>2</sub>) Etch

XeF<sub>2</sub> is employed as a dry-chemical (plasmaless) etchant capable of isotropically etching Si. It was initially proposed as an etchant of Si in the late 1970's.[166], [167] XeF<sub>2</sub> in its vapor phase spontaneously etches Si at room temperature. The primary chemical reaction of XeF<sub>2</sub> with Si is given in Eq. (5.1):[168]–[171]



In the case of a clean Si surface, a Fluorine (F) atom is abstracted from the XeF<sub>2</sub> molecule by a reactive site, i.e., dangling bond, without energy barrier, whereby the complementary XeF scatters off the surface.[172] As a result, the surface layer Si {100} and Si {111} surfaces with possibly some SiF<sub>2</sub> at step edges. Once dangling bonds are passivated, the next reaction step requires breaking of Si–Si backbonds which is an activated process with a much smaller reaction probability. Since F is known to be very electronegative, bond charges will reside preferentially close to the F atom, leading to an effective charge separation between the Si (δ<sup>+</sup>) and F (δ<sup>−</sup>).[173] The backbonds are weakened by this phenomenon and, hence, backbonds are susceptible to subsequent F-atom insertion, which is supplied by physisorbed XeF<sub>2</sub> molecules, or as proposed by Morikawa *et al.*[174] and Winters *et al.*[175], by F<sup>−</sup> atoms already interstitially present in between the Si lattice atoms. Subsequent steps of F-atom attachment to SiF<sub>x</sub> surface species leads eventually to the formation of SiF<sub>4</sub> molecules, which are volatile and can desorb from the surface as the main etch product at room temperature.[176], [177]

The silicon fluoride reaction layer thickness remains this way typically 1.5 ML (monolayers)[178], composed of a surface layer of SiF and SiF<sub>2</sub> species (partially) covered by a layer of SiF<sub>2</sub> /SiF<sub>3</sub> species. Lo *et al.* showed that it takes about 10<sup>3</sup> ML of XeF<sub>2</sub> dose to reach an intermediate, steady-state reaction layer consisting of primarily SiF followed by SiF<sub>3</sub> and a minor

amount of  $\text{SiF}_2$ . [179] Due to the removal of Si in the etch process, the surface is believed to roughen and hence, the total amount of  $\text{SiF}_x$  species increases. [176] Surface roughness measurements by Chu *et al.* [180] and Sugano *et al.* [181] are presented in Figure 5.3.

#### 5.1.4 Plasma Etch

A plasma is a (partially) ionized gas. [182] In low-pressure gas, plasma is produced by the dissipation of electrical power to the medium. Atoms, radicals and ion species, which are produced in this way, are at the origin of further reactions and, therefore, the plasma phase is generally a very complex mixture of chemical species. [183] Ultimately, the plasma species interact with the walls and the sample surface. Adsorption of species will occur depending on the chemical affinity and surface temperature. Adsorbed species may react with the surface to form a product or desorb without or before reaction. If the product is volatile, it will desorb into the plasma phase and, thus, cause etching of the material. [183]

There are several theories regarding how surface roughness occurs during plasma etching. Two popular theories are: shadowing mechanism [184] and re-emission reaction [185]. The basic principle of shadowing is that the crest of the surface receives a higher flux of reactant radicals than the valley of the surface because the crest sees the plasma with a wider solid angle than in the valley. Therefore, in a sputter deposition process, the deposition rate at the peak is higher than at the valley, leading to growth instability and the surface buildup into a mountain landscape, which coarsens in time. [184], [186], [187] On the other hand, re-emission theory suggests that the etchant species have a surface reaction probability of zero when they collide with the surface for the first time but are re-emitted and react with the silicon surface with a high probability after this first re-emission. The result of this assumption is obvious: because the reactivity of the etchant is

significant only after the second collision with the surface, they react much less on the crest than on the valley—the latter receiving the re-emitted flux from the peaks. Hence, the etch rate of the valleys is higher than the etch rate of the hills, leading to the roughness growth.[185], [187], [188] The common perception is that these two theories combined contribute to the roughening of the sample surface. Roughness measurement for  $\text{Cl}_2$  and  $\text{SF}_6$  plasmas is illustrated in Figure 5.3.

### 5.1.5 Oxide Growth and Removal

Another trimming process for silicon film is oxidation and removal of the oxide layer. In this process 100nm-1000nm oxide is grown at the top layer of the silicon film and then this oxide layer is etched away using a buffered oxide etch (BOE). This is a very slow and time-consuming process since oxidation takes several hours depending on the desired thickness. Besides, this is a diffusion limited problem which means maximum  $1\mu\text{m}$  oxide can be grown at a time in the oxidation furnace. Hence if the thinning process requires the removal of several microns of silicon, there need to be several oxidation and removal cycles.

The positive side of this method is the smoother surface it provides. Every polished wafer has 0-2nm native oxide layer at the top.[189]–[191] During the thermal oxidation process, oxygen atoms diffuse into the native oxide layer and react with the silicon at the Si-SiO<sub>2</sub> interface.[192] Since the reaction occurs deep into the silicon, the surface morphology at the top does not change. As a result, there is little to no difference in the roughness of the surface before and after the oxidation and the surface can retain its smoothness upon the removal of the oxide layer. Iacona *et al.* report of surface roughness, as shown in Figure 5.3, which supports this claim since the silicon dioxide removal process produces a smoother surface than any other process shown in the figure. Moreover, it is easy to control the etch depth. The desired silicon dioxide thickness can easily be

calculated using the Deal-grove model[193]. BOE has a very low etch rate for silicon. So, the etch stops after the removal of the oxide layer.

There are some mechanical thinning processes as well, such as grinding[194], chemical mechanical planarization (CMP)[195], and dicing[196]. But grinding leaves a backside damage that extends 5–15  $\mu\text{m}$  deep into the substrate. For thin wafer applications, backside damage enhances the risk of wafer breakage.[196] CMP also develop defects in the thin layers and these defects become critical for sub-0.25 $\mu\text{m}$  feature sizes. Besides, it is difficult to control features size in CMP and the process is costly as well.[197] All the mechanical thinning processes develop some residual stress[194] in the film which is difficult to get rid of and can yield some unintentional properties in the film. Considering all the facts, mechanical processes are not a good choice for sub-micron thinning of wafers.

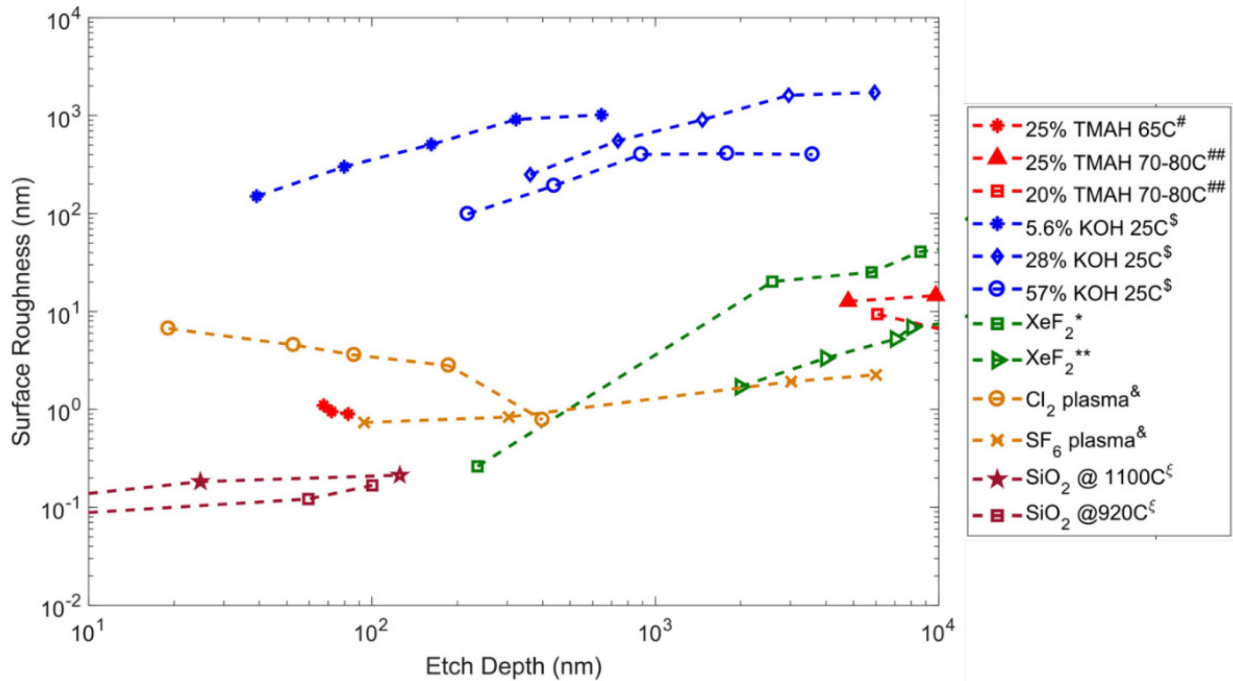


Figure 5.3 Relation between etch depth and surface roughness of the sample for different etching techniques. Samples are etched with # 25% TMAH at 65°C [198], ## 25% and 20 % TMAH at 70°C -80°C [199], \$ 5.6% to 57% KOH at 25°C [200], \* XeF<sub>2</sub> gas by Chu et al.[180], \*\* XeF<sub>2</sub> gas by Sugano et al.[181], & Cl<sub>2</sub> and SF<sub>6</sub> plasma[187], ξ removal of thermally grown SiO<sub>2</sub> at 1100°C and 920°C [201].

## 5.2 Relation Between Light Scattering and Surface Roughness

Little attention has been given to the surface roughness in thermorefectance studies. It is typically assumed that the effect of the scattering will be very small when the surface roughness is less than the probing light wavelength. But, thermorefectance signal quality, and hence the accuracy of the measurement, can be improved by reducing the roughness. The relation between roughness of different thinning techniques and light scattering is explored in this section and the best thinning technique is reported.

First, the amount of scattered light is calculated from the surface roughness and then the scattering is correlated to the etch depth. The relation between light scattering and surface roughness is formed based on a few assumptions, such as the material has good electrical conductivity and the distribution height of the surface irregularities are Gaussian about the mean. Moreover, light wavelength and frequency remain unchanged (or only that frequency is considered which is the same as the incoming frequency) and hence inelastic scattering doesn't play a role for thermorefectance. The diffusive reflection alone contributes to the light scattering from the surface and the intensity loss for specular reflection is negligible for a perpendicularly incident light beam.[202]–[204]

The power Spectral Density (PSD) function defines the power of different roughness components in terms of the lateral surface spatial frequencies  $f_x$  and  $f_y$ . It contains all the statistical information of the random-rough surfaces. PSD is defined as the squared modulus of the Fourier transform of the interface topography, as given in Eqn. (162).

$$PSD(f_x, f_y) = \lim_{L \rightarrow \infty} \frac{1}{L^2} \left| \int_0^L \int_0^L z(x, y) e^{2\pi i(f_x x + f_y y)} dx dy \right|^2 \quad (162)$$

where  $L$  is the length of the scanned profile and  $z(x, y)$  is the vertical distance from the mean.

Stochastic surfaces often exhibit isotropic roughness corresponding to a PSD with a polar symmetry. The 2D isotropic PSD is calculated by averaging the 2D PSD over all azimuthal directions.

$$PSD(f) = \frac{1}{2\pi} \int_0^{2\pi} PSD(f, \psi) d\psi \quad (163)$$

Using the transformation  $f = \sqrt{f_x^2 + f_y^2}$  and  $\psi = \tan^{-1} \left( \frac{f_y}{f_x} \right)$

Every real profile or roughness measurement technique is confined to a certain spatial frequency range, which is limited, for instance, by the investigated surface area and the instrument resolution.[205], [206] Therefore, it is useful to define the roughness as the square root of the surface height standard deviation of  $z(x,y)$  from its mean value also known as the rms roughness. The rms roughness is calculated by integrating the 2D isotropic PSD.

$$\sigma = 2\pi \left[ \int_{f_{min}}^{f_{max}} PSD(f) f df \right]^{\frac{1}{2}} \quad (164)$$

The following equation describes the diffusive reflectance at an angle from 0 to  $\theta$ .

$$R = \int_0^\theta R_0 2\pi^4 \left( \frac{a}{\lambda} \right)^2 \left( \frac{\sigma}{\lambda} \right)^2 (\cos\theta + 1)^4 \sin\theta \times e^{\left[ -\frac{(\pi a \sin\theta)^2}{\lambda^2} \right]} d\theta \quad (165)$$

After applying the value of the autocovariance length  $a = \frac{\sqrt{2}\sigma}{m}$  and doing the integration, the contribution from diffusive reflectance becomes

$$R = R_0 \left[ e^{-\frac{(4\pi\sigma\cos\theta)^2}{\lambda^2}} + \left( \frac{2^5\pi^4}{m^2} \right) \left( \frac{\sigma}{\lambda} \right)^4 \theta^2 \right] \quad (166)$$

where  $R_0$  is the specular reflection from a perfectly smooth surface,  $\sigma$  is the root mean square roughness, and  $\lambda$  is the wavelength of the light. If the wavelength is sufficiently larger than the rms roughness, the total integrated scatter (TIS) light can be found using eqn. 5.7. [207]–[211]

$$TIS = R_0 \left[ 1 - e^{-\frac{(4\pi\sigma\cos\theta)^2}{\lambda^2}} \right] \quad (167)$$

This equation is used to find the light scattering in Figure 5.4. The smooth surface reflection ( $R_0$ ) is taken as 0.72 from Figure 4.7 and light incident is considered as normal to the surface.

It is evident from Figure 5.4 that oxidation and removal is the best thinning process for silicon film. This process is used to thin the silicon cantilever, used in the experiment, to the desired thickness. KOH etched surface scatters almost hundred percent of the light since the surface irregularities size is comparable to the probe wavelength.  $\text{SF}_6$  plasma etch can also be used for thinning. But due to its complexity, plasma etch is not utilized in the fabrication process for silicon cantilevers.

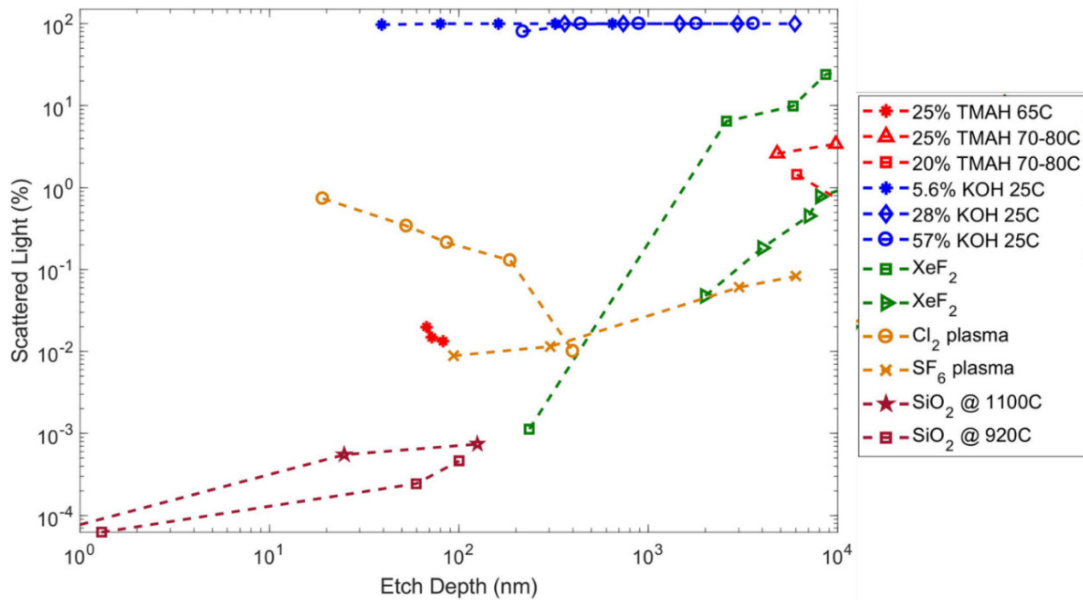


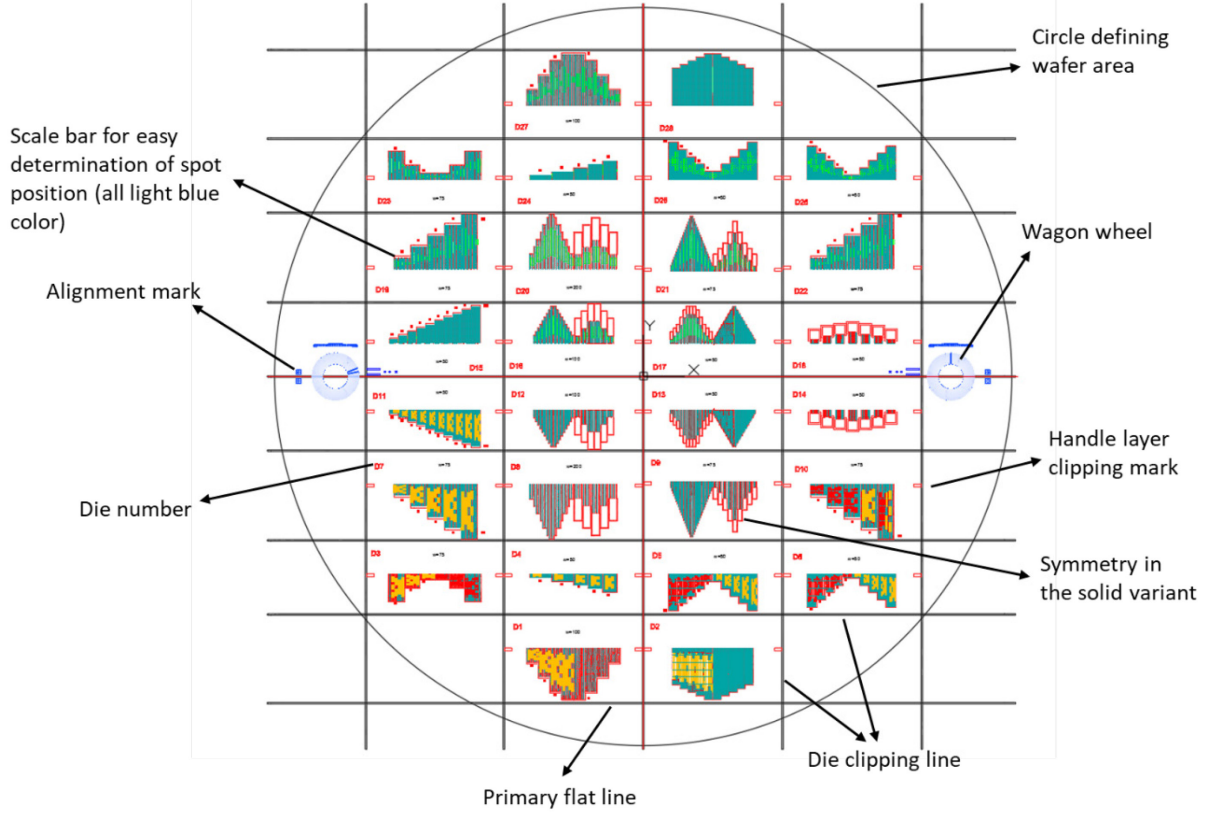
Figure 5.4 Relation between scattered light and etch depth of different etching technique. The scattered light percentage is calculated as the ration of scattered and incident light.



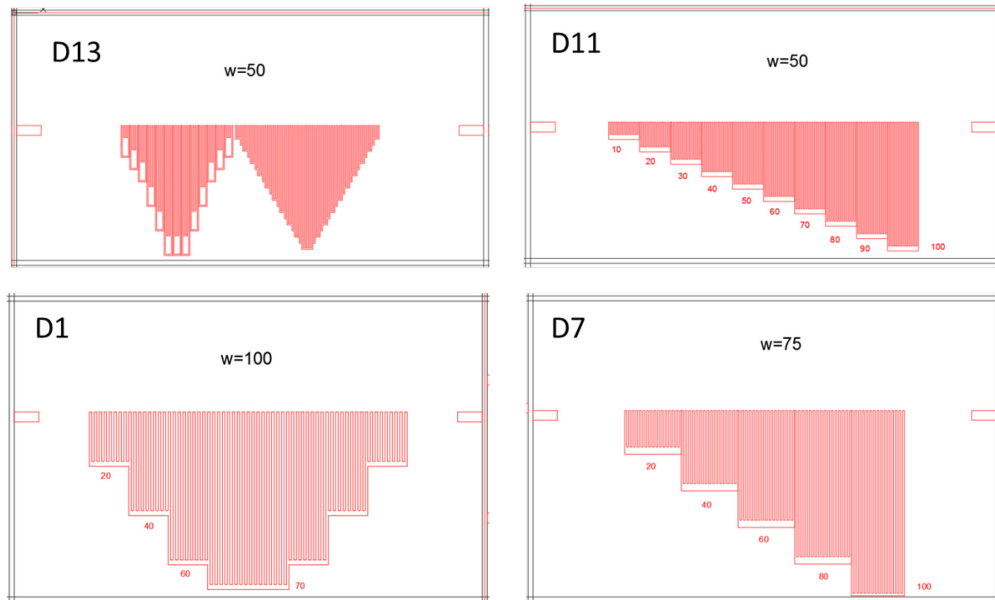
### 5.3 Photomask Design

A photomask is used to transfer patterns from a glass plate to the wafer using standard photolithographic techniques. The photomask was designed to pattern a 4" wafer. The light-field mask was printed on a 5" quartz plate with a chrome coating. As shown in Figure 5.5a, this mask has 28 dies where upper half dies are the mirror of the lower half. Since this mask was designed before characterizing the pump and probe laser spots, there are cantilevers with different widths varying from 50  $\mu\text{m}$  to 200  $\mu\text{m}$ . Similarly, there are several L/w ratios corresponding to each width. These L/w ratios vary from 10 to 100.

Each die has its unique number in the left corner which helps in identifying wafer pieces after dicing. The dicing lines are 20  $\mu\text{m}$  wide. These lines assist the dicing saw to cut in straight lines and keep the die intact. There are two clipping marks on either side of the cantilevers in each die. These marks start from the dicing line and face perpendicular to the cantilevers' length. Their direction guides the crack propagation after clipping with the diamond scribe while chopping the handle layer off. Alignment marks help aligning the photomask with the primary and secondary flat of the wafer. The blossom-like patterns on the mask are called wagon-wheel and are used for qualitative guidance of the etching rates. The wagon-wheel pattern technique has been used to obtain detailed experimental data on the crystal orientation dependence of etch rates.[212] Another important feature is the scale bar between two adjacent cantilevers. The scale bar is a narrow cantilever which has marker like patterns on both sides which guide the probe laser along the cantilevers' length during measurement. The area between dicing line and cantilever's base matches exactly the grooves of the sample holder to ensure better thermal contact between them.



(a)



(b)

Figure 5.5 (a) Photomask containing cantilever's patterns, (b) Die D13, D11, D1 and D7 is enlarged.

## 5.4 The Suspended Cantilevers

This section details the silicon cantilever fabrication from the SOI wafer. The wafer is cleaned before the fabrication and the cantilever beams are geometrically characterized after the fabrication.

### 5.4.1 Cleaning Procedure

Any contamination, such as metal, organic or inorganic material, present in the thin film can alter the thermal property measured using STR. So, the SOI wafer is cleaned properly before the fabrication process.

The silicon on insulator wafer cleaning process in itself is not that easy. This is because, apart from being easily contaminated, SOI wafers are also very fragile. They need to be handled with the utmost care to ensure that there is no damage done to their surface. The issue is that smaller particles are physically more difficult to remove, because it is harder to deliver the necessary force to minuscule dimensions. Thus, more energy is required to remove smaller particles. Types and source of contamination are discussed briefly below.[213]

**Particles** - dust, pollen, clothing particles, bacteria, etc. Particles with diameter more than 20 micron will settle down readily. Particles of diameter from 0.1 to 20 micron are the main problem.

**Inorganic contaminants** - salts, positive and negative ions in solution, heavy metal atoms. Inorganics are removed by cleaning the wafer in water recirculation systems and using special solutions.

**Organic contaminants** - smog, skin oil, fluxes, lubricants, solvent vapors, monomers from plastic tubing and storage boxes that can condense on substrate. They usually are removed using strong oxidizers, gaseous or liquid.

**Impurities** - incorporated during the formation of substrates or overlayer films. Generally, they cannot be removed.

There are several steps associated with the cleaning process. These steps are discussed sequentially. The process starts with dipping the SOI wafers in the piranha bath for 20 minutes. Piranha is a chemical mixture of water, hydrogen peroxide and sulfuric acid. All of these chemicals are mixed in equal volume. Because it is a strong oxidant solution, it removes metals and organic contaminants, and will hydroxylate most surfaces (add OH groups) rendering them hydrophilic[214]. The wafers are then dipped into the buffered oxide etch (BOE) for 3 minutes. BOE is mixture of buffering agents like ammonium fluoride ( $\text{NH}_4\text{F}$ ) and hydrofluoric acid (HF). The volume of  $\text{NH}_4\text{F}$  is six times more than HF in the mixture. This step helps removing OH groups from previous step and any oxide, ionic, and metal particles from the surface. Next, the wafers are cleaned in a mixture of water and hydrogen peroxide for 20 minutes. Any particulate and metal contamination present in the wafer reacts with the hydroxide group and is eliminated.

The wafers are then dipped in BOE again for 3 minutes. Finally, the wafers are cleaned in a solution called RCA-2 clean which is a mixture of water, hydrogen peroxide and hydrochloric acid. This process removes any ionic and metal surface contaminations. The wafers are cleaned in de-ionized (DI) water in between every step to clean the residue associated with the previous step. The cleaning and rinsing steps are performed by using the so-called Marangoni technique[215]. The Marangoni principle involves the slow withdrawal of wafers from a DI water bath to an environment of isopropyl alcohol (IPA) and nitrogen such that only the portion of the surface that is at the interface of the liquid and vapor phases is "drying" at any one time. In this way, uncontrolled evaporative drying on the wafer is prevented.

### 5.4.2 Cantilever Fabrication

A multi-stage process was utilized to fabricate the free-standing Si cantilever, beginning with a Silicon on Insulator (SOI) wafer with {100} crystal orientation, around a 5  $\mu\text{m}$  thick device layer and  $10^{13} \text{ cm}^{-3}$  -  $10^{15} \text{ cm}^{-3}$  doping concentration (p-type). The full fabrication process is illustrated in Figure 5.6.

As shown in the previous chapter, the desired cantilever's thickness is around 3  $\mu\text{m}$ . Hence two cycles of 1  $\mu\text{m}$  thick  $\text{SiO}_2$  growth and removal was performed. The device layer thickness became  $3.03 \pm 0.057 \mu\text{m}$  after the  $\text{SiO}_2$  removal step. Then, another 100nm silicon dioxide was grown in the device layer by placing the wafer in a tube furnace. The oxide was grown using only oxygen, known as dry oxidation, at  $1000^\circ\text{C}$  for 3 hours. The patterns from the photomask is then transferred to the device layer of the wafer through standard photolithographic techniques. After this step, some area of the oxide layer was covered with the photoresist and some area was exposed as shown in Figure 5.6(c). Buffered oxide etch (BOE) removes the oxide from exposed area. A Tetramethylammonium hydroxide (TMAH) bath was then applied to anisotropically etch the silicon.[216] TMAH also reacts with photoresist and dissolves it immediately into the solution. The silicon dioxide was used as the masking material in this step. TMAH etching leaves nearly atomically smooth sidewalls in order to avoid scattering of thermal energy carriers during experiments. As depicted in Figure 5.6(e) the cantilevers were formed after this step. But they are still attached to the  $\text{SiO}_2$  underneath them. Though, commonly, BOE is used to etch the  $\text{SiO}_2$  layer, it was not usable in this case due to the stiction failure upon taking out the cantilevers from the BOE bath.[171] Therefore, vapor HF was used to remove the oxide under the cantilevers. The process takes around 7-8 hours at  $30^\circ\text{C}$  due to the low etch rate of vapor HF. But the cantilevers were still not accessible from the backside due to the handle layer. Finally, the handle layer was

removed from under the cantilever beams by clipping it off using a diamond scribe but the handle layer remains under the fixed support point.

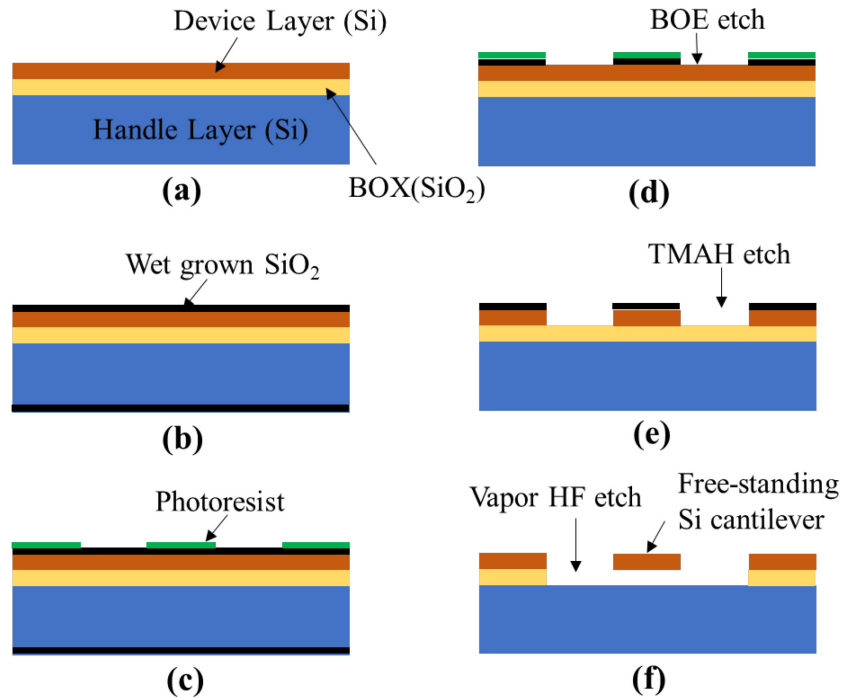


*Figure 5.6 Fabrication steps for the free-standing Si cantilever: a) Beginning SOI wafer, b) Dry oxide is grown on the device layer, c) The pattern from the mask is transferred using photolithographic, d) BOE etches away the exposed oxide, e) TMAH etches the silicon, f) Cantilevers are released using a vapor HF.*

Though one sample is enough to check the effectiveness of the STR technique to measure the thermal conductivity of the materials, another sample of around 2  $\mu\text{m}$  thick silicon film was fabricated to further confirm the versatility of the STR application. This second sample had three cycles of oxide growth and removal resulting in a device layer of about 2  $\mu\text{m}$ .

Figure 5.7 shows the actual cantilever beams after step (f) of Figure 5.6 for 3  $\mu\text{m}$  sample. Upon scraping the handle layer from underneath the cantilevers, it is extremely difficult to take SEM images since cantilevers at that level are very vulnerable and will be destroyed in handling.

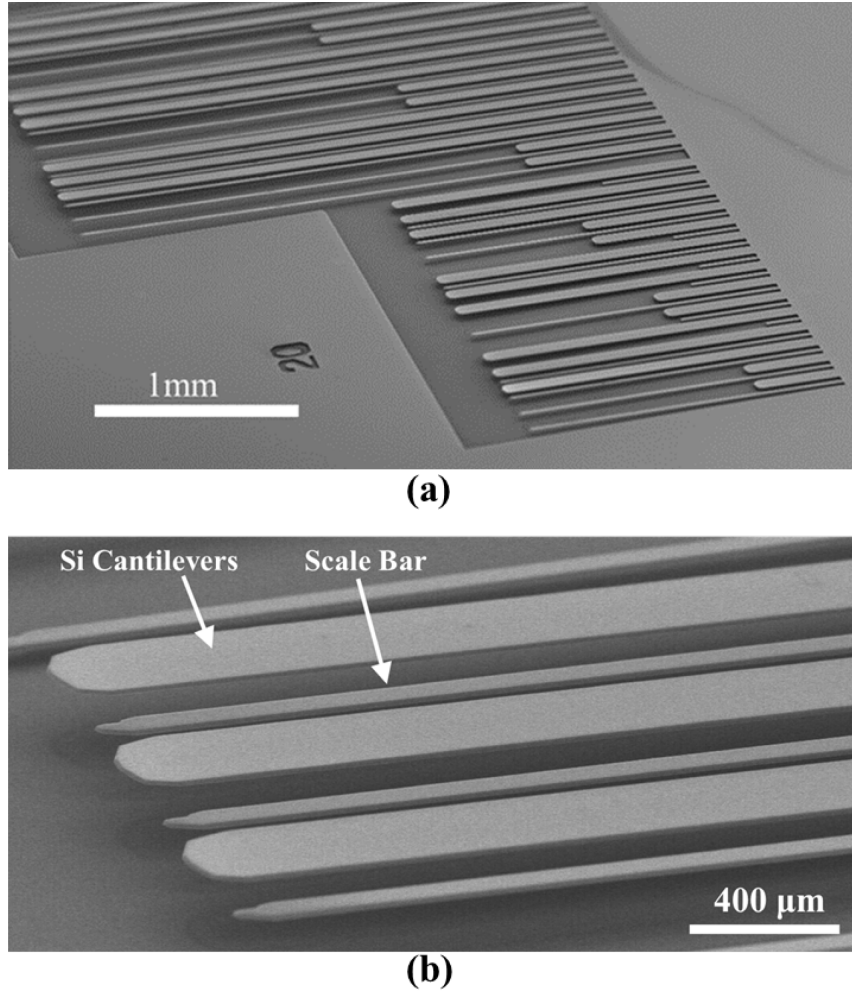


*Figure 5.7 SEM image of 200  $\mu\text{m}$  wide freestanding silicon cantilever beams, (a) larger area, (b) zoomed at the tip. Cantilevers with different lengths were fabricated but only 7.5 mm long cantilevers are used as their  $L/w$  ratio is above 30.*

### 5.4.3 Cantilever Beam Geometry Characterization

Final sample dimensions were measured using a profilometer (Dektak 150) and SEM. The samples are 7.5 mm long, 194  $\mu\text{m}$  wide and  $2.93 \pm 0.06$   $\mu\text{m}$  thick. Figure 5.8 depicts the profilometer measurement of the cantilever's thickness. Thicknesses of the other samples were  $2.03 \pm 0.09$   $\mu\text{m}$ . The surface roughness was also measured using the profilometer and it was around 4 nm.

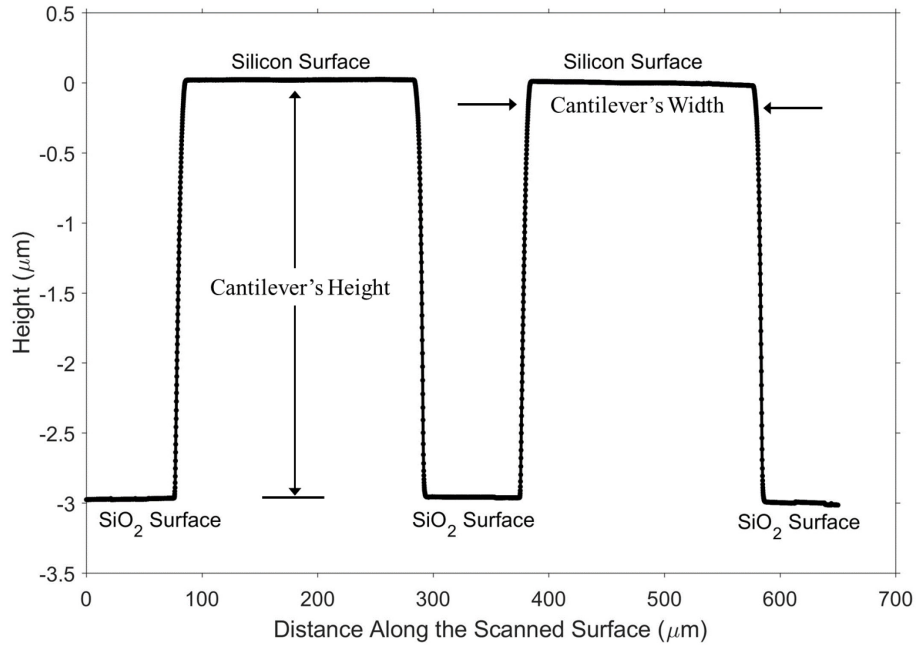


*Figure 5.8 A profilometer scan of the step from silicon dioxide to  $\sim 3\mu\text{m}$  thick silicon cantilever.*

Sometimes residual stress may develop in the cantilevers during the fabrication. In that case, the beams will be bent outward with the handle layer showing a radius of curvature. This indicates that the  $\text{SiO}_2$  underneath the cantilevers was not completely removed and the sample should be kept in the vapor HF for a longer period. The cantilevers presented here do not have any residual stress and are completely flat.



## Chapter 6 - Experimental Results

The first part of this chapter provides information on the characteristics of the laser beam when focused on the sample. Probe frequency is selected in the second part based on the stability of the signal, whereas, temperature and thermal conductivity of the suspended films are analyzed in the last segment.

### 6.1 Laser Beam profile

Light propagates as an electromagnetic wave through a medium. In the transverse direction, the amplitude of this wave field has a Gaussian pattern.[217] In addition to longitudinal or axial oscillation modes, which are associated with standing waves set up along the cavity or z-axis, transverse modes are also retained. The single mode laser used in the experiment corresponds to the lowest order of these transverse modes. As a result, the flux distribution over the cross section of the laser spot is preferably Gaussian and there are no electrical phase changes across the laser beam.[218]

The width of the laser spot can be defined in several possible ways. Some of these methods are  $D4\sigma$ , 10/90 or 20/80 knife-edge,  $1/e^2$ , FWHM, and D86. [219], [220]  $D4\sigma$  measures four-standard deviations from the peak value. 10/90 or 20/80 knife-edge calculates the transverse knife edge widths between 10%-90% or 20%-80% integrated intensities. The  $1/e^2$  width is equal to the distance between the two points on the marginal distribution that are  $1/e^2 = 0.135$  times the maximum value. FWHM defines the horizontal distance at half of the laser's maximum intensity. The "D86" diameter contains 86% of the total beam energy. These definitions when applied to different beam profiles can give very different width values. Out of these, the  $D4\sigma$  is the ISO

international standard definition for beam width[221] and is used here to report the laser spot diameter when focused on the sample.

Figure 6.1 shows the pump and probe laser profiles which are measured using a DataRay XHR scanning slit profiler. The normalized intensity of the lasers, termed as the ADC value, is plotted against a horizontal distance. X and Y-profiles describe the distance in x and y-axis of the 2D laser spots. The 4 standard deviation range shown in the figure is known as the beam profile in both directions under the Gaussian curves. X and Y-profiles of the pump laser spot are 109.8  $\mu\text{m}$  and 96.9  $\mu\text{m}$  wide, respectively. The probe laser spot widths are 151.8  $\mu\text{m}$  and 169.6  $\mu\text{m}$ . These profiles indicate that both pump and probe spots are of elliptical shape.

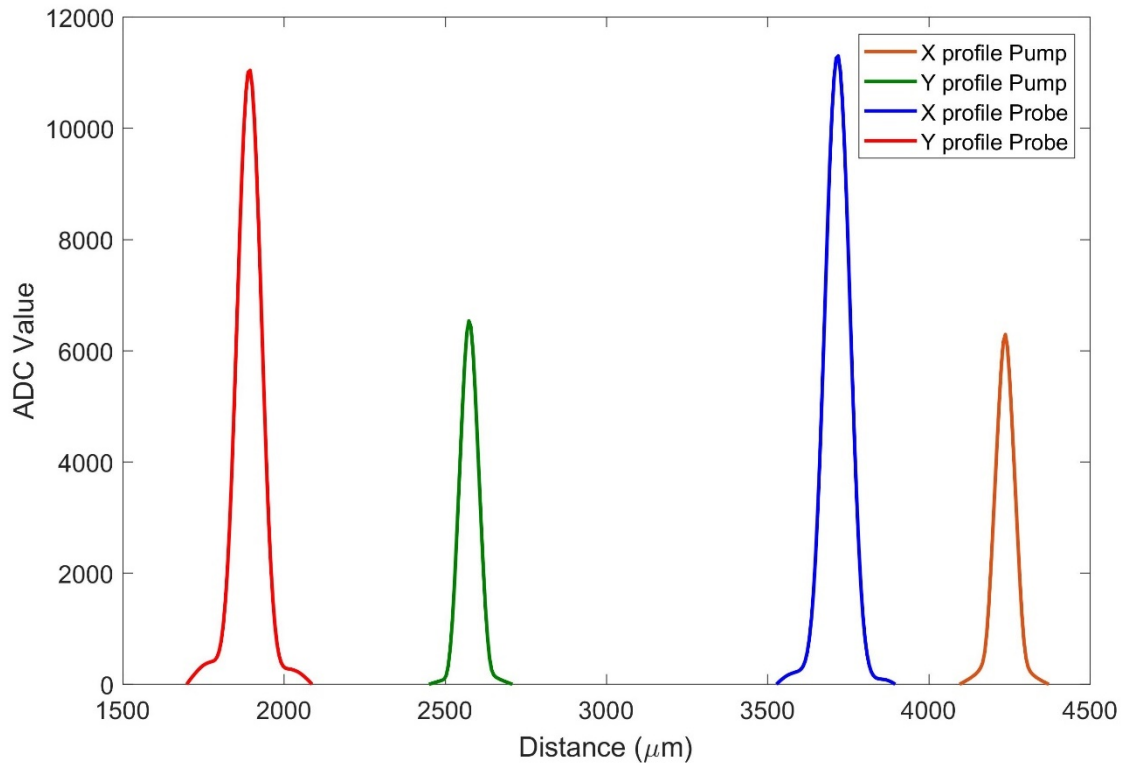


*Figure 6.1 Pump and probe laser spot size on the sample. X and Y profile represents the major and minor axis of the elliptical spot.*

## 6.2 Suspended ThermoReflectance Data

First step of the measurement process is determination of thermorefectance coefficient ( $C_{TR}$ ) using the probe laser beam and the internal temperature controller of the cryostat.[95] Eqn. (168) is applied for the  $C_{TR}$  calculation.[222], [223]

$$C_{TR}(\lambda) = \frac{1}{R_T(\lambda)} \frac{R_{T+\Delta T}(\lambda) - R_T(\lambda)}{\Delta T} \quad (168)$$

here  $R_T$  is the probe laser reflectance from the cantilever at temperature  $T$ . As soon as the cryostat temperature is increased by  $\Delta T$  using its own PID controller, the reflectance of the probe laser changes to  $R_{T+\Delta T}$ .  $\Delta T$  is kept around 5 K during the  $C_{TR}$  measurement to keep the temperature dependent thermal properties constant. The PID takes around 5 mins to increase the cryostat temperature and reach a stable point. The cantilever's temperature is monitored by the sensor mounted in the sample holder. It is very important for the full cantilever beam to be at the same temperature. Though the time constant for the cantilever is very small, its temperature keeps changing when the PID adjusts the cryostat condition. As a result, each measurement is done at a 10 mins interval. The measurement procedure is repeated several times and the  $C_{TR}$  is obtained over a temperature range of 20 K to 300 K. The thermorefectance coefficient varies in a narrow range with an average value of  $3.53 \times 10^{-4} \text{ K}^{-1}$  and standard deviation of  $9.09 \times 10^{-5} \text{ K}^{-1}$ . This value of  $C_{TR}$  shows a good agreement with the value reported by Kim et al.[223] which is  $2 \times 10^{-4} \text{ K}^{-1}$  for 800nm wavelength. Change in the  $C_{TR}$  due to the change in sample thickness is very small and falls within the average value mentioned above. According to Eqn. (168), the  $C_{TR}$  value does not depend on the thickness; it rather depends on the wavelength at which the measurement was made.

### 6.2.1 Probe Frequency Selection

To assist in signal detection using the lock-in amplifier, the probe laser is modulated with an external frequency. Several experiments are carried out to find out the optimal modulation frequency for the probe laser. It was observed that the signal was noisy at the lower frequency and as the frequency increases, the signal to noise ratio also increases (Figure 6.2). Change in temperature does not alter the signal to noise ratio behavior indicating that the cryostat temperature does not affect the noisiness of the signal.

Several factors contribute to the noisy signal at the lower frequency. These includes low frequency vibration from the laboratory environment, instability of laser and electronics, and natural frequency vibration of the cantilever. The probe laser exerts a radiation pressure on the sample which is calculated by following equation.

$$P = \frac{q}{Ac} + R \frac{q}{Ac} \quad (169)$$

where P is the radiation pressure, R is the reflectivity of the surface, and q is the laser power incident on an area A. This pressure is around 0.3mPA for 5 mW laser power. Since the laser has a sinusoidal frequency, the amplitude of radiation pressure changes within every wave period and hence causes positive and negative deflection in the sample. The period decreases at the higher frequency, but the response time of cantilever tip deflection remains unchanged which mitigates the effect of sample vibration in the signal.

Around 200 data points are collected at each frequency and the average of these data is shown as the signal while the standard deviation is considered as the noise. It is evident from Figure 6.2 that the signal to noise ratio becomes approximately 30 dB at and above 10 kHz and does not change much after that. Therefore, 10 kHz is considered as the optimum frequency and all the experiments described in this chapter were conducted at this frequency.

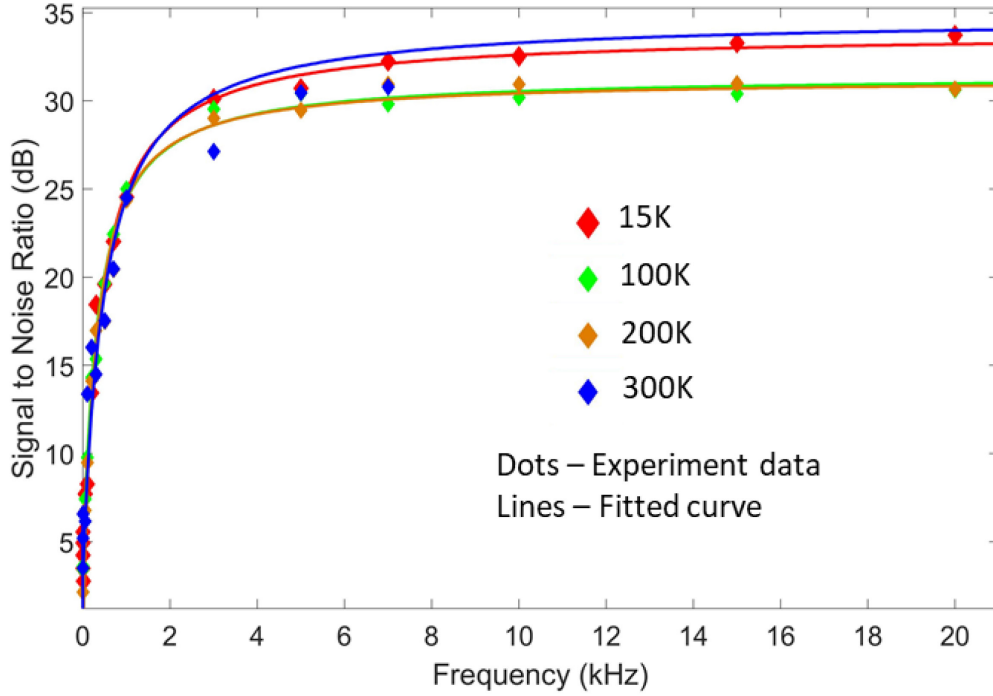


Figure 6.2 Signal to noise ratio relation with the probe laser frequency. Experiments are conducted at 15 K, 100 K, 200 K and 300 K temperatures.

### 6.2.2 Temperature and Thermal Conductivity Measurement

A separate set of experiments were conducted to find the temperature along the cantilever's length. All experiments were conducted at  $3.8 \times 10^{-5}$  Torr. In the first experiment, probe reflection from the sample was captured at 7 different cryostat temperatures from 20 K to 300 K. The pump laser was inactive during this experiment. A second experiment was run in a similar way as the first one, but with the presence of pump heating at the tip. The sample absorbed 4.8 mW pump laser power which was measured using photodetectors 1 and 2. The same experiment was repeated at 3 different points, each 1 mm apart, along the length of the  $2.03 \pm 0.09$   $\mu\text{m}$  thick sample. The result is presented in Figure 6.3.

Instead of presenting the temperature at each point, the difference ( $\Delta T$ ) from the atmospheric or cryostat temperature ( $T_{\text{sub}}$ ) is presented in the figure. This helps to provide better

representation of the temperature change along the length. 7.5 mm points represent the tip of the cantilever and temperature rise at this point is around 4 K for all the  $T_{\text{sub}}$ . In contrast, thermal conductivity dictates the temperature of the following points. Most of the heat is transmitted through the cantilever at higher thermal conductivity and thus the temperature difference between two subsequent points is small and vice versa. For this reason, the lowest and highest  $\Delta T$  at 5.5 mm are 1.56 K and 3.52 K, which occurred at 20 K and 100 K, respectively. The experiments were repeated at least 5 times, and each experiment contained 200 readings at each point. The average of 5 experiments are shown as the square markers in Figure 6.3 while the standard deviation is shown as the error bar. The maximum deviation is within  $\pm 8\%$  of the average reading.

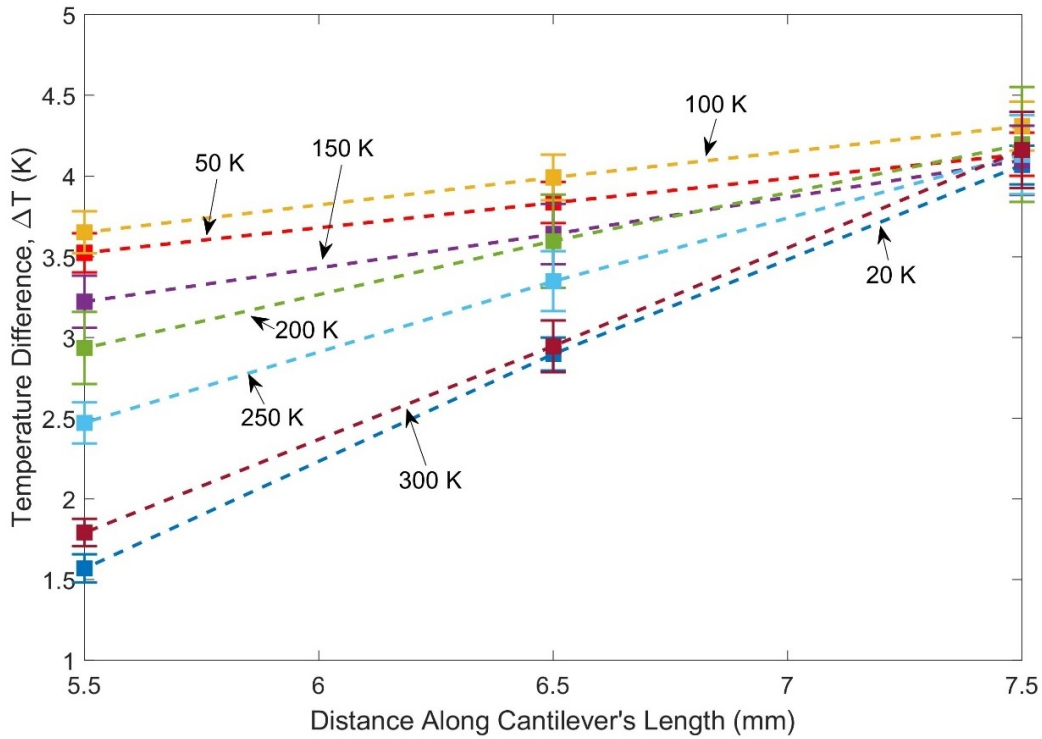


Figure 6.3 Experimentally measured temperature along  $2.03 \pm 0.09 \mu\text{m}$  thick cantilever. Dots represent the measured value while dashed line are the fitted curve. Experiments are done at 7 different temperatures from 20 K to 300 K.

The inverse slope of the curves, in Figure 6.3, indicates the thermal conductivity of the sample. Hence, steeper slope denotes a lower thermal conductivity and vice versa. This can be

observed from Figure 6.4. The sharpest slope at 20 K corresponds to 115.4 W/mK thermal conductivity while the relatively flat slope at 50 K corresponds to a thermal conductivity of 471.5 W/mK. The thermal conductivity gradually decreases from 437 W/mK to 121 W/mK with the change of temperature from 100 K to 300 K, respectively. Since, the standard deviation propagates from the temperature readings to the thermal conductivity, error bars here are within  $\pm 8\%$  as well.

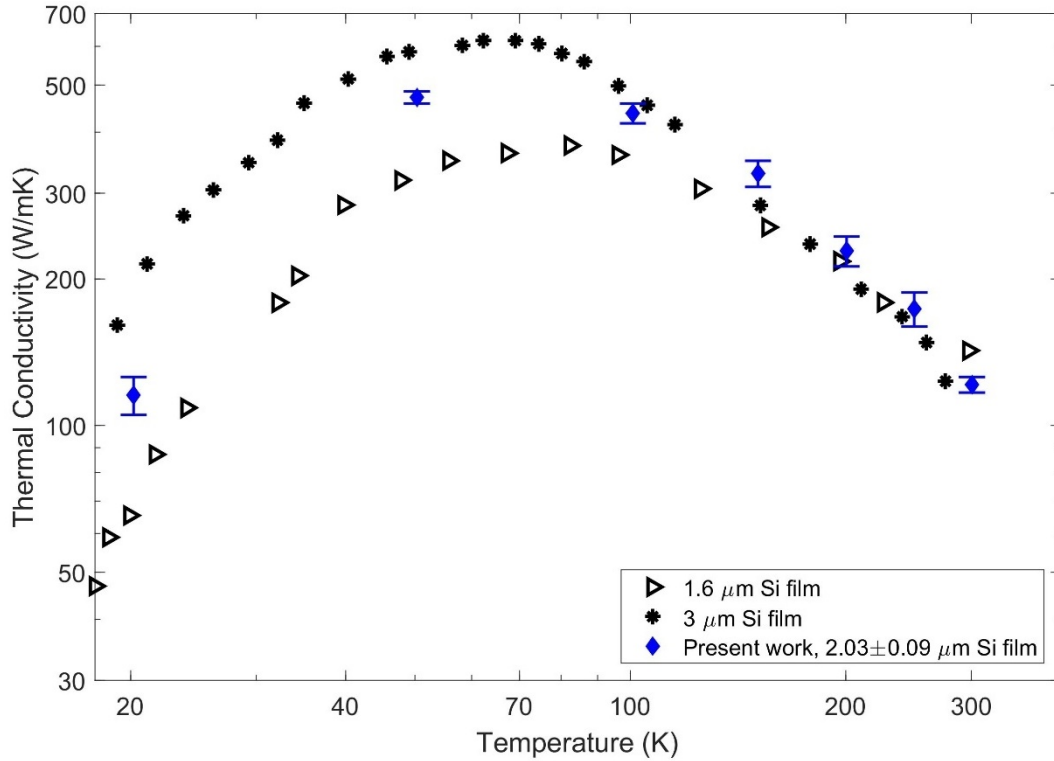


Figure 6.4 The thermal conductivity of 2 $\mu\text{m}$  sample changes with the temperature. Reference data is adopted from literature for 1.6  $\mu\text{m}$  silicon film[29] and 3  $\mu\text{m}$  silicon film[30].

The measured thermal conductivity of the silicon film is compared with the value reported by Asheghi et al. [29], [30] for {100} single crystal sample. These are two of the very first and highly cited reports of single crystal silicon film's thermal conductivity, and has been used as the reference for new technique development ever since [224]–[232]. Measured values notably agree with the reference. It is well known that heat conduction in the solid is phonon dominant even in

the presence of free charge carriers.[29] More phonons scatter from the boundary with the reduction of size in thin films. Therefore, thermal conductivity reduces in the thinner films and can be noticed readily from Figure 6.4. In addition, the mean free path (MFP) of phonons varies with temperature change, and phonons with large MFP scatter more than smaller MFP phonons [233]. The shift of thermal conductivity with temperature is regulated by this phonon characteristic.

Similar experiments were done for a  $2.93 \pm 0.06 \mu\text{m}$  thick silicon sample, and temperatures were measured at 3 points along the length of the cantilever. Results are presented in Figure 6.5. Temperature at the tip was around 3.1 K and varied according to the thermal conductivity in the subsequent points.

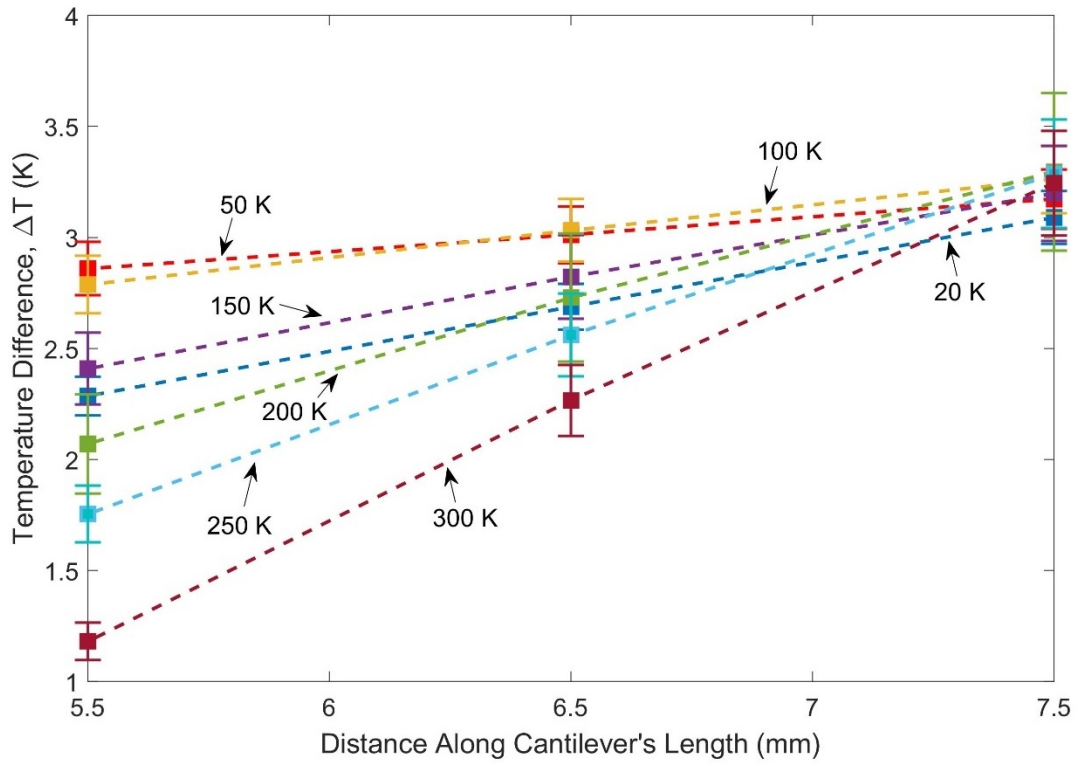


Figure 6.5 Change of temperature along cantilever's length for  $2.93 \pm 0.06 \mu\text{m}$  thick silicon sample. Measurement are done in the temperature range of 20 K to 300 K.



As mentioned above, the slope of the curves in Figure 6.5 represents thermal conductivity. The sample is p-type doped with doping concentration varying from  $10^{13}$ - $10^{15}$   $\text{cm}^{-3}$ . Results obtained from this work compare with the data similar from the literature. It is important to mention that doping changes the thermal conductivity of silicon since the scattering of phonons on the dopant atoms in the lattice decreases the effective conductivity of the phonon. In addition, the scattering on free electrons associated with dopant atoms can significantly reduce the conductivity of phonons at low temperatures below the normal thermal conductivity [10], [234]. For this reason, the thermal conductivity of heavily doped ( $>10^{17}$   $\text{cm}^{-3}$ ) silicon film is lower than lightly doped silicon film (present work) values for all temperatures below 300 K. Thermal conductivity of the bulk silicon, on the other hand, is much higher at below 100 K temperature, attribute to the high phonon MFP and low scattering.

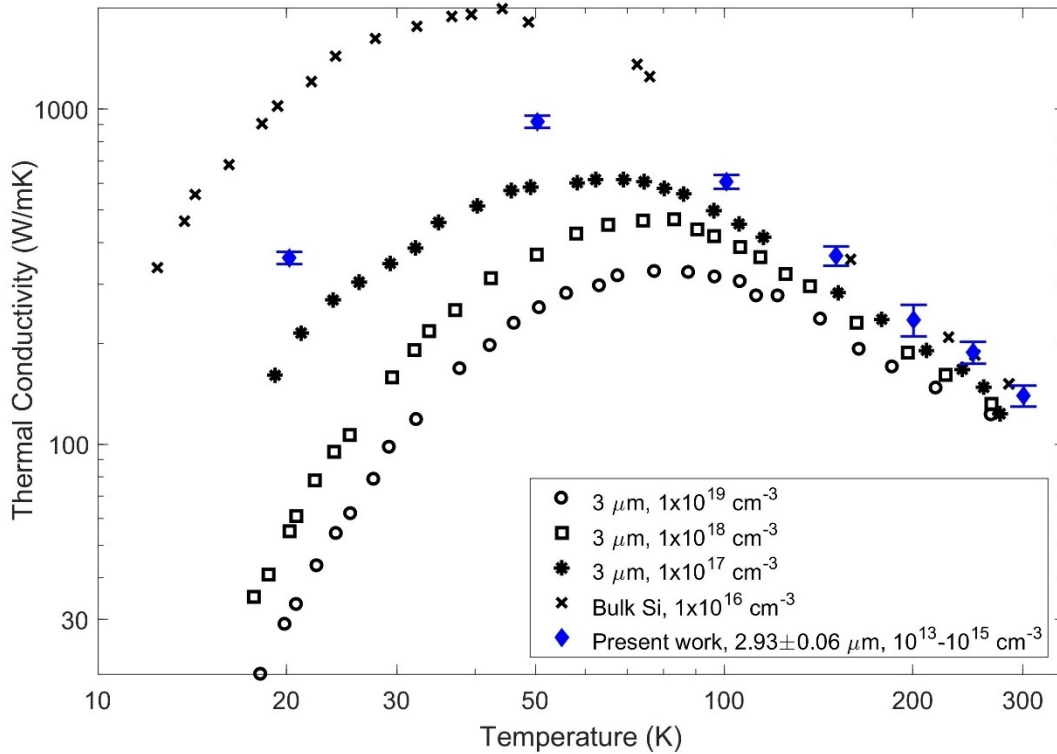


Figure 6.6 Thermal conductivity change of 3  $\mu\text{m}$  sample with temperature. Reference data are for {100} single crystal and comes from literature for 3  $\mu\text{m}$  doped Si [30] and bulk Si [14].

## Chapter 7 - Conclusion and Future Work

A new thermoreflectance technique is presented in this dissertation which is used to analyze the thermal conductivity of suspended thin films. This technique, termed Suspended ThermoReflectance (STR), is a significant improvement over other pump-probe based thermoreflectance techniques. The limiting characteristics of most of these techniques are that they can probe the temperature at only one spot on the sample, assume a value for either heat capacity or thermal conductivity to find the other, require a metal layer to absorb the laser flux and can report thermal properties of only the top few nanometers of the surface due to low penetration depth of pulsed lasers. On the contrary, STR reports thermal conductivity of the full sample without assuming heat capacity and without using any absorber metal layer. Measurements are conducted by probing multiple points along the length of a suspended micro/nano-scale sample. This technique involves a pump laser for heating the tip of a suspended Si  $\mu$ -cantilever and a probe laser to scan the temperature along the  $\mu$ -cantilever's length. Thermal conductivity is obtained by applying the heat diffusion equation for the temperature gradient along the cantilever length. Thermal conductivity of 2  $\mu\text{m}$  and 3  $\mu\text{m}$  thin silicon film is measured using the technique. The cantilever's tip temperature was around 3 K and 4 K for these two samples. The temperature gradient changes based on the thermal conductivity. For both samples, thermal conductivity was high for the temperature range of 50 K -100 K and decreased gradually after 100 K till reaching room temperature. Measured thermal conductivity concurs remarkably with the literature values. The experimentally measured thermoreflectance coefficient of silicon at 980 nm wavelength was reported for the first time. The coefficient is  $\sim 10^{-4} \text{ K}^{-1}$  over the temperature range mentioned in this dissertation.

An analytical model was developed to check the diffusion equation's applicability and analyze the experimental data of STR. The analytical solution was compared with a 3D Finite Element Model for Si. Temperature difference between the models is higher for the lower length to width ratios. This indicates that a micro/nano-cantilever beam, with length comparable to width, acts like a three-dimensional object and 1D model cannot predict its properties properly. However, as the length to width ratio increases, specifically for  $L/w > 20$ , the difference becomes smaller than 4%. Beyond  $L/w$  of 30 a three-dimensional cantilever acts like a one-dimensional object (around 2% difference). This finding is highly important as it allows analysis of the thermal conductivity of material using the simple closed form temperature equation instead of requiring the use of complex 3D models and finite element simulation.

## **7.1 Suggestions for Future work**

The Suspended ThermoReflectance (STR) is a versatile measurement technique. This technique can be applied to several thermal studies including the following.

### **1. Thermal boundary conductance Measurement**

Application of bare silicon in the semiconductor industry is very rare. Often silicon is coated with metals in microprocessors, transistors and semiconductor detectors [235]. Thermal boundary conductance (TBC) between the metal and silicon is, therefore, of tremendous interest in the MEMS industry. TBC is measured currently using pulsed laser in frequency domain thermoreflectance (FDTR) and time domain thermoreflectance (TDTR). Sometimes thermal boundary conductance between metal and silicon is very low in comparison to the thermal conductivity of the silicon. As a result, a very small amount of heat is transferred from the metal film to the silicon and the heat dissipates as soon as it reaches the silicon due to its high thermal

conductivity and small pulse duration. This makes the measurement very difficult. Besides, TBC measurement for a thick metal layer is complicated because of low penetration depth.

On the other hand, STR uses continuous wave lasers which allows the full sample to be heated uniformly. Besides, pump and probe lasers are applied from opposite sides of the sample. This helps with the detection of any small amount of heat in the silicon layer transferred via low TBC. The measurement can be done in three simple steps as shown in Figure 7.1.

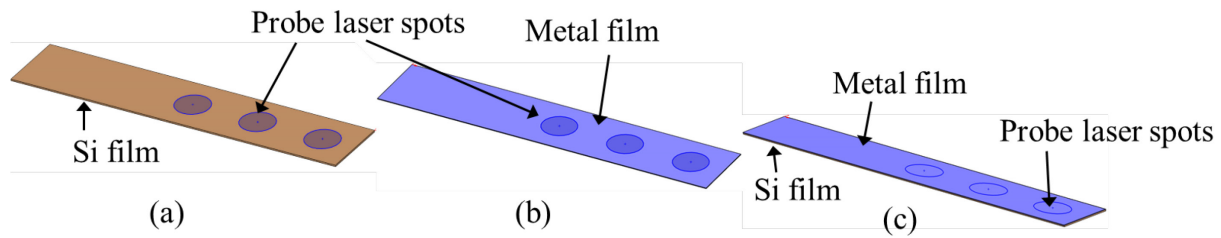


*Figure 7.1 Thermal boundary conductance measurement steps. Temperature measured a) only on Si, b) only on metal film, c) on Si + metal film*

Thermal conductivity of silicon and metal films will be measured in the first and second steps, respectively. In the third step, a metal film of same thickness will be deposited on the silicon film and thermal conductivity will be measured. Finally, It is necessary to develop an analytical model to extract Si and metal film conductivity from the final measurement to provide TBC.

## **2. Thermal conductivity of thin film with phononic crystals**

Thin film thermal conductivity decreases with reduced thickness due to phonon scattering from the boundary. In the thin film, defects can also be rendered to scatter more phonons and reduce thermal conductivity to a very low level. The defects can be square or circular holes or an array of the holes in thin film. This type of structure is interpreted as phononic crystals

(PNCs). The dimension of these structure is less than the phonon mean free path. As a result, PNCs work as phonon scatterers in the membrane. Such decrease in conductivity is particularly useful for thermoelectric applications where higher thermal to electrical conversion efficiency can be achieved by reducing thermal conductance. Figure 7.2 shows the PNCs fabricated in silicon.

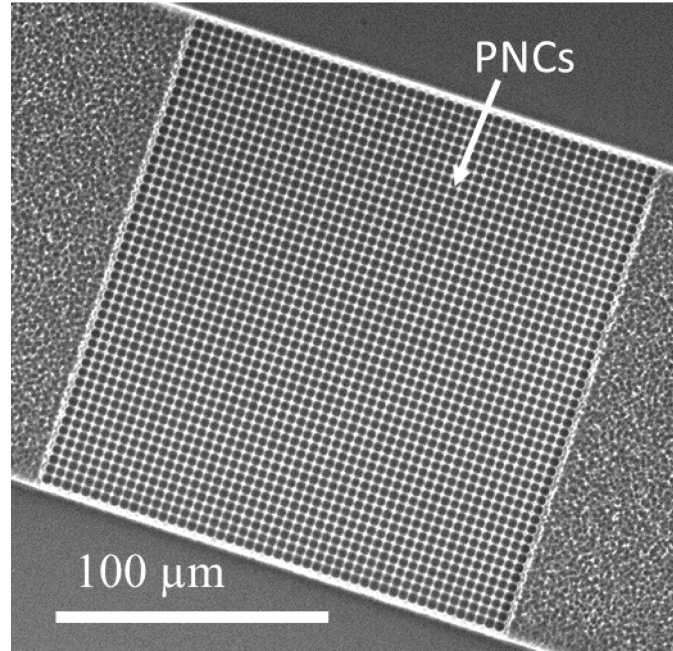


*Figure 7.2 Scanning electron microscope image of Phononic crystals fabricated in silicon.*

It is understandable that the probe laser will not be reflected if it is focused on PNCs. Therefore, PNCs will be fabricated in certain areas of the cantilever (10% - 50% area) instead of over the full cantilever and the solid region of cantilever will reflect the probe laser. Analytical models need to be developed based on first principles to analyze the thermal conductivity. Fourier equation-based models will not be applicable because heat does not transport continuously in these structures.

## List of Publications

### Journals Published and In-Progress

- **Dipta Sarkar**, J. Brady, L. Xu, M.G. Baboly, G. Singh and Z.C. Leseman. 1D Thermal Characterization of Micro /Nano-Cantilevers for Suspended ThermoReflectance Measurements. AIP Advances 9, no. 8 (2019): 085315.
- **Dipta Sarkar**, M.G. Baboly, M.M. Elahi, K. Abbas, J. Butner, D. Piñon, T.L. Ward, Tyler Hieber, Austin Schuberth and Zayd C. Leseman. Determination of etching parameters for pulsed XeF<sub>2</sub> etching of silicon using chamber pressure data. J. Micromechanics Microengineering 28, 45007 (2018).
- **Dipta Sarkar**, Z.C. Leseman and Gurpreet Singh. Suspended ThermoReflectance (STR) a novel technique to characterize thermal property of suspended thin films. Review of Scientific Instrument. (In progress)

### Peer Reviewed Conference Papers

- **Dipta Sarkar**, Samuel Oxandale, Tyler Hieber, M.G. Baboly and Zayd C. Leseman. Thermal Property Measurements of Si  $\mu$ -Cantilever Beams Using the Suspended Thermoreflectance Technique. In Proceedings of the International Mechanical Engineering Congress & Exposition, November 2019, Salt Lake City, Utah.
- **Dipta Sarkar**, Partha P. Chakraborty, B. Terry Beck and Zayd C. Leseman. Two-Dimensional Heat Transfer Considerations for Thermoreflectance Measurements. In Proceedings of the International Mechanical Engineering Congress & Exposition, November 2018, Pittsburgh, PA.
- **Dipta Sarkar**, Md. Sanaul Rabbi, J. U. Ahamed and M. A. Razzaq. Experimental Investigation of Thermoelectric Power Using Candlelight. In Proceedings of the International Conference on Mechanical Engineering and Renewable Energy November 2015, Chittagong, Bangladesh.
- Luke A Stegeman, Quentin Pease, Tyler J Hieber, **Dipta Sarkar**, Samuel W Oxandale, Steven L Bellinger, Zayd C Leseman, and Amir A Bahadori. Neutron Spectrum Unfolding with a Planar Miniaturized Fast-Neutron Detector. In Transactions of the American Nuclear Society, June 2019, Minneapolis, Minnesota.
- Samuel Oxandale, Luke Stegeman, Tyler Hieber, **Dipta Sarkar**, Steven L. Bellinger, Amir Bahadori, Zayd C. Leseman. Fabrication, Modeling, and Testing of a Miniaturized Fast Neutron Detector. In Proceedings of the International Mechanical Engineering Congress & Exposition, November 2019, Salt Lake City, Utah.

## References

- [1] P. E. Raad, P. L. Komarov, and M. G. Burzo, “Thermal characterization of embedded electronic features by an integrated system of CCD thermography and self-adaptive numerical modeling,” *Microelectronics J.*, vol. 39, no. 7, pp. 1008–1015, 2008.
- [2] K. E. Goodson, M. I. Flik, L. T. Su, and D. A. Antoniadis, “Prediction and Measurement of Temperature Fields in Silicon-on-Insulator Electronic Circuits,” *J. Heat Transf.*, vol. 117, pp. 574–581, 1995.
- [3] Semiconductor Industry Association, “International Technology Roadmap for Semiconductors,” *Executive Summery*, 2001. .
- [4] M. Farzaneh *et al.*, “CCD-based thermorefectance microscopy: principles and applications,” *J. Phys. D. Appl. Phys.*, vol. 42, no. 14, p. 143001, 2009.
- [5] S. M. Sze, *VLSI Technology*. New York: McGraw-Hill, 1988.
- [6] P. Peumans, A. Yakimov, and S. R. Forrest, “Small molecular weight organic thin-film photodetectors and solar cells,” *J. Appl. Phys.*, vol. 93, no. 7, pp. 3693–3723, 2003.
- [7] L. Jiang, M. Wong, and Y. Zohar, “Micromachined Polycrystalline Thin Film Temperature Sensors,” *Meas. Sci. Technol.*, vol. 10, pp. 653–664, 1999.
- [8] M. S. Dresselhaus *et al.*, “New directions for low-dimensional thermoelectric materials,” *Adv. Mater.*, vol. 19, no. 8, pp. 1043–1053, 2007.
- [9] D. Sarkar, M. S. Rabbi, J. U. Ahamed, and M. A. Razzaq, “Experimental Investigation of Thermoelectric Power Using Candlelight,” in *Proceedings of the International Conference on Mechanical Engineering and Renewable Energy*, 2015, vol. November, pp. ICMERE2015-PI-013.
- [10] K. Goodson and A. D. McConnell, “Thermal conduction in silicon micro-and nanostructures,” *Annu. Rev. heat Transf.*, vol. 14, no. 14, 2005.
- [11] M. Asheghi, M. N. Touzelbaev, K. E. Goodson, Y. K. Leung, and S. S. Wong, “Temperature-Dependent Thermal Conductivity of Single-Crystal Silicon Layers in SOI Substrates,” *J. Heat Transfer*, vol. 120, no. 1, pp. 30–36, 1998.
- [12] Y. S. Ju and K. E. Goodson, “Phonon scattering in silicon films with thickness of order 100 nm,” *Appl. Phys. Lett.*, vol. 74, no. 20, pp. 3005–3007, 1999.
- [13] A. J. Schmidt, R. Cheaito, and M. Chiesa, “A frequency-domain thermorefectance method for the characterization of thermal properties,” *Rev. Sci. Instrum.*, vol. 80, no. 9, p. 094901, 2009.

- [14] G. A. Slack, “Thermal conductivity of pure and impure silicon, silicon carbide, and diamond,” *J. Appl. Phys.*, 1964.
- [15] M. G. Holland and L. J. Neuringer, “The Effect of Impurities on the Lattice Thermal Conductivity of Silicon,” in *Proceeding of International Conference on Physics of Semiconductors, Institute of Physics and the Physical Society of London*, 1962, pp. 474–481.
- [16] R. L. Hamilton and O. K. Crosser, “Thermal conductivity of heterogeneous two-component systems,” *Ind. Eng. Chem. Fundam.*, vol. 1, no. 3, pp. 187–191, 1962.
- [17] R. C. Zeller and R. O. Pohl, “Thermal conductivity and specific heat of noncrystalline solids,” *Phys. Rev. B*, vol. 4, no. 6, pp. 2029–2041, 1971.
- [18] M. G. Cooper, B. B. Mikic, and M. M. Yovanovich, “Thermal contact conductance,” *Int. J. Heat Mass Transf.*, vol. 12, no. 3, pp. 279–300, 1969.
- [19] Y. S. Touloukian, R. W. Powell, C. Y. Ho, and P. G. Klemens, “Thermal Conductivity of Metallic Elements and Alloys,” *IFI/Plenum*, vol. 1, no. New York, 1970.
- [20] J. A. Carruthers, T. H. Geballe, H. M. Rosenberg, and J. M. Ziman, “The thermal conductivity of germanium and silicon between 2 and 300° K,” *Proc. R. Soc. Lond. A*, vol. 238, no. 1215, pp. 502–514, 1957.
- [21] M. G. Holland, “Proceedings of the International Conference on Semiconductor Physics, Prague, 1960,” in *Academic Press*, 1962, p. 633.
- [22] J. C. Thompson and B. A. Younglove, “Thermal conductivity of silicon at low temperatures,” *J. Phys. Chem. Solids*, vol. 20, no. 1–2, pp. 146–149, 1961.
- [23] H. M. Rosenberg, “Thermal conductivity of germanium and silicon at low temperatures,” *Proc. Phys. Soc.*, vol. Section A, no. 9, p. 837, 1954.
- [24] A. V. Inyushkin, A. N. Taldenkov, A. M. Gibin, A. V. Gusev, and H. J. Pohl, “On the isotope effect in thermal conductivity of silicon,” *Phys. Status Solidi C*, vol. 1, no. 11, pp. 2995–2998, 2004.
- [25] P. Jiang, X. Qian, and R. Yang, “Tutorial: Time-domain thermoreflectance (TDTR) for thermal property characterization of bulk and thin film materials,” *J. Appl. Phys.*, vol. 124, no. 16, pp. 1–82, 2018.
- [26] D. G. Cahill, K. Goodson, and A. Majumdar, “Thermometry and Thermal Transport in Micro/Nanoscale Solid-State Devices and Structures,” *J. Heat Transfer*, vol. 124, no. 2, p. 223, 2002.
- [27] K. E. Goodson and M. I. Flik, “Solid Layer Thermal-Conductivity Measurement



- Techniques,” *Appl. Mech. Rev.*, vol. 47, no. 3, p. 101, 2009.
- [28] T. M. Tritt and D. Weston, “Measurement techniques and considerations for determining thermal conductivity of bulk materials,” in *Thermal Conductivity*, Springer, 2004, pp. 187–203.
  - [29] M. Asheghi, M. N. Touzelbaev, K. E. Goodson, Y. K. Leung, and S. S. Wong, “Temperature-Dependent Thermal Conductivity of Single-Crystal Silicon Layers in SOI Substrates,” *J. Heat Transfer*, vol. 120, no. 1, p. 30, 1998.
  - [30] M. Asheghi, K. Kurabayashi, R. Kasnavi, and K. E. Goodson, “Thermal conduction in doped single-crystal silicon films,” *J. Appl. ...*, vol. 5079, no. 2002, 2002.
  - [31] M. Asheghi, Y. K. Leung, S. S. Wong, and K. E. Goodson, “Phonon-boundary scattering in thin silicon layers,” *Appl. Phys. Lett.*, vol. 71, no. 13, pp. 1798–1800, 1997.
  - [32] X. Y. Zheng, S. Z. Li, M. Chen, and K. L. Wang, “Giant Reduction in Lateral Thermal Conductivity of Thin Nitride/Silicon/Oxide Membrane Measured with a Suspended Micro Structure,” *Micro-Electro-Mechanical Syst. Microscale Therm. Phenom. Electron. Syst. Proc. ASME Int. Mech. Eng. Congr. Expo.*, pp. 93–98, 1996.
  - [33] M. VonArx, O. Paul, and H. Baltes, “Process-Dependent Thin-Film Thermal Conductivities for Thermal CMOS MEMS,” *J. Microelectromech. Syst.*, vol. 9, no. 1, pp. 136–145, 2000.
  - [34] F. Völklein and H. Baltes, “A Microstructure for Measurement of Thermal Conductivity of Polysilicon Thin Films,” *J. Microelectromechanical Syst.*, 1992.
  - [35] O. Paul and H. Baltes, “Thermal conductivity of CMOS materials for the optimization of microsensors,” *J. Micromechanics Microengineering*, 1993.
  - [36] O. M. Paul, J. Korvink, and H. Baltes, “Determination of the thermal conductivity of CMOS IC polysilicon,” *Sensors Actuators A. Phys.*, 1994.
  - [37] O. Paul, M. von Arx, and H. Baltes, “Process-dependent Thermophysical Properties Of CMOS IC Thin Films,” 2005.
  - [38] Y. C. Tai, C. H. Mastrangelo, and R. S. Muller, “Thermal conductivity of heavily doped LPCVD polysilicon,” 2008.
  - [39] Y. C. Tai, C. H. Mastrangelo, and R. S. Muller, “Thermal conductivity of heavily doped low-pressure chemical vapor deposited polycrystalline silicon films,” *J. Appl. Phys.*, vol. 63, no. 5, pp. 1442–1447, 1988.
  - [40] A. D. McConnell, S. Uma, and K. E. Goodson, “Thermal conductivity of doped polysilicon layers,” *J. Microelectromechanical Syst.*, vol. 10, no. 3, pp. 360–369, 2001.

- [41] A. Irace and P. M. Sarro, "Measurement of thermal conductivity and diffusivity of single and multilayer membranes," *Sensors Actuators, A Phys.*, 1999.
- [42] D. G. Cahill, H. E. Fischer, T. Klitsner, E. T. Swartz, and R. O. Pohl, "Thermal conductivity of thin films: Measurements and understanding," *J. Vac. Sci. Technol. A Vacuum, Surfaces, Film.*, vol. 7, no. 3, pp. 1259–1266, 2002.
- [43] K. E. Goodson, M. I. Flik, L. T. Su, and D. A. Antoniadis, "Prediction and measurement of the thermal conductivity of amorphous dielectric layers," *J. Heat Transfer*, vol. 116, no. 2, pp. 317–324, 1994.
- [44] T. Borca-Tasciuc and G. Chen, "Experimental Techniques for Thin- Film Thermal Conductivity Characterization," *Therm. Conduct.*, no. Springer, Boston, MA, pp. 205–237, 2004.
- [45] D. Zhao, X. Qian, X. Gu, S. A. Jajja, and R. Yang, "Measurement Techniques for Thermal Conductivity and Interfacial Thermal Conductance of Bulk and Thin Film Materials," *J. Electron. Packag.*, vol. 138, no. 4, p. 040802, 2016.
- [46] D. G. Cahill, "Thermal conductivity measurement from 30 to 750 K: The  $3\omega$  method," *Rev. Sci. Instrum.*, vol. 61, pp. 802–808, 1990.
- [47] B. Yang, W. L. Liu, J. L. Liu, K. L. Wang, and G. Chen, "Measurements of anisotropic thermoelectric properties in superlattices," *Appl. Phys. Lett.*, 2002.
- [48] K. Kurabayashi, M. Asheghi, M. Touzelbaev, and K. E. Goodson, "Measurement of the thermal conductivity anisotropy in polyimide films," *J. Microelectromechanical Syst.*, 1999.
- [49] Y. S. Ju, K. Kurabayashi, and K. E. Goodson, "Thermal characterization of anisotropic thin dielectric films using harmonic Joule heating," *Thin Solid Films*, 1999.
- [50] B. Yang, J. L. Liu, K. L. Wang, and G. Chen, "Simultaneous measurements of Seebeck coefficient and thermal conductivity across superlattice," *Appl. Phys. Lett.*, 2002.
- [51] R. Chhabra, *CRC handbook of thermal engineering*. 2017.
- [52] P. E. Raad, "Thermo-Reflectance Thermography For Submicron Temperature Measurements," *Electron. Cool.*, vol. 14, no. 1, 2008.
- [53] M. N. Touzelbaev, P. Zhou, R. Venkatasubramanian, and K. E. Goodson, "Thermal characterization of Bi<sub>2</sub>Te<sub>3</sub>/Sb<sub>2</sub>Te<sub>3</sub> superlattices," *J. Appl. Phys.*, vol. 90, no. 2, pp. 763–767, 2001.
- [54] P. M. Norris, J. L. Smoyer, J. C. Duda, and P. E. Hopkins, "Prediction and Measurement of Thermal Transport Across Interfaces Between Isotropic Solids and Graphitic

- Materials,” *J. Heat Transfer*, vol. 134, no. 2, p. 020910, 2012.
- [55] D. Sarkar, P. P. Chakraborty, B. T. Beck, and Z. C. Leseman, “Two-Dimensional Heat Transfer Considerations for Thermoreflectance Measurements,” in *ASME 2018 International Mechanical Engineering Congress and Exposition*, 2018, p. V08BT10A013-V08BT10A013.
  - [56] L. Wei, M. Vaudin, C. S. Hwang, G. White, J. Xu, and A. J. Steckl, “Heat conduction in silicon thin films: Effect of microstructure,” *J. Mater. Res.*, vol. 10, no. 8, pp. 1889–1896, 1995.
  - [57] C. A. Paddock and G. L. Eesley, “Transient thermoreflectance from thin metal films Transient thermoreflectance from thin,” *J. Appl. Phys.*, vol. 60, no. 1, pp. 285–290, 1986.
  - [58] P. E. Hopkins, L. M. Phinney, and J. R. Serrano, “Re-examining Electron-Fermi Relaxation in Gold Films With a Nonlinear Thermoreflectance Model,” *J. Heat Transfer*, vol. 133, no. 4, p. 044505, 2011.
  - [59] K. E. Goodson, O. W. Käding, M. Rösler, and R. Zachai, “Experimental investigation of thermal conduction normal to diamond-silicon boundaries,” *J. Appl. Phys.*, vol. 77, no. 4, pp. 1385–1392, 1995.
  - [60] T. Favaloro, J. H. Bahk, and A. Shakouri, “Characterization of the temperature dependence of the thermoreflectance coefficient for conductive thin films,” *Rev. Sci. Instrum.*, vol. 86, no. 2, p. 024903, 2015.
  - [61] R. B. Wilson, B. A. Apgar, L. W. Martin, and D. G. Cahill, “Thermoreflectance of metal transducers for optical pump-probe studies of thermal properties,” *Opt. Express*, vol. 20, no. 27, pp. 28829–28838, 2012.
  - [62] D. G. Cahill, “Analysis of heat flow in layered structures for time-domain thermoreflectance,” *Rev. Sci. Instrum.*, vol. 75, no. 12, pp. 5119–5122, 2004.
  - [63] R. Cheaito, C. S. Gorham, A. Misra, K. Hattar, and P. E. Hopkins, “Thermal conductivity measurements via time-domain thermoreflectance for the characterization of radiation induced damage,” *J. Mater. Res.*, vol. 30, no. 9, pp. 1403–1412, 2015.
  - [64] D. G. Cahill *et al.*, “Nanoscale thermal transport. II. 2003–2012,” *Appl. Phys. Rev.*, vol. 1, no. 1, p. 11305, Mar. 2014.
  - [65] P. Jiang, X. Qian, and R. Yang, “Tutorial: Time-domain thermoreflectance (TDTR) for thermal property characterization of bulk and thin film materials,” *J. Appl. Phys.*, vol. 124, no. 16, 2018.
  - [66] W. S. Capinski and H. J. Maris, “Improved apparatus for picosecond pump-and-probe optical measurements,” *Rev. Sci. Instrum.*, vol. 67, no. 8, pp. 2720–2726, 1996.

- [67] D. G. Cahill *et al.*, “Nanoscale thermal transport,” *J. Appl. Phys.*, vol. 93, no. 2, pp. 793–818, 2003.
- [68] K. Kang, Y. K. Koh, C. Chiritescu, X. Zheng, and D. G. Cahill, “Two-tint pump-probe measurements using a femtosecond laser oscillator and sharp-edged optical filters,” *Rev. Sci. Instrum.*, vol. 79, no. 11, 2008.
- [69] J. Zhu, D. Tang, W. Wang, J. Liu, K. W. Holub, and R. Yang, “Ultrafast thermoreflectance techniques for measuring thermal conductivity and interface thermal conductance of thin films,” *J. Appl. Phys.*, vol. 108, no. 9, p. 94315, 2010.
- [70] C. Wei, X. Zheng, D. G. Cahill, and J.-C. Zhao, “Invited article: micron resolution spatially resolved measurement of heat capacity using dual-frequency time-domain thermoreflectance,” *Rev. Sci. Instrum.*, vol. 84, no. 7, p. 71301, Jul. 2013.
- [71] B. Sun and Y. K. Koh, “Understanding and eliminating artifact signals from diffusely scattered pump beam in measurements of rough samples by time-domain thermoreflectance (TDTR),” *Rev. Sci. Instrum.*, 2016.
- [72] L. S. Larkin, J. L. Smoyer, and P. M. Norris, “Laser repetition rate in time-domain thermoreflectance techniques,” *Int. J. Heat Mass Transf.*, 2017.
- [73] A. J. Schmidt, “Optical Characterization of Thermal Transport from the Nanoscale to the Macroscale,” *Doctoral dissertation, Massachusetts Institute of Technology*, 2008. .
- [74] S. Dilhaire, G. Pernot, G. Calbris, J. M. Rampnoux, and S. Grauby, “Heterodyne picosecond thermoreflectance applied to nanoscale thermal metrology,” *J. Appl. Phys.*, 2011.
- [75] Q. D’Acremont *et al.*, “High-throughput heterodyne thermoreflectance: Application to thermal conductivity measurements of a Fe-Si-Ge thin film alloy library,” *Rev. Sci. Instrum.*, 2017.
- [76] A. J. Schmidt, X. Chen, and G. Chen, “Pulse accumulation , radial heat conduction , and anisotropic thermal conductivity in pump-probe transient thermoreflectance,” *Rev. Sci. Instrum.*, vol. 79, no. 11, p. 114902, 2008.
- [77] P. M. Norris, A. P. Caffrey, R. J. Stevens, J. M. Klopff, J. T. McLeskey, and A. N. Smith, “Femtosecond pump-probe nondestructive examination of materials (invited),” *Rev. Sci. Instrum.*, vol. 74, no. 1 II, pp. 400–406, 2003.
- [78] A. Schmidt, M. Chiesa, X. Chen, and G. Chen, “An optical pump-probe technique for measuring the thermal conductivity of liquids,” *Rev. Sci. Instrum.*, vol. 79, no. 6, p. 64902, 2008.
- [79] J. L. Braun and P. E. Hopkins, “Upper limit to the thermal penetration depth during

- modulated heating of multilayer thin films with pulsed and continuous wave lasers: A numerical study,” *J. Appl. Phys.*, vol. 121, no. 17, 2017.
- [80] A. J. Schmidt, R. Cheaito, and M. Chiesa, “Characterization of thin metal films via frequency-domain thermoreflectance,” *J. Appl. Phys.*, vol. 107, no. 2, p. 24908, 2010.
  - [81] J. Epstein, W.-L. Ong, C. J. Bettinger, and J. A. Malen, “Temperature Dependent Thermal Conductivity and Thermal Interface Resistance of Pentacene Thin Films with Varying Morphology,” *ACS Appl. Mater. Interfaces*, vol. 8, no. 29, pp. 19168–19174, Jul. 2016.
  - [82] K. B. Myers, P. R. Gaddam, X. Ding, V. Kochergin, S. T. Huxtable, and H. D. Robinson, “Measuring Thermal Conductivity with Magnitude-Dependent Frequency–Domain Thermoreflectance Using Modulated CW Lasers,” *Int. J. Thermophys.*, vol. 39, no. 12, Dec. 2018.
  - [83] J. A. Malen, K. Baheti, T. Tong, Y. Zhao, J. A. Hudgings, and A. Majumdar, “Optical Measurement of Thermal Conductivity Using Fiber Aligned Frequency Domain Thermoreflectance,” *J. Heat Transfer*, vol. 133, no. 8, p. 081601, 2011.
  - [84] X. Y. Yu, L. Zhang, and G. Chen, “Thermal-wave measurement of thin-film thermal diffusivity with different laser beam configurations,” *Rev. Sci. Instrum.*, 1996.
  - [85] P. G. Sverdrup, S. Sinha, M. Asheghi, S. Uma, and K. E. Goodson, “Measurement of ballistic phonon conduction near hotspots in silicon,” *Appl. Phys. Lett.*, 2001.
  - [86] M. S. Aubain and P. R. Bandaru, “Determination of diminished thermal conductivity in silicon thin films using scanning thermoreflectance thermometry,” *Appl. Phys. Lett.*, 2010.
  - [87] M. S. Aubain and P. R. Bandaru, “In-plane thermal conductivity determination through thermoreflectance analysis and measurements,” *J. Appl. Phys.*, 2011.
  - [88] R. Anufriev, J. Maire, and M. Nomura, “Reduction of thermal conductivity by surface scattering of phonons in periodic silicon nanostructures,” *Phys. Rev. B*, vol. 93, no. 4, pp. 1–6, 2016.
  - [89] L. Wang, R. Cheaito, J. L. Braun, A. Giri, and P. E. Hopkins, “Thermal conductivity measurements of non-metals via combined time- and frequency-domain thermoreflectance without a metal film transducer,” *Rev. Sci. Instrum.*, vol. 87, no. 9, 2016.
  - [90] M. Li, J. S. Kang, and Y. Hu, “Anisotropic thermal conductivity measurement using a new Asymmetric-Beam Time-Domain Thermoreflectance (AB-TDTR) method,” *Rev. Sci. Instrum.*, vol. 89, no. 8, 2018.
  - [91] C. Mastrangelo, R. M.-S. and Materials, and U. 1988, “Thermal diffusivity of heavily doped low pressure chemical vapor deposited polycrystalline silicon films,” *Sensors Mater.*, vol. 3, pp. 133-142., 1988.

- [92] “Thermal conductivities of thin, sputtered optical films,” *Appl. Opt.*, vol. 32, no. 1, pp. 91–101, 1993.
- [93] S. Graham, B. Olson, C. Wong, and E. Piekos, “The Effects of Processing Conditions on the Thermal Conductivity of Polycrystalline Silicon Films,” 2008.
- [94] T. Shiga, M. Isogawa, J. Shiomi, T. Oyake, L. Feng, and Y. Nakamura, “Ultimate Confinement of Phonon Propagation in Silicon Nanocrystalline Structure,” *Phys. Rev. Lett.*, vol. 120, no. 4, p. 45901, 2018.
- [95] D. Sarkar, S. W. Oxandale, T. J. Hieber, M. G. Baboly, and Z. Leseman, “Thermal property measurements of si  $\mu$ -cantilever beams using the suspended thermoreflectance technique,” in *Proceedings of the ASME-2019 International Mechanical Engineering Congress & Exposition*, 2019, pp. IMECE2019-11690.
- [96] M. M. Elahi, M. G. Baboly, and Z. C. Leseman, “1-D Thermoreflectance Measurement Technique for Freestanding Micro/Nano Cantilever Beams,” in *ASME 2016 International Mechanical Engineering Congress and Exposition*, 2016, p. V008T10A022-V008T10A022.
- [97] E. Chávez, J. Cuffe, F. Alzina, and C. M. S. Torres, “Calculation of the specific heat in ultra-thin free-standing silicon membranes,” *J. Phys. Conf. Ser.*, vol. 395, p. 012105, 2012.
- [98] J. Hone, B. Batlogg, Z. Benes, A. T. Johnson, and J. E. Fischer, “Quantized phonon spectrum of single-wall carbon nanotubes,” *Science (80-. )*, vol. 289, no. 5485, pp. 1730–1733, Sep. 2000.
- [99] M. Mertig, G. Pompe, and E. Hegenbarth, “Specific heat of amorphous silicon at low temperatures,” *Solid State Commun.*, vol. 49, no. 4, pp. 369–372, 1984.
- [100] K. Park and C. Bayram, “Thermal resistance optimization of GaN/substrate stacks considering thermal boundary resistance and temperature-dependent thermal conductivity,” *Appl. Phys. Lett.*, vol. 109, no. 15, Oct. 2016.
- [101] J. L. Braun, C. J. Szwejkowski, A. Giri, and P. E. Hopkins, “On the steady-state temperature rise during laser heating of multilayer thin films in optical pump↓probe techniques,” *J. Heat Transfer*, vol. 140, no. 5, May 2018.
- [102] A. J. Schmidt, R. Cheaito, and M. Chiesa, “A frequency-domain thermoreflectance method for the characterization of thermal properties,” *Rev. Sci. Instrum.*, vol. 80, no. 9, 2009.
- [103] E. Matatagui, A. G. Thompson, and M. Cardona, “Thermoreflectance in Semiconductors,” *Phys. Rev.*, vol. 176, no. 3, pp. 950–960, Dec. 1968.

- [104] Baltz B, *Semiconductors and Semimetals*. Academic Press, 1972.
- [105] D. Pierścińska, “Thermoreflectance spectroscopy - Analysis of thermal processes in semiconductor lasers,” *J. Phys. D. Appl. Phys.*, vol. 51, no. 1, p. 013001, 2017.
- [106] R. Weil, “The Variation with Temperature of Metallic Reflectivity,” *Proc. Phys. Soc.*, vol. 60, no. 1, p. 8, 1948.
- [107] P. Yu and M. Cardona, *Fundamentals of semiconductors: physics and materials properties*. 2010.
- [108] G. Tessier, S. Hole, and D. Fournier, “Quantitative thermal imaging by synchronous thermoreflectance with optimized illumination wavelengths,” *Appl. Phys. Lett.*, vol. 78, no. 16, pp. 2267–2269, 2001.
- [109] C. L. Tien and G. Chen, “Challenges in Microscale Conductive and Radiative Heat Transfer,” *J. Heat Transfer*, vol. 116, no. 4, pp. 799–807, 1994.
- [110] M. I. Flik, B. I. Choi, and K. E. Goodson, “Heat Transfer Regimes in Microstructures,” *J. Heat Transfer*, vol. 114, no. 3, pp. 666–674, 1992.
- [111] A. Majumdar, “Microscale Heat Conduction in Dielectric Thin Films,” *J. Heat Transfer*, vol. 115, no. 1, pp. 7–16, 1993.
- [112] K. Ch’en, “Microscale thermal phenomena in optical and optoelectronic thin-film devices,” University of California, Berkeley, 1993.
- [113] S. I. Anisimov, B. L. Kapeliovich, and T. L. Perelman, “Electron emission from metal surfaces exposed to ultrashort laser pulses,” *J. Exp. Theor. Phys.*, vol. 66, no. 2, p. 776, 1974.
- [114] T. Yajima, K. Yoshihara, C. B. Harris, S. Shionoya, and Eds., “Ultrafast Phenomena VI,” *Springer-Verlag, Berlin*, 1988.
- [115] W. S. Fann, R. Storz, H. W. K. Tom, and J. Bokor, “Direct measurement of nonequilibrium electron-energy distributions in sub-picosecond laser-heated gold films,” *Phys. Rev. Lett.*, vol. 68, no. 18, p. 2834, 1992.
- [116] T. Q. Qiu and C. L. Tien, “Heat Transfer Mechanisms During Short-Pulse Laser Heating of Metals,” *J. Heat Transfer*, vol. 115, no. 4, pp. 835–841, 1993.
- [117] C. J. Glassbrenner and G. A. Slack, “Thermal conductivity of silicon and germanium from 3°K to the melting point,” *Phys. Rev.*, vol. 134, no. 4A, p. A1058, 1964.
- [118] S. Uma, A. D. McConnell, M. Asheghi, K. Kurabayashi, and K. E. Goodson, “Temperature-dependent thermal conductivity of undoped polycrystalline silicon layers,”

- Int. J. Thermophys.*, vol. 22, no. 2, pp. 605–616, 2001.
- [119] K. T. Regner, D. P. Sellan, Z. Su, C. H. Amon, A. J. H. McGaughey, and J. A. Malen, “Broadband phonon mean free path contributions to thermal conductivity measured using frequency domain thermoreflectance,” *Nat. Commun.*, vol. 4, no. March, pp. 1640–1647, 2013.
  - [120] J. Yang, E. Ziade, and A. J. Schmidt, “Modeling optical absorption for thermoreflectance measurements,” *J. Appl. Phys.*, vol. 119, no. 9, p. 095107, 2016.
  - [121] R. B. Wilson and D. G. Cahill, “Anisotropic failure of Fourier theory in time-domain thermoreflectance experiments,” *Nat. Commun.*, vol. 5, p. 5075, 2014.
  - [122] Y. K. Koh, “Heat transport by phonons in crystalline materials and nanostructures,” *Doctoral dissertation, University of Illinois*, 2011. .
  - [123] V. M. Glazov and A. S. Pashinkin, “The Thermophysical Properties ( Heat Capacity and Thermal Expansion ) of Single-Crystal Silicon,” *High Temp.*, vol. 39, no. 3, pp. 413–419, 2001.
  - [124] A. Smakula and V. Sils, “Precision density determination of large single crystals by hydrostatic weighing,” *Phys. Rev.*, vol. 99, no. 6, p. 1744, 1955.
  - [125] D. Sarkar, J. Brady, L. Xu, M. G. Baboly, and Z. C. Leseman, “1D Thermal Characterization of Micro/Nano-Cantilevers for Suspended ThermoReflectance Measurements,” *AIP Adv.*, vol. 9, no. 8, p. 085315, 2019.
  - [126] S. G. Volz and G. Chen, “Molecular-dynamics simulation of thermal conductivity of silicon crystals,” *Phys. Rev. B*, vol. 61, no. 4, pp. 2651–2656, 2000.
  - [127] E. Pop, “Energy dissipation and transport in nanoscale devices,” *Nano Res.*, vol. 3, no. 3, pp. 147–169, 2010.
  - [128] Thorlabs, “Operating Manual.” [Online]. Available: <https://www.thorlabs.com/>.
  - [129] Edmund Optics, “Simplifying Laser Alignment.” [Online]. Available: <https://www.edmundoptics.com>.
  - [130] Stanford Research Systems, “DSP Lock-In Amplifier SR830.” 2011.
  - [131] Thorlabs.com, “TCLDM9 Temperature controlled, laser diode mount for 5.6 and 9 mm LD.” 2015.
  - [132] I. B. A. Laboratory, “BNC Terminators,” *Indian Institute of Technology Kanpur*, 2018. .
  - [133] Thorlabs, “DET10A Si Biased Detector User.” 2017.



- [134] Z. C. Leseman, “A novel method for testing freestanding nanofilms using a custom MEMS load cell,” University of Illinois Urbana-Champaign, 2006.
- [135] J. Rogers, “Transient, interferometric imaging of polycrystalline silicon MEMS devices during laser heating,” *Microscale Thermophys. Eng.*, vol. 8, no. 1, pp. 43–59, 2004.
- [136] H. A. Macleod, *Thin-film optical filters*. CRC Press, 2010.
- [137] C. Schinke *et al.*, “Uncertainty analysis for the coefficient of band-to-band absorption of crystalline silicon,” *Aip Adv.*, vol. 5, no. 6, p. 67168, 2015.
- [138] M. R. Vogt, “Development of physical models for the simulation of optical properties of solar cell modules,” Technische Informationsbibliothek (TIB), 2016.
- [139] B. Tatian, “Fitting refractive-index data with the Sellmeier dispersion formula,” *Appl. Opt.*, vol. 23, no. 24, pp. 4477–4485, Dec. 1984.
- [140] Thorlabs.com, “Laser Diode Selection Guide.” .
- [141] A. Kheyraddini Mousavi, “Characterization of Mechanical Properties at the Micro / Nano Scale : Stiction Failure of MEMS , High-Frequency Michelson Interferometry and Carbon NanoFibers,” 2015.
- [142] Advanced Research System, “CS204-DMX-20,” 2019. [Online]. Available: <https://www.arscryo.com/cs204-dmx-20>.
- [143] Wikipedia contributors, “List of thermal conductivities,” *Wikipedia, The Free Encyclopedia*, 2019. [Online]. Available: [https://en.wikipedia.org/w/index.php?title=List\\_of\\_thermal\\_conductivities&oldid=916841762](https://en.wikipedia.org/w/index.php?title=List_of_thermal_conductivities&oldid=916841762).
- [144] Y. S. Touloukian, R. W. Powell, C. Y. Ho, and P. G. Klemens, “Thermophysical properties of matter-the tprc data series. volume 1. thermal conductivity-metallic elements and alloys,” 1970.
- [145] Harland G. Tompkins, *The Fundamentals of Vacuum Technology*. 1997.
- [146] ARS Cryo, “Closed Cycle Cryocooler Principles of Operation.” [Online]. Available: <https://www.arscryo.com/cryocooler-principles-of-operation>.
- [147] S. Y. Lien *et al.*, “Fabrication and chracterization silicon thin film solar cells deposited by HF-PECVD,” *Conf. Rec. IEEE Photovolt. Spec. Conf.*, pp. 1545–1548, 2010.
- [148] S. L. Holl, C. A. Colinge, S. Song, R. Varasala, K. Hobart, and F. Kub, “Fabrication techniques for thin-film silicon layer transfer,” *ECS Trans.*, vol. 3, no. 6, pp. 67–73, 2006.

- [149] S. C. Wang, C. F. Yeh, C. T. Hsu, and J. C. Lou, "Fabricating thin-film transistors on plastic substrates using spin etching and device transfer," *J. Electrochem. Soc.*, vol. 152, no. 3, pp. 227–233, 2005.
- [150] H. Muraoka, M. Asano, and T. Ohashi, "Method of etching a semiconductor substrate." U.S. Patent 4,172,005."
- [151] O. Tabata, "Anisotropic etching of silicon in TMAH solutions," *Sensors Mater.*, vol. 13, no. 5, pp. 271–283, 2001.
- [152] S. Oxandale *et al.*, "Fabrication, Modeling, and Testing of a Miniaturized Fast Neutron Detector," in *Proceedings of the International Mechanical Engineering Congress & Exposition*, 2019, pp. IMECE2019-11534.
- [153] T. S. Monteiro, P. Kastytis, L. M. Gonçalves, G. Minas, and S. Cardoso, "Dynamic wet etching of silicon through isopropanol alcohol evaporation," *Micromachines*, vol. 6, no. 10, pp. 1534–1545, 2015.
- [154] H. Seidel, L. Csepregi, A. Heuberger, and H. Baumgörtel, "Anisotropic Etching of Crystalline Silicon in Alkaline Solutions: I. Orientation Dependence and Behavior of Passivation Layers," *J. Electrochem. Soc.*, vol. 137, no. 11, pp. 3612–3626, 1990.
- [155] X. Duan, "Microfabrication using bulk wet etching with TMAH," *Masters Abstr. Int.*, vol. 45, no. 4, p. 103, 2006.
- [156] V. Swarnalatha, A. V. Narasimha Rao, A. Ashok, S. S. Singh, and P. Pal, "Modified TMAH based etchant for improved etching characteristics on Si{1 0 0} wafer," *J. Micromechanics Microengineering*, vol. 27, no. 8, Jun. 2017.
- [157] M. A. Gosálvez, P. Pal, N. Ferrando, H. Hida, and K. Sato, "Experimental procurement of the complete 3D etch rate distribution of Si in anisotropic etchants based on vertically micromachined wagon wheel samples," *J. Micromechanics Microengineering*, vol. 21, no. 12, p. 125007, Dec. 2011.
- [158] P. Pal, K. Sato, M. A. Gosálvez, and M. Shikida, "Study of rounded concave and sharp edge convex corners undercutting in CMOS compatible anisotropic etchants," *J. Micromechanics Microengineering*, vol. 17, no. 11, pp. 2299–2307, Nov. 2007.
- [159] B. Tang *et al.*, "Ellipsometry study of the adsorbed surfactant thickness on Si{1 1 0} and Si{1 0 0} and the effect of pre-adsorbed surfactant layer on etching characteristics in TMAH," *Sensors Actuators, A Phys.*, vol. 156, no. 2, pp. 334–341, Dec. 2009.
- [160] Y. W. Xu, A. Michael, and C. Y. Kwok, "Formation of ultra-smooth 45° micromirror on (1 0 0) silicon with low concentration TMAH and surfactant: Techniques for enlarging the truly 45° portion," *Sensors Actuators, A Phys.*, vol. 166, no. 1, pp. 164–171, Mar. 2011.

- [161] D. Cheng, M. A. Gosálvez, T. Hori, K. Sato, and M. Shikida, "Improvement in smoothness of anisotropically etched silicon surfaces: Effects of surfactant and TMAH concentrations," *Sensors Actuators, A Phys.*, vol. 125, no. 2, pp. 415–421, Jan. 2006.
- [162] P. M. Sarro, D. Brida, W. V.D. Vlist, and S. Brida, "Effect of surfactant on surface quality of silicon microstructures etched in saturated TMAHW solutions," *Sensors Actuators, A Phys.*, vol. 85, no. 1, pp. 340–345, Aug. 2000.
- [163] E. D. Palik, O. J. Glembocki, I. Heard, P. S. Burno, and L. Tenerz, "Etching roughness for (100) silicon surfaces in aqueous KOH," *J. Appl. Phys.*, vol. 70, no. 6, pp. 3291–3300, 1991.
- [164] P. Krause and E. Obermeier, "Etch rate and surface roughness of deep narrow U-grooves in (110)-oriented silicon," *J. Micromechanics Microengineering*, vol. 5, no. 2, pp. 112–114, 1995.
- [165] M. H. Yun, V. A. Burrows, and M. N. Kozicki, "Analysis of KOH etching of (100) silicon on insulator for the fabrication of nanoscale tips," *J. Vac. Sci. Technol. B Microelectron. Nanom. Struct.*, vol. 16, no. 5, pp. 2844–2848, 1998.
- [166] H. F. Winters and J. W. Coburn, "The etching of silicon with XeF<sub>2</sub> vapor," *Appl. Phys. Lett.*, vol. 34(1), no. 1 January, p. 70, 1979.
- [167] J. W. Coburn and H. F. Winters, "Ion- and electron-assisted gas-surface chemistry -An important effect in plasma etching," *J. Appl. Physics*, vol. 50(5), no. May, 1979.
- [168] M. Kojima, H. Kato, M. Gatto, S. Morinaga, and N. Ito, "Model for dry etching," *J. Appl. Phys.*, pp. 3–4, 1991.
- [169] T. J. Chuang, "Electron spectroscopy study of silicon surfaces exposed to XeF<sub>2</sub> and the chemisorption of SiF<sub>4</sub> on silicon," *J. Appl. Phys.*, vol. 51, no. 5, p. 2614, 1980.
- [170] D. Xu, B. Xiong, G. Wu, Y. Wang, X. Sun, and Y. Wang, "Isotropic Silicon Etching With XeF<sub>2</sub> Gas for Wafer-Level Micromachining Applications," *J. Microelectromechanical Syst.*, vol. 21, no. 6, pp. 1436–1444, 2012.
- [171] D. Sarkar *et al.*, "Determination of etching parameters for pulsed XeF<sub>2</sub> etching of silicon using chamber pressure data," *J. Micromechanics Microengineering*, vol. 28, no. 4, p. 045007, 2018.
- [172] R. C. Hefty, J. R. Holt, M. R. Tate, and S. T. Ceyer, "Mechanism and dynamics of the reaction of XeF<sub>2</sub> with fluorinated Si(100): possible role of gas phase dissociation of a surface reaction product in plasmaless etching," *J. Chem. Phys.*, vol. 130, no. 16, p. 164714, Apr. 2009.
- [173] R. Q. Zhang, Y. L. Zhao, and B. K. Teo, "Fluorination-induced back-bond weakening and

- hydrogen passivation on HF-etched Si surfaces,” *Phys. Rev. B - Condens. Matter Mater. Phys.*, vol. 69, no. 12, Mar. 2004.
- [174] Y. Morikawa *et al.*, “Reaction of the fluorine atom and molecule with the hydrogen-terminated Si(111) surface,” *J. Vac. Sci. Technol. A Vacuum, Surfaces, Film.*, vol. 16, no. 1, pp. 345–355, Jan. 1998.
  - [175] H. F. Winters, D. B. Graves, D. Humbird, and S. Tougaard, “Penetration of fluorine into the silicon lattice during exposure to F atoms, F<sub>2</sub>, and XeF<sub>2</sub>: Implications for spontaneous etching reactions,” *J. Vac. Sci. Technol. A Vacuum, Surfaces, Film.*, vol. 25, no. 1, pp. 96–103, Jan. 2007.
  - [176] A. A. E. Stevens, M. C. M. van de Sanden, H. C. W. Beijerinck, and W. M. M. Kessels, “Roughening during XeF<sub>2</sub> etching of Si(100) through interface layers: H:Si(100) and a-Si/Si(100),” *J. Vac. Sci. Technol. A Vacuum, Surfaces, Film.*, vol. 27, no. 2, pp. 367–375, 2009.
  - [177] A. A. E. Stevens and H. C. W. Beijerinck, “Surface roughness in XeF<sub>2</sub> etching of a-Si/c-Si(100),” *J. Vac. Sci. Technol. A Vacuum, Surfaces, Film.*, vol. 23, no. 1, pp. 126–136, 2005.
  - [178] J. Dabrowski and H.-J. Müssig, *Silicon Surfaces and Formation of Interfaces*. WORLD SCIENTIFIC, 2000.
  - [179] C. W. Lo, D. K. Shuh, V. Chakarian, T. D. Durbin, P. R. Varekamp, and J. A. Yarmoff, “XeF<sub>2</sub> etching of Si(111): The geometric structure of the reaction layer,” *Phys. Rev. B*, vol. 47, no. 23, pp. 15648–15659, 1993.
  - [180] P. B. Chu *et al.*, “Berkeley Sensor and Actuator Center , Department of EECS , Sample Preparation,” no. June, 1997.
  - [181] K. Sugano; O. Tabata, “Reduction of surface roughness and aperture size effect for etching of Si with XeF<sub>2</sub>,” *J. Micromechanics Microengineering*, vol. 12, pp. 911–916, 2002.
  - [182] P. Verdonck, P. B. Caliope, E. D. M. Hernandez, and A. N. R. da Silva, “Plasma etching of electrospun polymeric nanofibres,” *Thin Solid Films*, vol. 515, no. 2 SPEC. ISS., pp. 831–834, 2006.
  - [183] C. Cardinaud, M. C. Peignon, and P. Y. Tessier, “Plasma etching: Principles, mechanisms, application to micro- and nano-technologies,” *Appl. Surf. Sci.*, vol. 164, no. 1–4, pp. 72–83, 2000.
  - [184] J. H. Yao, K. R. Elder, H. Guo, and M. Grant, “Theory and simulation of Ostwald ripening,” *Phys. Rev. B*, vol. 47, no. 21, pp. 14110–14125, 1993.

- [185] J. T. Drotar, Y. Zhao, T. Lu, and G. Wang, "Mechanisms for plasma and reactive ion etch-front roughening," *Phys. Rev. B - Condens. Matter Mater. Phys.*, vol. 61, no. 4, pp. 3012–3021, 2000.
- [186] P. Brault, P. Dumas, and F. Salvan, "Roughness scaling of plasma-etched silicon surfaces," *Journal of Physics Condensed Matter*, vol. 10, no. 1. 12-Jan-1998.
- [187] M. Martin and G. Cunge, "Surface roughness generated by plasma etching processes of silicon," *J. Vac. Sci. Technol. B Microelectron. Nanom. Struct.*, vol. 26, no. 4, pp. 1281–1288, 2008.
- [188] Y. P. Zhao, J. T. Drotar, G. C. Wang, and T. M. Lu, "Roughening in plasma etch fronts of Si(100)," *Phys. Rev. Lett.*, vol. 82, no. 24, pp. 4882–4885, 1999.
- [189] M. Morita and T. Ohmi, "Characterization and control of native oxide on silicon," *Jpn. J. Appl. Phys.*, vol. 33, no. 1, pp. 370–374, 1994.
- [190] C. Bohling and W. Sigmund, "Self-Limitation of Native Oxides Explained," *Silicon*, vol. 8, no. 3, pp. 339–343, Jul. 2016.
- [191] M. Morita, T. Ohmi, E. Hasegawa, M. Kawakami, and M. Ohwada, "Growth of native oxide on a silicon surface," *J. Appl. Phys.*, vol. 68, no. 3, pp. 1272–1281, 1990.
- [192] J. Gass, H. H. Müller, H. Stüssi, and S. Schweitzer, "Oxygen diffusion in silicon and the influence of different dopants," *J. Appl. Phys.*, vol. 51, no. 4, pp. 2030–2037, 1980.
- [193] J. Blanc, "A revised model for the oxidation of Si by oxygen," *Appl. Phys. Lett.*, vol. 33, no. 5, pp. 424–426, 1978.
- [194] B. Laura Mauer, J. Taddei, S. Kroeger, and J. Clark Veeco, "Wafer thinning for advanced packaging applications."
- [195] F. Inoue *et al.*, "Characterization of Extreme Si Thinning Process for Wafer-to-Wafer Stacking," 2016.
- [196] M. Feil *et al.*, "Ultra thin ICs and MEMS elements: Techniques for wafer thinning, stress-free separation, assembly and interconnection," *Microsyst. Technol.*, vol. 9, no. 3, pp. 176–182, 2003.
- [197] G. Theses and P. B. Zantye, "Scholar Commons Processing, Reliability And Integration Issues In Chemical Mechanical Planarization," 2005.
- [198] S. N. Yusoh and K. A. Yaacob, "Effect of tetramethylammonium hydroxide/isopropyl alcohol wet etching on geometry and surface roughness of silicon nanowires fabricated by AFM lithography," *Beilstein J. Nanotechnol.*, vol. 7, no. 1, pp. 1461–1470, 2016.

- [199] P.-H. Chen, C.-M. Hsieh, H.-Y. Peng, and M. K. Chyu, "The characteristic behavior of TMAH water solution for anisotropic etching on both Silicon substrate and SiO<sub>2</sub> layer," *Micromach. Microfabr. Process Technol. VI*, vol. 4174, no. August, pp. 462–466, 2000.
- [200] S. An, S.-G. Lee, B.-H. O, H.-H. Kim, S.-G. Park, and E.-H. Lee, "The effect of KOH and KOH/IPA etching on the surface roughness of the silicon mold to be used for polymer waveguide imprinting," *Optoelectron. Integr. Circuits X*, vol. 6897, p. 689717, 2008.
- [201] F. Iacona, V. Raineri, F. La Via, and E. Rimini, "Roughness of thermal oxide layers grown on ion implanted silicon wafers," *J. Vac. Sci. Technol. B Microelectron. Nanom. Struct.*, vol. 16, no. 2, pp. 619–627, 1998.
- [202] H. E. Bennett and J. O. Porteus, "Relation Between Surface Roughness and Specular Reflectance at Normal Incidence," *J. Opt. Soc. Am.*, vol. 51, no. 2, p. 123, Feb. 1961.
- [203] P. Ghosh, W. Fu, M. J. Harrison, P. K. Doyle, J. A. Roberts, and D. S. McGregor, "Factors affecting performance of the micro-layered fast-neutron detector," *Nuclear Instruments and Methods in Physics Research, Section A: Accelerators, Spectrometers, Detectors and Associated Equipment*, Elsevier B.V., 2019.
- [204] J. M. Elson and J. M. Bennett, "Relation between the angular dependence of scattering and the statistical properties of optical surfaces," *J Opt Soc Am*, vol. 69, no. 1, pp. 31–47, 1979.
- [205] P. Ghosh *et al.*, "A high-efficiency, low-Čerenkov Micro-Layered Fast-Neutron Detector for the TREAT hodoscope," *Nucl. Instruments Methods Phys. Res. Sect. A Accel. Spectrometers, Detect. Assoc. Equip.*, vol. 904, pp. 100–106, Oct. 2018.
- [206] P. Ghosh, W. Fu, R. Fronk, D. S. McGregor, and J. A. Roberts, "Evaluation of MSNDs for Fast-Neutron Detection and the TREAT Hodoscope," *Transactions*, vol. 115, no. 1, pp. 1009–1012, Nov. 2016.
- [207] S. Schröder, A. Duparré, L. Coriand, A. Tünnermann, D. H. Penalver, and J. E. Harvey, "Modeling of light scattering in different regimes of surface roughness," *Opt. Express*, vol. 19, no. 10, p. 9820, May 2011.
- [208] P. G. Nelson, "An analysis of scattered light in reflecting and refracting primary objectives for coronagraphs," *Coronal Sol. Magn. Obs. Tech. Note 4*, vol. 10, no. 6, pp. 1–28, 2006.
- [209] E. L. Church, H. A. Jenkinson, and J. M. Zavada, "Relationship between Surface Scattering and Microtopographic Features," *Opt. Eng.*, vol. 18, no. 2, Apr. 1979.
- [210] F. E. Nicodemus, "Directional Reflectance and Emissivity of an Opaque Surface," *Appl. Opt.*, vol. 4, no. 7, p. 767, Jul. 1965.

- [211] “Optical Scattering and Surface Roughness - Eckhardt Optics.” [Online]. Available: <https://eckop.com/completed-projects/scatterometers/optical-scattering-versus-surface-roughness/>. [Accessed: 14-Dec-2019].
- [212] M. Madou, *Fundamentals of microfabrication*, 2nd ed. Boca Raton, FL, USA: CRC Press LLC, 2002.
- [213] N. G. T. Inc., “Cleaning of Silicon Wafers,” 2006.
- [214] J. Moran-Miraba, “Piranha cleaning - glass surfaces,” 2014.
- [215] J. Marra, “Ultraclean Marangoni Drying,” in *Particles in Gases and Liquids 3*, Springer US, 1993, pp. 269–282.
- [216] O. Tabata, “Anisotropic Etching of Silicon in TMAH Solutions,” *Sensors Mater.*, vol. 13, no. 5, pp. 271–283, 2001.
- [217] “Gaussian Beam - an overview | ScienceDirect Topics.” [Online]. Available: <https://www.sciencedirect.com/topics/engineering/gaussian-beam>. [Accessed: 24-Dec-2019].
- [218] E. Hecht, *Optics*, 4th ed. San Francisco, CA: Addison Wesley, 2002.
- [219] A. E. Siegman, “How to (Maybe) Measure Laser Beam Quality,” 2014, p. MQ1.
- [220] G. E. Slobodzian, “Apples to Apples: Which Camera Technologies Work Best for Beam Profiling Applications, Part 1,” 2016.
- [221] I. 11146-1:2005(E), “Lasers and laser-related equipment — Test methods for laser beam widths, divergence angles and beam propagation ratios — Part 1: Stigmatic and simple astigmatic beams,” 2005.
- [222] R. Schlag, M. A. Ras, V. Arlt, D. May, T. Winkler, and B. Wunderle, “Precision determination of thermorefectance coefficients for localised thermometry,” in *2015 21st International Workshop on Thermal Investigations of ICs and Systems (THERMINIC)*, 2015, pp. 1–5.
- [223] D. U. Kim, K. S. Park, C. B. Jeong, G. H. Kim, and K. S. Chang, “Quantitative temperature measurement of multi-layered semiconductor devices using spectroscopic thermorefectance microscopy,” *Opt. Express*, vol. 24, no. 13, p. 13906, Jun. 2016.
- [224] B. Kwon, M. Rosenberger, R. Bhargava, D. G. Cahill, and W. P. King, “Dynamic thermomechanical response of bimaterial microcantilevers to periodic heating by infrared radiation,” *Review of Scientific Instruments*, vol. 83, no. 1. Jan-2012.
- [225] J. S. Reparaz *et al.*, “A novel contactless technique for thermal conductivity

- determination: Two-laser Raman thermometry,” *THERMINIC 2014 - 20th Int. Work. Therm. Investig. ICs Syst. Proc.*, vol. 034901, no. 2014, 2014.
- [226] S. Alaie *et al.*, “Microfabricated suspended island platform for the measurement of in-plane thermal conductivity of thin films and nanostructured materials with consideration of contact resistance,” *Rev. Sci. Instrum.*, 2013.
  - [227] A. Greppmair, N. Galfe, K. Amend, M. Stutzmann, and M. S. Brandt, “Thermal characterization of thin films via dynamic infrared thermography,” *Review of Scientific Instruments*, vol. 90, no. 4. American Institute of Physics Inc., 01-Apr-2019.
  - [228] M. Goni, M. Patelka, S. Ikeda, T. Sato, and A. J. Schmidt, “Frequency domain thermoreflectance technique for measuring the thermal conductivity of individual micro-particles,” *Review of Scientific Instruments*, vol. 89, no. 7. American Institute of Physics Inc., 01-Jul-2018.
  - [229] L. Ramiandrisoa, A. Allard, Y. Joumani, B. Hay, and S. Gomés, “A dark mode in scanning thermal microscopy,” *Rev. Sci. Instrum.*, vol. 88, no. 12, Dec. 2017.
  - [230] S. Kommandur and S. Yee, “A suspended 3-omega technique to measure the anisotropic thermal conductivity of semiconducting polymers,” *Rev. Sci. Instrum.*, vol. 89, no. 11, Nov. 2018.
  - [231] B. Graczykowski *et al.*, “Thermal conductivity and air-mediated losses in periodic porous silicon membranes at high temperatures,” *Nat. Commun.*, vol. 8, no. 1, Dec. 2017.
  - [232] Y. Zeng and A. Marconnet, “A direct differential method for measuring thermal conductivity of thin films,” *Rev. Sci. Instrum.*, vol. 88, no. 4, Apr. 2017.
  - [233] O. Bourgeois *et al.*, “Reduction of phonon mean free path: From low-temperature physics to room temperature applications in thermoelectricity,” *Comptes Rendus Physique*, vol. 17, no. 10. Elsevier Masson SAS, pp. 1154–1160, 01-Dec-2016.
  - [234] G. P. Srivastava, *The physics of phonons*. A. Hilger, 1990.
  - [235] L. A. Stegeman *et al.*, “Neutron Spectrum Unfolding with a Planar Miniaturized Fast-Neutron Detector,” in *Transactions of the American Nuclear Society 120*, 2019, pp. 740–743.



## Appendix A - 1D Heat Diffusion Model

%This MATLAB program calculates temperature for one-dimensional heat transfer  
 %in solid. The code is able to analyze heat in three different regimes of  
 %heat conduction; steady-state, transient and harmonic.  
 %In steady-state a constant heat flux is given as input and defined as  
 %I in the code.  
 %In transient analysis constant heat flux is needed a time as well has to  
 %be defined over which transient response will be observed.  
 %For harmonic analysis, a modulation amplitude A is provided on top of  
 %constant heat flux. Here the frequency is needed to be mentioned.  
 %Again, there are three options of heat analysis in transient and  
 %harmonic. First option will provide temperature vs time graph for  
 %different point along the length of the solid. The second option will  
 %provide temperature vs time graph only at the mentioned position of the  
 %solid. Third option will look at temperature at any given time along the  
 %length of the solid and provide temperature vs length graph.

```
clear;
clc;
%Define States
s = menu('Steady State or Transient or Harmonic:', 'Steady State',
'Transient', 'Harmonic');
%Define Parameters
width = 100.000e-6;           %{m}
thickness = 100.000e-6;       %{m}
Area = width*thickness;       %{m^2}
I = 8e-4/Area;                %{Watt/m^2}
A = 8e-4/Area;                %{Watt/m^2}
L_in = input('Length of the cantilever beam in micron:');
%{micron}{Actual Length of the beam}
L = (L_in)/1e6;               %{m}{Length of the beam after subtracting Al pad
length+5 micron clearence border}
C = 679.0;                    %{J/kg.K}
p = 2328.0;                   %{kg/m^3}
K = 897.03;                   %{Watt/m.K}
T = 50;                       %{K}
diff =K/(p*C);                %{m^2/s}
Tao = (4/(pi^2))*((L^2)/diff));
iteration=0;
if s == 3
    delete Harmonic.xlsx;
    %Define Data Points
    m = menu('Do you want data on all points along the length?', 'Yes',
'No', 'Del_T vs x graph');
    if m==1
        f = input('Frequency in HZ:');           %{HZ}
        w = 2*pi*f;                               %{rad/s}
        t_i=input('Initial time(s):');           %{s}
        t_o = input('Final time(s):');           %{s}
        all_T=zeros(length(t_i:(t_o-t_i)/1000:t_o),10);
        RT=zeros(length(t_i:(t_o-t_i)/1000:t_o),1);
        time=zeros(length(t_i:(t_o-t_i)/1000:t_o),1);
        for x =1:10
```

```

d_x=x/10;
iteration=0;
for t=t_i:((t_o-t_i)/1000):t_o
    iteration=iteration+1;
    %Dimensionless
    d_w = w*(L^2)/diff;
    d_i=(L*I)/(T*K);
    d_a=(A*L)/(T*K);
    d_t=diff*t/(L^2);
    %Equation
    fun0 = d_x*(d_i+(d_a*sin(d_w*d_t)));
    total = 0;
    for n = 1:10000
        kn=(n-1/2)*pi;
        fun1=2.0*((-1)^n)/((kn^2)*((kn^4)+(d_w^2)));
        fun2=((d_i*((kn^4)+(d_w^2)))-((kn^2)*d_w*d_a))*exp(-(kn^2)*d_t));
        fun3=(kn^2)*d_w*d_a*cos(d_w*d_t)+(d_w^2)*(d_a*sin(d_w*d_t));
        fun4=(fun3)*sin(kn*d_x);
        fun6=fun1*fun4;
        total=total + fun6;
    end
    d_T = total + fun0;
    RT(iteration,1) = d_T*T;
    all_T(iteration,x)=d_T*T;
    fprintf('Temperature: %f k \n', RT);
    time(iteration,1) = t;
end
hold on;
h(x)=plot(time,RT,'linewidth',2);
legendInfo{x} = ['X = ' num2str(d_x)];
legend(legendInfo);
end
xlabel('Time (s)');
ylabel('Temperature Difference (K)');
set(findall(gcf,'-property','FontSize'),'FontSize',14);
hold off;
filename = 'Harmonic.xlsx';
xlswrite(filename,all_T,'Sheet1','B2');
xlswrite(filename,time,'Sheet1','A2');
q = {'Temperature(k)'};
r = {'Time(sec)'};
xlswrite(filename,q,'Sheet1','B1:K1');
xlswrite(filename,r,'Sheet1','A1');
elseif m==2
    x_1 = input('Position in micron:'); %{\mu m}
    x = x_1/1e6; %{m}
    f = input('Frequency in HZ:'); %{HZ}
    w = 2*pi*f; %{rad/s}
    t_i=input('Initial time(s):'); %{s}
    t_o = input('Final time(s):'); %{s}
    iteration=0;
    RT=zeros(length(t_i:(t_o-t_i)/100:t_o),1);
    time=zeros(length(t_i:(t_o-t_i)/100:t_o),1);
    for t=t_i:((t_o-t_i)/100):t_o
        iteration=iteration+1;

```

```

%Demensionless
d_w = w*(L^2)/diff;
d_i=(L*I)/(T*K);
d_a=(A*L)/(T*K);
d_x=x/L;
d_t=diff*t/(L^2);
%Equation
fun0 = d_x*(d_i+(d_a*sin(d_w*d_t)));
total = 0;
for n = 1:10000
    kn=(n-1/2)*pi;
    fun1=2.0*((-1)^n)/((kn^2)*((kn^4)+(d_w^2)));
    fun2=((d_i*((kn^4)+(d_w^2))-(kn^2)*d_w*d_a)*exp(-(kn^2)*d_t));
    fun3=(kn^2)*d_w*d_a*cos(d_w*d_t)+(d_w^2)*(d_a*sin(d_w*d_t));
    fun4=(fun3)*sin(kn*d_x);
    fun6=fun1*fun4;
    total=total + fun6;
end
d_T = total + fun0;
RT(iteration,1) = d_T*T;
fprintf('Temperature: %f k \n', RT);
time(iteration,1) = t;
end
filename = 'Harmonic.xlsx';
xlswrite(filename,RT,'Sheet1','B2');
xlswrite(filename,time,'Sheet1','A2');
q = {'Temperature(k)'};
r = {'Time(sec)'};
xlswrite(filename,q,'Sheet1','B1');
xlswrite(filename,r,'Sheet1','A1');
num = xlsread('Harmonic.xlsx');
plot(num(:,1),num(:,2));
saveas(gcf,'Harmonic.fig');
elseif m==3
%Define Frequency Mode
u=menu('What type of frequency do you want?','Single
Frequency','Multiple Frequency');
if u==1
    f = input('Frequency in HZ:');           %{HZ}
    t = input('Time (s):');                 %{s}
    iteration =0;
    w = 2*pi*f;
    for x =1:1000
        d_x=x/1000;
        %Demensionless
        d_w = w*(L^2)/diff;
        d_i=(L*I)/(T*K);
        d_a=(A*L)/(T*K);
        d_t=diff*t/(L^2);
        %Equation
        fun0 = d_x*(d_i+(d_a*sin(d_w*d_t)));
        total = 0;
        for n = 1:10000
            kn=(n-1/2)*pi;
            fun1=2.0*((-1)^n)/((kn^2)*((kn^4)+(d_w^2)));

```

```

        fun2=((d_i*((kn^4)+(d_w^2)))-((kn^2)*d_w*d_a))*exp(-(
(kn^2)*d_t));

fun3=(kn^2)*d_w*d_a*cos(d_w*d_t)+(d_w^2)*(d_a*sin(d_w*d_t));
        fun4=(fun2+fun3)*sin(kn*d_x);
        fun6=fun1*fun4;
        total=total + fun6;

    end
    d_T = total + fun0;
    RT(x,1) = d_T*T;
    fprintf('Temperature: %f k \n', RT);
    len(x,1) = d_x;

end
plot(len,RT);
elseif u==2
    f = input('Frequency in HZ:');           %{HZ}
    t = input('Time (s):');                 %{s}
    iteration = 0;
    for feq = 1:f/10:f
        iteration = iteration + 1;
        w = 2*pi*feq;
        for x = 1:10
            d_x=x/10;
            %Dimensionless
            d_w = w*(L^2)/diff;
            d_i=(L*I)/(T*K);
            d_a=(A*L)/(T*K);
            d_t=diff*t/(L^2);
            %Equation
            fun0 = d_x*(d_i+(d_a*sin(d_w*d_t)));
            total = 0;
            for n = 1:10000
                kn=(n-1/2)*pi;
                fun1=2.0*((-1)^n)/((kn^2)*((kn^4)+(d_w^2)));
                fun2=((d_i*((kn^4)+(d_w^2)))-((kn^2)*d_w*d_a))*exp(-(
(kn^2)*d_t));

fun3=(kn^2)*d_w*d_a*cos(d_w*d_t)+(d_w^2)*(d_a*sin(d_w*d_t));
                fun4=(fun2+fun3)*sin(kn*d_x);
                fun6=fun1*fun4;
                total=total + fun6;

            end
            d_T = total + fun0;
            RT(x,1) = d_T*T;
            fprintf('Temperature: %f k \n', RT);
            len(x,1) = d_x;

        end
        hold on;
        h(iteration)=plot(len,RT,'linewidth',2);
        legendInfo{iteration} = ['f = ' num2str(feq)];
        legend(legendInfo);

    end
end
end
elseif s == 2
    delete Transient.xlsx;
    %Define Data Points

```

```

m = menu('Do you want data on all points along the length?', 'Yes',
'No', 'Del_T vs x graph');
if m==1
    t_i=input('Initial time(s):');           %{s}
    t_o = input('Final time(s):');           %{s}
    RT=zeros(length(t_i:(t_o-t_i)/100:t_o),1);
    time=zeros(length(t_i:(t_o-t_i)/100:t_o),1);
    for x =1:10
        d_x=x/10;
        iteration=0;
        for t=t_i:((t_o-t_i)/100):t_o
            iteration=iteration+1;
            %Demensionless
            d_w = 0;
            d_a= 0;
            d_i=(L*I)/(T*K);
            d_t=diff*t/(L^2);
            %Equation
            fun0 = d_x*(d_i+(d_a*sin(d_w*d_t)));
            total = 0;
            for n = 1:10000
                kn=(n-1/2)*pi;
                fun1=2.0*((-1)^n)/(kn^2);
                fun2=d_i*exp(-(kn^2)*d_t);
                fun3=sin(kn*d_x);
                fun4=d_x*kn*(cos(kn)-1)/((-1)^n);
                fun5=fun1*fun2*fun3;
                total=total + fun5;
            end
            d_T = total + fun0;
            RT(iteration,1) = d_T*T;
            all_T(iteration,x)=d_T*T;
            fprintf('Temperature: %f k \n', RT);
            time(iteration,1) = t;
        end
        hold on;
        h(x)=plot(time,RT,'linewidth',2);
        legendInfo{x} = ['X = ' num2str(d_x)];
        legend(legendInfo);
    end
    xlabel('Time (s)');
    ylabel('Temperature Difference (K)');
    set(findall(gcf,'-property','FontSize'),'FontSize',14);
    hold off;
    filename = 'Transient.xlsx';
    xlswrite(filename,all_T,'Sheet1','B2');
    xlswrite(filename,time,'Sheet1','A2');
    q = {'Temperature(k)'};
    r = {'Time(sec)'};
    xlswrite(filename,q,'Sheet1','B1:K1');
    xlswrite(filename,r,'Sheet1','A1');
elseif m==2
    x_1 = input('Position in micron:');
    x = x_1/1e6;
    t_i=input('Initial time(s):');           %{s}
    t_o = input('Final time(s):');           %{s}
    iteration=0;

```

```

RT=zeros(length(t_i:(t_o-t_i)/100:t_o),1);
time=zeros(length(t_i:(t_o-t_i)/100:t_o),1);
for t=t_i:(t_o-t_i)/100:t_o
    iteration=iteration+1;
    %Dimensionless
    d_w = 0;
    d_a= 0;
    d_i=(L*I)/(T*K);
    d_x=x/L;
    d_t=diff*t/(L^2);
    %Equation
    fun0 = d_x*(d_i+(d_a*sin(d_w*d_t)));
    total = 0;
    for n = 1:10000
        kn=(n-1/2)*pi;
        fun1=2.0*((-1)^n)/(kn^2);
        fun2=d_i*exp(-(kn^2)*d_t);
        fun3=sin(kn*d_x);
        fun4=d_x*kn*(cos(kn)-1)/((-1)^n);
        fun5=fun1*fun2*fun3;
        total=total + fun5;
    end
    d_T = total + fun0;
    RT(iteration,1) = d_T*T;
    fprintf('Temperature: %f k \n', RT);
    time(iteration,1) = t;
end
filename = 'Transient.xlsx';
xlswrite(filename,RT,'Sheet1','B2');
xlswrite(filename,time,'Sheet1','A2');
q = {'Temperature(k)'};
r = {'Time(sec)'};
xlswrite(filename,q,'Sheet1','B1');
xlswrite(filename,r,'Sheet1','A1');
num = xlsread('Transient.xlsx');
plot(num(:,1),num(:,2));
saveas(gcf,'Transient.fig');
xlabel('Time (s)');
ylabel('Temperature Difference (K)');
set(findall(gcf,'-property','FontSize'),'FontSize',14);
elseif m==3
    t = input('Time (s):');
    iteration =0;
    for x =1:10
        d_x=x/10;
        %Dimensionless
        d_w = 0;
        d_a= 0;
        d_i=(L*I)/(T*K);
        d_t=diff*t/(L^2);
        %Equation
        fun0 = d_x*(d_i+(d_a*sin(d_w*d_t)));
        total = 0;
        for n = 1:10000
            kn=(n-1/2)*pi;
            fun1=2.0*((-1)^n)/(kn^2);
            fun2=d_i*exp(-(kn^2)*d_t);

```

```

        fun3=sin(kn*d_x);
        fun4=d_x*kn*(cos(kn)-1)/((-1)^n);
        fun5=fun1*fun2*fun3;
        total=total + fun5;
    end
    d_T = total + fun0;
    RT(x,1) = d_T*T;
    fprintf('Temperature: %f k \n', RT);
    len(x,1) = d_x;
end
plot(len,RT);
xlabel('Length');
ylabel('Temperature Difference (K)');
set(findall(gcf, '-property', 'FontSize'), 'FontSize', 14);
hold off;
end
elseif s == 1
delete Steady_State.xlsx;
%Dimensionless
d_i=(L*I)/(T*K);
Position=zeros(length(0:0.1:1),1);
RT=zeros(length(0:0.1:1),1);
iteration=0;
for x= 0:L/10:L
    d_x=x/L;
    iteration=iteration+1;
    %Equation
    d_T = d_x*d_i;
    RT(iteration,1) = d_T*T;
    fprintf('Temperature: %f k \n', RT);
    Position(iteration,1) = d_x*L*100;
end
filename = 'Steady_State.xlsx';
xlswrite(filename,RT, 'Sheet1', 'B2');
xlswrite(filename,Position, 'Sheet1', 'A2');
q = {'Temperature(k)'};
r = {'Dimensional Distance'};
xlswrite(filename,q, 'Sheet1', 'B1');
xlswrite(filename,r, 'Sheet1', 'A1');
num = xlsread('Steady_State.xlsx');
plot(num(:,1),num(:,2));
saveas(gcf, 'Steady_State.fig');
end

```

## Appendix B – Wavelength Dependence of Optical Properties

```
%This MATLAB program calculates reflectivity,  
%transmittivity, and absorptivity as a function of the wavelength.  
%This is done for a perfectly smooth surface considering interference  
%effects. Coherence length must be determined by the user to see if this  
%is and appropriate assumption or not.  
%  
%input files: lambda is in nm  
%All the input files contain n and k values for 300nm to 1600nm wavelength  
%with an interval of 1nm. If new materials need to be added please follow  
%the format. n and k for most of the materials are taken from  
https://refractiveindex.info  
%  
%Variables used in this program  
%INDEXING VARIABLES: A, B, C, D, E, F, G  
%numlay = number of material layers in the problem  
%matlbylayer = a column vector, the row number is the material layer number  
% and the number in that position is the material  
%props = is the master materials' properties matrix containing:  
% lambda first, then n1 / k1 / n2 / k2 / etc  
%r = amplitude reflection coefficient as calculated from the Fresnel  
Equations  
%t = amplitude transmission coefficient as calculated from the Fresnel  
Equations  
%h = is the thicknesses of the layers  
%beta = is a named variable containing h and lambda (among other things)  
%rembed = is the embedded amp refl coeff  
%tembed = is the embedded amp trans coeff  
%reflectivity = as advertised  
%transmissivity = as advertised  
%absorptivity = as advertised  
  
clear all;  
clc;  
  
%Define inputs  
  
answer = inputdlg('How many layers are in the problem? >', 'Number of  
layers', [1 20], {'3'});  
numlay = str2num( answer{:} );  
  
prompt = {'Please list the layers, using their material number listed below,  
from the first layer that is encounter by the EM wave to the last layer it  
encounters, in this format [1;5;23;etc...]. The materials that you have to  
choose from are: 1-Al 2-Au 3-Sn 4-Pb 5-Cr 6-Pt 7-In 8-Ge 9-ZnSe 10-  
SiO 11-SiO2 12-Ag 13-H2O 14-Air 15-Vacuum 16-Si '};  
title = 'Select Layers';  
dims = [1 100];  
definput = {'[14;16;14]'};  
% opts.Interpreter = 'tex'  
answer = inputdlg(prompt,title,dims,definput);  
matlbylayer = str2num( answer{:} );
```



```

%Read in the material data

for a = 1 : numlay
    if matlbylayer(a,1) == 1
        al = xlsread('Al_data.xlsx');
    elseif matlbylayer(a,1) == 2
        au = xlsread('Au_data');
    elseif matlbylayer(a,1) == 3
        sn = xlsread('Tin_data.xlsx');
    elseif matlbylayer(a,1) == 4
        pb = xlsread('Pb_data.xlsx');
    elseif matlbylayer(a,1) == 5
        cr = xlsread('Cr_data.xlsx');
    elseif matlbylayer(a,1) == 6
        pt = xlsread('Pt_data.xlsx');
    elseif matlbylayer(a,1) == 7
        in = fopen('Indium.xlsx');
    elseif matlbylayer(a,1) == 8
        ge = xlsread('Germanium.xlsx');
    elseif matlbylayer(a,1) == 9
        znse = fopen('ZnSe_data.xlsx');
    elseif matlbylayer(a,1) == 10
        sio = xlsread('SiO_data.xlsx');
    elseif matlbylayer(a,1) == 11
        sio2 = xlsread('SiO2_data.xlsx');
    elseif matlbylayer(a,1) == 12
        ag = xlsread('Ag_data.xlsx');
    elseif matlbylayer(a,1) == 13
        h2o = xlsread('H2O_data.xlsx');
    elseif matlbylayer(a,1) == 14
        air = xlsread('Air_data.xlsx');
    elseif matlbylayer(a,1) == 15
        vac = xlsread('Vacuum_data.xlsx');
    elseif matlbylayer(a,1) == 16
        si = xlsread('Si_data.xlsx');
    end
end

%construct the master materials' properties matrix

%first read in the first 3 columns of props which will consist of lambda
%then n and then k

props = zeros(1301,2*numlay+1);

if matlbylayer(1,1) == 1
    for a = 1 : length(al)
        props(a,1) = al(a,1); %lambda
        props(a,2) = al(a,2); %n value
        props(a,3) = al(a,3); %k value
    end
elseif matlbylayer(1,1) == 2
    for a = 1 : length(au)
        props(a,1) = au(a,1); %lambda
        props(a,2) = au(a,2); %n value
    end
end

```

```

        props(a,3) = au(a,3); %k value
    end
elseif matlbylayer(1,1) == 3
    for a = 1 : length(sn)
        props(a,1) = sn(a,1); %lambda
        props(a,2) = sn(a,2); %n value
        props(a,3) = sn(a,3); %k value
    end
elseif matlbylayer(1,1) == 4
    for a = 1 : length(pb)
        props(a,1) = pb(a,1); %lambda
        props(a,2) = pb(a,2); %n value
        props(a,3) = pb(a,3); %k value
    end
elseif matlbylayer(1,1) == 5
    for a = 1 : length(cr)
        props(a,1) = cr(a,1); %lambda
        props(a,2) = cr(a,2); %n value
        props(a,3) = cr(a,3); %k value
    end
elseif matlbylayer(1,1) == 6
    for a = 1 : length(pt)
        props(a,1) = pt(a,1); %lambda
        props(a,2) = pt(a,2); %n value
        props(a,3) = pt(a,3); %k value
    end
elseif matlbylayer(1,1) == 7
    for a = 1 : length(in)
        props(a,1) = in(a,1); %lambda
        props(a,2) = in(a,2); %n value
        props(a,3) = in(a,3); %k value
    end
elseif matlbylayer(1,1) == 8
    for a = 1 : length(ge)
        props(a,1) = ge(a,1); %lambda
        props(a,2) = ge(a,2); %n value
        props(a,3) = ge(a,3); %k value
    end
elseif matlbylayer(1,1) == 9
    for a = 1 : length(znse)
        props(a,1) = znse(a,1); %lambda
        props(a,2) = znse(a,2); %n value
        props(a,3) = znse(a,3); %k value
    end
elseif matlbylayer(1,1) == 10
    for a = 1 : length(sio)
        props(a,1) = sio(a,1); %lambda
        props(a,2) = sio(a,2); %n value
        props(a,3) = sio(a,3); %k value
    end
elseif matlbylayer(1,1) == 11
    for a = 1 : length(sio2)
        props(a,1) = sio2(a,1); %lambda
        props(a,2) = sio2(a,2); %n value
        props(a,3) = sio2(a,3); %k value
    end
elseif matlbylayer(1,1) == 12

```

```

    for a = 1 : length(ag)
        props(a,1) = ag(a,1); %lambda
        props(a,2) = ag(a,2); %n value
        props(a,3) = ag(a,3); %k value
    end
elseif matlbylayer(1,1) == 13
    for a = 1 : length(h2o)
        props(a,1) = h2o(a,1); %lambda
        props(a,2) = h2o(a,2); %n value
        props(a,3) = h2o(a,3); %k value
    end
elseif matlbylayer(1,1) == 14
    for a = 1 : length(air)
        props(a,1) = air(a,1); %lambda
        props(a,2) = air(a,2); %n value
        props(a,3) = air(a,3); %k value
    end
elseif matlbylayer(1,1) == 15
    %again, we will incorporate the constant properties for a vacuum later
    if matlbylayer(2,1) == 1
        for a = 1 : length(al)
            props(a,1) = al(a,1); %lambda
            props(a,2) = al(a,2); %n value
            props(a,3) = al(a,3); %k value
        end
    elseif matlbylayer(2,1) == 2
        for a = 1 : length(au)
            props(a,1) = au(a,1); %lambda
            props(a,2) = au(a,2); %n value
            props(a,3) = au(a,3); %k value
        end
    elseif matlbylayer(2,1) == 3
        for a = 1 : length(sn)
            props(a,1) = sn(a,1); %lambda
            props(a,2) = sn(a,2); %n value
            props(a,3) = sn(a,3); %k value
        end
    elseif matlbylayer(2,1) == 4
        for a = 1 : length(pb)
            props(a,1) = pb(a,1); %lambda
            props(a,2) = pb(a,2); %n value
            props(a,3) = pb(a,3); %k value
        end
    elseif matlbylayer(2,1) == 5
        for a = 1 : length(cr)
            props(a,1) = cr(a,1); %lambda
            props(a,2) = cr(a,2); %n value
            props(a,3) = cr(a,3); %k value
        end
    elseif matlbylayer(2,1) == 6
        for a = 1 : length(pt)
            props(a,1) = pt(a,1); %lambda
            props(a,2) = pt(a,2); %n value
            props(a,3) = pt(a,3); %k value
        end
    elseif matlbylayer(2,1) == 7
        for a = 1 : length(in)

```

```

        props(a,1) = in(a,1); %lambda
        props(a,2) = in(a,2); %n value
        props(a,3) = in(a,3); %k value
    end
elseif matlbylayer(2,1) == 8
    for a = 1 : length(ge)
        props(a,1) = ge(a,1); %lambda
        props(a,2) = ge(a,2); %n value
        props(a,3) = ge(a,3); %k value
    end
elseif matlbylayer(2,1) == 9
    for a = 1 : length(znse)
        props(a,1) = znse(a,1); %lambda
        props(a,2) = znse(a,2); %n value
        props(a,3) = znse(a,3); %k value
    end
elseif matlbylayer(2,1) == 10
    for a = 1 : length(sio)
        props(a,1) = sio(a,1); %lambda
        props(a,2) = sio(a,2); %n value
        props(a,3) = sio(a,3); %k value
    end
elseif matlbylayer(2,1) == 11
    for a = 1 : length(sio2)
        props(a,1) = sio2(a,1); %lambda
        props(a,2) = sio2(a,2); %n value
        props(a,3) = sio2(a,3); %k value
    end
elseif matlbylayer(2,1) == 12
    for a = 1 : length(ag)
        props(a,1) = ag(a,1); %lambda
        props(a,2) = ag(a,2); %n value
        props(a,3) = ag(a,3); %k value
    end
elseif matlbylayer(2,1) == 13
    for a = 1 : length(h2o)
        props(a,1) = h2o(a,1); %lambda
        props(a,2) = h2o(a,2); %n value
        props(a,3) = h2o(a,3); %k value
    end
elseif matlbylayer(2,1) == 14
    for a = 1 : length(air)
        props(a,1) = air(a,1); %lambda
        props(a,2) = air(a,2); %n value
        props(a,3) = air(a,3); %k value
    end
elseif matlbylayer(2,1) == 16
    for a = 1 : length(si)
        props(a,1) = si(a,1); %lambda
        props(a,2) = si(a,2); %n value
        props(a,3) = si(a,3); %k value
    end
end
%back to the original (non-vacuum) if statement
elseif matlbylayer(1,1) == 16
    for a = 1 : length(si)
        props(a,1) = si(a,1); %lambda

```

```

        props(a,2) = si(a,2); %n value
        props(a,3) = si(a,3); %k value
    end
end
%This section sorts the data according to the available wavelengths for
%each material. Here we first keep all values of lambda for material one.
%Then we inspect material two's wavelengths if there isn't a match with
%material one then it puts a zero in props(x,1). Then later we will remove
%that row. If there is data for that wavelength for material 2 then we
%write data into the corresponding columns of that wavelength (row).
for a = 2 : numelay
    if matlbylayer(a,1) == 1
        for b = 1 : length(props)
            c = 0;
            for d = 1 : length(al)
                if props(b,1) == al(d,1)
                    props(b,2*a) = al(d,2);
                    props(b,2*a+1) = al(d,3);
                    g = 0;
                else
                    c = c + 1;
                end
                if c == length(al)
                    props(b,1) = 0; %Here we set the lambda = 0 and remember
we must go back and remove all values associated with that lambda
                end
            end
        end
    end
    if matlbylayer(a,1) == 2
        for b = 1 : length(props)
            c = 0;
            for d = 1 : length(au)
                if props(b,1) == au(d,1)
                    props(b,2*a) = au(d,2);
                    props(b,2*a+1) = au(d,3);
                    c = 0;
                else
                    c = c + 1;
                end
                if c == length(au)
                    props(b,1) = 0; %Here we set the lambda = 0 and remember
we must go back and remove all values associated with that lambda
                end
            end
        end
    end
    if matlbylayer(a,1) == 3
        for b = 1 : length(props)
            c = 0;
            for d = 1 : length(sn)
                if props(b,1) == sn(d,1)
                    props(b,2*a) = sn(d,2);
                    props(b,2*a+1) = sn(d,3);
                    c = 0;
                else
                    c = c + 1;
                end
            end
        end
    end
end

```

```

        end
        if c == length(sn)
            props(b,1) = 0; %Here we set the lambda = 0 and remember
we must go back and remove all values associated with that lambda
        end
    end
end
end
if matlbylayer(a,1) == 4
    for b = 1 : length(props)
        c = 0;
        for d = 1 : length(pb)
            if props(b,1) == pb(d,1)
                props(b,2*a) = pb(d,2);
                props(b,2*a+1) = pb(d,3);
                c = 0;
            else
                c = c + 1;
            end
            if c == length(pb)
                props(b,1) = 0; %Here we set the lambda = 0 and remember
we must go back and remove all values associated with that lambda
            end
        end
    end
end
end
if matlbylayer(a,1) == 5
    for b = 1 : length(props)
        c = 0;
        for d = 1 : length(cr)
            if props(b,1) == cr(d,1)
                props(b,2*a) = cr(d,2);
                props(b,2*a+1) = cr(d,3);
                c = 0;
            else
                c = c + 1;
            end
            if c == length(cr)
                props(b,1) = 0; %Here we set the lambda = 0 and remember
we must go back and remove all values associated with that lambda
            end
        end
    end
end
end
if matlbylayer(a,1) == 6
    for b = 1 : length(props)
        c = 0;
        for d = 1 : length(pt)
            if props(b,1) == pt(d,1)
                props(b,2*a) = pt(d,2);
                props(b,2*a+1) = pt(d,3);
                c = 0;
            else
                c = c + 1;
            end
            if c == length(pt)

```

```

        props(b,1) = 0; %Here we set the lambda = 0 and remember
we must go back and remove all values associated with that lambda
    end
end
end
if matlbylayer(a,1) == 7
    for b = 1 : length(props)
        c = 0;
        for d = 1 : length(in)
            if props(b,1) == in(d,1)
                props(b,2*a) = in(d,2);
                props(b,2*a+1) = in(d,3);
                c = 0;
            else
                c = c + 1;
            end
            if c == length(in)
                props(b,1) = 0; %Here we set the lambda = 0 and remember
we must go back and remove all values associated with that lambda
            end
        end
    end
end
if matlbylayer(a,1) == 8
    for b = 1 : length(props)
        c = 0;
        for d = 1 : length(ge)
            if props(b,1) == ge(d,1)
                props(b,2*a) = ge(d,2);
                props(b,2*a+1) = ge(d,3);
                c = 0;
            else
                c = c + 1;
            end
            if c == length(ge)
                props(b,1) = 0; %Here we set the lambda = 0 and remember
we must go back and remove all values associated with that lambda
            end
        end
    end
end
if matlbylayer(a,1) == 9
    for b = 1 : length(props)
        c = 0;
        for d = 1 : length(znse)
            if props(b,1) == znse(d,1)
                props(b,2*a) = znse(d,2);
                props(b,2*a+1) = znse(d,3);
                c = 0;
            else
                c = c + 1;
            end
            if c == length(znse)
                props(b,1) = 0; %Here we set the lambda = 0 and remember
we must go back and remove all values associated with that lambda
            end
        end
    end
end

```

```

        end
    end
end
if matlbylayer(a,1) == 10
    for b = 1 : length(props)
        c = 0;
        for d = 1 : length(sio)
            if props(b,1) == sio(d,1)
                props(b,2*a) = sio(d,2);
                props(b,2*a+1) = sio(d,3);
                c = 0;
            else
                c = c + 1;
            end
            if c == length(sio)
                props(b,1) = 0; %Here we set the lambda = 0 and remember
we must go back and remove all values associated with that lambda
            end
        end
    end
end
if matlbylayer(a,1) == 11
    for b = 1 : length(props)
        c = 0;
        for d = 1 : length(sio2)
            if props(b,1) == sio2(d,1)
                props(b,2*a) = sio2(d,2);
                props(b,2*a+1) = sio2(d,3);
                c = 0;
            else
                c = c + 1;
            end
            if c == length(sio2)
                props(b,1) = 0; %Here we set the lambda = 0 and remember
we must go back and remove all values associated with that lambda
            end
        end
    end
end
if matlbylayer(a,1) == 12
    for b = 1 : length(props)
        c = 0;
        for d = 1 : length(ag)
            if props(b,1) == ag(d,1)
                props(b,2*a) = ag(d,2);
                props(b,2*a+1) = ag(d,3);
                c = 0;
            else
                c = c + 1;
            end
            if c == length(ag)
                props(b,1) = 0; %Here we set the lambda = 0 and remember
we must go back and remove all values associated with that lambda
            end
        end
    end
end
end
end

```



```

if matlbylayer(a,1) == 13
    for b = 1 : length(props)
        c = 0;
        for d = 1 : length(h2o)
            if props(b,1) == h2o(d,1)
                props(b,2*a) = h2o(d,2);
                props(b,2*a+1) = h2o(d,3);
                c = 0;
            else
                c = c + 1;
            end
            if c == length(h2o)
                props(b,1) = 0; %Here we set the lambda = 0 and remember
we must go back and remove all values associated with that lambda
            end
        end
    end
end
if matlbylayer(a,1) == 14
    for b = 1 : length(props)
        c = 0;
        for d = 1 : length(air)
            if props(b,1) == air(d,1)
                props(b,2*a) = air(d,2);
                props(b,2*a+1) = air(d,3);
                c = 0;
            else
                c = c + 1;
            end
            if c == length(air)
                props(b,1) = 0; %Here we set the lambda = 0 and remember
we must go back and remove all values associated with that lambda
            end
        end
    end
end
if matlbylayer(a,1) == 16
    for b = 1 : length(props)
        c = 0;
        for d = 1 : length(si)
            if props(b,1) == si(d,1)
                props(b,2*a) = si(d,2);
                props(b,2*a+1) = si(d,3);
                c = 0;
            else
                c = c + 1;
            end
            if c == length(si)
                props(b,1) = 0; %Here we set the lambda = 0 and remember
we must go back and remove all values associated with that lambda
            end
        end
    end
end
end

%Gets rid of zero element rows and rows where lambda is zero

```

```

%*****

%Shifts the rows, overwriting the rows with 0 for lambda

[a,b] = size(props);
f = 1;
for d = 1 : a
    if props(d,1) > 0
        for e = 1 : numlay*2+1
            props(f,e) = props(d,e);
        end
        f = 1 + f;
    end
end

%takes out the bottom rows with 0 for lambda

[a,b] = size(props);
for c = 1 : a
    [a,b] = size(props);
    if props(a,1) == 0
        props(a,:) = [];
    end
end

%trims the repeat columns from line 556-565

a = f-1;
[b,c] = size(props);
for d = 1 : b-a
    [e,g] = size(props);
    props(e,:) = [];
end

%adds in the lines for a vacuum

[a,b] = size(props);
props4model = zeros(a,b);
for c = 1 : a
    d = 1;
    for e = 1 : numlay
        if matlbylayer(e,1) == 15
            props4model(c,2*e) = 1;
            props4model(c,2*e+1) = 0;
        else
            props4model(c,2*e) = props(c,2*d);
            props4model(c,2*e+1) = props(c,2*d+1);
            d = d + 1;
        end
    end
end
end
props4model = [props(1:a,1) props4model(1:a,2:numlay*2+1)];
props = props4model;
clear props4model

```

```

%%%%%%%%%%%%%%%%%%%%%%%%%%%%%%%%%%%%%%%%%%%%%%%%%%%%%%%%%%%%%%%%%%%%%%%%%%%%%%Data ALL read in

[a,b] = size(props);
disp('The range of wavelengths available is (nm) :');
display(props(1,1));
disp('to');
display(props(a,1));

%Define layer thicknesses

answer = inputdlg('What is the thickness of each layer? (Express in
Angstroms and this form [1;2;3;4;etc])','Thickness of each layers',[1
35],{'[1000;1000;1000]'});
h = str2num( answer{:} );

%define reflectances and transmittances for normal incidence
%eg r = [r12;r23;r34;r45;etc]

r = zeros(a,numlay-1);
t = zeros(a,numlay-1);
clear i
for c = 1 : a
    for f = 1 : numlay-1
        r(c,f) = ( (props(c,2*f+2) - (props(c,2*f+3)*1i)) - (props(c,2*f) -
(props(c,2*f+1)*1i)) ) / ( (props(c,2*f+2) - (props(c,2*f+3)*1i)) +
(props(c,2*f) - (props(c,2*f+1)*1i)) );
        t(c,f) = ( 2 * (props(c,2*f)-(props(c,2*f+1)*1i)) ) / ( (props(c,2*f+2) -
(props(c,2*f+3)*1i)) + (props(c,2*f) - (props(c,2*f+1)*1i)) );
    end
end

%define beta
%eg beta = [beta1=0, beta2, beta3, etc, betan=0      all at lambda1
%           [beta1=0, beta2, beta3, etc, betan=0      all at lambda2
%           [beta1=0, beta2, beta3, etc, betan=0]      etc

beta = zeros(a,numlay);

for d = 1 : a
    for e = 2 : numlay-1
        beta(d,e) = ( 2 * pi * ( props(d,2*e) - (props(d,2*e+1)*1i)) *
h(e,1)) / (props(d,1) * 10); %the lambda * 10 is to convert to angstroms
    end
end

%embedding of r and t
% rembed = [r13,r14,r15,r16,etc...r1n]

%gotta do the rembed13 and tembed13 first and then can set up a loop to
finish out
%rembed

rembed = zeros(a,numlay-2);
tembed = zeros(a,numlay-2);

```

```

for g = 1 : a
    rembed(g,1) = (r(g,1) + r(g,2) * exp(-1i*2*beta(g,2))) / (1 +
((r(g,1) * r(g,2) * exp(-1i*2*beta(g,2)))));
    tembed(g,1) = (t(g,1) * t(g,2) * exp(-1i * beta(g,2))) / (1 +
((r(g,1) * r(g,2) * exp(-1i*2*beta(g,2)))));
end

%now do the loop

for c = 1 : a
    for d = 2 : numlay-2
        rembed(c,d) = (rembed(c,d-1) + (r(c,d+1) * exp(-1i*2*beta(c,d+1)))) /
(1 + (rembed(c,d-1) * (r(c,d+1) * exp(-1i*2*beta(c,d+1)))));
        tembed(c,d) = (tembed(c,d-1) * (t(c,d+1) * exp(-1i * beta(c,d+1)))) /
(1 + (rembed(c,d-1) * (r(c,d+1) * exp(-1i*2*beta(c,d+1)))));
    end
end

%calculate reflectivity and transmissivity and absorptivity (note though i
%have all data for R, T, and A at every layer increment I am choosing to
%calculate R, T, and A for the whole system only

reflectivity = zeros(a,1);
transmissivity = zeros(a,1);
absorptivity = zeros(a,1);

for c = 1 : a
    reflectivity(c,1) = (abs(rembed(c,numlay-2)))^2;
    transmissivity(c,1) = (props(c,b-1) / props(c,2)) *
(abs(tembed(c,numlay-2)))^2;
    absorptivity(c,1) = 1 - reflectivity(c,1) - transmissivity(c,1);
end
plot(props(:,1),reflectivity,props(:,1),transmissivity,props(:,1),absorptivit
y);
legend('R','T','A');
xlabel('Wavelength (nm)');
ylabel('R, T, A');
set(findall(gcf,'-property','FontSize'),'FontSize',14);

```

## Appendix C – Thickness Dependence of Optical Properties

```
%This MATLAB code is written as a part of 'suspended thermoreflectance (STR)'
%calculation.
%This calculates reflectance, absorbance and transmittance for a range of
%thicknesses once refractive index and extinction coefficient (can also be
% found using the code) for all the layers are given.
% All the equations in this code are taken from 'Thin-film optical filters
% (4th edition)' by H Angus Macleod
clear all;
clc;
f = menu('Do you need to understand how this code works?', 'Yes', 'No');
if f == 1
    fprintf('Proceeding to the main program\n');
elseif f == 2
    figure=imshow('Explanation.JPG');
end
numint=input('How many interfaces are in the problem? > ');
deltathick = input('Which layers thickness will change? >');
%Creating Material Properties
nummedia = numint + 1;
%Number of media light will travel through
s = menu('Is the first and last layers are same?', 'Yes', 'No');           %If
they are same, no need to give same input twice
n = zeros(nummedia,1);
k = zeros(nummedia,1);
m_pros = input('For how many materials you need to know refractive index and
extinction coefficient?');
for x = 1:m_pros
    m_pros2 = menu('Which material property you need to find?', 'Silver',
'Aluminum', 'Aluminum Oxide', 'Gold', 'Chromium', 'Lead', 'Platinum',
'Silicon', 'Silicon mono-oxide', 'Silicon di-oxide', 'Tin');
    if m_pros2 == 1
        figure=openfig('Ag_n_k.fig');
    elseif m_pros2 == 2
        figure=openfig('Al_n_k.fig');
    elseif m_pros2 == 3
        figure=openfig('Al2O3_n_k.fig');
    elseif m_pros2 == 4
        figure=openfig('Au_n_k.fig');
    elseif m_pros2 == 5
        figure=openfig('Cr_n_k.fig');
    elseif m_pros2 == 6
        figure=openfig('Pb_n_k.fig');
    elseif m_pros2 == 7
        figure=openfig('Pt_n_k.fig');
    elseif m_pros2 == 8
        figure=openfig('Si_n_k.fig');
    elseif m_pros2 == 9
        figure=openfig('SiO_n_k.fig');
    elseif m_pros2 == 10
        figure=openfig('SiO2_n_k.fig');
    elseif m_pros2 == 11
```

```

        figure=openfig('Sn_n_k.fig');
    end
end
if s == 1
    for z = 1:nummedia-1
        if z == deltathick
            n(z,1) = input(['What is the value of n(',num2str(z),'')? >']);
            k(z,1) = input(['What is the value of k(',num2str(z),'')? >']);
        else
            fprintf('n = 1 and k = 0 for air and Vacuum \n');
            n(z,1) = input(['What is the value of n(',num2str(z),'')? >']);
            k(z,1) = input(['What is the value of k(',num2str(z),'')? >']);
        end
    end
    n(nummedia,1) = n(1,1);
    k(nummedia,1) = k(1,1);
elseif s == 2
    for z = 1:nummedia
        if z == deltathick
            figure=openfig('Si_n_k.fig');
            n(z,1) = input(['What is the value of n(',num2str(z),'')? >']);
            k(z,1) = input(['What is the value of k(',num2str(z),'')? >']);
        else
            fprintf('n = 1 and k = 0 for air and Vacuum');
            n(z,1) = input(['What is the value of n(',num2str(z),'')? >']);
            k(z,1) = input(['What is the value of k(',num2str(z),'')? >']);
        end
    end
end
end
%Declaring the change of thickness of the layer whose thickness will change
thicknessinitial = input('What thickness will the layer whose thickness
changes start at? (nanometer) >');
thicknessfinal = input('What thickness will the layer whose thickness changes
end at? (nanometer) >');
steps = input('How many increments, between these thicknesses, do want to
take? > ');
thicknesses = zeros(steps+1,1);
%thicknesses the problem will be solved for
thicknesses(1,1) = thicknessinitial;
for x = 2:steps
    thicknesses(x,1) = ((thicknessfinal-thicknessinitial)/steps) +
thicknesses(x-1,1);
end
thicknesses(steps+1,1) = thicknessfinal;
thick = zeros(nummedia,1);
for u = 2:nummedia-1
    if u == deltathick
        thick(u,1) = thicknessinitial;
    end
end
end
%Define the optical admittance of free space Y
Y = 2.6544*10^-3;
%Macleod Book - Symbols and Abbreviations
%Turn n's and k's into imaginary indexes of refraction and define etas
m = zeros(nummedia,1);
eta = zeros(nummedia,1);
for y = 1:nummedia

```

```

clear i
m(y,1) = n(y,1) - k(y,1)*1i;
%Macleod Book - Symbols and Abbreviations - Complex refractive index
eta(y,1) = Y * m(y,1);
%Macleod Book - equation 2.103 (Considering perpendicular incident)
end
%Define the wavelength of light in the experiment
lambda = input('What is the wavelength of light in this experiment
(nanometer)? > ');
%Begin solution for characteristic matrices
deltas = zeros(nummedia,1);
charamatrix = 1;
for a = 2 : nummedia - 1
    deltas(a,1) = (2*pi*m(a,1)*thick(a,1))/lambda;
%Macleod Book - Symbols and Abbreviations - Phase thickness of a coating
    matrix =
[cos(deltas(a,1)), (1i*sin(deltas(a,1)))/eta(a,1); 1i*eta(a,1)*sin(deltas(a,1))
,cos(deltas(a,1))]; %Macleod Book - equation 2.103
    charamatrix = charamatrix*matrix;
    if a == deltathick - 1
        unxmatrix = charamatrix;
    elseif a == 2
        unxmatrix = charamatrix;
    end
end
BC = zeros(2,steps+1);
BC(1:2,1) = charamatrix*[1;eta(nummedia,1)];
for b = 2 : steps + 1
    delta = (2*pi*(m(deltathick,1))*thicknesses(b,1))/lambda;
%Macleod Book - Symbols and Abbreviations - Phase thickness of a coating
    matrix =
[cos(delta), (1i*sin(delta))/eta(deltathick,1); 1i*eta(deltathick,1)*sin(delta)
,cos(delta)]; %Macleod Book - equation 2.103
    charamatrix = unxmatrix*matrix;
    for c = deltathick + 1 : nummedia
        matrix =
[cos(deltas(c,1)), (1i*sin(deltas(c,1)))/eta(c,1); 1i*eta(c,1)*sin(deltas(c,1))
,cos(deltas(c,1))]; %Macleod Book - equation 2.103
        charamatrix = charamatrix * matrix;
    end
    BC(1:2,b) = charamatrix * [1;eta(nummedia,1)];
end
%Determine R, T, A
R = zeros(steps + 1,1);
T = zeros(steps + 1,1);
A = zeros(steps + 1,1);
for d = 1 : steps + 1
    R(d,1) = ((eta(1,1)*BC(1,d)-BC(2,d))/(eta(1,1)*BC(1,d)+BC(2,d))) *
conj(((eta(1,1)*BC(1,d)-BC(2,d))/(eta(1,1)*BC(1,d)+BC(2,d)))); %Macleod
Book - equation 2.113
    T(d,1) =
(4*eta(1,1)*real(eta(nummedia,1)))/((eta(1,1)*BC(1,d)+BC(2,d))*conj(eta(1,1)*
BC(1,d)+BC(2,d))); %Macleod Book - equation
2.115
    A(d,1) = 1 - R(d,1) - T(d,1);
end
plot(thicknesses,R,thicknesses,T,thicknesses,A);

```

```
legend('R','T','A');  
xlabel('Thickness (nanometer)');  
ylabel('R, T, A');  
set(findall(gcf,'-property','FontSize'),'FontSize',14);
```



## **Appendix D – STR Control and Data Collection Program**

A LabView program was written to collect data and control electronics during the STR experiment. Only the user interface is provided in this dissertation. The full program can be divided into five major sections (shown in Figure D.1): cryostat temperature control (Figure D.2), cryostat data collection (Figure D.3), data collection from both lock-in amplifiers (Figure D.4), function generator control (Figure D.5) and data collection from both nanovoltmeters (Figure D.6).

Heater, heater range, gain, mode, input current, polarity and end state are selected for the PID controller using the cryostat temperature control section. The cryostat data collection section shows the real-time temperature of the cryo-head and sample. The temperature ramp rate for multipoint measurement is also defined through this section. The lock-in data collection section not only shows real-time lock-in data, but it also allows control of parameters such as signal and reference type, sensitivity, filter type, and time interval. On the other hand, the function generator section assists in setting up the modulation frequency, amplitude, function type and dc offset. The nanovolt meter section presents the pump data collected using the meters.

Time-dependent data like cryostat temperature, lock-in amplifier signals, and nanovolt meter readings are stored in the same Excel file with time-independent data, including modulated frequency and amplitude. This allows all data to be obtained in one file and analyzed later using short MATLAB scripts.

The cryostat is first turned on manually. The program is usually started when the cryostat temperature reaches its minimum level. The ramp rate, which is stated in the program, then raises the temperature to the desired value, and waits for the full measurement to be completed.

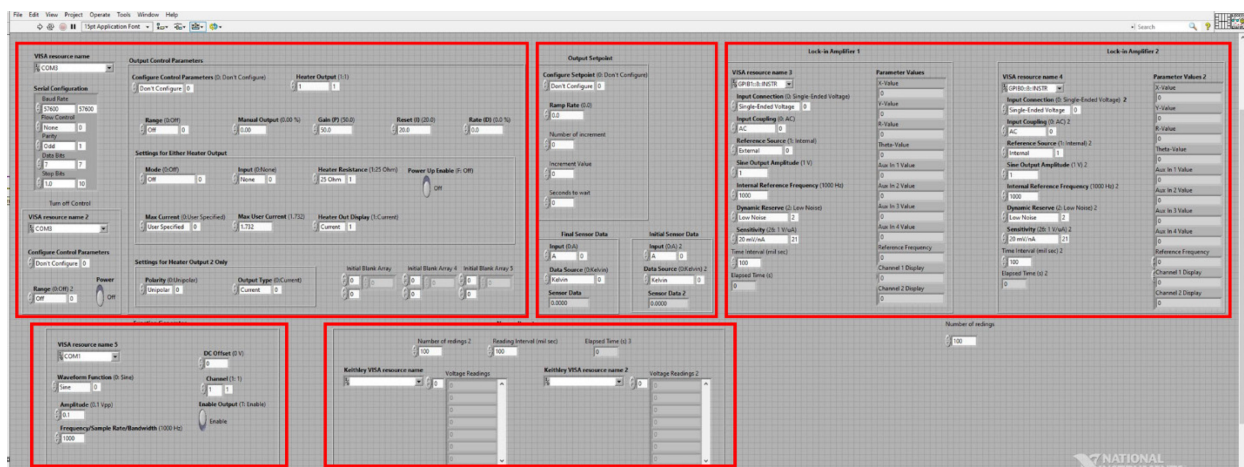


Figure D.1 Full user interface for STR data collection and control. Five sections are (upper left to right) cryostat temperature control, cryostat temperature collection, lock-in amplifiers data collection, (lower left to right) function generator control, nanovolt meters data collection.

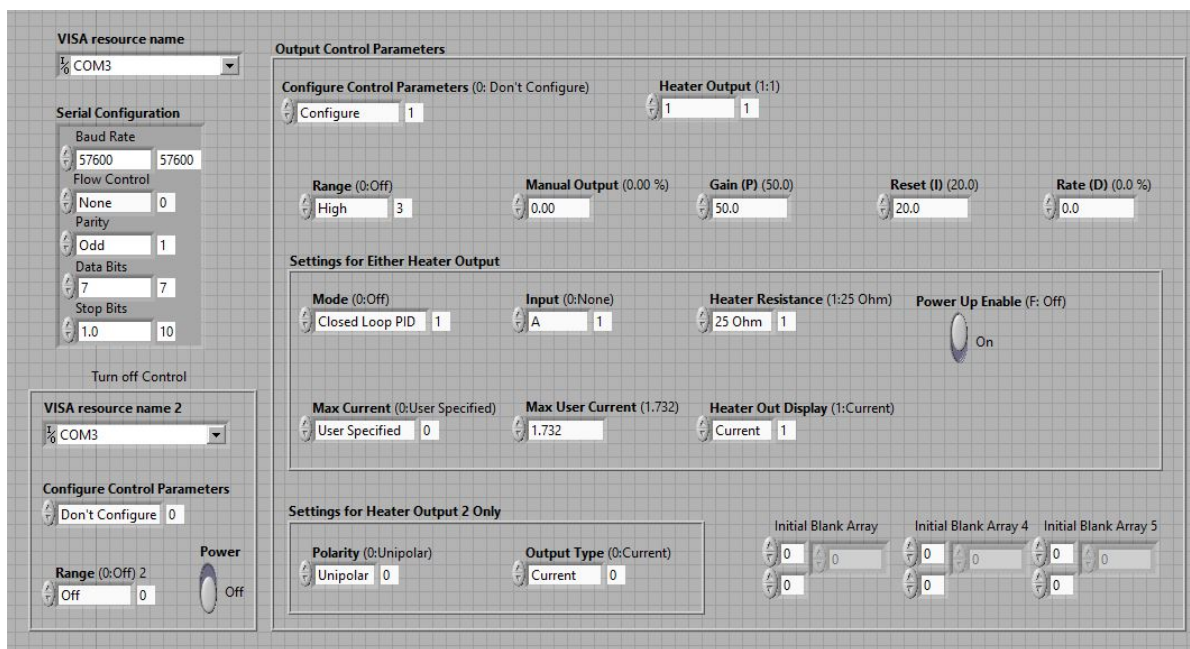


Figure D.2 This section controls the cryostat temperature by setting values for PID controller.

**Output Setpoint**

**Configure Setpoint (0: Don't Configure)**

Configure ☐ 1

**Ramp Rate (0.0)**

0.0

**Number of increment**

6

**Increment Value**

50

**Seconds to wait**

720

---

**Final Sensor Data**

**Input (0:A)**

B ☐ 1

**Data Source (0:Kelvin)**

Kelvin ☐ 0

**Sensor Data**

264.0100

**Initial Sensor Data**

**Input (0:A) 2**

B ☐ 1

**Data Source (0:Kelvin) 2**

Kelvin ☐ 0

**Sensor Data 2**

264.0100

Figure D.3 This section measures the cryostat and sample temperature. It also sets the temperature ramp rate for cryostat.

**Lock-in Amplifier 1**

**VISA resource name 3**

GPIB1::8::INSTR

**Input Connection (0: Single-Ended Voltage)**

Single-Ended Voltage ☐ 0

**Input Coupling (0: AC)**

AC ☐ 0

**Reference Source (1: Internal)**

External ☐ 0

**Sine Output Amplitude (1 V)**

1

**Internal Reference Frequency (1000 Hz)**

1000

**Dynamic Reserve (2: Low Noise)**

Low Noise ☐ 2

**Sensitivity (26: 1 V/uA)**

10 mV/nA ☐ 20

**Time Interval (mil sec)**

100

**Elapsed Time (s)**

4094.66

**Parameter Values**

X-Value: -0.000439169

Y-Value: -0.00179864

R-Value: 0.00185061

Theta-Value: -103.716

Aux In 1 Value: 0.00233333

Aux In 2 Value: 0.00133333

Aux In 3 Value: -0.000333333

Aux In 4 Value: 0.00833333

Reference Frequency: 9999.96

Channel 1 Display: -0.000436785

Channel 2 Display: -0.00179625

**Lock-in Amplifier 2**

**VISA resource name 4**

GPIB0::8::INSTR

**Input Connection (0: Single-Ended Voltage) 2**

Single-Ended Voltage ☐ 0

**Input Coupling (0: AC) 2**

AC ☐ 0

**Reference Source (1: Internal) 2**

External ☐ 0

**Sine Output Amplitude (1 V) 2**

1

**Internal Reference Frequency (1000 Hz) 2**

1000

**Dynamic Reserve (2: Low Noise) 2**

Low Noise ☐ 2

**Sensitivity (26: 1 V/uA) 2**

20 mV/nA ☐ 21

**Time Interval (mil sec) 2**

100

**Elapsed Time (s) 2**

4094.66

**Parameter Values 2**

X-Value: -0.00515559

Y-Value: -0.0179483

R-Value: 0.0186731

Theta-Value: -106.026

Aux In 1 Value: 0.000333333

Aux In 2 Value: -0.00233333

Aux In 3 Value: 0.00666667

Aux In 4 Value: 0.031

Reference Frequency: 10000.2

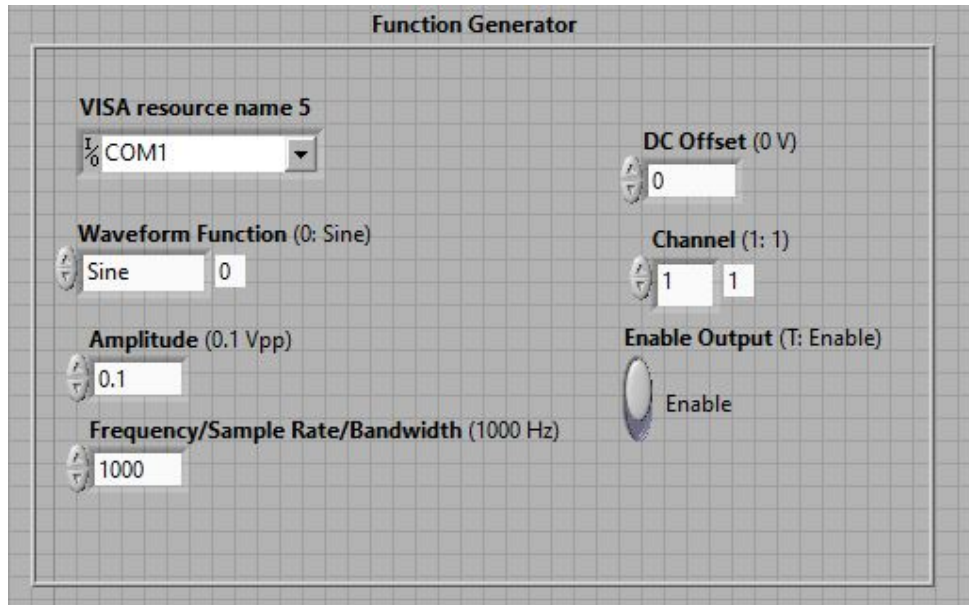
Channel 1 Display: -0.0051575

Channel 2 Display: -0.0179569

Number of readings ☐ 200

NATIONAL INSTRUMENTS  
LabVIEW Evaluation Software

Figure D.4 Lock-in amplifiers data is collected using this section of the program. Parameters like signal and reference type, sensitivity, filter type, time interval etc. are set here.



**Function Generator**

VISA resource name 5  
COM1

Waveform Function (0: Sine)  
Sine 0

Amplitude (0.1 Vpp)  
0.1

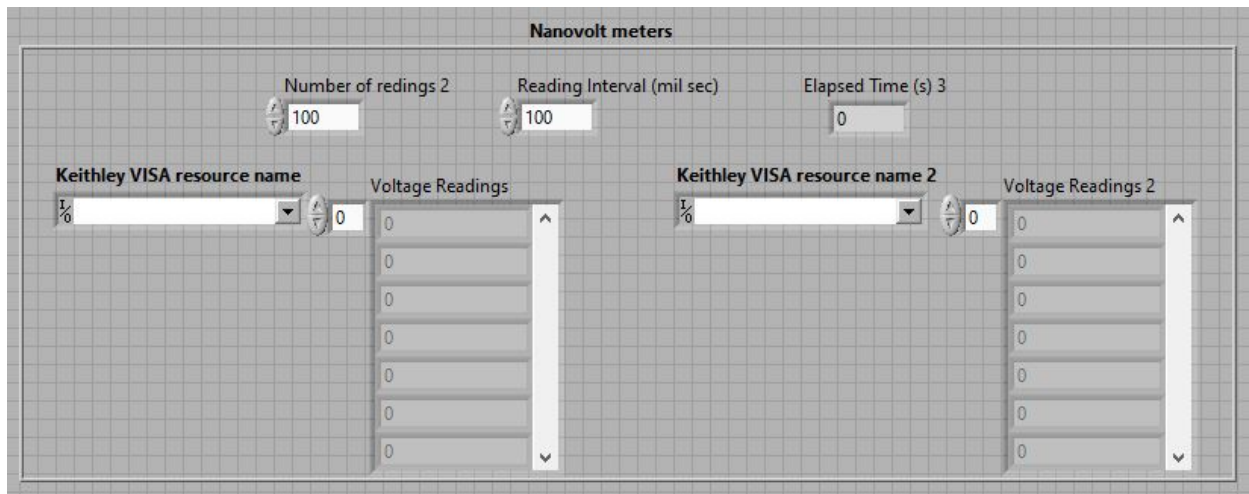
Frequency/Sample Rate/Bandwidth (1000 Hz)  
1000

DC Offset (0 V)  
0

Channel (1: 1)  
1 1

Enable Output (T: Enable)  
Enable

Figure D.5 Function generator parameters are controlled through this section.



**Nanovolt meters**

Number of readings 2  
100

Reading Interval (mil sec)  
100

Elapsed Time (s) 3  
0

Keithley VISA resource name  
COM1

Voltage Readings  
0  
0  
0  
0  
0  
0  
0

Keithley VISA resource name 2  
COM1

Voltage Readings 2  
0  
0  
0  
0  
0  
0  
0

Figure D.6 This section sets the parameters for nanovoltmeter data collection.